# Étude numérique du transfert de matière à travers l'interface d'une goutte sphérique en mouvement : mise en évidence des effets 3D

Azeddine Rachih

## To cite this version:

Azeddine Rachih. Étude numérique du transfert de matière à travers l'interface d'une goutte sphérique en mouvement : mise en évidence des effets 3D. Dynamique des Fluides [physics.flu-dyn]. Institut National Polytechnique de Toulouse - INPT, 2019. Français. NNT : 2019INPT0033 . tel-04166353

**HAL Id: tel-04166353**
**https://theses.hal.science/tel-04166353**

Submitted on 19 Jul 2023

# THÈSE

**En vue de l'obtention du**

## DOCTORAT DE L'UNIVERSITÉ DE TOULOUSE

**Délivré par :**

Institut National Polytechnique de Toulouse (Toulouse INP)

**Discipline ou spécialité :**

Dynamique des fluides

---

**Présentée et soutenue par :**

M. AZEDDINE RACHIH
le mardi 9 avril 2019

**Titre :**

# Etude numérique du transfert de matière à travers l'interface d'une goutte sphérique en mouvement : mise en évidence des effets 3D.

---

**Ecole doctorale :**

Mécanique, Energétique, Génie civil, Procédés (MEGeP)

**Unité de recherche :**

Institut de Mécanique des Fluides de Toulouse (I.M.F.T.)

**Directeur(s) de Thèse :**

M. ERIC CLIMENT
MME SOPHIE CHARTON

**Rapporteurs :**

M. BENOIT HAUT, UNIVERSITE LIBRE DE BRUXELLES
M. KOSUKE HAYASHI, UNIVERSITE DE KOBE

**Membre(s) du jury :**

M. HUAI-ZHI LI, UNIVERSITÉ LORRAINE, Président
M. DOMINIQUE LEGENDRE, INP TOULOUSE, Membre
M. EMMANUEL BELUT, INRS, Membre
M. ERIC CLIMENT, INP TOULOUSE, Membre
Mme SOPHIE CHARTON, CEA MARCOULE, Membre
Mme STEPHANIE MARTIN, CEA SACLAY, Membre

# Contents

# List of Figures

# List of Tables

## *Remerciements*

La thèse est une occasion de s'investir dans une aventure dont on arrive assez difficilement au début à définir les tenants et les aboutissants. Malgré sa nature passionnante et pleine d'enjeux, elle se montre mystérieuse voire intimidante. On s'y plonge finalement avec détermination et enthousiasme dans l'espoir d'apporter une contribution qui soit reconnue. Si cette thèse a abouti avec succès, c'est avant tout grâce à certaines personnes qui ont fait partie de cette grande aventure et à qui je dois ma reconnaissance.

J'exprime toute ma gratitude aux membres de jury : Kosuke Hayashi, Benoît Haut, Emmanuel Belut, Huai-Zhi Li, Stéphanie Martin, Dominique Legendre, Éric Climent et Sophie Charton pour l'intérêt qu'ils ont manifesté à l'égard de ce travail et je salue leurs remarques intéressantes qui ont mis en perspective l'ensemble des résultats présentés. Je remercie en particulier Benoît Haut et Kosuke Hayashi pour le temps qu'ils ont consacré à la lecture de mon manuscrit de thèse et pour la qualité de leurs remarques.

J'ai eu la chance de travailler dans différents laboratoires d'accueil pendant mon expérience doctorale qui, grâce à leurs équipes et les moyens matériels fournis, ont créé les meilleures conditions pour le bon déroulement de la thèse. Je tiens donc à remercier le CEA Marcoule et en particulier le laboratoire LGCI pour l'accueil qui m'a été réservé et le programme « SIACY » qui a financé ce travail. Je remercie également l'Institut de Mécanique des Fluides de Toulouse d'avoir mis à ma disposition les moyens de calcul dont j'avais besoin pendant ces trois années. Je remercie enfin le laboratoire EMU (Engineering Mechanics Unit) de JNCASR (Jawaharlal Nehru Centre For Advanced Scientific Research) à Bangalore en Inde qui m'a accueilli en février/mars 2018 dans le cadre du programme mobilité de l'école doctorale MeGeP.

La réussite d'une thèse est intimement liée à l'équipe encadrante. Je remercie chaleureusement les personnes qui ont encadré ce travail et contribué activement aux avancements réalisés le long de cette aventure. Merci à Dominique Legendre, Sophie Charton et Éric Climent pour la confiance qu'ils m'ont manifestée durant la thèse. J'exprime toute ma gratitude à Dominique qui a supervisé ce travail, non seulement pour avoir été l'un des créateurs du magnifique JADIM, mais aussi pour son œil d'expert, sa disponibilité, ses conseils avisés et ses fiches explicatives précieusement gardées. Avec un sens de l'humour indéniable, il a donné si souvent un aspect chaleureux à nos échanges et a permis de mieux gérer la compétition féroce entre Beamer et Powerpoint. Je remercie Sophie pour avoir co-dirigé cette thèse. Malgré son emploi du temps très chargé, elle s'est montrée toujours disponible pour m'aider à peaufiner mes rapports, analyser certains résultats et m'apprendre également le jargon marcoulien qui a facilité le coté applicatif de la thèse. Je salue également la grande sympathie dont elle a fait preuve lors des moments difficiles ainsi que ses efforts considérables pour créer l'environnement de travail le plus favorable possible. Enfin, j'adresse mes sincères remerciements à Éric. Il a su diriger cette thèse en préservant un climat serein tout au long de ces trois années et notamment durant la phase finale qui était un peu délicate. Je retiendrai l'aspect cordial de nos échanges, je salue sa pédagogie qui s'est manifestée clairement lors des petites réunions d'où je sortais avec la phrase « pourquoi je n'y ai pas pensé ?! ». Globalement, j'ai beaucoup appris sous leur tutelle et leur implication dans cette thèse en a fait un succès.

En plus de l'équipe encadrante, j'ai eu la chance de travailler avec d'autres personnes dont je souligne l'implication considérable dans cette thèse. Un grand merci à Kevin Larnier du Service COSINUS à l'IMFT pour les petites formations au début de la thèse. J'exprime aussi ma reconnaissance à Annaïg Pedrono qui a repris le flambeau en me facilitant grandement la phase développement dans le code JADIM et l'aspect informatique d'une manière générale. J'admire sa grande gentillesse et son efficacité m'a souvent impressionné. Je remercie également le service informatique du CEA Marcoule en particulier Jean Luxin qui m'a apporté une aide précieuse lors des complications informatiques Linux. Un grand merci à Claire Souilliez : je ne l'ai jamais rencontré personnellement mais ses travaux de son master m'ont accompagné le long de cette thèse. Je remercie Éric de m'avoir fait part du programme mobilité de MeGeP, celui-ci étant à l'origine de ma rencontre avec le professeur Ganesh Subramanian qui m'a accueilli dans son labo à JNCASR lors d'un séjour ineffable. J'exprime toute ma gratitude à Ganesh pour les échanges scientifiques de qualité que j'ai pu avoir avec lui. J'ai énormément apprécié les activités de son groupe. Les réunions de labo qu'il organisait étaient d'un niveau scientifique soutenu qui, je dois dire, m'ont rendu un peu nostalgique des khôlles en prépas.

J'exprime ma reconnaissance aux personnes des différents laboratoires d'accueil avec qui j'ai eu le plaisir d'échanger. Merci à Denis Ode qui était à la tête du LCGI au tout début de ma thèse et qui était également présent à ma soutenance. Je remercie également Éric Tronche qui a pris le relais du LGCI et Thierry Poinsot qui m'a accueilli au sein du groupe anciennement appelé PSC (Particule, Spray, Combustion). J'adresse mes remerciements à tous mes collègues de bureau (CEA, IMFT et à JNCASR) qui ont su créer une ambiance conviviale et amicale tout au long de ma thèse et qui sont arrivés à supporter mes histoires de goutte. Je commence par remercier Ainur Nigmetova qui m'a fait découvrir sa très belle culture kazakhe et qui m'a souvent calmé avec sa fameuse phrase « la vie est dure !» et ses délicieux muffins. Rahmet pour tout la Nour ! Merci à Tharnasis « Thanos » Boutskakis pour les discussions philosophiques qui commençaient souvent au bureau et finissaient en Grèce antique. Merci également à François Muller d'avoir continué les débats avec Tharnasis quand nous n'avions plus d'argument. Je fais part de mes remerciements à des gens que j'ai eu le plaisir de côtoyer à l'IMFT : Ibrahima « jeune homme de bonne famille » Thiam, Salvo « Roberto » Loveccheo, Solène Chevrier, Asmaa Aissaoui, Mostafa Soulaiman, Gorkem Oztarlik, Thomas Kaiser, Valentin Gosselin, Amine Chadil, Oliver Scorsim, Guiquan Wang, Laurent Selle et Thierry Shuller qui a été témoin de mes deux soutenances (master et thèse). Je remercie à présent toute l'équipe du LGCI pour la bonne ambiance et la bonne humeur qui a régné pendant mon séjour marcoulien : Hervé, Tojo, Fabrice, Gilles, Fabienne, Mireille, David×2 et Léa. Je remercie particulierement Simone « Prosperetti » Castellano pour avoir essayé de m'apprendre une chanson italienne connue d'un certain public ainsi que pour les discussions en frantalien. Je n'oublie pas les anciens à qui je dois aussi mes remerciements : un immense merci à Mathieu de Langlard, mon tout premier collègue de bureau, pour m'avoir initié à la via ferrata et qui partage ce titre avec le grimpeur de qualité Matthias Sentis pour qui j'ai de la gratitude. Merci à Mariam Oattarra pour les petites démonstrations "goutte-arc-en-ciel". Même si mon séjour indien a été court, l'équipe EMU a fait preuve d'une hospitalité et d'un accueil exemplaires, certains m'ayant même aidé à travailler mon accent indien, chose qui a beaucoup facilité mon intégration. Je remercie : Nishant, Shaurya, Pulkit, Prateek, Albin, Rafiuddin, Piyush, Swastik et Diwankar.

Je remercie naturellement toute personne qui m'a accompagné ou qui a croisé mon chemin durant ce chapitre de ma vie, qui a été consciente des difficultés de la thèse et qui n' a pas hésité à m'apporter de l'aide. J'exprime tous mes remerciements à la grande famille Taekwondo Traditionnel Avignon (Kevin, Fabien, Lilou, Laura, Elise aka Valérie, Alix, Thierry, Florence, Gétuza, Pascal, Vincent, Gab...) en particulier Kyosanim Georg « Margariiiiitti » Reinartz pour l'accueil très chaleureux et les aventures inoubliables (Osterkick, Erasmuskick). Merci à Laura Gary d'avoir suivi de près mes périples de logement. Je ne saurais jamais assez remercier Omar Bellahsen pour ses conseils perspicaces et pour sa bonne humeur permanente. J'exprime toute ma reconnaissance à mon vieil ami Anas Fettach pour les longues discussions qui n'avaient strictement aucun sens mais qui m'ont permis si souvent d'esquisser des rires malgré les « segmentaion fault ». Je remercie mon amie Pauline Marty pour les discussions intéressantes, la délicieuse pâte de coing et d'être toujours aussi encourageante et sympathique.

Enfin, je conclue ces lignes en rendant hommage à deux personnes qui ont fait de moi ce que je suis maintenant et sans qui rien de tout cela n'aurait été possible. Malgré la distance qui nous sépare, ils se sont constamment montrés à mes côtés pendant les hauts et les bas. Leurs pensées et prières m'ont accompagné tout au long de mon parcours et, grâce à eux, tout ce que je réalise dans cette vie prend sens. Les voir heureux est la meilleure récompense que je puisse avoir. C'est vrai qu'un simple merci ne suffira jamais pour exprimer toute la reconnaissance que j'éprouve à l'égard de mes parents, mais ce que je pourrais leur dire :« رَب ارْحَمْهُمَا كَمَا رَبَيانِي صَغِيرًا » (« Ô Seigneur, accorde leur ta miséricorde, ils m'ont élevé »). Je remercie également ma seule et unique sœur Sanaâ, toujours là pour m'insuffler du courage et me corriger les fois où j'oubliais certains mots de ma langue maternelle.

إِلَـــى أَبَوايَ وَ أُخْتِـــي

***Résumé***

L'étude du transfert de matière entre deux phases immiscibles, l'une étant dispersée dans l'autre, constitue une étape clé dans le développement et l'optimisation des procédés d'extraction par solvant. Le caractère multiphasique et multi-échelles de ces procédés rend souvent leur étude très complexe. Aussi, une description fine à l'échelle d'une goutte isolée est un préalable indispensable à la compréhension du comportement des procédés mettant en jeu des nuages ou des populations de gouttes (de formes et tailles variées).
Ce travail est consacré particulièrement à l'étude par simulation numérique directe de l'hydrodynamique et du transfert de matière couplés à travers l'interface d'une goutte sphérique, placée dans une autre phase immiscible en écoulement uniforme. Les équations complètes de Navier-Stokes et de transport de la concentration du soluté sont pour cela résolues, en coordonnées curvilignes orthogonales, par une méthode de volumes finis. Une attention particulière est portée à l'implémentation des conditions à l'interface liquide-liquide afin de correctement représenter le couplage des phénomènes internes et externes à la goutte.
On s'intéresse dans cette étude au transfert sans réaction chimique d'un soluté extractible, de la goutte vers la phase continue. Nous avons conduit une étude de sensibilité paramétrique couvrant une large gamme de conditions opératoires (rapport de densité, viscosité, et diffusivité, coefficient de partage de soluté) sur la variation du nombre de Sherwood. Les résultats montrent que la structure du champ de vitesse dépend fortement du nombre de Reynolds et du rapport de viscosité. L'évolution du nombre de Sherwood révèle en outre une forte influence du coefficient de partage et du rapport de diffusivité, tant sur son évolution temporelle que sur sa valeur asymptotique. L'ensemble des configurations étudiées a permis de relier le nombre Sherwood global aux valeurs représentatives des problèmes de transfert interne et externe. Les résultats numériques montrent que le comportement axisymétrique typique des configurations à Reynolds interne/externe modéré ($Re \leq 100$), n'est plus valable au delà de $Re = 300$. Dans ces conditions, les simulations mettent en évidence des bifurcations tridimensionnelles internes du champ de vitesse ce qui impacte fortement la distribution spatiale de la concentration et ainsi la physique et la rapidité du transfert.

**Mots-clès** : Goutte, Transfert de matière, Simulation Numérique Directe, Nombre de Sherwood

### *Abstract*

The study of mass transfer in dispersed two-phase flows is a major key step toward the development and optimization of extraction solvent processes. The description of these processes is generally intricate due to the multiphase and multi-scale flow nature. In addition, a description of the process at the scale of an isolated drop is an elementary step toward a good understanding of systems involving droplet swarms (with different shapes and sizes).

This work is devoted primarily to the study, by mean of DNS, of the hydrodynamics and conjugate mass transfer through the interface of a spherical droplet set in a uniform flow of another immiscible phase. The Navier-Stokes equations and the concentration transport equations are solved in orthogonal curvilinear coordinates using a finite volume method. A specific boundary condition is implemented in order to accurately represent the convection/diffusion and mass transfer coupling at the interface.

Considering the internal and external phenomena, we focus in this study on the solute transfer through the interface, from the drop to the continuous phase. A parametric study is performed, covering a large range of operational conditions including viscosity ratio, density ratio, diffusivity ratio and solute distribution coefficient. The results show a strong dependence of the flow structure on the Reynolds number and viscosity ratio. The analysis of the Sherwood number reveals a significant impact of physical properties (distibution coefficient, diffusivity ratio) on both its temporal evolution and its steady value. The studied configurations allows to relate the global Sherwood number to the ones representing internal and external problems. The numerical simulations show that the axisymmetric assumption of the velocity field valid, at moderate internal/external Reynolds number ($Re \leq 100$), is no longer correct beyond $Re = 300$. Simulations reveal three-dimensional internal bifurcations of the velocity field that impact significantly the concentration spatial distribution and thus the physics and rate of the transfer

**Keywords** : Drop, Mass transfer, Direct Numerical Simulation, Sherwood number

# Nomenclature

## List of symbols

| | |
|---|---|
| $(\xi_i)_{1\leq i\leq 3}$ | curvilinear coordinates |
| $\mu$ | kinematic viscosity |
| $\nu$ | dynamic viscosity |
| $\omega$ | vorticity |
| $\overline{C_s}$ | surface average mass concentration |
| $\overline{C}$ | volume average mass concentration |
| $\Phi$ | total mass flux |
| $\Psi$ | stream function |
| $\rho$ | density |
| $\sigma$ | surface tension |
| $\theta$ | angle between droplet front and a given point at the interface |
| $C$ | mass concentration |
| $C_0$ | initial mass concentration |
| $C_\infty$ | free-stream mass concentration (far from drop) |
| $D$ | mass diffusivity |
| $d$ | sphere diameter |
| $h$ | mass transfer coefficient |
| $h^e$ | external mass transfer coefficient |
| $h^i$ | internal mass transfer coefficient |
| $H^i_j$ | curvature terms |
| $h_i$ | metric parameter |
| $k$ | equilibrium coefficient |
| $R$ | sphere radius |
| $t$ | time |
| $U_0$ | free-stream velocity |
| $V_i$ | curvilinear velocity along the coordinate $\xi_i$ |

## Subscript

| | |
|---|---|
| $s$, $I$ | refers to the surface/interface of the drop |

## Dimensionless numbers

| | |
|---|---|
| $C_D$ | drag coefficient |
| $Eo$ | Eötvös number |
| $Fo$ | Fourier number based on the radius |
| $M$ | Morton number |
| $Pe^e$ | internal Peclet number |
| $Pe^i$ | internal Peclet number |
| $Re^e$ | external Reynolds number |
| $Re^i$ | internal Reynolds number |
| $Sc^e$ | external Schmidt number |
| $Sc^i$ | internal Schmidt number |
| $Sh$ | global Sherwood number |
| $Sh^E$ | Sherwood number of an external problem (concentration constant and uniform at the interface) |
| $Sh^e$ | external Sherwood number: driving force $(\overline{C^e_s} - C^e\infty)$ |

| | |
|---|---|
| $Sh^I$ | Sherwood number of an internal problem (concentration constant and uniform at the interface) |
| $Sh^i$ | internal Sherwood number: driving force $(\overline{C^i} - \overline{C^i_s})$ |
| $Sh_\theta$ | local Sherwood number of an internal problem |

**Superscript**

| | |
|---|---|
| $*$ | refers to dimensionless ratio of a physical property $x$ : $x^i/x^e$ |
| $'$ | dimensional quantity |
| $e$ | refers to the surrounding fluid |
| $i$ | refers to the interior of the drop |

# Chapter 1

# Introduction

## Contents

## 1.1 General context and industrial interest

This study is part of a CEA project dedicated to the simulation of the fuel treatment process, which is an essential part of the nuclear fuel cycle in France. Fuel treatment is primarily aimed at selectively separating uranium and plutonium to be recycled in new fuel assemblies. By isolating these major actinides from other irradiated fuel components, it also enables a significant reduction of the nuclear wastes, as only the fission products and minor actinides (the ultimate wastes) have to be managed. The latter are vitrified and thus stabilized before their deep geological disposal.

### 1.1.1 The PUREX process

The fuel processing plant at La Hague is based on the PUREX process (Plutonium and Uranium Refining by Extraction). This hydrometallurgical process implement a succession of multiphase steps. It starts from the dissolution of the irradiated fuel in a hot nitric acid liquor, followed by a series of extraction /purification steps achieved in liquid-liquid contactors, and ending by the reactive precipitation of plutonium oxalate particles. Finally, thanks to proper thermal and mechanical transformations, a powder of plutonium oxide with precise specifications is obtained, that is used for MOX fuel fabrication.

Solvent extraction is a key step of the PUREX process, and more generally of hydrometallurgical processes, such as rare earth and transition metals purification. In this liquid-liquid process, an organic solvent, 30% tributyl phosphate (TBP) diluted in kerozene-like hydrocarbon, is contacted with the nitric acid solution containing the elements to be separated.

TBP was chosen for its high selectivity towards uranium and plutonium, its good resistance to radiolysis and hydrolysis in nitric media, and for its good purification and recycling capacity. The metallic species are extracted as neutral organophilic complexes that nitrates form with TBP according the reaction:

$$M^{m+}_{(aq)} + mNO_3^-{}_{(aq)} + \overline{nTBP_{(org)}} \rightleftharpoons \overline{M(NO_3)_m \cdot nTBP_{(org)}}$$

The separation is based on the stability differences of these complexes: the nitrates of metallic species with oxidation levels $IV$ and $VI$ are more strongly complexed by TBP, than those with oxidation levels $I$, $II$, $III$ and $V$. They are therefore more likely to be extracted.

### 1.1.2 Today's needs and challenges in solvent extraction

Although it is a mature technology, solvent extraction is still an important field of research in order to meet the new environmental challenges. Especially, circular economy requires higher selectivity to be reached, in order to improve recovery yields from dilute and multicomponent ores and wastes, while minimizing the required amounts of water, chemicals and organic solvent.

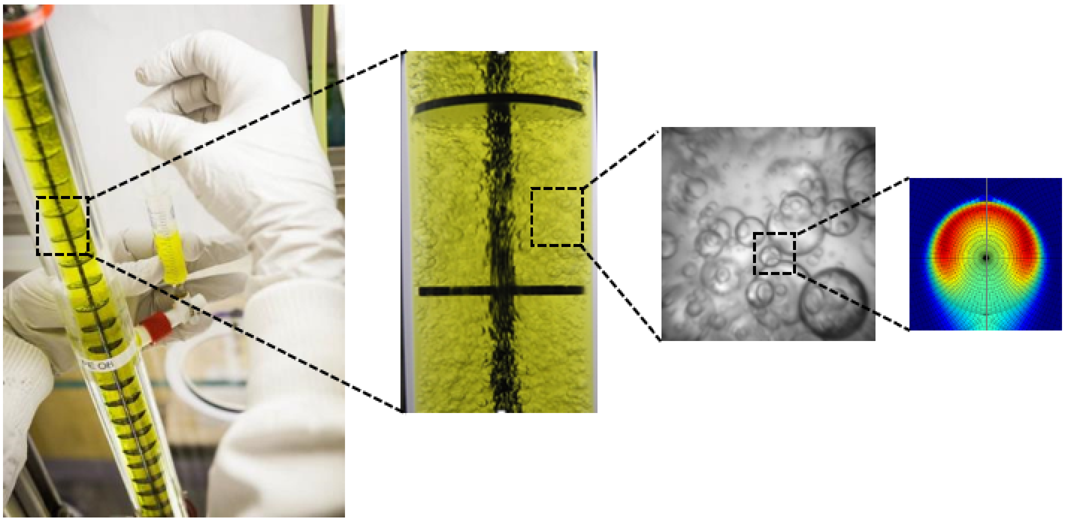

Figure 1.1: From left to right: Small scale pulsed column used for R&D study in nuclear ennvironment at CEA Marcoule, details of the droplets swarm, schematic of mass transfer phenomena at the drop level.

Similar challenges have to be faced by the nuclear industry for the development of future nuclear systems involving repeated recycle of plutonium. In this aim, replacing tributyl phosphate (TBP) by a new solvent with higher resistance to radiation damages, and allowing to minimize the use of Redox and chemical agents, is an active field of research at CEA.

On the other hand, the development of phenomenological models for liquid-liquid extraction processes is essential to design new fuel treatment processes. Numerical simulation would indeed reduce the need for large-scale pilots and the amount of chemical and radioactive materials involved in R&D studies. This would of course be very beneficial from an economic and environmental point of views.

The derivation of reliable numerical models however requires a sound understanding of the many phenomena involved, and their coupling. In particular, understanding the role of hydrodynamic on how, where, and how fast mass transfer occurs between the organic and the aqueous phase is of prime importance.

In solvent extraction columns (Fig. 1.1), the contact surface between the two immiscible liquids is enhanced by dispersing one phase in the form of droplets in the second. This dispersion is generally achieved by supplying energy to the system (mechanical stirring, pulsation, etc.). The estimation of mass transfer rate in such an apparatus is inherently a complex task Slater [1994]: droplets are present in swarms with different sizes and shapes, the relative velocity and residence time of these droplets moreover depends on the physical properties (density, viscosity, surface tension), themselves possibly evolving with the exchanged solute(s) concentration, etc.

In this context, having a precise knowledge of the mechanisms responsible for the transfer of a solute at the level of a single drop, would be a major step towards the prediction of the apparent mass transfer rate in industrial contactors. This is the aim this thesis.

## 1.2 Mass transfer in multiphase flow

Solute transfer occurs primarily at the interface between the conitnuous phase and the droplets. Considering a single droplet (see figure 1.2), the transferred flux, $\Phi$, can be written as the product of a transfer coefficient, $h$, a transfer surface, $S$, and a driving force $\Delta C$: $\Phi = h \times S \times \Delta C$. In this classical representation, $h$ is an unknown, but major parameter, which depends not only on the physical and chemical parameters of the problem, but also on the flow characteristics that can affect the transport of solute outside and inside the droplet (*i.e.* whether the drop is internally stagnant, circulating, or oscillating).

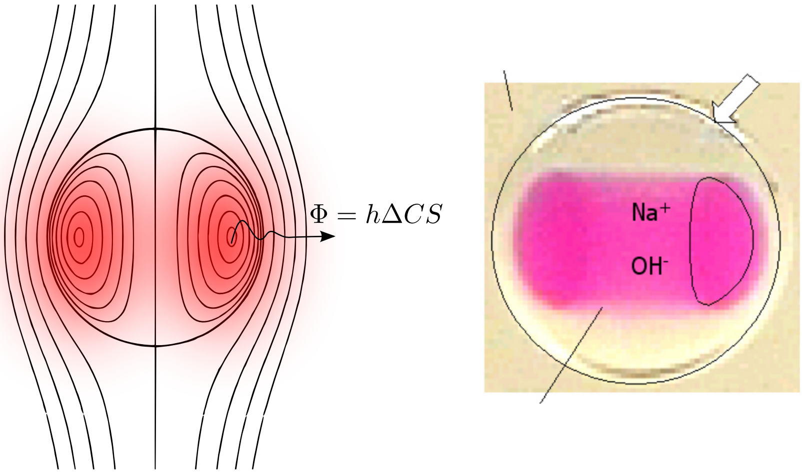

Figure 1.2: Left: Mass transfer from a rising droplet in a liquid phase, Right: Experimental evidence of internal transport due to the internal circulation: case of a sodium hydroxide droplet in cyclohexanol. The transfer of acetic acid is evidenced by phenolphthalein Schulze [2007].

### 1.2.1 Hydrodynamic aspects

The motion of small particles, bubbles and droplets, in fluid media is of fundamental concern in various industrial and environmental problems. Even though we will be focusing essentially on droplets behaviour in a immiscible liquid medium, it is meaningful to introduce the behaviour of particles and bubbles in a fluid phase, as they can be seen as limiting cases of droplets. Indeed, in a continuous liquid phase, when $\mu^* \rightarrow 0$, the droplet may be considered as a bubble, while $\mu^* \rightarrow \infty$ corresponds to a rigid particle. In practice for a droplet in the liquid phase the range of $\mu^*$ is in the interval $[0.1, 10]$

Paschedag et al. [2005].

A characteristic feature of bubbles and drops undergoing mass transfer is their free surface determined by the force balance acting thereon (cf. 2.1.2), and responsible for the various shapes they can take. As the motion and rate of mass transfer of bubbles and drops are highly related to their shapes, it is usual to introduce shape parameters, such as the sphericity coefficient or the circularity coefficient, to enable to refer the simpler study of spherical particles (see Clift et al. [1978] and Michaelides [2006] for discussions on that topic).

#### 1.2.1.1 Shapes of bubbles/droplets

Below a critical diameter $d_c$, that indicates the onset of oscillations Johnson and Braida [1957], the equilibrium shape achieved by a moving bubble or droplet is function of several parameters. Among them, the interactions of the surface tension and the shear stress exerted by the surrounding fluid, the physical properties of the system, the size and shape of the flow domain/container are the more influent ones.

Many studies have been dedicated to the shape of a moving bubble or droplet in a fluid in the case of a fully mobile interface (i.e. a complete absence of impurities or surfactants). Three main shape categories have been highlighted: spheres, ellipsoids and spherical (or elliptical) caps. The experimental studies have considered freely rising or falling bubble or droplet in an infinite fluid medium. The different shapes achieved have been mapped by Clift et al. [2005] in what is commonly called the "Clift diagram" (cf Figure 1.3). The latter relates the bubble/droplet shape to three dimensionless numbers (see Figure 2.1 for notations):

- The Reynolds number $Re$:

$$Re = \frac{\rho^e v_t d}{\mu^e} \tag{1.2.1}$$

- The Eötvös number, $Eo$, that represents the ratio of the buoyancy and the surface tension forces:

$$Eo = \frac{\Delta\rho g d^2}{\sigma} \tag{1.2.2}$$

- The Morton number $M$, which depends only on the physical properties, and is hence commonly used in dimensional analysis:

$$M = \frac{g {\mu^e}^4 |\rho^e - \rho^i|}{{\rho^e}^2 \sigma^3} \tag{1.2.3}$$

| | Aqueous phase | Typical solvents | New solvents |
|---|---|---|---|
| Density (Kg/L) | 1.17 | 0.97 | 0.97 |
| Viscosity (mPa/.s) | 1.0 | 2.4 | 14 |
| Surface tension (mN/m) | - | 10 | 20 |
| Morton number $(-)$ | - | $1.43\,10^{-09}$ | $1.34\,10^{-10}$ |

Table 1.1: Physico-chemical properties of liquids used in solvent extraction processes. "Typical solvents" stands for the TBP 30% in TPH mixture used in the PUREX process whereas "New solvents" gives envelope values for alternative solvents under development.

In these expressions, the diameter $d$ or the volume-equivalent diameter $d_e$ [1] is used as a reference lenght scale, and the terminal velocity $v_t$ as a velocity reference.

The Clift diagram was initially derived for bubbles. Grace et al. [1976] made slight modifications to adapt it to droplets. However, it does not apply to particles with extreme $\rho^*$ and $\mu^*$ values. A first observation of this diagram enables to draw quick conclusions regarding the particle's shape:

- Spheres prevail at low $Re$, regardless of the $Eo$ value, and at intermediate values of Re when $Eo < 1$;
- Ellipsoids prevail at intermediate values of $Eo$ and high $Re$;
- Spherical cap is the preferred shape at high $Eo$ numbers and relatively high $Re$.

These results apply only for surfactant-free systems, or pure fluid particles, where no additional effect (such as Marangoni, wall, etc.) is present.

### 1.2.1.2 Droplet's shape of interest for the study

As illustrated in Figure 1.3, a significant proportion of the map corresponds to spherical and oblate ellipsoidal droplets, and most of liquid-liquid extraction studies in literature consider the droplets in this area. In order to further assess the shape of the droplets under typical operating conditions, we considered the two sets of physical properties gathered in Table 1.1. The first set of data refers to the liquid-liquid system used in the nuclear fuel treatment process (PUREX). These properties are also typical of most industrial solvent extraction processes. The second set of data ("new solvent"), on the other hand, represents envelope values of the possible physical properties of the solvents being studied for repeated recycle of plutonium (Sec. 1.1.2).

The Morton number values obtained for a drop of each of the solvents in the considered aqueous phase are also shown in Table 1.1. If we postpone these $M$ values

---

[1] $d_e$ stands for the equivalent sphere diameter of the deformed bubble or droplet, defined by $d_e = \sqrt[3]{\frac{6V}{\pi}}$ where $V$ is the fluid particle volume

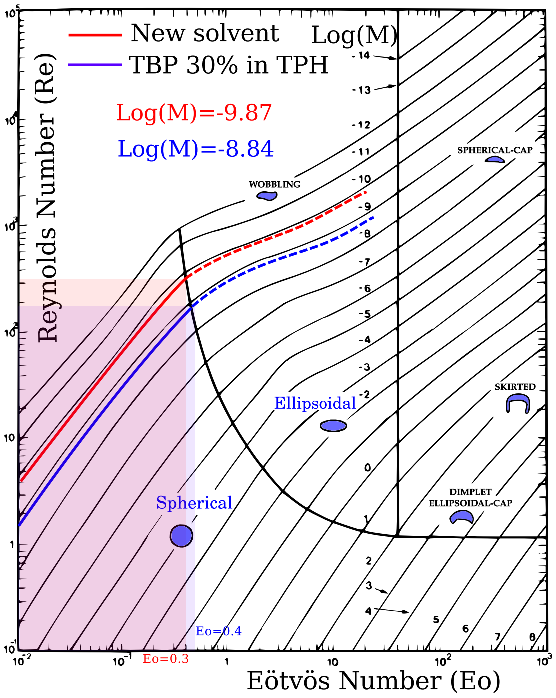

Figure 1.3: The shape map of the bubbles/dropsClift et al. [1978], coloured areas delimit shapes of droplets with diameter inferior to 2.5mm.

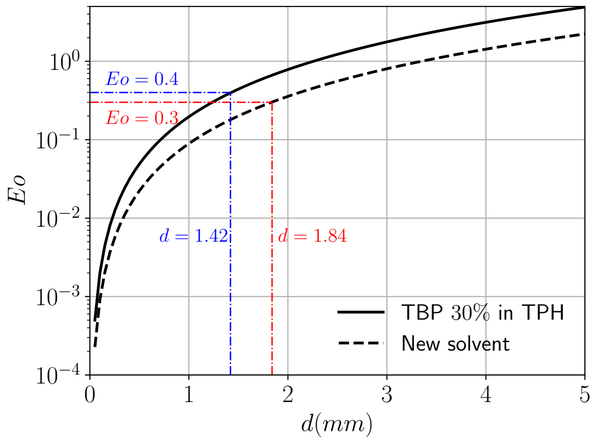

Figure 1.4: Variation of the $Eo$ number with the diameter for droplets of each solvent in the aqueous phase.

in the adjusted Clift diagram (Fig. 1.3) we find that the droplets will have a spherical shape as long as $Eo \leq 0.3$ and $Eo \leq 0.4$ respectively, which corresponds to droplets smaller than $d = 1.42$ and 1.84 mm according to Figure 1.4. These limits are greater than the typical droplet size achieve in liquid liquid extraction processes, lying between some 100 micrometers and 1mm, depending on the considered contactor (pulsed or agited column, mixer-settler, annular centrifugal contactor). Spherical droplets will therefore be the focus of our study.

#### 1.2.1.3 Drag coefficient

The drag coefficient of a translating single particle (rigid particle, bubble or drop) is a major hydrodynamic parameter that has been heavily investigated (see Clift et al. [1978] for a review of these studies). The main correlations published for spherical particles are gathered in Table 1.2.

While it is primarily presented as a function of $Re$ and the viscosity ratio $\mu^*$, the drag coefficient $C_D$ depends on the droplet/bubble shape as well. Liquid(s) purity might be influencing too. Indeed, traces of surface-active contaminants may have a substantial effect on the interface mobility and consequently on the behaviour of drops and bubbles. Thus, even if there is no measurable change in the bulk fluid properties, a contaminant can eliminate internal circulation within a droplet, thereby significantly increasing its drag coefficient Sadhal and Johnson [1983].

It is expected that drops undergo slight deformations by moving in a viscous fluid. Harper [1972] calculated the variation of the droplet drag coefficient as a function of their eccentricity, $\epsilon$. His results show that, at low values of $\epsilon$, the increase in the drag coefficient is proportional to the eccentricity.

#### 1.2.1.4 Terminal velocity

The terminal velocity, $v_t$ , is defined as the final velocity a particle can reach when it falls or rises in a quiescent fluid. It is the reference velocity for the Reynolds number figured in the Clift diagram 1.3. It is closely related to the drag coefficient $C_D$.

$v_t$ can be derived from the motion equation of the particle. The forces acting on the particles are the buoyancy force, which is proportional to $\Delta\rho$, and the friction exerted on its surface by the continuous phase. Once the terminal velocity is reached, there is no more acceleration, and the two forces balance ($drag = buoyancy$). For a spherical particle it writes:

$$\frac{3}{4}\frac{\rho_c}{\rho_d + \kappa\rho_c} C_D \frac{\mathbf{v_t^2}}{d} = \frac{|\Delta\rho|}{\rho_d + \kappa\rho_c}\mathbf{g} \tag{1.2.4}$$

where $\kappa$ is a coefficient accounting for the fraction of the continuous fluid that is accelerated by the particle (added mass force).

Although fluid particles generally exhibit a higher terminal velocity than the solid particles, because of their interface mobility, it should be noted that the common

| Source | $C_D$ correlation | Range of validity |
|---|---|---|
| Stokes [1851] | $C_D = \frac{24}{Re}$ | $Re \ll 1$ (rigid) |
| Schiller [1933] | $C_D = \frac{24}{Re}\left(1 + 0.15Re^{0.687}\right)$ | $Re < 800$ (rigid) |
| Mei and Klausner [1992] | $C_D = \frac{16}{Re}\left[1 + \left(\frac{8}{Re} + 0.5\left(1 + 3.315Re^{-0.5}\right)\right)^{-1}\right]$ | $0.1 \leq Re \leq 200$ (bubble) |
| Rybczynski [1911] | $C_D = \frac{8}{Re}\frac{2+3\mu^*}{1+\mu^*}$ | $Re \ll 1$ |
| Saboni and Alexandrova [2002] | $C_D = \frac{\left[\mu^*\left(\frac{24}{Re}+\frac{4}{Re^{1/3}}\right)+\frac{14.9}{Re^{0.78}}\right]\cdot Re^2+40\frac{3\mu^*+2}{Re}+15\mu^*+10}{(1+\mu^*)(5+Re^2)}$ | $Re < 400$; $0.01 < \mu^* \leq 1$ |
| Ryvkind and Ryskin [1976] | $C_D = \frac{1}{\mu^*+1}\left[\mu^*\left(\frac{24}{Re} + \frac{4}{Re^{1/3}}\right) + \frac{14.9}{Re^{0.78}}\right]$ | $10 \leq Re < 100$ |
| Feng and Michaelides [2001a] | $C_D = \frac{2-\mu^*}{2}C_D(Re,0) + \frac{4\mu^*}{6+\mu^*}C_D(Re,2)$ | $5 < Re < 1000$; $0 \leq \mu^* \leq 2$ |
| | $C_D = \frac{4}{\mu^*+2}C_D(Re,2) + \frac{\mu^*-2}{\mu^*+2}C_D(Re,\infty)$ | $5 < Re < 1000$; $2 < \mu^* \leq \infty$ |
| With functions | $C_D(Re,0) = \frac{48}{Re}\left(1 - \frac{2.21}{\sqrt{Re}} + \frac{2.14}{Re}\right)$ | |
| | $C_D(Re,2) = 17.0Re^{2/3}$ | |
| | $C_D(Re,\infty) = \frac{24}{Re}\left(1 + \frac{1}{6}Re^{2/3}\right)$ | |

Table 1.2: Main correlations for the drag coefficient $C_D$ of spherical particles.

observation is that bubbles and drops tend to fall with the solid-sphere terminal velocity, especially if they are small. This is mainly due to surface impurities that tend to reduce surface tension. Clift et al. [1978] gives a detailed discussion about this.

Wegener et al. [2014], in its experimental study, highlighted 3 distinct regimes for a given liquid/liquid system (i.e. with+fixed physical properties), according to the shape of the droplet's interface:

- Spherical regime, in which $v_t$ increases with the droplet diameter,
- Transition regime, in which droplets deform more and more to oblate shape. $v_t$ reaches a maximum and then decreases with the diameter,
- Oscillatory regime, in which $v_t$ slightly decreases with droplet diameter, droplets can oscillate and exhibit more irregular shapes.

### 1.2.2 Mass Transfer aspects

One particularity of mass transfer problems with respect to heat transfer problems is that the value of the scalar at the interface is not only fixed by the continuity of the flux, but that it also obey the partition law (i.e. equilibrium distribution) of the solute between the two phases

Three distinct behaviours are distinguished for the mass transfer related to rigid particles, bubbles or drops, depending on the location of the main resistance to mass transfer. They are generally referred to as: internal problem (when the main resistance is located in the particle), external problem (main resistance outside) and conjugate problem (when both resistances are comparable) respectively.

For a solute with a partition coefficient $k$, and assuming diffusion is the only transport mechanism, the mass transfer regime can be assessed by the value of the quantity $k\sqrt{D^i/D^e}$ Brauer [1978]. Hence, if $k\sqrt{D^i/D^e} << 1$ the problem is supposed to be internal, it is considered external when $k\sqrt{D^i/D^e} >> 1$, and a conjugate problem prevails when $k\sqrt{D^i/D^e} \approx 1$.

#### 1.2.2.1 External problem

In external problems (i.e. when the solute transport is fast inside the droplet), uniform solute concentration prevails in the droplet and along the interface at any time of the transfer process. Most of the numerical studies labelled as external mass transfer consider a constant concentration at the interface which might be sometimes misleading.

Abramzon and Fishbein [1977] addressed numerically the convection-diffusion transport of a solute transferred from a droplet in a Stokes flow ($Re \ll 1$), for Peclet numbers $Pe < 1000$. The same authors also considered the very closed transient heat transfer problem in a Stokes flow, in a rather large range of Peclet number $1 < Pe < 10000$ [Abramzon and Elata, 1984].

Many numerical studies were proposed for intermediate Reynolds flows (see e.g. Alexandrova et al. [2014a]; Feng and Michaelides [2001b]; Saboni et al. [2011]), and correlations of mass transfer coefficient have been proposed by Feng and Michaelides [2001b].

A review of the main correlations for external problems in circulating drops is given by Kumar and Hartland [1999]. Table 1.2 displays some of the most used Sherwood correlations for spheres in uncontaminated systems. However, many studies (Beitel and Heideger [1971]; Lewis and Pratt [1953]) evidence an enhanced mass transfer rate in contaminated systems.

| Author (Source) | correlation | Range of validity |
|---|---|---|
| Acrivos and Taylor [1962] | $Sh = 0.991 Pe^{1/3}\left(1 + \frac{1}{16}Re + \frac{3}{160}Re^2\ln(Re) + O(Re^2)\right)$ | $Re \leq 1$; $Pe \gg 1$ (rigid) |
| Clift et al. [1978] | $Sh = 1 + (1 + Pe)^{1/3}$ | $Re \leq 1$ (rigid) |
| Feng and Michaelides [2001b] | $Sh = 0.651 Pe^{1/2} + 1.6$ | $Re << 1$; $\mu^* = 0$ (bubble) |
| Levich et al. [1962] | $Sh = \left(\frac{4}{3\pi}\frac{1}{1+\mu^*}Pe\right)^{1/2}$ | $Re \ll 1$; $Pe \gg 1$ |
| Clift et al. [1978] | $Sh = \frac{2}{\sqrt{\pi}}\left[1 - \frac{\frac{2+3\mu^*}{3(1+\mu^*)}}{\left[1+\left[\frac{(2+3\mu^*)Re^{1/2}}{(1+\mu^*)(8.67+6.45\mu^*)}\right]^n\right]^{1/n}}\right]^{1/2} Pe^{1/2}$<br>With $n = \frac{4}{3} + 3\mu^*$ | $10 < Re < 100$; $\mu^* < 2$; $\rho^* < 4$; $Sc \gg 1$ |
| Feng and Michaelides [2001b] | $Sh = \frac{2-\mu^*}{2}Sh(0, Pe, Re) + \frac{4\mu^*}{6+\mu^*}Sh(2, Pe, Re)$ | $1 \ll Re \leq 500$; $0 \leq \mu^* \leq 2$; $10 \leq Pe \leq 1000$ |
| | $Sh = \frac{4}{\mu^*+2}Sh(2, Pe, Re) + \frac{\mu^*-2}{\mu^*+2}Sh(\infty, Pe, Re)$ | $1 \ll Re \leq 500$; $2 \leq \mu^* \leq \infty$; $10 \leq Pe \leq 1000$ |
| With functions | $Sh(0, Pe, Re) = 0.651 Pe^{1/2}\left(1.032 + \frac{0.61Re}{Re+21}\right) + \left(1.6 - \frac{0.61Re}{Re+21}\right)$<br>$Sh(\infty, Pe, Re) = 0.852 Pe^{1/3}\left(1 + 0.233 Re^{0.287}\right) + 1.3 - 0.182 Re^{0.355}$<br>$Sh(2, Pe, Re) = 0.64 Pe^{0.43}\left(1 + 0.233 Re^{0.287}\right) + 1.41 - 0.15 Re^{0.287}$ | |

Table 1.3: Main $Sh$ correlations of external mass transfer.

#### 1.2.2.2 Internal problem

The solution of the internal problems, where the stream flow imposes the concentration value at the interface, was first derived analytically by Newman [1931]. For this problem controlled by pure diffusion ($Pe/(\mu^* + 1) \longrightarrow 0$) in the spherical droplet, the author showed that the asymptotic value of the Sherwood number converges toward $Sh_{Newman} = 6.58$.

Later, Kronig and Brink [1951] considered the case of a circulating droplet in a creeping flow, with $Pe/(\mu^* + 1) \rightarrow \infty$. They highlighted another asymptotic value of the Sherwood number $Sh_{Kronig} = 17.9$.

In all other configurations however, finding an analytical solution is less straightforward and a numerical approach is required. Thus, Juncu [2001b] numerically solved the mass transport equation for intermediate Peclet numbers, based on the Hadamard-Rybczynski solution for creeping flow, and Colombet et al. [2013] addressed intermediate Reynolds flows in the case of a small viscosity ratio ($\mu^* = 0.018$).

More recently, Juncu [2010], by means of direct numerical simulations, derived a correlation of the Sherwood number as a function of an effective Peclet number.

#### 1.2.2.3 Conjugate problem

While the internal/external problems have been heavily studied, the solution of the conjugate problems is still an active area of research. This type of problems requires the knowledge of the spatial and time evolutions of the solute concentration in both the continuous and the dispersed (i.e. droplet) phases.

In creeping flow, Ruckenstein [1967] derived an analytical equation for the Sherwood number based on similarity variables. Cooper [1977] found an analytical solution for the conjugate transfer at low Peclet.

Still in creeping flows, Oliver and Chung [1986] considered the heat transfer from a translating droplet. The transient diffusive convective heat conservation equation is solved in a flow field governed by the Hadamard-Rybczynski equation. The effect of the volumetric heat capacities ratio was illustrated for different Peclet numbers. A similar configuration was considered by Kleinman and Reed [1996] and Juncu [2001a] for mass transfer where the parametric study moreover considered the influence of the partition coefficient $k$. The showed that the direct application of the addition rule (see Sec.1.2.2.4), was not rigorous in these configurations, due to differences in the interface concentration. The authors proposed a correction to take into account the interface concentration in the definition of the Sherwood number.

A more general sensitivity study of the temporal evolution of the Sherwood number was proposed by Paschedag et al. [2005].

#### 1.2.2.4 Classical mass transfer theories

In earlier works, many theories and models have been developed in order to quantify the mass flux from one phase to another. Although not universal, these models are commonly used in chemical engineering for the estimation of mass transfer coefficients. Here we present the most classical theories.

**The film theory**, first proposed by Lewis and Whitman [1924] is based on the presence of a fictitious laminar fluid film close to the interface. In the case of two immiscible fluids in contact, two films are considered, one on each side of the interface (i.e. double-film theory). The solute transport is considered to be entirely driven by steady-state molecular diffusion in the film, generally assuming a linear concentration gradient (linear driving force approximation), while a uniform concentration is considered outside (bulk). If $\delta_c$ is the film thickness in the continuous phase (phase 2 with the notations that will be introduced in Chap. 2), the transfer coefficient $h_c$ writes:

$$h_c = \frac{D_c}{\delta_c} \tag{1.2.5}$$

This theory offers some explanation of the mechanism of the mass transfer in fluid media, it does not provide any means to estimate the thickness of the concentration film.

In the film theory, the mass transfer resistances are considered in series, which is convenient to relate the flux to the known (or measurable) concentrations. As depicted in Figure 1.5, the mass transfer flux, $\varphi$, can be written using each of the following formulas:

$$\begin{aligned}\varphi &= -D_1 \nabla C_{A1} = h_1(C_{A1} - C^i_{A1}) = H_1(C_{A1} - C^{eq}_{A1}) &(1.2.6)\\ &= -D_2 \nabla C_{A2} = h_2(C^i_{A2} - C_{A2}) = H_2(C^{eq}_{A2} - C_{A2}) &(1.2.7)\end{aligned}$$

$h_i$ is the mass-transfer coefficient in phase $i$ whereas $H_i$ stands for the overall mass-transfer coefficient based on phase $i$, meanings that it accounts for the resistances from both sides. Both $h_i$ and $H_i$ are expressed in [moles of A transferred/(time)(interfacial area)].

The set of relations above is complemented by the equilibrium relation at the interface (see Fig. 1.5). After some simplifications, we obtain the following system:

$$\begin{aligned}\frac{1}{H_1} &= \frac{1}{h_1} + \frac{k}{h_2} &(1.2.8)\\ \frac{1}{H_2} &= \frac{1}{h_2} + \frac{1}{kh_1} &(1.2.9)\end{aligned}$$

The film, or double-film, model is one of the most used in the chemical engineering community, given its simplicity and reliable estimations in simple cases. It is used in the PUREX process simulator developed at CEA.

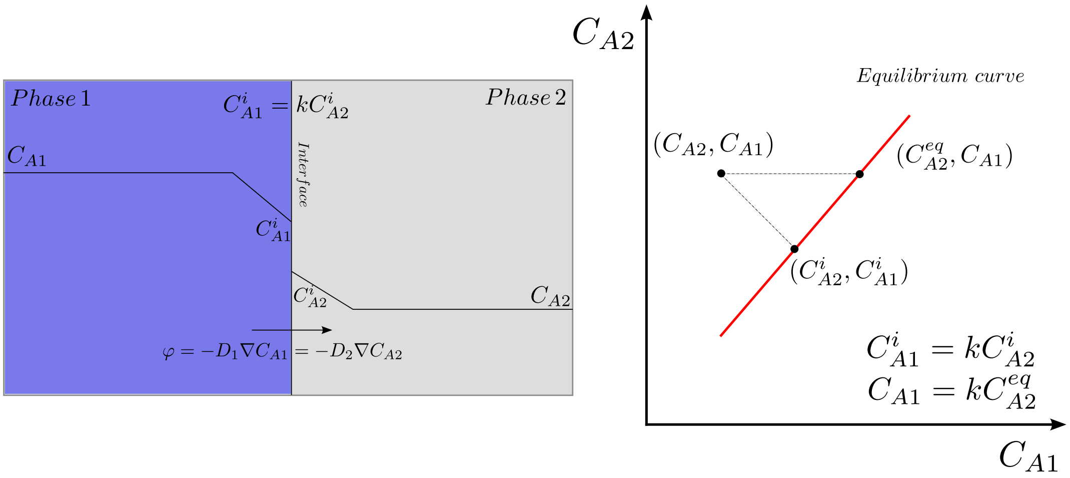

Figure 1.5: Schematic representation of mass transfer of $A$ from phase 1 to phase 2 (left) and related thermodynamic equilibrium curve (right).

**Penetration theory** This model is especially appropriate for unsteady-state problems, e.g. when the contact time between the two phases is too small to achieve stationary mass transfer (i.e. in gas absorption from bubbles or falling-film columns). In this model, the mass transfer resistance is deduced from the analytical solution of the transient diffusion problem in a semi-infinite slab Higbie [1935]:

$$h_c = \sqrt{\frac{D_c}{\pi t}} \tag{1.2.10}$$

where $t$ is the constant contact time.

**Surface renewal model** In order to overcome the limitation of constant contact time $t$ in the penetration model, and gives a more realistic physical representation of the phenomena occurring in the films, Danckwerts [1951] proposed to account for the residence time distribution of the fluid elements at the interface. Assuming that each element has the same probability to be removed from the interface by the turbulent eddies, he showed that:

$$h_c = \sqrt{D_c s} \tag{1.2.11}$$

where $s$ is the rate of surface renewal (in s−1. The surface renewal model has been very successful in the explanation and analysis of convective mass transfer, particularly when the mass transport is accompanied by chemical reactions in the liquid phase.

## 1.3 Thesis plan

A vast number of both empirical and theoretical correlations have been developed over the last decades for determining the mass transfer coefficients between drop(s) and the surrounding fluid. They are mostly based on curve fitting with adjustable parameters or adapted to a few simple geometries. Therefore, most of these correlations are not universal and are strongly configuration dependant (properties of the liquid-liquid system, hydrodynamic conditions, boundary conditions, etc), it is hence difficult to select the appropriate correlation for a given system (if available).

In this study we will be focusing on the hydrodynamics and conjugate mass transfer at the scale of a single translating liquid spherical droplet in an immiscible liquid. Dimensionless parameters like Reynolds number, Peclet number and viscosity ratio are highly relevant for mass transfer problems involving particles, and will be the key parameters for our sensitivity of the Sherwood number. Using direct numerical simulation, the problem will be investigated in intermediate/high Reynolds configurations, that are not addressed in literature. The document is written according to the following plan:

chapter 2 focuses on the theory behind our studied cases. Equations describing hydrodynamics and mass transfer are presented, followed by a set of parameters that will be used in the thesis.

chapter 3 introduces the numerical tools used to solve the numerical problem. A brief introduction of JADIM will be given, then all the details of the developed numerical model and its implementation will be considered. Finally, model validation is addressed, considering both hydrodynamic and the mass transfer aspects.

chapter 4 gathers the original contribution from the thesis. From the hydrodynanic point of view, the results on the external recirculation, separation angle, velocity fields, drag coefficient correlation are presented. The parametric study of mass transfer is then described, together with the analysis of the Sherwood number evolution. New correlations are proposed for the conjugate problem.

chapter 5 tackles recent results of 3D studies. Special attention is paid to description of the flow structure, and especially to the internal bifurcation appearance at high Re. The effect of 3D flow structure on the mass transfer rate is considered as well.

At last, chapter 6 sums up all the results and findings of the thesis, and sheds the light to possible applications and outlooks of this work.

# Chapter 2

# Problem statement

## Contents

The transport phenomena involved in mass transfer can be modelled mathematically by a set of equations based on mass and momentum balances. These equations are involving mass, momentum and species temporal and spatial evolutions. In some specific configurations (*e.g.* drop in Stokes flow), a well defined analytical solution can be derived and solved for this set of governing equations. However, in most cases, and especially in most industrially relevant applications, these equations cannot be solved analytically. Instead, computational methods are required to solve numerically the problem.
In this chapter, the configuration under investigation will be defined first, relevant assumptions are listed afterwards. The governing equations will then be introduced which describe the hydrodynamic behaviour of the droplet along with mass transfer. Finally, notations and useful dimensionless parameters are presented and commented.

## 2.1 Notions and elements of theory

In this section, a mathematical description is provided to address a flow of two separated immiscible fluids (droplet in flow) and the transfer of the solute across the interface $S$ from one phase to another (figure 2.1). We suppose that the length scales are macroscopic so that we can treat each phase as a continuum medium.

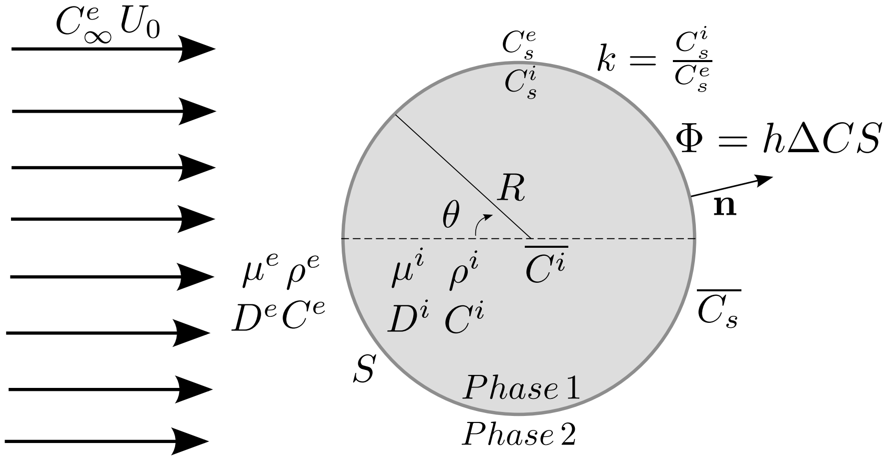

Figure 2.1: Sketch of a droplet in uniform flow.

Superscript "i" (resp. "e") is used to refer to the internal or dispersed phase physical quantities (resp. external or continuous phase), while the subscript "s" refers to interfacial quantities at the surface $S$. The over-bar upon a variable indicates either its volume or mean surface average.

### 2.1.1 Governing equations

The governing equations or conservation laws that describe the hydrodynamic behaviour of the two phases, and the solute $A$ transport are given by the Navier Stokes equations

and mass balance equations respectively.
Both fluids are supposed Newtonian, homogeneous, incompressible and experience gravity as the only body force. Hence for each phase $\delta$ ($\delta \equiv i$ for the droplet phase,$\delta \equiv e$ for the external fluid), the conservation principles are written as follows.

- Mass continuity equation:

$$\boldsymbol{\nabla} \cdot \mathbf{u}^{\boldsymbol{\delta}} = 0 \tag{2.1.1}$$

- Conservation of momentum:

$$\rho^{\delta}\left(\frac{\partial \mathbf{u}^{\boldsymbol{\delta}}}{\partial t} + \nabla \cdot \left(\mathbf{u}^{\delta}\mathbf{u}^{\delta}\right)\right) = \boldsymbol{\nabla} \cdot \mathbf{T}^{\boldsymbol{\delta}} + \rho^{\delta}\mathbf{g} \tag{2.1.2}$$

where $\rho^{\delta}$ is the fluid density, $\mathbf{u}^{\boldsymbol{\delta}}$ the velocity field, $t$ the time, $\mathbf{g}$ the gravity acceleration, and $\mathbf{T}^{\boldsymbol{\delta}}$ is the stress tensor, which writes for an incompressible Newtonian fluid:

$$\mathbf{T}^{\boldsymbol{\delta}} = -p^{\delta}\mathbf{I} + \boldsymbol{\tau}^{\boldsymbol{\delta}} \tag{2.1.3}$$

Here $p$ is the pressure, $\mathbf{I}$ the identity second order tensor, $\mu^{\delta}$ is the fluid dynamic viscosity, and $\boldsymbol{\tau}^{\boldsymbol{\delta}}$ denotes the viscous stress tensor from Newton's law:

$$\boldsymbol{\tau}^{\boldsymbol{\delta}} = \mu^{\delta}\mathbf{D} = 2\mu^{\delta}\left((\boldsymbol{\nabla} \cdot \mathbf{u}^{\delta}) + (\boldsymbol{\nabla} \cdot \mathbf{u}^{\delta})^{T}\right) \tag{2.1.4}$$

It is convenient to write the set of equations in a dimensionless form. Usually, the stream velocity , $U_0$, is considered as the reference scale, while the droplet diameter $d = 2R$, or the equivalent diameter, is taken for the length scale. These references are adequate to make all the parameters dimensionless in Navier-Stokes equations, the latter will be denoted with a prime "′". Thus:

$$\mathbf{x'} = \frac{\mathbf{x}}{d} \qquad\qquad \mathbf{u'}^{\boldsymbol{\delta}} = \frac{\mathbf{u'}^{\boldsymbol{\delta}}}{U_0} \tag{2.1.5}$$

The dimensionless forms of equations 2.1.1 and 2.1.2 write:

$$\boldsymbol{\nabla} \cdot \mathbf{u'}^{\boldsymbol{\delta}} = 0 \tag{2.1.6}$$

$$\frac{\partial \mathbf{u'}^{\boldsymbol{\delta}}}{\partial t'} + \nabla \cdot \left(\mathbf{u'}^{\delta}\mathbf{u'}^{\delta}\right) = -\boldsymbol{\nabla} p'^{\delta} + \frac{1}{Re^{\delta}}\boldsymbol{\nabla}^{2}\mathbf{u'}^{\boldsymbol{\delta}} \tag{2.1.7}$$

Where $Re^{\delta} = \frac{\rho^{\delta}U_0 2R}{\mu^{\delta}}$ is the Reynolds number. According to the notation of Fig. 2.1, $Re^{e}$ will be referred to as the external Reynolds number, $Re^{i}$ is the inner or the internal Reynolds number. $p'^{\delta}$ is the dimensionless modified pressure given by:

$$p'^{\delta} = (p^{\delta} - p_0 - \rho^{\delta}\mathbf{g} \cdot \mathbf{x})/\rho^{\delta}U_0^2 \tag{2.1.8}$$

$p_0$ is a constant. A detailed discussion of the modified pressure is given in Batchelor [2000].

- The solute mass balance equation, in absence of chemical reaction, involves only advective and diffusive transport terms:

$$\frac{\partial C^\delta}{\partial t} + \nabla \cdot \left( \mathbf{u}^\delta C^\delta \right) = D^\delta \nabla^2 C^\delta \tag{2.1.9}$$

Where $C^\delta$ represents the solute concentration in phase $\delta$, $D^\delta$ its diffusivity, which is assumed constant.
Taking the stream concentration $C_\infty^e$ and initial solute concentration $C_0^i$ as references, the following dimensionless concentrations are introduced:

$$C'^e = \frac{C^e - C_\infty^e}{C_0^i - C_\infty^e} \qquad\qquad C'^i = \frac{C^i - C_\infty^e}{C_0^i - C_\infty^e} \tag{2.1.10}$$

The dimensionless form of the solute transport equation writes:

$$\frac{\partial C'^\delta}{\partial t'} + \nabla \cdot \left( \mathbf{u'}^\delta C'^\delta \right) = \frac{1}{Pe^\delta} \nabla^2 C'^\delta \tag{2.1.11}$$

where $Pe^\delta = \frac{U_0 2R}{D^\delta}$ is the Peclet number. Again, $Pe^e$ (resp. $Pe^i$) refers to the external (resp. internal) Peclet number. The Peclet number is an important dimensionless number, that represents the ratio of the solute's convection rate (*i.e.* by the flow) and its diffusion rate (molecular diffusion).

### 2.1.2 Conditions at the interface

It is necessary to formulate the conditions enforcing mass and momentum balance at the interface. The determination of appropriate interface formulations is a topic of ongoing research, and the correct macroscopic conditions remain uncertain, particularly for fluid systems that involve surface-active solutes in addition to the two primary fluids Gary Leal [1993]. Throughout this study, we adopt a classic approach that is consistent with equilibrium thermodynamics. We assume a zero thickness interface that can be entirely characterized by a surface or interfacial tension $\sigma$. In the numerical formulation (see Chap. 3), all the expressions imposed at the interface will be applied as boundary conditions for the partial differential equations, or as closure equations for the flux densities exchanged from one phase to the nother.

#### 2.1.2.1 Prevailing conditions at the interface

When there is no condensation or evaporation (*i.e.* no phase change involving mass variations of the fluids), all components of velocity are continuous over a fluid-fluid interface. This is expressed by:

$$\mathbf{u_s^i} = \mathbf{u_s^e} \tag{2.1.12}$$

where $\mathbf{u_s^i}$ is the fluid velocity in the dispersed phase located immediately near the interface, $\mathbf{u_s^e}$ is the interfacial velocity of the fluid on the continuous phase side. Condition 2.1.12 implies that the interface velocity equals the local fluids velocities, it is known as the "no slip" condition. Hence the normal and tangential components of the velocity are continuous across the interface.

#### 2.1.2.2 Stress condition at the interface

In addition to the velocity continuity condition 2.1.12, the stress balance at the interface should be treated with care. The difference in the total stress across the interface is accommodated by the interface which curvature gives rise to a normal stress, involving the surface tension, $\sigma$. $\sigma$ can be viewed as the surface free energy per unit area at constant temperature Lautrup [2011]. In tensorial notation, the condition at the interface writes (Gary Leal [1993]):

$$(\mathbf{T^e} - \mathbf{T^i}) \cdot \mathbf{n} + \nabla_s \sigma - \sigma \mathbf{n}(\boldsymbol{\nabla} \cdot \mathbf{n}) = 0 \tag{2.1.13}$$

The normal stress condition writes:

$$[\mathbf{T^e} \cdot \mathbf{n}] \cdot \mathbf{n} - \left[\mathbf{T^i} \cdot \mathbf{n}\right] \cdot \mathbf{n} = \sigma \boldsymbol{\nabla} \cdot \mathbf{n} = \sigma \left[1/R_1 + 1/R_2\right] \tag{2.1.14}$$

where $R_1$ and $R_2$ are the principal radii of curvature of the surface. For a spherical interface we have: $R_1 = R_2 = R$. Under static conditions, the condition 2.1.14 reduces to the Laplace equation.

The spatial variation of the interfacial tension leads to a tangential stress given by:

$$[\mathbf{T^e} \cdot \mathbf{n}] \cdot \mathbf{t} - \left[\mathbf{T^i} \cdot \mathbf{n}\right] \cdot \mathbf{t} = \nabla_s \sigma \tag{2.1.15}$$

where $\nabla_s = (\mathbf{I} - \mathbf{nn})\nabla$ is the surface gradient. The latter condition is especially important if concentration or temperature gradients prevail at the interface. According to Eq. 2.1.15, a surface tension variation induces a tangential stress along the interface. In mas transfer problem, this phenomenon, known as the Marangoni effect, is likely to happen with non-uniform distribution of pollutants or other surface active species at the interface.

In this study, we neglect such Marangoni effect, consequently $\sigma$ is uniform which means that tangential stress is constant at the interface (Eq 2.1.15). Moreover, the droplet shape is imposed as spherical which makes Eq 2.1.14 straightforward. Therefore, the hydrodynamic conditions at the interface are written as follows:

$$\begin{gathered}\mathbf{u^i} \cdot \mathbf{t} = \mathbf{u^e} \cdot \mathbf{t} \\ (\boldsymbol{\tau}^{\mathbf{i}} \cdot \mathbf{n}) \cdot \mathbf{t} = (\boldsymbol{\tau}^{\mathbf{e}} \cdot \mathbf{n}) \cdot \mathbf{t}\end{gathered} \tag{2.1.16}$$

#### 2.1.2.3 Mass transfer condition at the interface

Thermodynamic equilibrium (similar to Henry's law in liquid/gas systems) is generally satisfied locally across the interface. In addition mass flux passes continuously from one phase to another. Thus the interface conditions for a dilute solution are written as follows:

Equilibrium law $$C_s^i = kC_s^e \tag{2.1.17}$$

Conservation of mass fluxdensity $$-D^i \nabla C^i = -D^e \nabla C^e \tag{2.1.18}$$

$k$ is known as the partition or the distribution coefficient based on chemical thermodynamics.

## 2.2 Dimensionless numbers

Dimensionless numbers are frequently used in fluid dynamics to assess the relative magnitude of the different physical phenomena. Until now, the inner (resp. external) Reynolds number $Re^i$ (resp. $Re^e$) and the internal (resp. external) Peclet number $Pe^i$ (resp. $Pe^e$) have been introduced. Other dimensionless parameters related to mass transfer are introduced in this section. By convention, and for the sake of simplicity, we denote to external Reynolds (resp Peclet) numbers as $Re$ (resp. $Pe$) unless otherwise specified.

The drag coefficient $C_D$ is a dimensionless number calculated from the total drag force $F_D$ exerted by the uniform flow on the sphere using the classical definition:

$$C_D = 8\frac{\mathbf{F_D} \cdot \mathbf{e_x}}{\pi \rho^e U_0^2 d^2} \tag{2.2.1}$$

Where

$$\mathbf{F_D} = \int_S \left[-P^e \mathbf{n} + (\boldsymbol{\tau}_{\mathbf{I}}^{\mathbf{e}} \cdot \mathbf{n})\right] dS \tag{2.2.2}$$

In each phase, we define the Schmidt number $Sc^\delta$, which is a dimensionless number defined as the ratio of momentum diffusivity and mass diffusivity $Sc^\delta = \nu^\delta / D^\delta$ where $\nu^\delta = \mu^\delta / \rho^\delta$, it can be written in terms of the Reynolds and Peclet numbers as: $Sc^\delta = Pe^\delta / Re^\delta$. The total mass flux $\Phi$ across the drop surface $S$ can be expressed by the equations 2.2.3 where internal, external and overall mass transfer coefficients ($h^i$, $h^e$, $h$) have been introduced.

$$\begin{aligned}
\Phi &= \int_S -D^i \nabla C^i dS \cdot \mathbf{n} \\
&= \int_S -D^e \nabla C^e dS \cdot \mathbf{n} \\
&= h^i (\overline{C^i} - \overline{C^i_s}) S \\
&= h^e (\overline{C^e_s} - C^e_\infty) S \\
&= h (\overline{C^i} - k C^e_\infty) S
\end{aligned} \tag{2.2.3}$$

The Sherwood number is a dimensionless quantity that allows to characterize the interfacial mass transfer. Three types of Sherwood number are defined: internal, external and global Sherwood numbers denoted respectively $Sh^i$, $Sh^e$ and $Sh$ (Equations 2.2.4).

$$\begin{aligned}
Sh^i &= \frac{h^i R}{D^i} \\
Sh^e &= \frac{h^e R}{D^e} \\
Sh &= \frac{h R}{D^i}
\end{aligned} \tag{2.2.4}$$

Three additional dimensionless groups will be considered during the study, the density, the viscosity and mass diffusivity ratios of both phases

$$\boldsymbol{\mu}^* = \frac{\mu^i}{\mu^e} \qquad \boldsymbol{\rho}^* = \frac{\rho^i}{\rho^e} \qquad \mathbf{D}^* = \frac{D^i}{D^e} \tag{2.2.5}$$

It is worth noticing the relationship between internal and external quantities defined previously.

$$\begin{aligned}
Re^i &= (\rho^* / \mu^*) Re^e \\
Pe^i &= Pe^e / D^* \\
Sc^i &= \mu^* / (\rho^* D^*) Sc^e
\end{aligned} \tag{2.2.6}$$

The theory of stagnant film is one of the most used in the chemical engineering community given its reliable estimations in simple cases. It can be deduced easily by mass flux conservation from the previous definitions of mass transfer coefficients. After some simplifications, we obtain the following equation (also called additive rule of resistance to transfer):

$$\frac{1}{Sh} = \frac{1}{Sh^i} + \frac{kD^*}{Sh^e} \tag{2.2.7}$$

$$\tag{2.2.8}$$

In the previous chapter, a classification has been made depending on mass transfer resistance in order to have an intuition on limitations to mass transfer. For internal problems, the stagnant resistance to the transfer is located inside the drop, the concentration at the interface $C_s$ is then imposed by the ambient fluid. In this case, an internal mass transfer coefficient $h^I$ (a priori different from $h^i$ already defined in Eq 2.2.3) is defined by the mass flux at the interface as:

$$\Phi = h^I(\overline{C^i} - C_s)S \tag{2.2.9}$$

A similar coefficient denoted $h^E$ is defined for the external problem where the concentration of the drop is uniform and constant at the value $C_s$. The external mass flux is written as follows:

$$\Phi = h^E(C_s - C^e_\infty)S \tag{2.2.10}$$

The Sherwood numbers associated to internal and external problems are defined in Eq 2.2.11.

$$\begin{aligned} Sh^I &= h^I R/D^i \\ Sh^E &= h^E R/D^e \end{aligned} \tag{2.2.11}$$

At last, in the dimensionless framework considered here, the governing time-scale for the transport process is expressed by the Fourier number $Fo$:

$$Fo^\delta = \frac{D^\delta t}{R^2} \tag{2.2.12}$$

## 2.3 Thermal analogy

The mass transfer dimensionless equations are very similar in terms of formulation to the heat transfer dimensionless equations under the conditions of no dissipation, low mass flux and constant physical properties. The boundary conditions are identical as well when we assume continuity of temperature (e.g. concentration). As a result, the solutions to these equations in dimensionless form are also identical. Hence, the previously introduced dimensionless numbers for mass transfer find an equivalent definition in a heat transfer problems. Therefore, numerical studies on heat transfer can be used as validation cases.
The analogies between mass and heat transfer are summarised in table 2.1.

| Mass transfer | Heat transfer |
|---|---|
| Mass diffusivity: $D$ | Thermal diffusivity: $\alpha = \frac{\lambda}{\rho C_p}$ |
| Peclet number: $Pe = \frac{Ud}{D}$ | Peclet number: $Pe = \frac{Ud}{\lambda}$ |
| Schmidt number: $Sc = \frac{\nu}{D}$ | Prandtl number: $Pr = \frac{\nu}{\lambda}$ |
| Sherwood number: $Sh = \frac{hd}{D}$ | Nusselt number: $Nu = \frac{kd}{\lambda}$ |
| Fick's law: $\varphi = -D\nabla C$ | Fourier's law: $\varphi = -\lambda\nabla T$ |
| Convective flux: $\varphi_c = h_s \Delta C$ | Newton's law: $\varphi_c = k_s \Delta T S$ |
| Mass-transfer resistance: $\frac{1}{h}$ | Thermal resistance: $\frac{1}{k}$ |

Table 2.1: Mass transfer, heat transfer analogy.

## 2.4 Conclusion

In this chapter, a mathematical model of the hydrodynamics and the mass transfer across a droplet interface has been detailed. Most of variables that will appear in the rest of this Thesis are defined. Dimensionless numbers have been defined as well to ease physical interpretation of coupled phenomena. In the next chapter, the numerical code will be introduced to resolve the balance equations.

# Chapter 3

# Numerical model and Validation

## Contents

The purpose of this chapter is to present the numerical tool used to solve the numerical model describing hydrodynamics and mass transfer at the scale of a translating spherical droplet. The background of the physical modelling, mathematical description and numerical solving will be detailed and validated.
The numerical implementation of the present work has been carried out thanks to the Direct Numerical Simulation module of JADIM code. Some of the code features have been adapted to our studied case to take into consideration hydrodynamics and mass transfer inside and outside the droplet. A special care was particularly paid to the implementation of the coupling between the internal and the external resolution of the governing equations at the interface. Two interesting types of orthogonal curvilinear meshes were tested and analysed. Some validation tests were performed and compared against results found in literature, these results were proven mesh-independent.
In this chapter we start by giving overview of JADIM code and its features. With the assumptions considered in the first chapter, the governing equations along with boundary conditions will be written in orthogonal curvilinear coordinates. We present afterwards the studied mesh and the theory behind its generation. The resolution methodology will be developed and discussed. Finally, validation tests on both hydrodynamics and mass transfer will be presented and analyzed.

## 3.1 JADIM Code

JADIM is an in-house simulation code developed within the INTERFACE group at IMFT Calmet [1995]; Legendre [1996]; Rivero [1991]. Many publications have contributed to the development of the code features, we cite particularly Calmet and Magnaudet [1997]; Legendre and Magnaudet [1997]; Magnaudet et al. [1995]. The code is based on a Finite Volume Method that allows to solve incompressible, unsteady and three dimensional Navier Stokes equations. These equations are written in velocity-pressure variables in a general orthogonal curvilinear coordinates system. The code allows to solve a passive scalar advective–diffusive equation along with the Navier-Stokes equations.
The numerical schemes in JADIM grant a second order precision $(\mathcal{O}(\Delta x^2), \mathcal{O}(\Delta t^2))$. A third order Runge-Kutta scheme is also used to evaluate convective and source terms along with Crank-Nicolson scheme for the diffusive part. To ensure the incompressibility condition, a projection method is used to solve the pressure. This latter is estimated by solving a Poisson pseudo-equation of an auxiliary potential.
The code offers other features: LES, VOF, IBM, Boundary-fitted, *etc*

## 3.2 Governing equations in curvilinear coordinates

The flow fields are computed by solving the unsteady incompressible Navier-Stokes equations (*i.e.* the momentum conservation and continuity equations) in both phases.

In a general orthogonal curvilinear coordinates system $(\xi_i)_{i=1,3}$, the physical length is given by $\xi_i' = h_i d\xi_i$, introducing thus the metric parameter $h_i$. The superscript $\delta$ refers to either the dispersed/internal phase "$i$" or the continuous/external phase "$e$".
$V_i^\delta$ stands for the dimensionless velocity along the coordinate line $\xi_i$, $P^\delta$ represents the dimensionless pressure, $\mu^\delta$ is the dynamic viscosity. The Navier-Stokes equations can be written in each phase "$\delta$" in the dimensionless and compact conservative form (Legendre [1996]; Rivero [1991]):

$$\begin{aligned} &\frac{\partial V_j^\delta}{\partial \xi_j} = 0 \\ &\frac{\partial V_i^\delta}{\partial t} + \frac{\partial\left(V_i^\delta V_j^\delta\right)}{\partial \xi_j} = -\frac{\partial P^\delta}{\partial \xi_i} + \frac{\partial\left(\tau_{ij}^\delta\right)}{\partial \xi_j} + H_j^i\left(V_j^\delta V_j^\delta - \tau_{jj}^\delta\right) - H_j^i\left(V_i^\delta V_j^\delta - \tau_{ij}^\delta\right) \end{aligned} \tag{3.2.1}$$

The stretching factors (curvature terms) $H_j^i$ are defined as:

$$H_j^i = \frac{1}{h_j}\frac{\partial h_j}{\partial \xi_i} \tag{3.2.2}$$

$h_i$ denotes the scale factor along the direction $i$, and $\tau_{ij}^\delta$ represents the dimensionless components of the viscous stress given in the considered orthogonal curvilinear coordinates by:

$$\tau_{ij}^\delta = \frac{1}{Re^\delta}\left[\frac{\partial V_i^\delta}{\partial \xi_j} + \frac{\partial V_j^\delta}{\partial \xi_i} - H_j^i V_j^\delta - H_i^j V_i^\delta + 2H_i^k V_k^\delta \delta_{i,j}\right] \tag{3.2.3}$$

The Reynolds numbers $Re^\delta$ in the expression of $\tau_{ij}^\delta$ have been previously defined in section 2.1.1.

No a priori assumption is made regarding the location of the mass transfer resistance. Hence the inner and outer concentration fields are computed by solving the transient mass transport equations in both phases. The dimensionless concentration of the solute in each phase was defined previously (Eq. **??**). it is here rewritten in a generalized form (phase "$\delta$"):

$$C^\delta = \frac{C'^\delta - C'^e_\infty}{C'^i_0 - C'^e_\infty} \tag{3.2.4}$$

here the prime refers to dimensional concentration, $C'^i_0$ stands for the initial concentration inside the droplet, and $C'^e_\infty$ for the solute concentration in the stream flow, far from the droplet. In the absence of chemical reaction, the mass balance equation involves only advective and diffusive transport terms. In the considered coordinates system $(\xi_i)$ the dimensionless concentration equations read:

$$\frac{\partial C^\delta}{\partial t} + \frac{\partial\left(V_j^\delta C^\delta\right)}{\partial \xi_j} = \frac{1}{Pe^\delta}\frac{\partial^2 C^\delta}{\partial \xi_j^2} \tag{3.2.5}$$

where $Pe^\delta$ is the Peclet number defined in section 2.1.1

## 3.3 Resolution method

The set of conservation equations is solved using the in-house code JADIM. The spatial discretization is based on second order-centred central differences and has been described by Magnaudet et al. [1995].The numerical scheme for the time advancement has been described by Calmet and Magnaudet [1997]. The advective terms are calculated explicitly while the viscous terms are calculated semi-implicitly through a second order Range-Kutta/Crank-Nichelson scheme. At the end of a time step, the incompressibility is respected by solving a Poisson equation on a auxiliary potential.In this study involving two phases, the compressibility is satisfied independently inside and outside the droplet. The overall algorithm is second-order accurate in time. In the present study, we are mainly interested by the steady solution which is obtained after several time-steps, depending on the considered configuration. The hydrodynamic convergence is attained when the maximum variation of the velocity field between two consecutive time-steps becomes less than the imposed convergence criteria (typically $\Delta V \approx 10^{-6}$). After the hydrodynamic convergence is reached, the mass balance equation is solved in the thus obtained steady velocity field.

## 3.4 Mesh features

Two types of orthogonal curvilinear meshes have been considered in the study. In both cases the droplet is discretized using a polar mesh centred at the droplet center. Whereas two meshing strategies have been implemented for the external domain.
The first mesh is based on the streamlines $\xi_1$ and the equipotential lines $\xi_2$ of a potential flow around a cylinder. The expressions of $\xi_1$ and $\xi_2$ in the considered polar coordinates are:

$$\begin{cases} \xi_1 = -\cos(\theta)\left(r + R^2/r\right) \\ \xi_2 = -\sin(\theta)\left(1 - R^2/r^2\right) \end{cases} \tag{3.4.1}$$

It is important to note that $\xi_1$ and $\xi_2$ are orthogonal by definition.
In the second approach, the continuous domain is discretized using a polar mesh. With the notations of Sec. 3.2 we can write $(\xi_1, \xi_2, \xi_3) = (\xi, \eta, \phi))$. Figure 3.1 shows a close

up on the droplet neighborhood in both cases.
Note that the tightening of the potential lines from the droplet front and rear is solely a mesh property due the orthogonality condition.
In addition, refinement at the interface is necessary in order to solve both the hydrodynamic and the mass boundary layers with a good precision. The size of the first cell and the expansion factor were chosen such that at least four grids points are placed inside the hydrodynamic and mass transfer boundary layers. The thickness of these boundary layers can roughly be approximated by $Re^{\delta^{1/2}}$ and $Pe^{\delta^{1/2}}$ respectively. The global size of the computational domain is approximately $50R$.

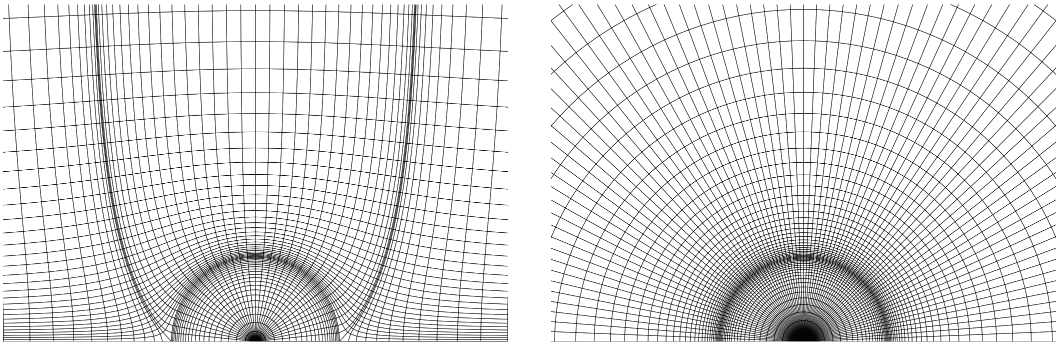

Figure 3.1: Left: LCE Mesh, Right: Polar Mesh.

In both cases, the mesh is axisymmetric and presents a bijection with the Cartesian coordinates as depicted in Figure 3.2.

For the mesh generation, the curvilinear coordinates are discretized first, then the Cartesian mesh is generated thanks to the bijection. The curvilinear mesh based on the streamlines and potential lines is called LCE mesh. The transformation used to move from one system of coordinates to the other is given by the following equations:

- *From Cartesian to curvilinear*

$$LCE \begin{cases} \xi_1 = x\left(1 + \dfrac{R^2}{x^2+y^2}\right) \\ \xi_2 = \sqrt{y^2+z^2}\left(1 - \dfrac{R^2}{x^2+y^2}\right) \end{cases} \tag{3.4.2}$$

$$Polar \begin{cases} \xi_1 = \sqrt{x^2+y^2} \\ \xi_2 = \arctan\left(\dfrac{y}{x}\right) \end{cases} \tag{3.4.3}$$

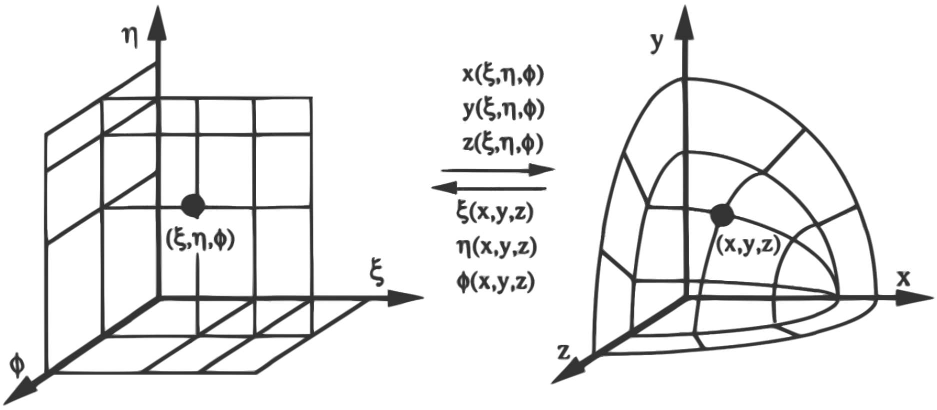

Figure 3.2: Bijection between Cartesian and curvilinear coordinates Legendre [1996].

- *From curvilinear to Cartesian*

$$LCE \begin{cases} x = \dfrac{\xi_1}{1 + \dfrac{2}{a + \sqrt{a^2 - 4}}} \\ y = \dfrac{-\xi_2}{1 - \dfrac{2}{a + \sqrt{a^2 - 4}}} \end{cases} \quad (3.4.4) \qquad Polar \begin{cases} x = \xi_1 \sin(\xi_2) \\ y = \xi_1 \cos(\xi_2) \end{cases} \quad (3.4.5)$$

where

$$a = \frac{1}{2}\left(\frac{\xi_2^2 + \xi_1^2}{R^2} + \sqrt{\left(\frac{\xi_2^2 + \xi_1^2}{R^2}\right)^2 + 8\left(2 - \frac{\xi_1^2}{R^2} + \frac{\xi_2^2}{R^2}\right)}\right) \quad (3.4.6)$$

The Navier Stokes and the advection-diffusion transport equations are solved using a staggered mesh. The pressure nodes are located at the center of the cell, while curvilinear velocities are computed on the cells faces, as shown in Figure 3.3.
At last, curvature terms (given by Eq. 3.2.2) have to be handled in the equations considered in curvature coordinates. A special treatment of these curvature terms, that minimizes the discretization error induced by these terms, has been proposed by Legendre [1996].

## 3.5 Numerical domain

### 3.5.1 Boundary conditions

A set of boundary conditions complements the previous equations to enable to solve the problem. Hydrodynamic and mass transfer boundary conditions have been implemented

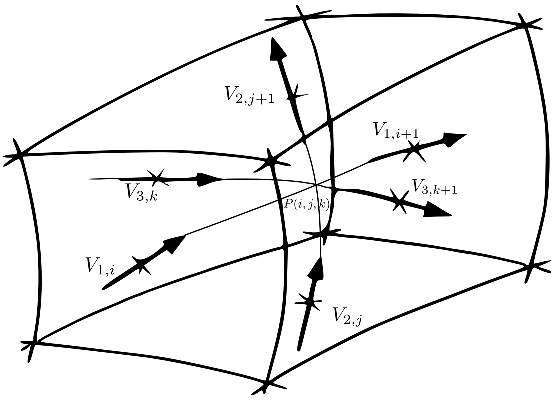

Figure 3.3: General scheme of a calculation cell in 3D (Legendre [1996]).

and detailed by previous works, the reader may refer to Calmet [1995] and Legendre [1996] thesis for more details about the implementation method. Thanks to the Finite Volume Method and the mesh structure, only conditions on the velocity field $\mathbf{V}^{\delta}$ and concentration must be defined. The staggered mesh allows to get rid of a condition on the pressure, which is unknown.

Figure 3.4 summarizes the implemented hydrodynamic and mass transfer boundary conditions in the considered curvilinear coordinates. At the domain inlet (on the left), a Direchlet condition is used, where a velocity equal to the stream velocity is imposed. A symmetry condition is defined along the axis (at the bottom) where no mass flux crossing is allowed. The top boundary is supposed to be far enough from the droplet to consider a constant velocity that is not influenced by the drop. An outflow is defined at the right boundary, where the fluid leaves the computational domain. Magnaudet et al. [1995] has outlined the heuristic technique developed and implemented for this type of boundary conditions. Jump conditions are prevailing at the interface (they will be detailed hereafter).
For the transfer aspect, a fixed concentration $C_{\infty}^{e}$ is set at the inlet. A Neumann condition is imposed everywhere elses (*i.e.* at the top, axis and domain's outlet) where the normal concentration gradient is set to zero.

*NB:* Due to its structure, the Polar mesh the domain boundary far from the droplet is a semi-circle. The stream velocity and the concentration have been imposed at this present boundary.

### 3.5.2 Interface condition

As stated in Chap. 2, the droplet interface is assumed spherical and free from any surface-active contaminants. Hence the tangential velocity and shear stress are continuous at the interface while the normal velocity component is equal to 0. Moreover, since the

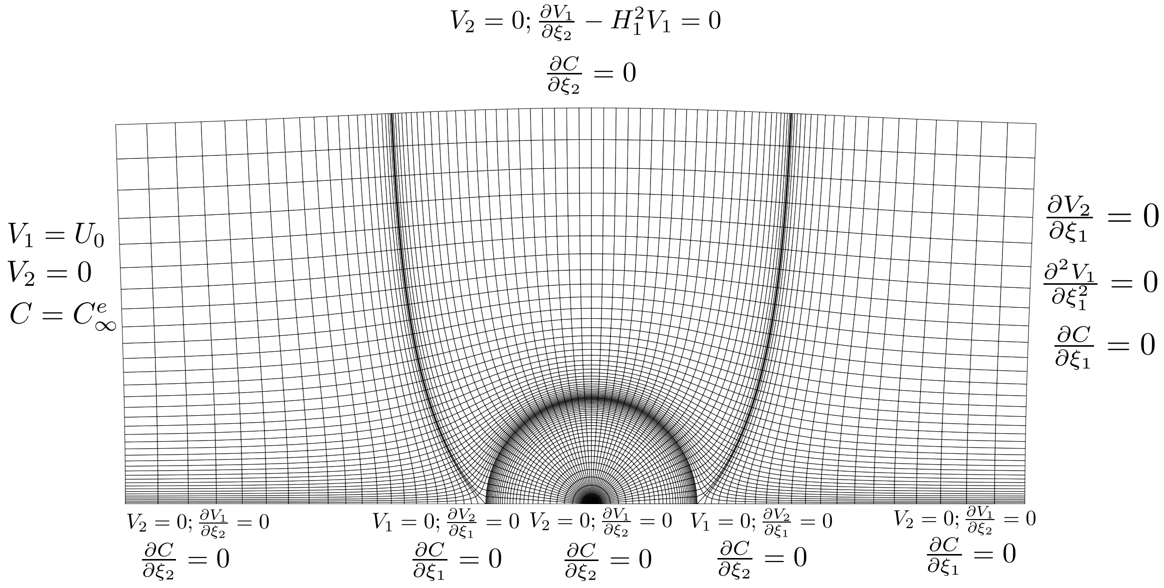

Figure 3.4: Boundary conditions for both the velocity and the concentration.

spherical droplet is non-deformable, no condition is required for the normal stress at the interface. Therefore, the hydrodynamic jump conditions at the interface are expressed as follow, where $(\boldsymbol{\xi_2}, \boldsymbol{\xi_1})$ are the normal and the tangential vectors to the interface, respectively:

$$\begin{aligned} V_1^i &= V_1^e \\ V_2^i &= V_2^e = 0 \\ \tau_{12,I}^i &= \tau_{12,I}^e \end{aligned} \tag{3.5.1}$$

Regarding the transferred species, an equilibrium distribution is assumed to prevail at the droplet's interface. Besides, as the mass flux at the interface is continuous, the mass jump conditions at the interface may be expressed using the following equations:

$$\begin{aligned} C_I^i &= k \cdot C_I^e \\ -\frac{D^i}{D^e} \frac{\partial C^i}{\partial \boldsymbol{\xi_2}} \bigg|_I &= -\frac{\partial C^e}{\partial \boldsymbol{\xi_2}} \bigg|_I \end{aligned} \tag{3.5.2}$$

where $k$ is the partition coefficient or the so called Henry coefficient in liquid-gas systems. These jump conditions have been implemented along with the boundary conditions, so that the governing equations are coupled by the boundary conditions at the interface. Figure 3.5 gives a schematic of the complete boundary conditions.

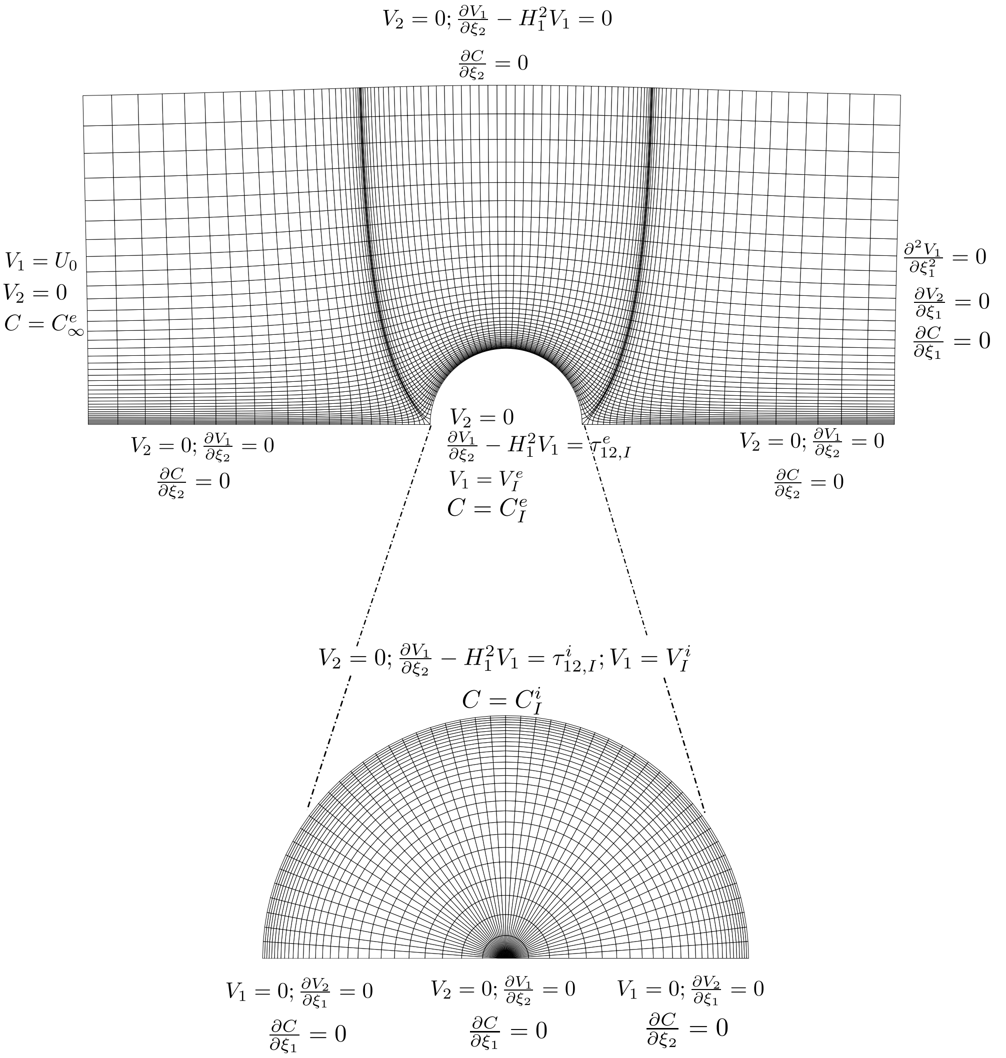

Figure 3.5: Boundary conditions and interface conditions.

### 3.5.3 Implementation of interface condition

In order to evaluate tangential velocities and tangential shear stress at the interface, four expansions to the second order have been performed using four neighboring cells of the interface, as shown in Figure 3.6.

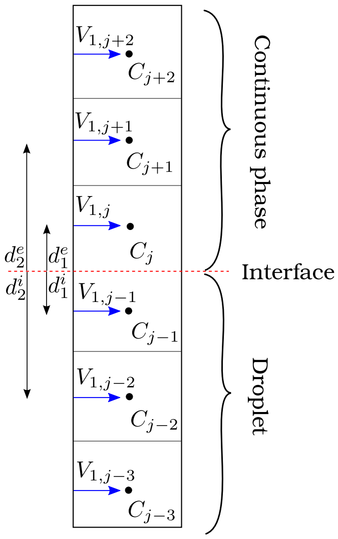

Figure 3.6: Discretization at the interface.

The objective is to express both the shear stress and the tangential velocity using the discretized velocity on both sides of the surface. After simplification and elimination of the second order velocity derivatives, we obtain the following set of equations:

$$\left\{\begin{aligned} {d_2^e}^2 V_{1,j} - {d_1^e}^2 V_{1,j+1} &= ({d_2^e}^2 - {d_1^e}^2) V^e_{1,I} + d^e_1 d^e_2 (d^e_2 - d^e_1) \left(\frac{\partial V_1}{\partial \xi_2}\right)_{I^+} \\ {d_2^i}^2 V_{1,j-1} - {d_1^i}^2 V_{1,j-2} &= ({d_2^i}^2 - {d_1^i}^2) V^i_{1,I} - d^i_1 d^i_2 (d^i_2 - d^i_1) \left(\frac{\partial V_1}{\partial \xi_2}\right)_{I^-} \end{aligned}\right. \tag{3.5.3}$$

Dimensionless parameters are introduced to simplify the final expressions

$$\left\{\begin{aligned} d1u^\delta &= \frac{{d_2^\delta}^2 - {d_1^\delta}^2}{{d^\delta}_1 {d^\delta}_2 ({d^\delta}_2 - {d^\delta}_1)} \\ d2u^\delta &= \frac{{d_2^\delta}^2}{{d^\delta}_1 {d^\delta}_2 ({d^\delta}_2 - {d^\delta}_1)} \\ d3u^\delta &= \frac{{d^\delta}^2_1}{{d^\delta}_1 {d^\delta}_2 ({d^\delta}_2 - {d^\delta}_1)} \end{aligned}\right. \tag{3.5.4}$$

The hydrodynamic conditions at the interface given by the system of Eq. (3.5.1) allow to express at time step $n+1$, both the velocity and stress at the interface in terms of physical properties and computed velocities in the neighbouring cells of the interface at the previous time step $n$.

The solution of the system (3.5.3) for the shear stress is given by:

$$\tau^e_{12,I} = \frac{\mu^i}{\mu^e} \frac{d3u^i\, V_{1,j-2} - d2u^i V_{1,j-1} + \dfrac{(d1u^i - H_1^2)(d2u^e\, V_{1,j} - d3u^e\, V_{1,j+1})}{d1u^e + H_1^2}}{1 + \dfrac{\mu^i}{\mu^e}\dfrac{d1u^i - H_1^2}{d1u^e + H_1^2}} \tag{3.5.5}$$

And for the tangential velocity by:

$$V^e_{1,I} = \frac{d2u^e\, V_{1,j} - d3u^e\, V_{1,j+1} - \tau^e_{12,I}}{d1u^e + H_1^2} \tag{3.5.6}$$

Similarly, the concentration at the interface has been examined along with the concentration gradient. The coupled boundary condition is given by the following expression:

$$C^e_I = \frac{d2p^e\, C^e_j - d3p^e\, C^e_{j+1} + \dfrac{D^i}{D^e}(d2p^i\, C^i_{j-1} - d3p^i\, C^i_{j-2})}{d1p^e + \dfrac{D^i}{D^e} k\, d1p^e} \tag{3.5.7}$$

$$\left(\frac{\partial C^e}{\partial \xi_2}\right)_I = \frac{k\, d1p^i(d2p^e\, C^e_j - d3p^e\, C^e_{j+1}) - d1p^e(d2p^i\, C^i_{j-1} - d3p^i\, C^i_{j-2})}{k\, d1p^i + \dfrac{D^e}{D^i} d1p^e} \tag{3.5.8}$$

These expressions are provided as boundary conditions at the interface to enable the coupling between the internal and the external flows, and mass transfer. It is worth noticing the appearance of the previously defined dimensionless ratios $\mu^* = \mu^i/\mu^e$, $D^* = D^i/D^e$ and $k$, as a result of the coupling. The presence of the curvature terms in the interface velocity is due to the curvilinear mesh.

## 3.6 Simulation strategy

The simulation strategy is the following. First, hydrodynamics is solved at given $Re$ number, viscosity ratio $\mu^*$ and density ratio $\rho^*$, until a steady state is reached. The concentration equation is then solved in the frozen velocity field with an initial value set to $C^i_0 = 1$ and $C^e_0 = 0$, respectively inside and outside the droplet. The calculation is stopped when the mean solute dimensionless concentration inside the droplet falls below the convergence criteria $10^{-5}$.

## 3.7 Post-processing

Dimensionless parameters will be used in this study to analyse the results (see Chap. 4). Some of them have been introduced in the dimensionless balance equations and the

discretization of hydrodynamic and mass transfer quantities at the interface. They are all defined in Chap.2.
With the considered curvilinear coordinates, the internal and the external Sherwood numbers, $Sh^i$ and $Sh^e$, are calculated as follows:

$$Sh^i = \frac{1}{\overline{C^i} - \overline{C^i_s}} \int_{drop} \frac{\partial C}{\partial \xi_2}\bigg|_{I^-} dS \tag{3.7.1}$$

$$Sh^e = \frac{1}{\overline{C^e_s} - C_\infty} \int_{drop} \frac{\partial C}{\partial \xi_2}\bigg|_{I+} dS \tag{3.7.2}$$

Where we recall that the driving forces are $\Delta C^i = \overline{C^i} - \overline{C^i_s}$ and $\Delta C^e = \overline{C^e_s} - \overline{C^e_\infty}$, $\overline{C^i}$ is the sphere volume average concentration, ($\overline{C^i_s}$, $\overline{C^e_s}$) stands for surface average concentrations, and $\overline{C^i_s} = k \cdot \overline{C^e_s}$. These quantities are calculated as

$$\overline{C^i_s} = \frac{1}{2}\int_0^\pi C^i_I(\theta, t)\sin(\theta)\, d\theta \tag{3.7.3}$$

$$\overline{C^e_s} = \frac{1}{2}\int_0^\pi C^e_I(\theta, t)\sin(\theta)\, d\theta \tag{3.7.4}$$

$$\overline{C^i} = 12\int_0^R \int_0^\pi C^i(r, \theta) r^2 \sin(\theta) dr d\theta \tag{3.7.5}$$

The global Sherwood number is calculated by the following expression:

$$Sh = \frac{1}{\overline{C^i} - C^e_\infty} \int_{drop} \frac{\partial C^i}{\partial \xi_2}\bigg|_{I} \cdot \sin(\theta) dS \tag{3.7.6}$$

The local Sherwood number is also considered:

$$Sh_\theta = -\frac{2}{\overline{C^i}} \frac{\partial C^i}{\partial \xi_2}\bigg|_{I} \tag{3.7.7}$$

## 3.8 Validations

In this section, we first assess the mesh convergence (*i.e.* the impact of the used mesh on the results). The accuracy of our simulations is then evaluated by comparison with literature studies. Accordingly, the hydrodynamic validation is based on the flow structure inside and outside the drop and the drag coefficient evolutions. Regarding mass transfer, different configurations are analyzed, reproduced numerically then compared with analytical solutions and numerical studies.

### 3.8.1 Mesh convergence

Mesh sensitivity has been studied by refining either the radial or angular discretization in the droplet (see Figure 3.7). We recall that the cell size over the interface was chosen to fulfill proper treatment of boundary layers, as discussed in Sec. 3.4. Regardless of the values of $N_r$ and $N_\theta$, the same expansion ratio is considered on each side of the interface in order to guarantee a smooth transition from the drop's interior to the external region. Due to the specific structure of the external LCE mesh, the refining of the angular mesh yields a tightening of the potential lines at $\theta = 0$ and $\theta = \pi$ in the outer region of the droplet. Radial refining is sometimes required outside the droplet to keep a good mesh quality.

The sensitivity of results to mesh for the steady-state values of the drag coefficient $C_D$ (Eq. (2.2.1)), and of the global Sherwood number $Sh$ (Eq. (3.7.6)) is reported in Tab. 3.1 and 3.2, respectively.
It can be seen that for the drag coefficient, the relative deviation between the finest $(100 \times 120)$ and the coarsest $(30 \times 48)$ mesh studied remains well below 1%. It is interesting to notice that $C_D$ values are also not sensitive to the mesh structure: Polar mesh and LCE mesh yield substantially the same results.
Regarding mass transfer (Table 3.2), no significant evolution of the Sherwood number is observed at low Peclet number over the wide range of conditions investigated, hence highlighting that mesh convergence is reached. However, at very high $Pe$ number $(Pe > 1000)$, although the differences are small, a finer mesh would be needed to achieve the convergence of numerical results. This is due to thickness reduction of the boundary layer with the flow velocity.
For our validation tests, the first mesh (i.e. $30 \times 48$) will be used for comparison with available data.

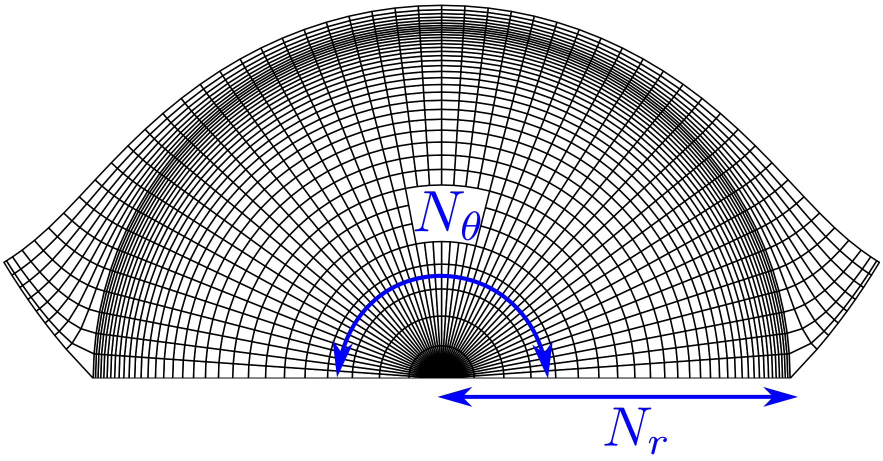

Figure 3.7: Radial and angular parameters of mesh refinement.

| $\mu^*$ | Mesh $N_r \times N_\theta$ | | | | |
|---|---|---|---|---|---|
| | $30 \times 48$ | $50 \times 80$ | $60 \times 100$ | $70 \times 100$ | $100 \times 120$ |
| 0.5 | 0.544 (0.548) | 0.541 | 0.542 | 0.541 | 0.541 |
| 1 | 0.662 (0.67) | 0.661 (0.67) | 0.6605 (0.669) | 0.660 (0.669) | 0.660 (0.669) |
| 2 | 0.806(0.81) | 0.803 | 0.803 | 0.803 | 0.803 |

Table 3.1: Evolution of the steady-state drag coefficient, $C_D$ with the size of the LCE (resp.Polar) mesh ($Re = 100$, $\rho^* = 1$).

| $Pe$ | Mesh $N_r \times N_\theta$ | | | | |
|---|---|---|---|---|---|
| | $30 \times 48$ | $50 \times 80$ | $60 \times 100$ | $70 \times 100$ | $100 \times 120$ |
| 10 | 1.742 | 1.742 | 1.745 | 1.745 | 1.746 |
| 100 | 5.500 | 5.501 | 5.505 | 5.507 | 5.507 |
| 1000 | - | 12.404 (12.425) | 12.413 (12.428) | 12.399 (12.42) | 12.385 (12.42) |
| 10000 | - | 16.911 | 16.903 | 16.9 | 16.87 |

Table 3.2: Evolution of the steady-state Sherwood number, $Sh$ with the size of the LCE (resp.Polar) mesh ($Re = 100$, $\mu^* = 1$, $\rho^* = 1$, $D^* = 1$).

## 3.8.2 Hydrodynamic validation

An extensive review of previous works on the hydrodynamics of a translating droplet has been introduced in the Chap. 1. In this section, some of these reference results will be used to test the accuracy of our DNS simulations to predict the drag coefficient, $C_D$, of a moving droplet.

### 3.8.2.1 Drag coefficient

The correlation reported by Feng and Michaelides [2001a] for $C_D$ was used to evaluate our model's predictions over a large range of flow conditions. The comparison of the $C_D$ values obtained from DNS results with the ones obtained by the correlation is given in Figure 3.8. The simulated evolution of $C_D$ with the viscosity ratio for different $Re$ shows excellent agreement with Feng and Michaelides [2001a] correlation (deviation is less than 1%). Moreover, we observe that the drag coefficient is monotonically increasing with the viscosity ratio $\mu^*$, and a decreasing function of the Reynolds number.

These results are reported in Table 3.3, complemented by additional simulations in the range $1 \leq Re \leq 200$ and $\mu^*$ varies between 0.05 (inviscid bubble) to $\mu^* = 100$ (solid sphere). Other $C_D$ values published by Oliver and Chung [1987] are also given for

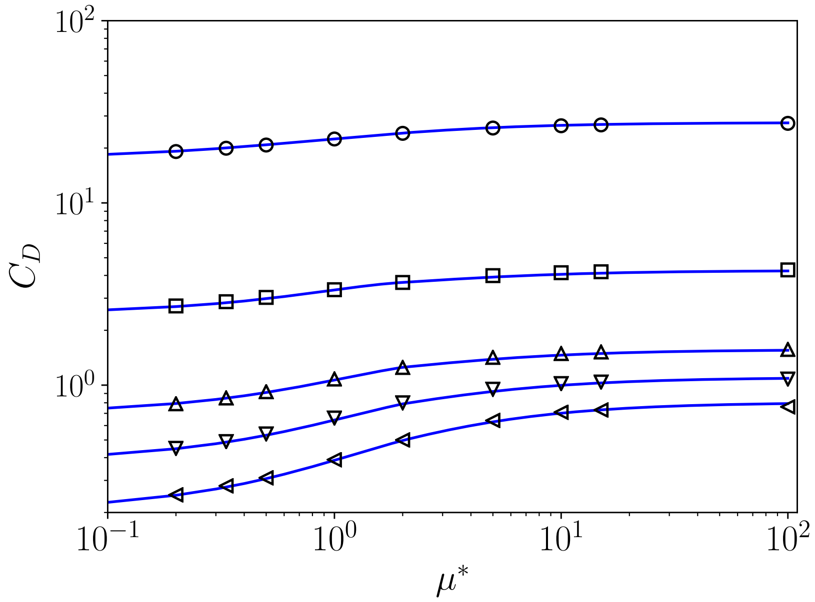

Figure 3.8: Evolution of the steady-state drag coefficient with the viscosity ratios: comparison between the DNS results; this study: $Re = 1$(○), 10(□), 50(△), 100(▽), 200(◁); and the correlation of Feng and Michaelides [2001a]: blue line.

comparison. Again, a very good agreement is observed between our simulation results and available literature data.

#### 3.8.2.2 Flow structure

For a fluid sphere, as the Reynolds number increases, the intensity of the internal circulation increases accordingly. This recirculation, which is driven by the sharp velocity gradient prevailing near the droplet interface, is likely to affect the mass transfer rate. It is therefore important to represent it correctly.

The streamline contours for two distinct flow configurations ($Re = 10$ on the left and $Re = 100$ on the right) are illustrated in Fig. 3.9. The viscosity ratio is $\mu^* = 7$, in both cases. The simulation results are depicted on top, and the corresponding flow fields taken from Feng and Michaelides [2001a] are reported on the bottom. Beyond the excellent qualitative agreement observed between our results and the literature, different flow features are observed in Fig. 3.9. While at low $Re$, the external flow field is relatively simple, for the higher value $Re = 100$, the external flow field is more complex and a recirculation region is present in the wake of the droplet.

To test the ability of the model to predict boundary layer detachment, additional simulations were performed for increasing $Re$, in the configuration $\mu^* = 3$ investigated by Oliver and Chung [1987] (see Figure 3.10). The separation angle, $\theta_d$, *i.e.* the angle at which the external boundary layer separates to generate the external recirculation,

| Re | 1 | 10 | 20 | 50 | 100 | 150 | 200 |
|---|---|---|---|---|---|---|---|
| $\mu^*$ | | | | | | | |
| 0.05 | 17.98 | 2.45 | 1.45 | 0.7 | 0.39 | 0.28 | 0.23 |
| 0.2 | 19.14 | 2.72 | 1.6 | 0.79 | 0.45 | 0.32 | 0.25 |
| 0.333 | 19.96 | 2.87 | 1.7 | 0.85 | 0.49 | 0.35 | 0.28 |
| | [19.9] | [2.87] | [1.71] | [0.89] | | | |
| 0.5 | 20.78 | 3.03 | 1.81 | 0.92 | 0.54 | 0.39 | 0.31 |
| | (20.74) | (3.030) | (1.818) | (0.939) | (0.552) | | (0.317) |
| 1 | 22.43 | 3.34 | 2.04 | 1.08 | 0.66 | 0.49 | 0.39 |
| | (22.42) | (3.339) | (2.037) | (1.097) | (0.666) | | (0.397) |
| 2 | 24.09 | 3.66 | 2.26 | 1.25 | 0.8 | 0.61 | 0.5 |
| | (24.02) | (3.655) | (2.26) | (1.25) | (0.803) | | (0.504) |
| 5 | 25.76 | 3.99 | 2.49 | 1.42 | 0.95 | 0.76 | 0.64 |
| | (25.67) | (3.974) | (2.484) | (1.412) | (0.955) | | (0.646) |
| 10 | 26.51 | 4.14 | 2.6 | 1.49 | 1.02 | 0.82 | 0.71 |
| | (26.43) | (4.117) | (2.584) | (1.479) | (1.011) | | (0.716) |
| 15 | 26.8 | 4.19 | 2.63 | 1.52 | 1.04 | 0.84 | 0.73 |
| 100 | 27.33 | 4.29 | 2.71 | 1.57 | 1.08 | 0.88 | 0.76 |

Table 3.3: Drag coefficients ($\rho^* = 1$), Values in parentheses are taken from Feng and Michaelides [2001a], Values in brackets are taken from Oliver and Chung [1987].

is strongly dependant on the $Re$. Oliver and Chung [1987] have reported $\theta_d = 41.7$ and $\theta_d = 44.76$ for $Re = 100$ and $Re = 150$ respectively. The values predicted by our simulations ($\theta_d = 41.1$ and $\theta_d = 46$ respectively) are in good agreement with the literature.

#### 3.8.2.3 Interfacial velocity

The last validation test focused on the interfacial velocity $V_I$. Figure 3.11 compares the velocity profiles along the interface predicted by our simulation code and the one reported by Oliver and Chung [1987]. We observe that $V_I$ is strongly influenced by $Re$. As the Reynolds number increases, the peak interfacial velocity increases, the symmetry about the axis is lost, and the peak shifts toward the droplet front. This evolution is correctly reproduced by our simulations

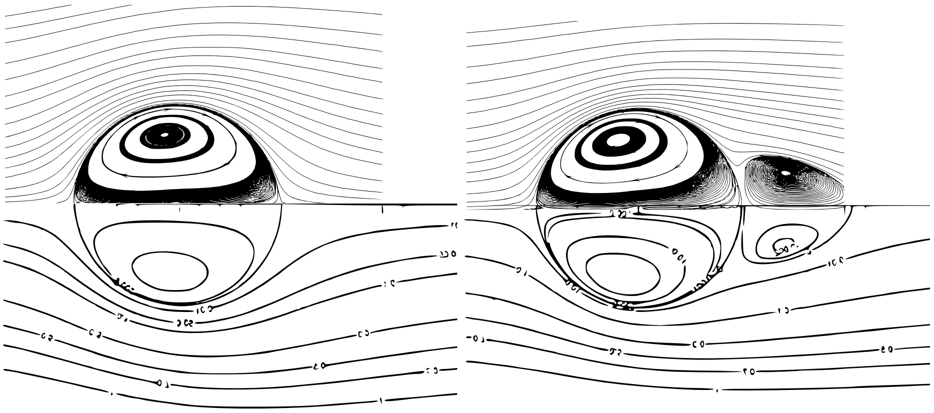

Figure 3.9: Internal/External Streamlines for a constant viscosity ratio $\mu^* = 7$, $Re = 10$(left), $Re = 100$(right), top: present simulations, bottom: Feng and Michaelides [2001a].

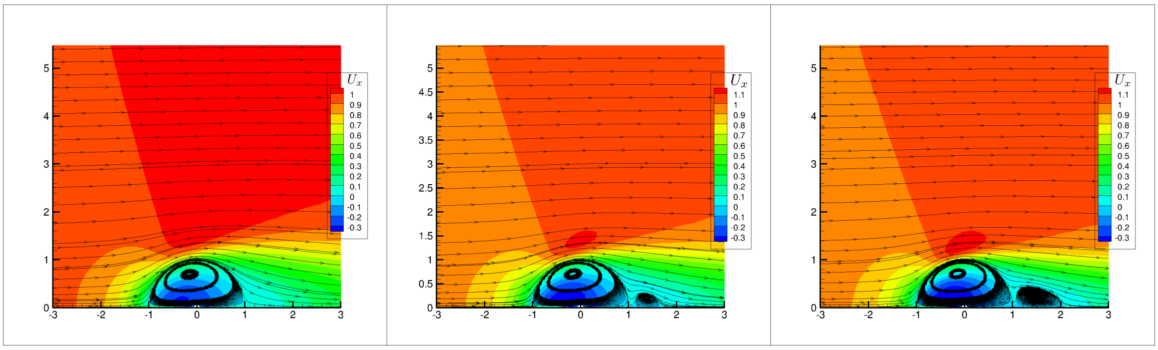

Figure 3.10: Streamlines for different Reynolds number $\mu^* = 3$, from left to right $Re = 50, 100, 150$.

## 3.8.3 Mass transfer

### 3.8.3.1 1D diffusion across a flat interface

In order to verify the implementation of the jump conditions for the concentration, especially in the case of discontinuous concentration at the interface ($k \neq 1$), we considered first the unsteady diffusion of a solute between two quiescent liquids (see Figure 3.12 [right]). The two phases are supposed to extend infinitely in the $x$ and $z$ directions, so that the problem is 1D in the $y$ direction. The mass transfer problem has an analytical solution, and the corresponding unsteady concentration evolution on each side of the interface is given by Eq (3.8.1).

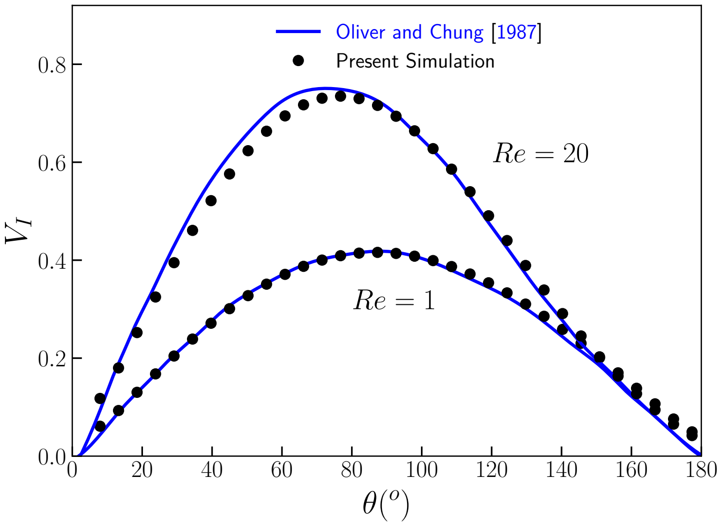

Figure 3.11: Interface velocity for $\mu^* = 0.333$.

$$\begin{aligned} C_1^+ &= \left(\frac{D_2}{D_2 + k \cdot D_1}\right)\left(\frac{k \cdot C_2^0 - C_1^0}{C_2^0 - C_1^0}\right) erfc(-u_1) \\ C_2^+ &= \left(\frac{D_1}{D_2 + k \cdot D_1}\right)\left(\frac{k \cdot C_2^0 - C_1^0}{C_2^0 - C_1^0}\right) erfc(u_2) \end{aligned} \tag{3.8.1}$$

This problem was solved numericaly using JADIM. The following conditions were considered: ($D_1 = D_2; C_1^0 = 1; C_0^0 = 0$). The influence of the partition coefficient $k$, responsible for the concentration discontinuity at the interface, was investigated. The corresponding boundary conditions are reported in Figure 3.12 (right).

The simulation results are reported in Figure 3.13. Excellent agreement is obtained with the analytical solution. as the Fourier number becomes significant compared to 1, the infinite-wall assumption is no longer valid and simulations deviate from the theory. It can be noticed that, whatever the value of $k$ (*i.e.* whether it is smaller or larger than 1), the concentration jump at the interface is well reproduced by the simulation, and that interface concentrations are independent of the time (equilibrium).

#### 3.8.3.2 Unsteady diffusion in a sphere

The second case considered for validation purpose is the basic problem of unsteady diffusion in a sphere ($Pe = 0$ and $Re = 0$) with mass transfer from the interface. The concentration inside the droplet is initially set at $C_0'$, and a fixed concentration is imposed at the interface $C_s'$. The instantaneous radial profile of the normalized concentration $C^i = \frac{C^{i\prime} - C_0'}{C_s' - C_0'}$ is given by the Newman [1931] equation (Eq. 3.8.3):

$$\begin{cases} C_1^+ = \dfrac{C_1 - C_1^0}{C_2^0 - C_1^0} \\ C_2^+ = \dfrac{C_2 - C_2^0}{C_1^0 - C_2^0} \\ u_1 = \dfrac{y}{2\sqrt{D_1 t}} \quad for \quad y < 0 \\ u_2 = \dfrac{y}{2\sqrt{D_2 t}} \quad for \quad y > 0 \end{cases} \tag{3.8.2}$$

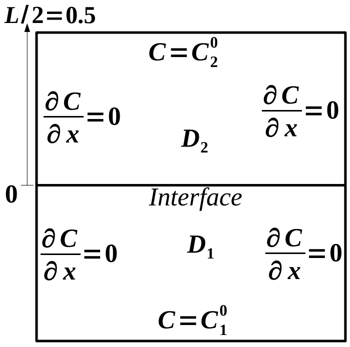

Figure 3.12: Left: Dimensionless variables, Right: Simulation domain with corresponding boundary conditions.

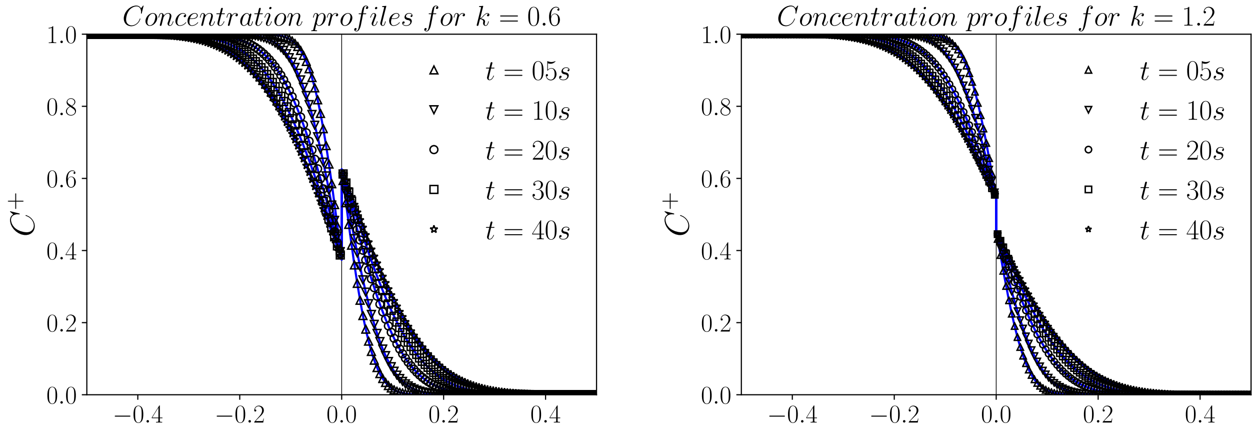

Figure 3.13: Temporal evolution of the concentration across the interface (Simulation: symbols, exact solution: blue line).

$$C^i = 1 + \frac{2}{r} \sum_{n=1}^{+\infty} \frac{(-1)^n}{n\pi} \exp\left(-(n\pi)^2 Fo^i\right) \sin\left(n\pi r\right) \tag{3.8.3}$$

Here, $R$, the droplet radius, which is chosen as the reference length, and the Fourier number is defined by $Fo^i = \dfrac{D^i t}{R^2}$.

The instantaneous Sherwood number is given by:

$$Sh = \frac{2\pi^2}{3} \frac{\sum_{n=1}^{+\infty} \exp\left(-(n\pi)^2 Fo^i\right)}{\sum_{n=1}^{+\infty} \frac{1}{n^2} \exp\left(-(n\pi)^2 Fo^i\right)} \tag{3.8.4}$$

Eq. 3.8.4 indicates that the Sherwood number tends towards the asymptotic value $Sh_{Newman} = 2\pi^2/3 \approx 6.58$, when $Fo \longrightarrow \infty$.

The radial concentration profiles deduced from Eq. (3.8.4) are compared with our DNS results in Figure 3.14, for different values of the dimensionless times. A very good agreement is observed between the numerical simulations (symbols) and the Newman's solution (lines). The corresponding asymptotic Sherwood number obtained from the simulations is $Sh_\infty = 6.56$, which differs only by 0.2% from the Newman's prediction.

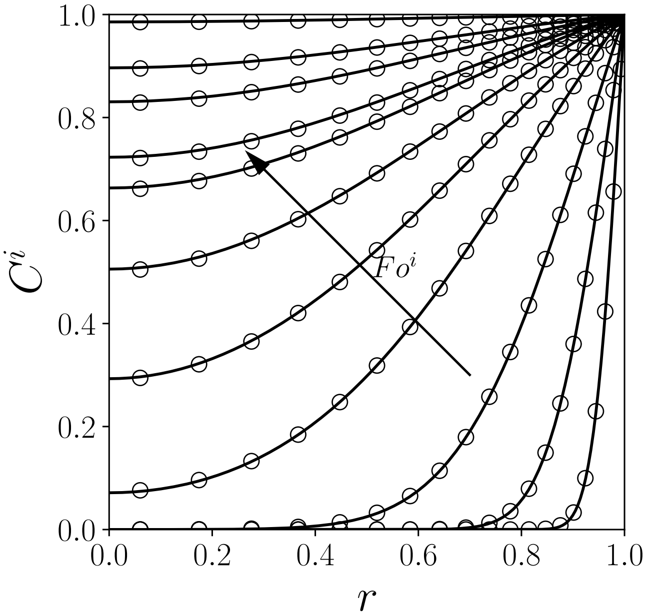

Figure 3.14: Temporal evolution of the concentration within the droplet.

### 3.8.3.3 Internal transfer under Stokes flow conditions

We now consider the transfer in the limit of a low Reynolds number, for which an analytical solution of the external and internal flows is given by Hadamard-Rybczynski (see e.g. in Clift et al. [1978]).

The simulations were performed in the case $Re = 0.1$. The concentration is imposed at the droplet interface, and a uniform concentration is assumed outside the drop (internal transfer). The simulation results are compared with available solutions from the literature Clift et al. [1978], in terms of the temporal evolution of the Sherwood number. The simulations reported in Fig 3.15 are performed with viscosity ratio $\mu^* = 1$.

In this configuration, which is closer to the case studied in this thesis, the numerical model again gives a good prediction of the expected evolution. It is worth noticing that the Sherwood number still converges to the steady value given by Eq. (3.8.4) as $\frac{Pe}{\mu^*+1} \longrightarrow 0$. Whereas for $\frac{Pe}{\mu^*+1} \longrightarrow \infty$, the theoretical prediction proposed by Kronig and Brink [1951] (Eq. (3.8.5)) is reached.

$$Sh = \frac{32}{3} \frac{\sum_{n=1}^{+\infty} A_n^2 \lambda_n \exp\left(-16\lambda_n Fo^i\right)}{\sum_{n=1}^{+\infty} A_n^2 \exp\left((-16\lambda_n Fo^i\right)} \tag{3.8.5}$$

with $A_n$ and $\lambda_n$ given the the lists (3.8.6)

$$\begin{aligned} A_n &= [1.33 \quad 0.60 \quad 0.36 \quad 0.35 \quad 0.28 \quad 0.22 \quad 0.16] \\ \lambda_n &= [1.678 \quad 8.48 \quad 21.10 \quad 38.5 \quad 63.0 \quad 89.8 \quad 123.8] \end{aligned} \tag{3.8.6}$$

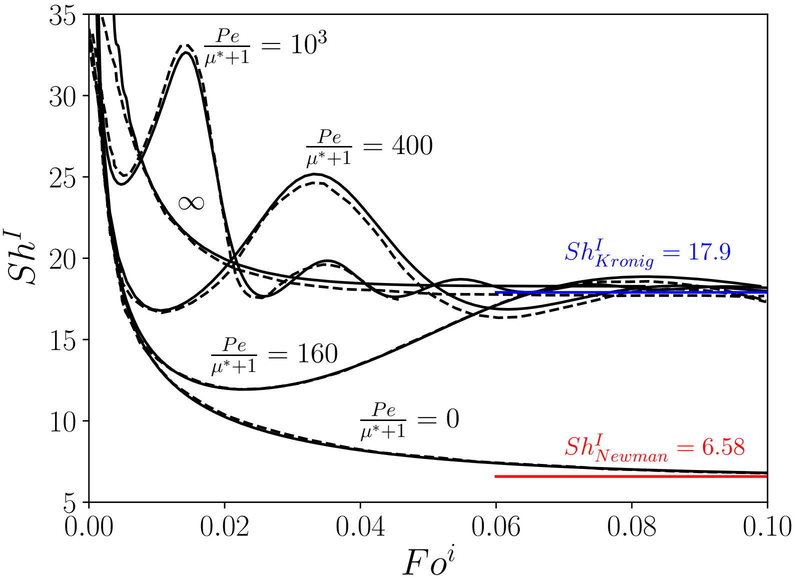

Figure 3.15: Temporal evolution of the Sherwood number for different values of $Pe/(\mu^* + 1)$, solid line: present results, dashed lines from Clift et al. [1978].

The Sherwood profile around the droplet for an internal problem was investigated by Juncu [2010]. His results have been chosen to validate the angular variation of the local Sherwood.

As highlighted in Figure 3.16, the angular evolution of $Sh_\theta$ along the interface predicted by DNS shows excellent agreement with Juncu [2010] results.

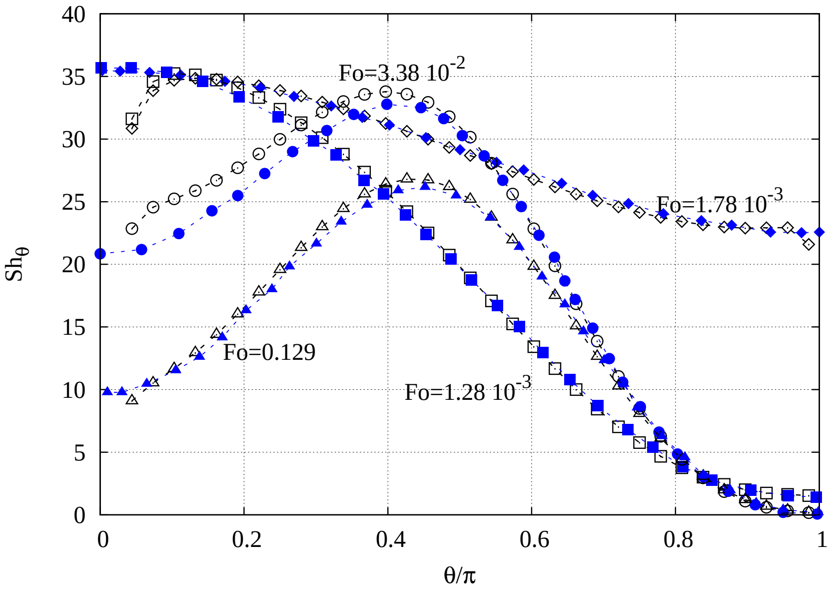

Figure 3.16: Local Sherwood number angular profiles for different Fourier numbers, - blue: Juncu's results Juncu [2010], - black: present simulations ($Pe = 1000$, $\rho^* = 1$, $\mu^* = 1$, $D^* = 1$).

### 3.8.3.4 Conjugate problem at low Reynolds number

In order to get even closer validation to the case studied in the thesis, we considered the study of Oliver and Chung [1986] related to conjugate mass transfer.

In the case of comparable transfer resistance in the two phases, one must solve the mass balance equations in both the internal and the external fluids, with the jump conditions at the interface discussed in Sec 3.5.2. The case considered by the authors is a spherical droplet in a low Reynolds flow (i.e. $Re = 0.1$). The viscosity ratio was set $\mu^* = 1$.

As depicted in Figure 3.17 (top left), the effect of convection becomes increasingly significant while increasing the Peclet number, hence the effect of the internal recirculation observed on the Sherwood number evolution (oscillations at short times). The DNS results reproduce very well the Sherwood evolution of Oliver and Chung [1986]. In the studied range of Peclet, the asymptotic values of the Sherwood number $Sh_{st}$, Table 3.4, are again consistent with the literature.

| $Pe$ | 50 | 100 | 200 | 500 | 1000 |
|---|---|---|---|---|---|
| Present simulations | 2.72 | 3.6 | 4.8 | 7.19 | 9.14 |
| Olivier & Chung | 2.67 | 3.6 | 4.8 | 7.2 | 9.2 |

Table 3.4: Steady Sherwood number $Sh_\infty$ for $Re = 0.1$ and $\mu^* = 1$.

In order to further assess the code accuracy, a parametric study has been carried out, still in the limit of low Reynolds number, based on the work of Kleinman and Reed [1996]. Three key parameters have been studied: the mass diffusivity ratio $D^*$, the partition coefficient $k$, and the viscosity ratio $\mu^*$ for $Re = 0.1$ and $Pe = 1000$. These physical properties indeed have a significant effect on mass transfer. The main results of the parametric study are summarized in Figure 3.17.
An increase of the partition coefficient $k$, which means a decrease in the affinity of the solute for the continuous phase, induces a decrease in the mass transfer rate. This behaviour is well reproduced by our simulations (see Fig. 3.17 on the top right corner). It is worth noting that the $Sh$ oscillations emphasizing the presence of the internal circulations are damped when the partition coefficient increases.
Regarding the effect of the diffusivity ratio (Figure on the bottom left corner), no modification of $Sh$ oscillations frequency is evidenced. This result, also predicted by our simulations, confirms that these oscillations are due to the internal recirculation only, and not related to diffusion. $D^*$ is a key parameter for the location of the mass transfer resistance between the internal and external phases. The Sherwood number evolution is expected to converge towards the profiles associated to the internal problem for low $D^*$. However, for $D^* = 0.25$ the predicted $Sh_\infty$ is $Sh = 15.327$, which is lower than the theoretical value of 17.9. For $D^* = 0.1$ the Sherwood number converges asymptotically toward $Sh = 17.07$ which represents 95% of the asymptotic value predicted by Kronig and Brink [1951].

Both temporal and spatial evolutions of the solute concentration depend on the physical properties. The effect of the Peclet number on the temporal evolution of the solute distribution in the droplet is illustrated in Figures 3.18 and 3.19 for low (i.e. $Pe = 10$) and strong ($Pe = 1000$) convective effects. One can particularly notice, in Figure 3.19, the effect of the internal recirculation on the solute distribution. After a certain time, the process becomes diffusive limited from a torus located in the vortex zone toward the interface. This state corresponds to the steady regime of the Sherwood temporal evolution.

## 3.9 Conclusion

This chapter has been devoted to the presentation of the simulation tool JADIM used in this study, and the numerical method used to resolve the Navier-Stokes and the solute transport equations, inside and outside a spherical droplet. Many tests have been performed to ensure the independence of the results on the used mesh.
Validation tests were conducted using available data from literature. Regarding the hydrodynamics aspect, the drag coefficient was in good agreement with earlier studies of Feng and Michaelides [2001a] and Oliver and Chung [1987] for the studied range of $\mu^*$ and $Re$. Local quantities, like streamlines and interface velocity, equally showed a consistent trend with the literature results.
Concerning the mass transfer, many validation tests of growing complexity (and similarity

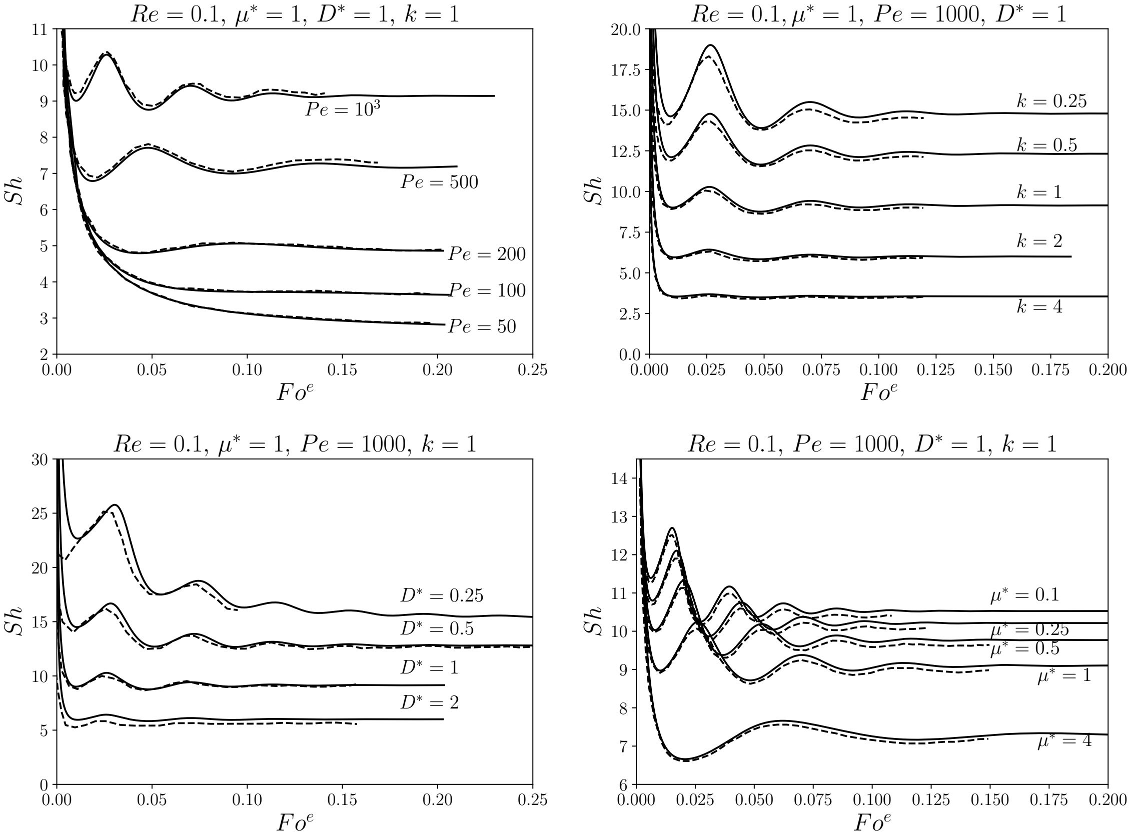

Figure 3.17: Temporal evolution of Sherwood number. Top left figure: comparison of DNS with the results of Oliver and Chung [1986] for $Re = 0.1$ and $\mu^* = 1$. Other figures: comparison with the results of Kleinman and Reed [1996] for $Re = 0.1$ and $Pe = 1000$. Solid lines represent our simulations, dashed lines the literature results.

with the case study) were performed. The concentration jump conditions implementation at the interface was first examined by studying 1D diffusion across a flat interface. The results showed excellent agreement with the theoretical analytical solution. Then, internal and conjugated mass transfer have been validated for low Reynolds flows. Again, in the studied range of partition coefficient and diffusivity ratio, the temporal evolution of the local and the global Sherwood number revealed good agreement with the earlier works of Kleinman and Reed [1996] and Juncu [2010]. In both the conjugate and internal mass transfer cases, the Sherwood number was shown to converge toward to a steady value consistent with the one reported in literature.

The results presented in the following Chapters will focus on the hydrodynamics and conjugate mass transfer for intermediate and high Reynolds flows.

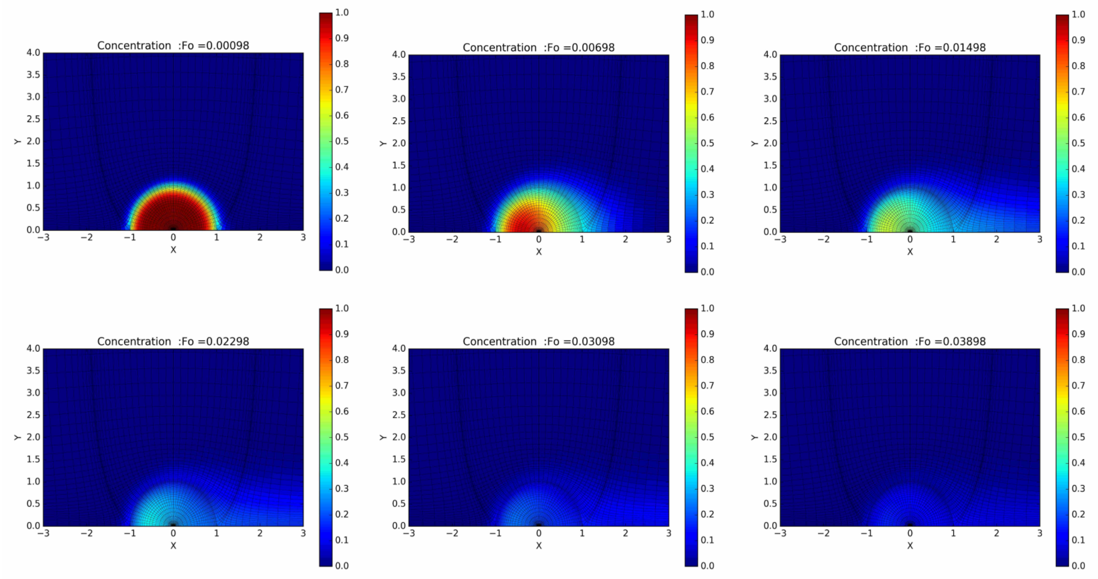

Figure 3.18: Temporal evolution of the concentration spatial distribution ($Re = 10$, $\mu^* = 1,\ D^* = 1,\ Pe = 10$).

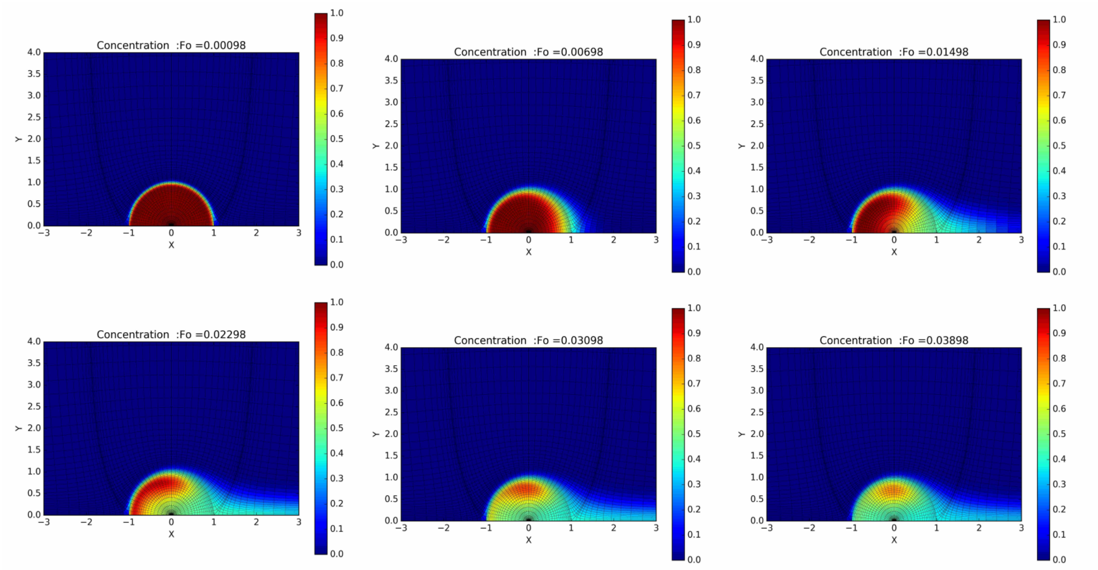

Figure 3.19: Temporal evolution of the concentration spatial distribution ($Re = 10$, $\mu^* = 1,\ D^* = 1,\ Pe = 1000$).

# Chapter 4

# Simulations for low to moderate *Re*

## Contents

After hydrodynamic and mass transfer validations, the focus of this chapter is to investigate moderate Reynolds flows. Under such configuration where inertial forces prevail, both droplet hydrodynamic and mass transfer deviate from low Reynolds behaviour. Two main parts are investigated separately in this chapter.
For the hydrodynamic part, three aspects are studied: *i)* the evolution of the drag coefficient with hydrodynamic parameters, *ii)* the appearance and location of the separation angle responsible of an external recirculation, and *iii)* the Basset-Boussinesq history force for the drop, considering the analogy between the viscosity ratio and the slip length at the interface.
Regarding mass transfer, a detailed analysis relating conjugate problem and the extreme internal/external problems is proposed. A correlation of the global Sherwood number is then analyzed.

## 4.1 Hydrodynamics

### 4.1.1 Drag coefficient

For a fully developed flow around a spherical droplet in a Stokes flow, an analytical expression of the drag coefficient Eq. (4.1.1) has been derived by Hadamard [1911]; Rybczynski [1911] where inertia can be neglected in comparison with viscous forces.

$$C_D(Re, \mu^*) = \frac{8}{Re}\frac{2+3\mu^*}{1+\mu^*} \tag{4.1.1}$$

Introducing the drag coefficient related to a rigid particle in a Stokes flow, $C_d^{solid}(Re) = 24/Re$, Stokes [1851] and the expression reported by Clift et al. [1978] for an immersed bubble in a Stokes flow, $C_d^{bubble}(Re) = 16/Re$, equation (4.1.1) can be rewritten as:

$$C_D(Re, \mu^*) = \frac{C_D^{bubble} + \mu^* C_D^{solid}}{1+\mu^*} \tag{4.1.2}$$

Equation (4.1.2) indicates that, regardless of the viscosity ratio, the value of $C_D$ remains between that of the particle, and that of the bubble at low Reynolds numbers.

For intermediate/high Reynolds flows, no analytical solution exits and many correlations can be found in literature to evaluate drag coefficient of a bubble or a particle.

Figure 4.1 depicts the evolution of $C_D(Re, \mu^*)$ predicted by our simulations at intermediate to high $Re$. The correlation proposed by Mei and Klausner [1992] for bubble, and by Schiller [1933] for the rigid particle in an intermediate Reynolds number flow are also reported. It is interesting to observe that all the curves of the droplet drag coefficient $C_D(Re, \mu^*)$ lay between the corresponding values for the particle and the bubble (i.e. $C_D^{bubble}(Re) \leq C_D(Re, \mu^*) \leq C_D^{Particle}(Re)$)

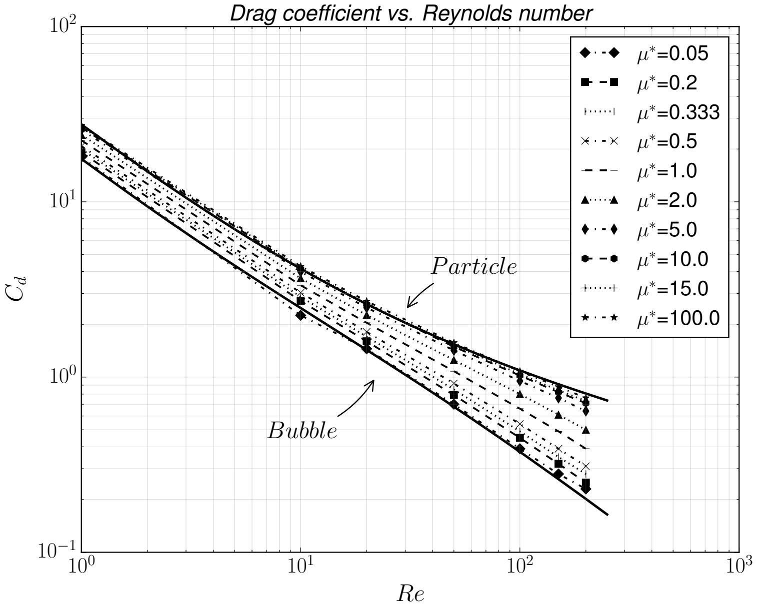

Figure 4.1: Drag coefficients, markers: present simulations, continuous line: correlations Mei and Klausner [1992], Schiller [1933] for bubble and particle respectively.

Ryvkind and Ryskin [1976] were the first to suggest such an analysis of drop drag coefficient by decomposing it into the sum of bubble and particle contributions. His method gives an error of less than $5-7\%$ for $0.5 < Re < 200$ and $\mu^*$ close to one.
In order to check the extension of relation (4.1.2) for a larger range of viscosity ratios, we compare in Table 4.1 the present simulations of drag coefficient with the values calculated from Eq. (4.1.2) combined with the Mei and Klausner [1992] correlation for the bubble and that from Schiller [1933] for the particle. Interestingly Equation (4.1.2) yields a very good approximation of the $C_D$ values calculated by simulation for all the range of viscosity ratio considered (the values in Tab. 4.1 correspond to the different symbols in Fig. 4.2).

We report in Table 4.2 the effect of the density ratio on the drag coefficient. The effect is really small, the maximum variation is less than 2%. This result is in agreement with previous simulations of Feng and Michaelides [2001a].

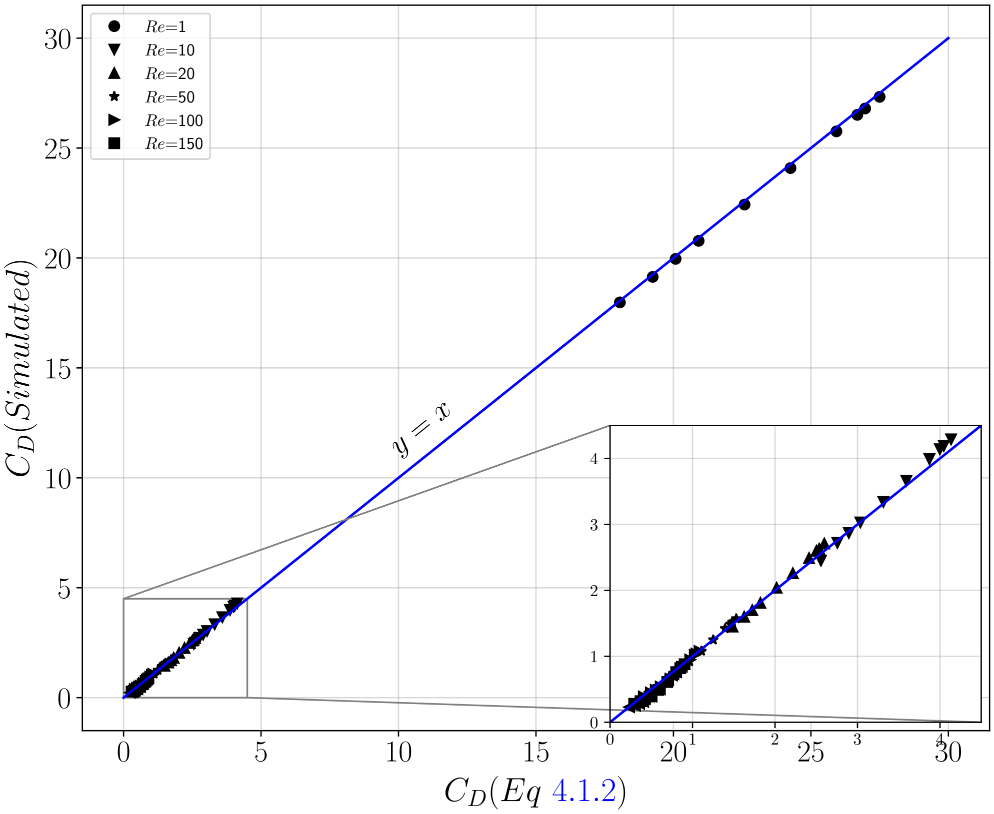

Figure 4.2: Parity plot of the drag coefficient: symbols: present simulations vs Eq. (4.1.2) combined with Mei and Klausner [1992] and Schiller [1933] correlations, blue lines: $y = x$ (each Reynolds number contains different viscosity ratios). Insert: zoom for smaller values of the drag coefficient (corresponding to larger $Re$).

### 4.1.2 Separation angle

For intermediate to high Reynolds number flow and viscosity ratio, an external circulation may occur in the droplet's wake. Unlike the solid particle case, for a droplet the internal circulation delays both the onset of flow separation and the wake formation in the external fluid. The separation angle, $\theta_d$, measures the angle at which the external boundary layer is detached from the sphere's surface drop ($theta_d = 180 - \theta$ with the notations of Figure 2.1 ). This angle might characterize as well the position at which

| $\mu^* \backslash Re$ | 1 | 10 | 20 | 50 | 100 | 150 | 200 |
|---|---|---|---|---|---|---|---|
| 0.5 | 20.78 | 3.03 | 1.81 | 0.92 | 0.54 | 0.39 | 0.31 |
| | (20.916) | (3.035) | (1.822) | (0.964) | (0.613) | (0.477) | (0.403) |
| 1.0 | 22.43 | 3.34 | 2.04 | 1.08 | 0.66 | 0.49 | 0.39 |
| | (22.587) | (3.314) | (2.019) | (1.1077) | (0.733) | (0.585) | (0.503) |
| 2.0 | 24.09 | 3.66 | 2.26 | 1.25 | 0.8 | 0.61 | 0.5 |
| | (24.258) | (3.593) | (2.216) | (1.251) | (0.852) | (0.693) | (0.604) |
| 5.0 | 25.76 | 3.99 | 2.49 | 1.42 | 0.95 | 0.76 | 0.64 |
| | (25.929) | (3.872) | (2.412) | (1.394) | (0.972) | (0.802) | (0.704) |

Table 4.1: Comparison between $C_D$ values deduced from the present simulations and those calculated from Eq.(4.1.2) (between parentheses).

| Re / $\rho^*$ | 0.1 | 0.5 | 1 | 5 | 10 |
|---|---|---|---|---|---|
| 10 | 3.345 | 3.345 | 3.344 | 3.342 | 3.342 |
| 50 | 1.088 | 1.086 | 1.083 | 1.07 | 1.07 |
| 100 | 0.671 | 0.667 | 0.662 | 0.66 | 0.66 |

Table 4.2: Drag coefficient (density ratio effect).

the vorticity at the interface changes sign.

$$\omega_s^e = \frac{\partial V_2}{\partial \xi_1}\bigg|_{R^+} - \frac{\partial V_1}{\partial \xi_2}\bigg|_{R^+} + H_2^1 V_2|_{R^+} - H_1^2 V_1|_{R^+} \qquad (4.1.3)$$

Clift et al. [1978] have shown that for a solid particle, the flow remains attached for $0 < Re < 20$. For $20 < Re < 130$, a steady wake region develops. Thus, $Re = 20$ represents the onset of separation for a solid particle. The authors report the following correlation of the separation angle which is valid for $20 < Re < 400$:

$$\theta_d = 42.5\,[\log(Re/20)]^{0.483} \qquad (4.1.4)$$

On the other hand, for a spherical gas bubble in an uncontaminated liquid (*i.e.* without surfactant), Blanco and Magnaudet [1995] predict no separation ($\theta_d = 0$) regardless of the Reynolds numbers. This is in agreement with our results at small viscosity ratios ($\mu^* = 0.02$), for which no recirculation is detected in the range of Reynold number $Re \leq 200$.

Figure 4.3 shows the vorticity profiles along the interface for different configurations. We note that for a given Reynolds number (here $Re = 100$), the maximum of the interface vorticity increases with the viscosity ratio. For $\mu^* \geq 5$, the vorticity changes its sign, which proves that an external separation occurs at an angle where $\omega_s^e = 0$.

We can characterize the presence or the absence of the external recirculation by a schematic curve (Figure 4.4). In the pink region (i.e. below the line) the external flow remains attached, whereas an external recirculation will appear in the blue area. As $\mu^*$ increases to high values, the droplet behaves like a solid particle, hence explaining that the critical Reynolds number of separation tends toward the particle's once, that is $Re \longrightarrow 20$. However at low viscosity, a bubble-like behaviour is observed and no separation occurs.

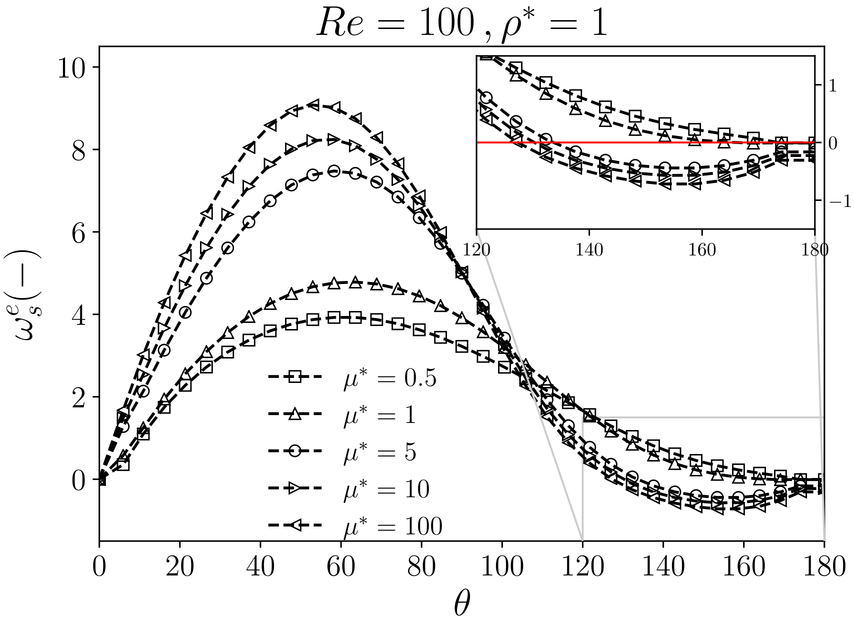

Figure 4.3: Vorticity profiles along the interface ($Re = 100$, $\rho^* = 1$).

Table 4.3 reports the angles of separation for different ($Re$,$\mu^*$), some of the corresponding streamlines are highlighted by Figure 4.5 . In order to extend relation (4.1.4) to fluid particle, we propose the relation:

$$\theta_d = 42.5\,[\log(Re/20)]^{0.483}\,\frac{\mu^*}{1+\mu^*} \tag{4.1.5}$$

Figure 4.6 shows the comparison between our results and this new correlation. With an error bar of ±1.5°, the correlation yields satisfactory agreement.

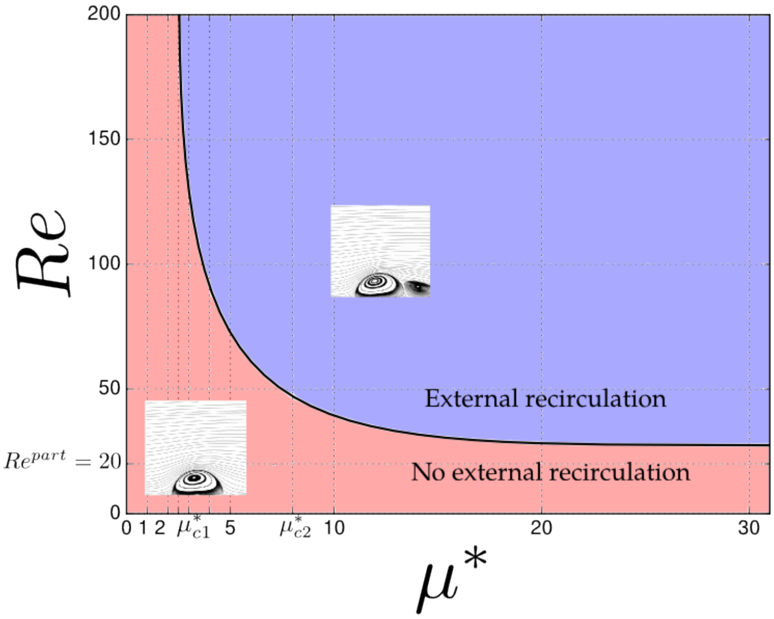

Figure 4.4: Schematic external bifurcation curve ( $\rho^* = 1$).

| $\mu^*$ / $Re$ | 50 | 100 | 150 | 200 |
|---|---|---|---|---|
| 3 | no | 41 | 46 | 48 |
| 5 | 34 | 46 | 51 | 55 |
| 10 | 37 | 50 | 55 | 59 |
| 15 | 38 | 51 | 57 | 61 |
| 100 | 40 | 53 | 60 | 65 |

Table 4.3: Separation angles $\theta_d$ in degrees (One digit precision).

## 4.1.3 History force

### 4.1.3.1 Introduction

In this section, we consider the unsteady force experienced by a spherical drop. More specifically, we focus on the so called Basset-Boussinesq history force under Stokes flow (creeping flow) conditions. The section is presented under the form of a paper submitted to the journal PR Fluids. We apologize for some repetitions related to the definition of variables and physical properties which are consistent with the rest of the thesis.

Under Stokes flow condition, the force experienced by a fluid sphere of radius $R$, viscosity $\mu^i$ and density $\rho^i$ moving with relative velocity $W(t) = U(t) - V(t)$ in an unbounded fluid of viscosity $\mu^e$ and density $\rho^e$ is composed of the steady drag force, the Basset-Boussinesq history force and the added mass force Gatignol [1983]; Maxey and

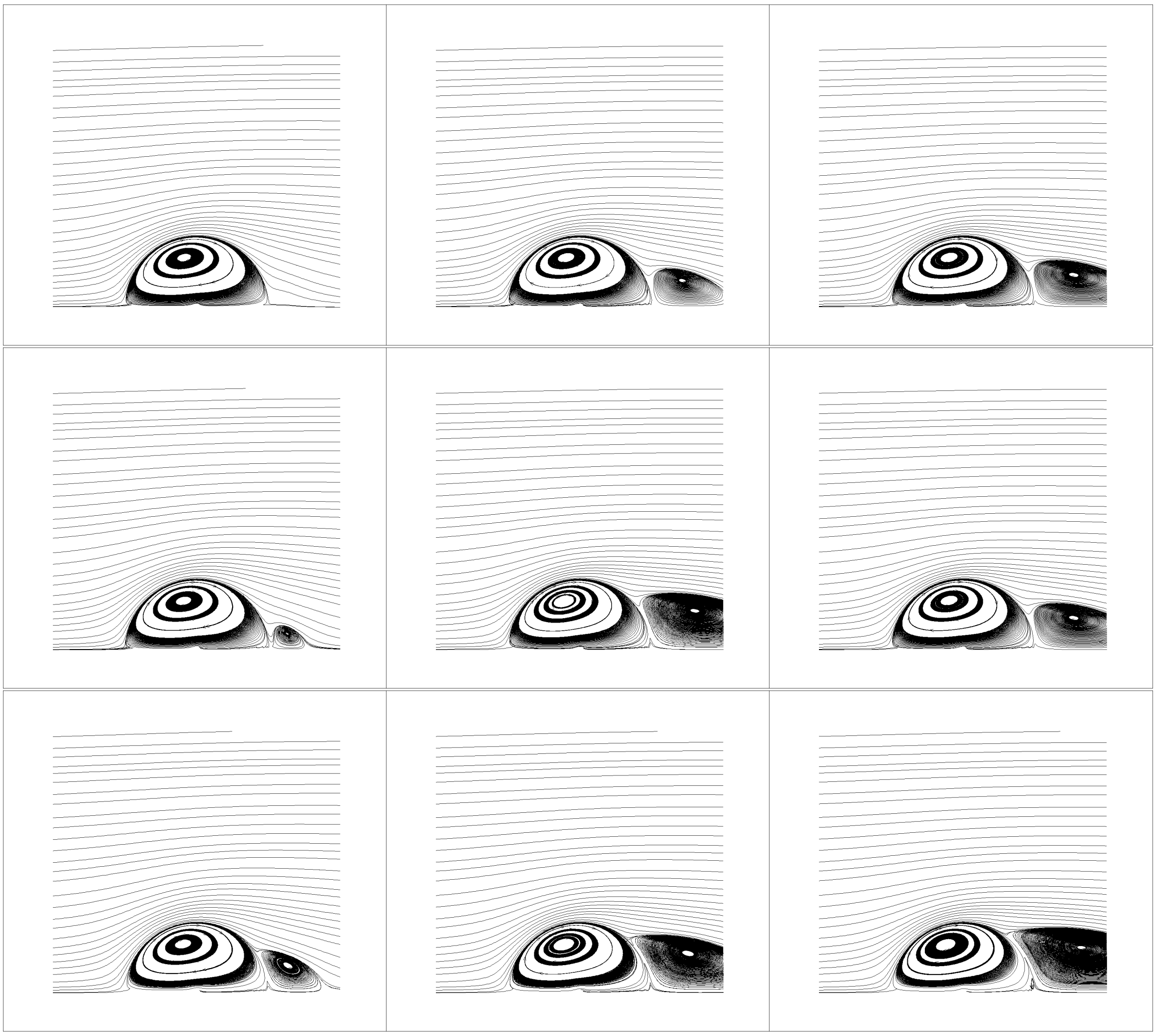

Figure 4.5: Streamlines for different Reynolds numbers and viscosity ratios: First row $\mu^* = 5$, second row $\mu^* = 10$, third row $\mu^* = 100$. First column $Re = 50$, second column $Re = 100$, third column $Re = 150$.

Riley [1983]:

$$F(t) = 6\pi\mu^e R\frac{2+3\mu^*}{3+3\mu^*}W(t) + 6\pi\mu^e R\int_0^t \frac{dW}{dt'}K_\mu(t-t',\mu^*)dt' + \frac{2}{3}\rho^e\pi R^3\frac{dW}{dt} \quad (4.1.6)$$

where $\mu^* = \mu^i/\mu^e$ is the viscosity ratio and $K_\mu$ is the memory kernel. The external Reynolds number $Re = 2RW\rho^e/\mu^e$ should satisfy $Re << 1$.

In the solid sphere limit ($\mu^* = \infty$), the Basset-Boussinesq history force is associated

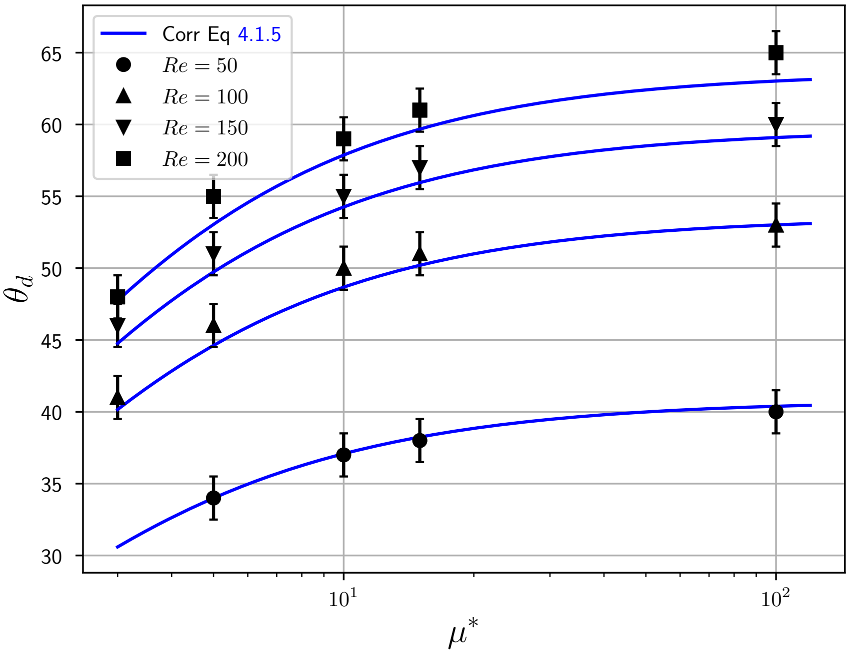

Figure 4.6: Separation angle. Symbols: present simulations, blue lines: Eq (4.1.5).

to the kernel Basset [1887]; Boussinesq [1885]

$$K_\mu(t, \mu^* = \infty) = \frac{1}{\sqrt{\pi t / t_\nu}} \tag{4.1.7}$$

where $t_\nu = R^2/\nu^e$ is the characteristic diffusion time scale based on the kinematic viscosity $\nu^e = \mu^e/\rho^e$ of the external fluid. We also introduce the characteristic diffusion time $t_{\nu\, i} = R^2/\nu^i$ based on the cinematic viscosity $\nu^i = \mu^i/\rho^i$ of the internal fluid.

In the bubble limit ($\mu^* = 0$), Yang and Leal [1991] showed that:

$$K_\mu(t, \mu = 0) = \frac{4}{3} \exp\left[9t/t_\nu\right] \operatorname{erfc}\left[3\sqrt{t/t_\nu}\right] \tag{4.1.8}$$

The general expression for $K_\mu$ as a function of $\mu^*$ has not been derived so far for a fluid particle. The analytic solution for the force has been obtained in the Fourier-transform space but the transform from the frequency domain to the time domain can only be achieved under the two limits of solid sphere and spherical bubble Michaelides and Feng [1995]; Yang and Leal [1991].

In parallel, the unsteady Stokes problem has also been considered for a slip sphere. The Navier slip condition is then considered on the sphere surface

$$w_\theta = \lambda r \frac{\partial}{\partial r}\left(\frac{w_\theta}{r}\right) \tag{4.1.9}$$

where $w_\theta$ is the tangential velocity, $\lambda$ is the surface slip length and $r$ is the radial position. The force experienced by the sphere is then Gatignol [2007]; Michaelides and Feng [1995]; Premlata and Wei [2019]

$$F(t) = 6\pi\mu^e R \frac{1+2\lambda/R}{1+3\lambda/R} W(t) + 6\pi\mu^e R \int_0^t \frac{dW}{dt'} K_\lambda(t,t',\lambda)dt' + \frac{2}{3}\pi\rho^e R^3 \frac{dW}{dt} \tag{4.1.10}$$

where the expression for the memory kernel $K_\lambda$ for a uniform slip along the surface is

$$K_\lambda(t,\lambda) = \frac{(1+2\lambda/R)^2}{\lambda/R(1+3\lambda/R)} \exp\left[\frac{(1+3\lambda/R)^2}{\lambda^2/R^2} t/t_\nu\right] \operatorname{erfc}\left[\frac{(1+3\lambda/R)}{\lambda/R}\sqrt{t/t_\nu}\right] \tag{4.1.11}$$

The solution for $K_\lambda$ can be connected to the solution for a solid sphere and a spherical bubble considering asymptotic values of the slip, i.e. $\lambda = 0$ for a no slip surface (solid sphere case) and $\lambda = \infty$ for a free slip surface (bubble case), considering that $K_\mu(t, \mu^* = 0) = K_\lambda(t, \lambda = \infty)$ and $K_\mu(t, \mu^* = \infty) = K_\lambda(t, \lambda = 0)$.

The aim of this work is first to relate the slip length at a fluid sphere interface and the viscosity ratio, and then use it to extend the Basset-Boussinesq history force acting on any fluid sphere. The relevance of the proposed history force is validated by direct numerical simulations obtained with the JADIM code. The simulations reported in this section are carried out for $\rho^* = 1$.

#### 4.1.3.2 Additional validation for Stokes flow ($Re << 1$)

The series of validation presented in Chapter 3 (see Table 3.3) report on simulations performed for Reynolds number $Re \geq 1$. The code has also been validated for the Stokes flow regime considered in this section. For that purpose, simulations have been conducted for the grid LCE presented above at $Re = 0.1$ and a wide range of viscosity ratio $\mu^*$. The two limits $\mu^* = 0$ (bubble) and $\mu^* = \infty$ (solid sphere) were found in close agreement with the values obtained by Legendre [1996]. The normalized drag coefficient $C_D^* = (C_D - C_D^{bubble})/(C_D^{Solid} - C_D^{bubble})$ is plotted as a function of $\mu^*$ in Figure 4.7. Considering the Stokes solution given by relation 4.1.1, $C_D^*$ is expected to evolve as

$$C_D^* = \frac{\mu^*}{1+\mu^*} \tag{4.1.12}$$

in the limit $Re \to 0$. As shown in the figure, this variation with $\mu^*$ is perfectly reproduced. Note that the values of $C_D^*$ at $Re = 1$ deduced from the results reported in Table 3.3 (Chapter 3) are also satisfactorily reproduced by relation 4.1.12.

#### 4.1.3.3 The relation between slip length and viscosity ratio at a fluid sphere interface

*Uniform flow*

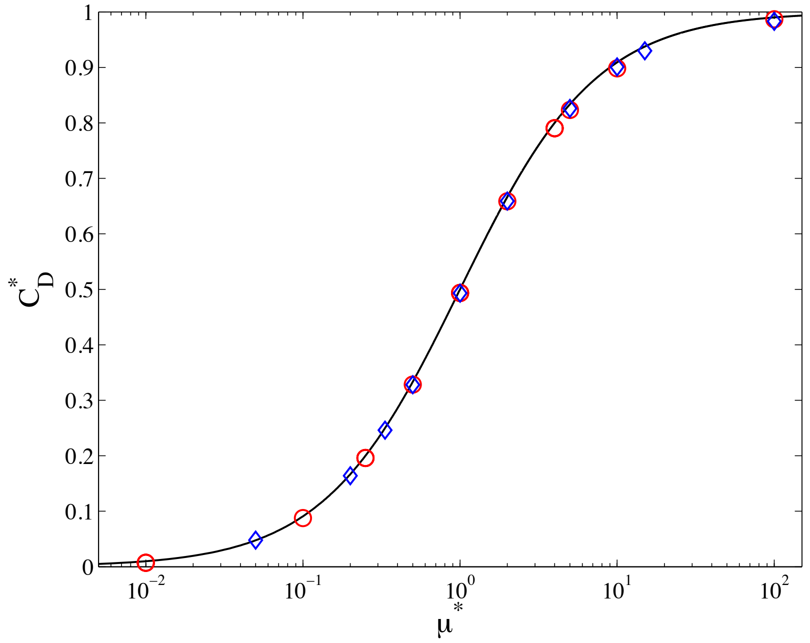

Figure 4.7: Normalized drag coefficient $C_D^*$ as a function of the viscosity ratio $\mu^*$ at $\rho^* = 1$. Numerical simulation: (○) $Re = 0.1$ and (◊) $Re = 1$. — relation 4.1.12.

We consider the steady uniform flow $W$ around a fixed fluid sphere of radius $R$. The stream functions for the flow inside and outside the fluid sphere are respectively Hadamard [1911]; Rybczynski [1911]:

$$\Psi_i = -\frac{Wr^2}{4}\frac{1}{1+\mu^*}\left[1-\frac{r^2}{R^2}\right]\sin^2\theta \tag{4.1.13}$$

$$\Psi_e = \frac{Wr^2}{2}\left[1-\frac{2+3\mu^*}{1+\mu^*}\frac{R}{2r}+\frac{\mu^*}{1+\mu^*}\frac{R^3}{2r^3}\right]\sin^2\theta \tag{4.1.14}$$

From this solution, we can calculate the tangential velocity

$$w_\theta = \frac{1}{2}\frac{1}{1+\mu^*}W\sin\theta \tag{4.1.15}$$

and the velocity gradient

$$r\frac{\partial}{\partial r}\left(\frac{w_\theta}{r}\right) = \frac{3}{2}\frac{\mu^*}{1+\mu^*}W\sin\theta \tag{4.1.16}$$

at the fluid sphere interface. Considering the Navier-slip condition at interface given by Eq. 4.1.9, we can define an effective surface slip length $\lambda$. From Eq. 4.1.15 and 4.1.16

we show that for the steady stokes flow the slip length is uniform at the interface and is directly related to the viscosity ratio through the relation

$$\lambda = \frac{R}{3\mu^*} \tag{4.1.17}$$

This expression is expected in the limit $Re \to 0$. Some interface distributions of $\lambda$ obtained using the Navier-Stokes solver JADIM are reported in Fig. 4.8. $\lambda/R$ is reported as a function of $\theta$ for $Re = 0.01$ and $Re = 0.1$. Different values of $\mu^*$ were considered: $\mu^* = 0.1$, 1 and 10. As shown $\lambda$ is remarkably uniform and close to the value $R/3\mu^*$. The maximum deviation of $\lambda$ is less than 2% for all cases we considered.

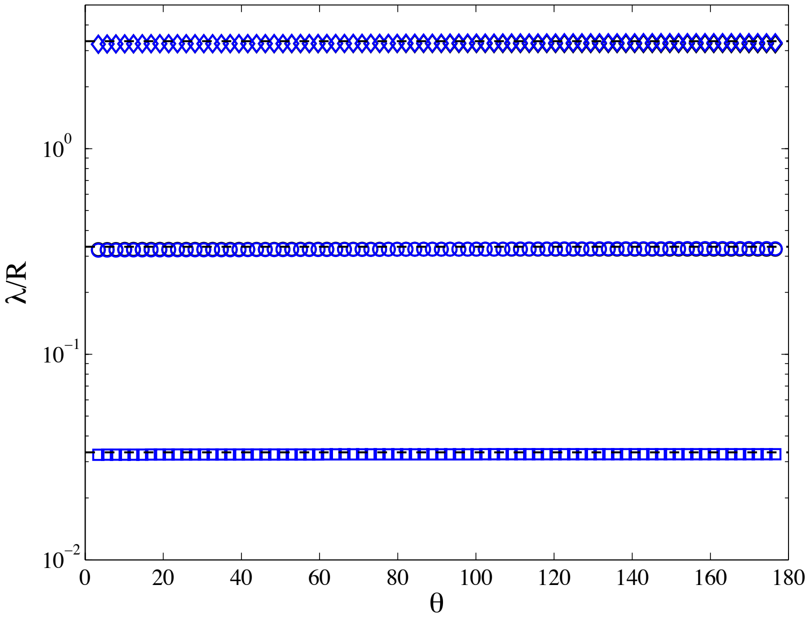

Figure 4.8: Effective interface slip length $\lambda$ for a steady uniform flow obtained from numerical simulations. Interface distribution of $\lambda$ is shown as a function of $\theta$ for $Re = 0.01$ (black symbols) and $Re = 0.1$ (blue symbols). ($\diamond$) $\mu^* = 0.1$, ($\circ$) $\mu^* = 1$ and ($\square$) $\mu^* = 10$. Dashed line: relation 4.1.17.

The evolution of the mean interfacial value of $\lambda$ with the viscosity ratio $\mu^*$ is reported in Fig. 4.9. Different Reynolds numbers were considered ($Re = 0.01$, $Re = 0.1$ and $Re = 1$). As shown in the figure, all the simulations collapse on the evolution given by relation 4.1.17 while no noticeable effect of the Reynolds number is observed on $\lambda$ up to $Re = 1$. We also report on this figure the results obtained with the two grids considered in this work. It should also be noted that we have compared the meshes of size $50R$ and

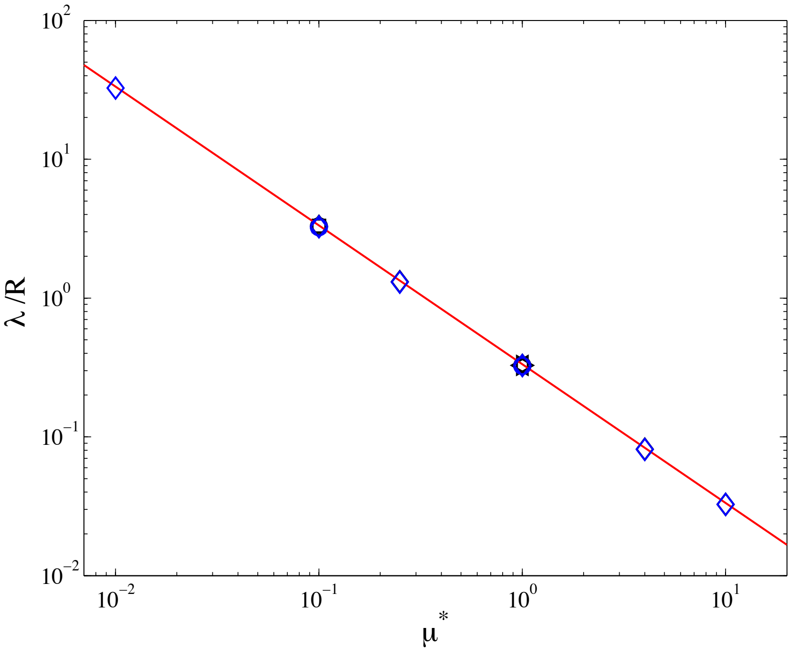

Figure 4.9: Effective interface slip length $\lambda$ for a steady uniform flow as a function of $\mu^*$ for $Re = 0.01$ (○), $Re = 0.1$ (◊) and $Re = 1$ (□). — $\lambda = R/3\mu^*$ (relation 4.1.17). (black symbols) simulation with the LCE grid. (blue symbols) simulation with the polar mesh.

$100R$ (not shown here for clarity). Both LCE and Polar meshes give very close values for the interface slip.

*Unsteady uniform flow*

We now analyze the variation of $\lambda$ under unsteady conditions. For that purpose, the case of a fixed fluid particle suddenly immersed in a uniform flow is considered. Distributions of $\lambda$ on the interface at $Re = 0.1$ and $\mu^* = 1$ are reported in Fig. 4.10 at different times. As shown $\lambda$ starts from $\lambda = 0$ and then increases. As observed for the steady uniform flow, the slip is remarkably uniform along the interface for all the times considered. A maximum is reached around $t = 0.12t_\nu$. Then $\lambda$ tends to $R/3\mu^*$ as expected for steady state. It should be stressed here that this asymptotic value is reached for a time $1/10^{th}$ of the characteristic diffusion time $t_\nu$. The evolution of $\lambda$ is directly connected to the development of the internal recirculation as illustrated in Fig. 4.11 for $Re = 0.1$ and $\mu^* = 1$. The liquid is first shear driven close to the interface generating the internal recirculation and a maximum reversal velocity near the drop axis of symmetry is then observed, corresponding to the maximum value of the slip observed in Fig. 4.10. Then, due to momentum diffusion inside the fluid particle, both the interfacial velocity and the reversal velocity decrease and converge to their steady state values.

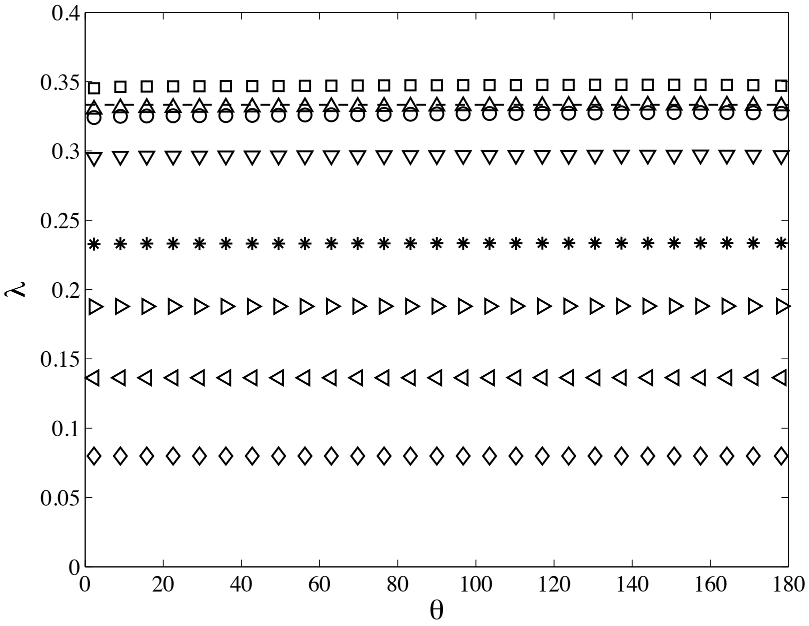

Figure 4.10: Value of the effective interface slip length $\lambda$ as a function of the polar angle $\theta$ for $Re = 0.1$ and $\mu^* = 1$ at different times: $\Diamond$ $t/t_\nu = 0.002$ $\triangleleft$ $t/t_\nu = 0.006$, $\triangleright$ $t/t_\nu = 0.012$, $*$ $t/t_\nu = 0.02$, $\nabla$ $t/t_\nu = 0.04$, $\Box$ $t/t_\nu = 0.12$, $\triangle$ $t/t_\nu = 0.4$, $\circ$ $t/t_\nu = 1$.
$- - -$ $\lambda_E = R/3\mu^*$ (relation 4.1.17).

The time evolution of $\lambda$ is reported in Fig. 4.12 for $Re = 0.1$ and different viscosity ratios. Two time scaling are presented: $t/t_{\nu\,e}$ (top) and $t/t_{\nu\,i}$ (bottom). As shown all the evolutions follow a unique curve when $\lambda\mu^*$ is reported as a function of $t/t_{\nu\,i}$. So $t_{\nu\,i}$ is the relevant time to describe the evolution of the interfacial slip of a fluid particle. The interface slip $\lambda$ increases, reaching a maximum slightly larger than $R/3\mu^*$ and then rapidly decreases toward the plateau value $\lambda = R/3\mu^*$ for $t > 0.15t_{\nu\,i}$. As shown, the maximum reached by the slip decreases when the viscosity ratio is increased for a given $Re$. A detailed inspection of $\lambda_{max}$ the maximum reached by $\lambda$ can be roughly described by $\lambda_{max} = (1 + 0.0047(\mu^*)^{1/3})R/3\mu^*$. The transient evolution for the slip length can be roughly approximated by

$$\lambda_E = \frac{R}{3\mu^*}\left(1 - \exp\left[-(60t/t_{\nu\,i})^{0.55}\right]\right)\cos(20t/t_{\nu\,i}) \qquad (4.1.18)$$

adjusted to the evolution observed for $\mu^* = 1$. This relation is reported in Fig. 4.12

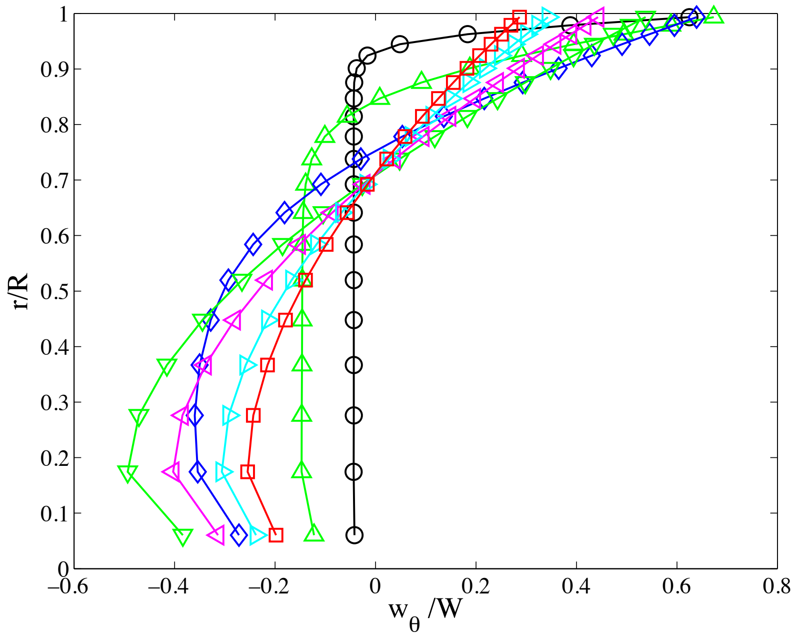

Figure 4.11: Tangential velocity profile across the middle of the drop ($\theta = 90^o$) for $Re = 0.1$ and $\mu^* = 1$ at different times: ○ $t/t_\nu = 0.0002$, △ $t/t_\nu = 0.002$, ◇ $t/t_\nu = 0.01$. ▽ $t/t_\nu = 0.04$, ◁ $t/t_\nu = 0.1$, ▷ $t/t_\nu = 0.4$, □ $t/t_\nu = \infty$ (steady state).

and clearly describes the fast increase of the slip and the relaxation time necessary to reach the steady value.

### 4.1.3.4 The memory Kernel $K_\mu$

Replacing $\lambda$ by $R/3\mu^*$ in the steady drag force (first term in Eq. 4.1.10) we recover the dependency of the drag force with the viscosity ratio (first term in Eq. 4.1.6). The idea is now to apply the same transform to the memory kernel. Thanks to the numerical simulations, we have shown that the slip is uniform at a fluid-fluid interface for the range of small Reynolds number considered here. We first consider the memory kernel obtained by simply combining relation 4.1.17 and the kernel of expression 4.1.11. The corresponding expression is then:

$$K_\mu(t,\mu^*) = \frac{(2+3\mu^*)^2}{3(1+\mu^*)} \exp\left[9(1+\mu^*)^2 t/t_\nu\right] \mathrm{erfc}\left[3(1+\mu^*)\sqrt{t/t_\nu}\right] \tag{4.1.19}$$

In the limit $\mu^* = \infty$ (solid sphere) and $\mu^* = 0$ (spherical bubble) we recover expressions 4.1.7 and 4.1.8, respectively. The evolution of $K_\mu$ given by relation 4.1.19 for different values of $\mu^*$ is reported in Fig. 4.13. Varying $\mu^*$ allows to evolve from the solid sphere to bubble limits. The case $\mu^* = 1$ stands in between these two limits.

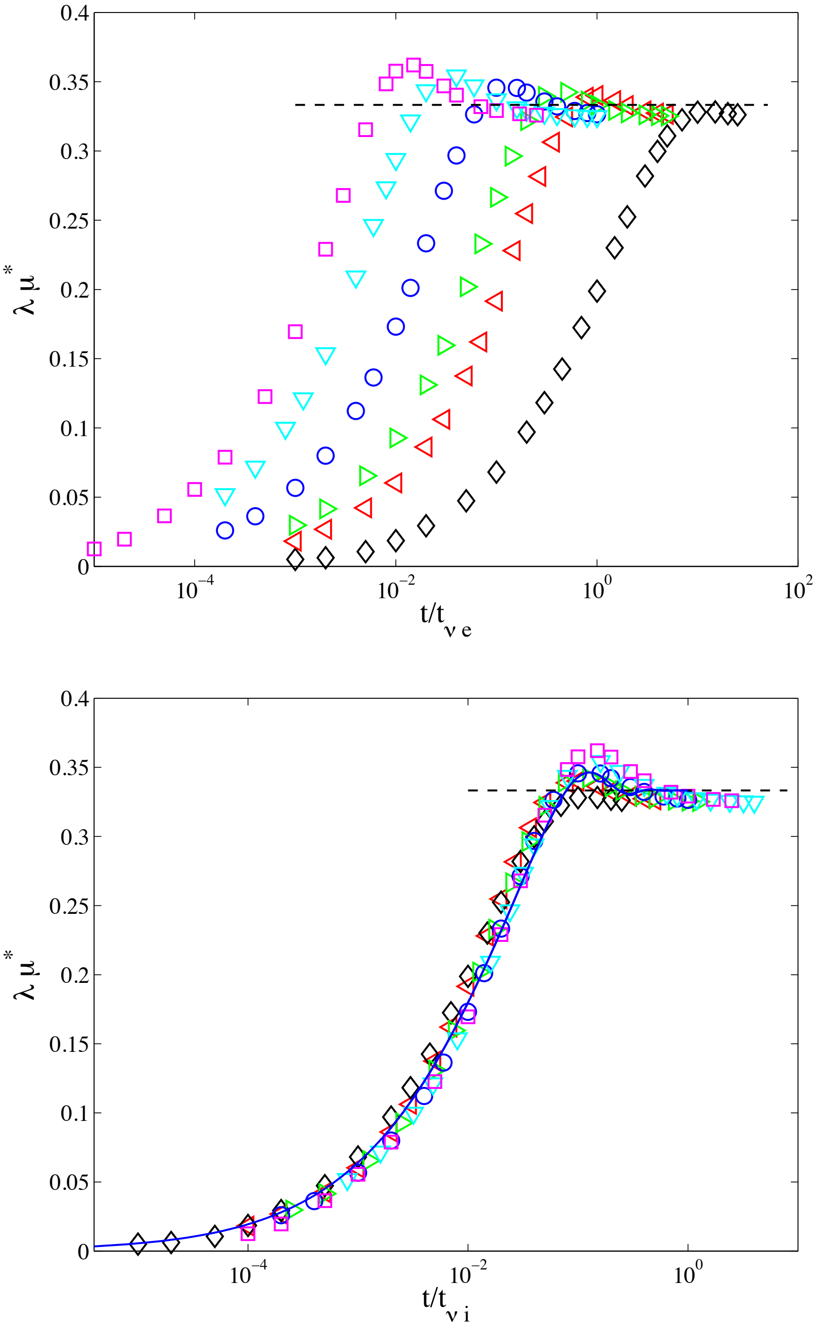

Figure 4.12: Time evolution of the effective interface slip length $\lambda$ for $Re = 0.1$. $\lambda\mu^*$ is reported as a function of: (top) $t/t_{\nu e}$, (bottom) $t/t_{\nu i}$. ◇ $\mu^* = 0.01$, ◁ $\mu^* = 0.1$, ▷ $\mu^* = 0.25$, ○ $\mu^* = 1.$, ▽ $\mu^* = 4.$, □ $\mu^* = 10.$, $- - -$ $\lambda_E = R/3\mu^*$ (relation 4.1.17), — relation 4.1.18.

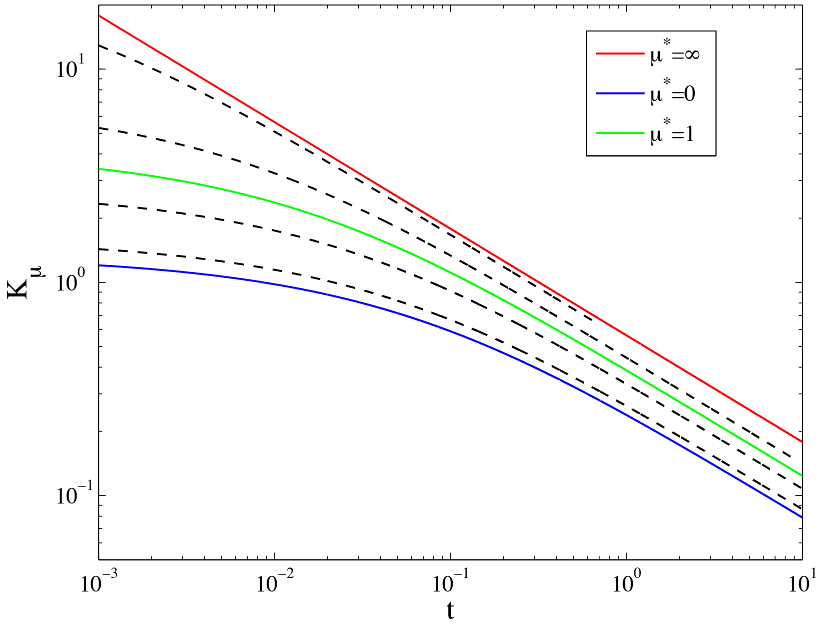

Figure 4.13: Evolution of the memory kernel for different viscosity ratio $\mu^*$. From top to bottom: $\mu^* = \infty$ (red curve),$10, 2, 1$ (green curve), $0.5, 0.1, 0$ (blue curve).

The force expression 4.1.6 is now compared to the direct numerical simulations obtained with the JADIM code for different viscosity ratio. For a fluid particle suddenly submitted to a uniform flow $U_0$ the force experienced is

$$F(t) = 6\pi\mu^e R \frac{2 + 3\mu^*}{3 + 3\mu^*} U_0 + 6\pi\mu^e R K_\mu(t) U_0 \tag{4.1.20}$$

Thus subtracting the steady drag force to the unsteady force $F(t)$ we have a direct access to the memory Kernel $K_\mu(t)$. The evolution of $K_\mu(t)$ measured in the direct numerical simulation is reported in Fig. 4.14 for $Re = 0.1$. It is compared to relation 4.1.19 reported using dashed line. A shown this relation is able to describe the memory kernel for a large range of time.

Concerning the behavior at long time, the effect of the Oseen wake is known to become more effective than the viscous diffusion Lovalenti and Brady [1993]; Mei and Adrian [1992] so that the sphere adjusts more rapidly to the velocity changes than predicted by the Basset-Boussinesq memory force. For time larger than $\nu/U_0^2$, i.e. $t > t_\nu Re^{-2}$ the kernel decays faster as observed in Fig. 4.13.

Considering now the behavior at early time, the evolution shows good agreement with relation 4.1.19 once the slip has reached the value $\lambda = R/3\mu^*$. Thus for time larger than $0.15t_\nu$, the evolution of the kernel is satisfactorily described using relation

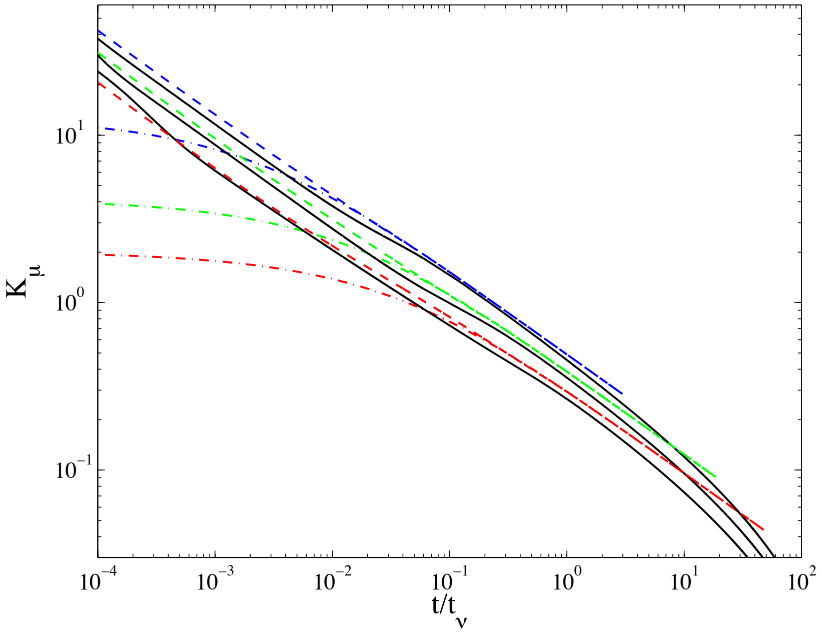

Figure 4.14: Evolution of the memory kernel $K_\mu(t)$. (Solid black line) Values measured in the numerical simulations for different viscosity ratio $\mu^*$ at $Re = 0.1$. (red) $\mu^* = 0.25$, (green) $\mu^* = 1$ and (blue) $\mu^* = 4$. (dotted dashed line) relation 4.1.19, (dashed line) kernel expression 4.1.11 combined with the unsteady slip length $\lambda(t)$ given by relation 4.1.18.

4.1.19. For early times, i.e. smaller than $0.15t_\nu$, the unsteady behavior of the interface slip needs to be considered. For that purpose, we propose to combine the fit given by relation 4.1.18 proposed for $\lambda(t)$ with the kernel expression 4.1.11. The corresponding evolution is reported in Fig. 4.14 using continuous lines. As shown, the first time are now correctly described by the proposed memory kernel.

#### 4.1.3.5 Conclusion

We have considered in this section the Basset-Boussinesq (history) force experienced by a fluid particle. We have first considered the slip at a fluid particle interface. We have shown that for both steady and unsteady conditions, the slip is remarkably uniform along the fluid particle interface and is directly related to the viscosity ratio. Combining the analytical expression of the Basset-Boussinesq kernel and the description of the slip at the interface we were able to describe for the first time the Basset-Boussinesq history force for a fluid sphere whatever the viscosity ratio considered, i.e. for bubbles, drops and particles.

## 4.2 Mass transfer

In this section, conjugate mass transfer in moderate Reynolds flow (typically $Re \leq 150$) is investigated . The impact of hydrodynamic and mass transfer parameters on local quantities is first analyzed. Particular attention is paid on the effect of the viscosity ratio and partition coefficient on the evolution of the solute spatial distribution, the interfacial concentration, and the local Sherwood number. (Sec. 4.2.1). In order to finally derive a general correlation for conjugate mass transfer, and based on the double film theory which considers resistances in series, we then examine the separate cases of the external (Sec. 4.2.2) and internal (Sec. 4.2.3) transfer. In both cases, the same methodology is used. First, simulations of the asymptotic external (resp. internal) problem are performed and the obtained $Sh^E$ (resp. $Sh^I$) values are compared to available data and correlations from literature. Then, simulations of the conjugate problem are performed for limiting values of the criteria proposed by Brauer [1978]. In the cases where $k\sqrt{D^*} >> 1$, the obtained external mass transfer coefficients are compared to the one typical of the asymptotic external problem, in terms of $Sh^e$ vs. $Sh^E$ (resp. $Sh^i$ is compared to $Sh^I$ for cases where $k\sqrt{D^*} << 1$). Finally, the global Sherwood number, $Sh$, is considered (Sec. 4.2.4). As for the local quantities, a sensitivity study to the physico-chemical and hydrodynamic parameters is carried out. Then different correlations based on the additivity rule of the mass transfer resistances are proposed and tested.

### 4.2.1 Local quantities

Thanks to DNS, all information and relevant variables regarding mass transfer are accessible. In this section we focus on the solute's concentration distribution along the interface (Figure 4.15), and on the corresponding local Sherwood number evolution (Figure 4.16).

*Surface concentration profile.* Logically, as the solute migrates from the droplet to the continuous phase, its mean concentration within the drop, $\overline{C^i}$, diminishes. As illustrated by the left column of Figure 4.15, the same trend is globally observed with the interface concentration $C^i_s$. Interestingly, a different evolution is observed for the ratio of these two quantities. A steady evolution of $C^i_s/\overline{C^i}$ is indeed rapidly achieved (see right part of Figure 4.15). This steady regime occurs at $Fo^e \approx 0.1$ in the considered configuration.

*Local Sherwood number.* A similar trend is exhibited by the local Sherwood number, $Sh_\theta$, defined by Eq. (3.7.7). As illustrated in Figure 4.16, the time-profiles merge into a unique curve. The rate at which the stationary profile is obtained, and the achieved $Sh$ distribution along the interface potentially depend on the problem parameters. The presence of an external recirculation in the hydrodynamic conditions considered (see Fig. 4.5) has a slight impact on attaining the steady behaviour near the droplets wake. At small times, when the mean concentration is still almost unchanged, i.e. $\overline{C^i} \approx 1$, a strong concentration gradient is however generally observed to prevail in the droplet

front, i.e. at the stagnation point, which explains the quite similar shape of the early $Sh_\theta$ profiles.
It should be noted that in some configurations, namely at low $Pe^e$ or high $\mu^*$, the steady behaviour is hardly reached before the droplet's mean concentration reaches its equilibrium value.

*Effect of the Viscosity ratio.* Whatever the $Re$ (here $Re = 100$), as the viscosity ratio increases, the droplet behaviour approaches that of a rigid particle, and the interface velocity decreases. It is worth reminding at this stage that the sign of the interface vorticity changes with the appearance of the external recirculation, which is the case at $\mu^* = 5$. For a given external Peclet, $Pe^e$, increasing $\mu^*$ hinders the interfacial fluid motion, causing a decrease of the surface concentration gradient, and consequently of the local Sherwood number. In the example illustrated in Figures 4.15- 4.17 (with $Re = 100$, $Pe^e = 1000$, and $D^* = 1$), the steady state of the local Sherwood number is reached around $Fo^i \approx 0.1$.
Figure 4.18 more specifically compares the steady local Sherwood number evolution with $\mu^*$ for three typical $k$ values: *i)* $k = 0.1$, when the solute has more affinity for the liquid in the bulk phase, rather than for the droplet, *ii)* $k = 1$, when no concentration discontinuity prevails at the interface, and *iii)* $k = 5$, when the solute has more affinity for the droplet than for the bulk phase. In each case, for $\theta \geq 60°$, $Sh_\theta$ is observed to increase with $\mu^*$. However, in the droplet's front, the local mass transfer rate is mainly sensitive to the value of $k$. This observed evolution of the local Sherwood number is non trivial. For $\mu^* = 5$, due to the external recirculation, the solute is trapped in the recirculation, which feeds in return the droplet. As a result, the concentration gradient changes sign at the droplet's rear, and the local Sherwood number becomes negative.

*Effect of partition coefficient.* The effect of the external recirculation is blurred as $k$ get greater than 1 (here $k = 5$). Indeed, in this case, the thermodynamics is opposed to the solute transfer. The problem hence is mainly external and the concentration inside the drop is nearly uniform, as highlighted in Figure 4.19. This figure indeed provides a good illustration of the combined effect of $\mu^*$ andMoreover, the combined effect of $\mu^*$ and the partition coefficient in the convective transfer regime considered. In the $Pe^e = 1000$ case, the internal circulation plays a major role in the mass transfer process. As the viscosity ratio increases (from left to right), the circulation slows down and its center shifts toward the droplet front. The solute diffuses then slowly from the droplet to the continuous phase. On the other hand, while $k$ increases (from top to bottom), the transfer resistance shifts from internal to external. The effect of the internal circulation on the concentration spatial distribution decreases, and the concentration inside the droplet becomes almost uniform. It is interesting to note that for $\mu^* = 5$, the effect of the external recirculation strongly depends on the value of $k$. In particular for $k = 0.1$ (top right figure), the concentration at the vicinity of the external recirculation is larger then the one inside the droplet.

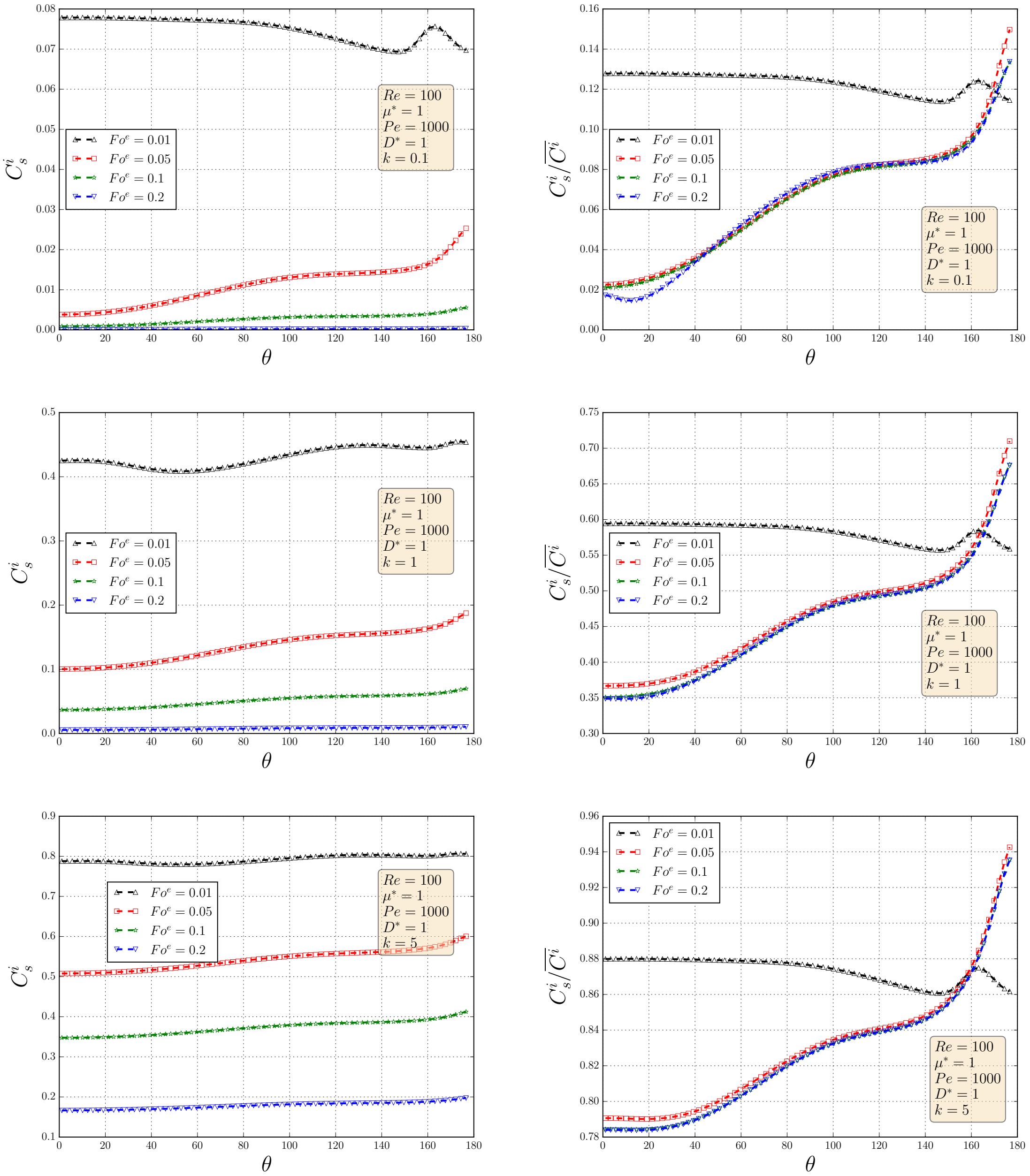

Figure 4.15: Evolution of the interface concentration profile (left), and of the ratio $C_s^i(\theta)/\overline{C^i}$ (right) in the case: $Re = 100$, $\mu^* = 1$, $Pe^e = 1000$, and $D^* = 1$. The curves in each sub-figure represent dimensionless times ranging from $Fo^e = 0.01$ (in black) to $Fo^e = 0.2$ (in blue). Three cases are considered for the partition parameter: $k = 0.1$ (top), $k = 1$ (middle), and $k = 5$ (bottom row).

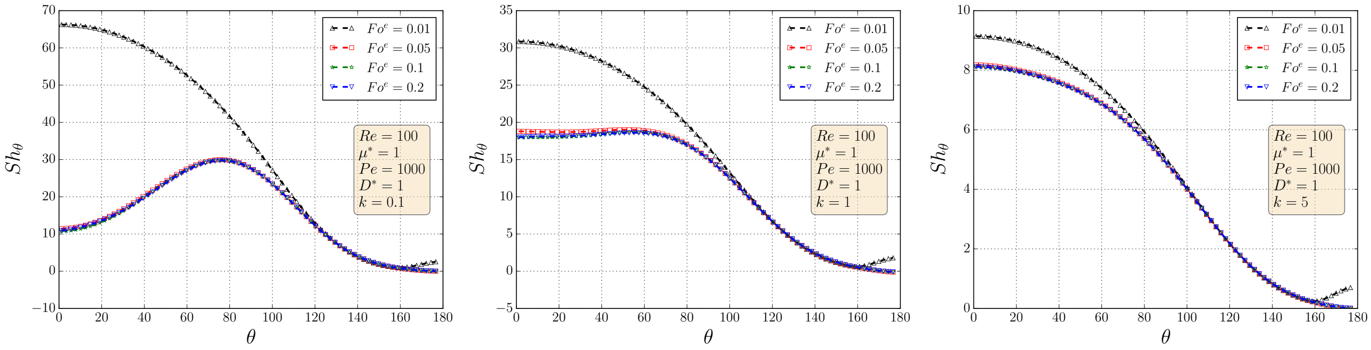

Figure 4.16: Temporal evolution of local Sherwood number.

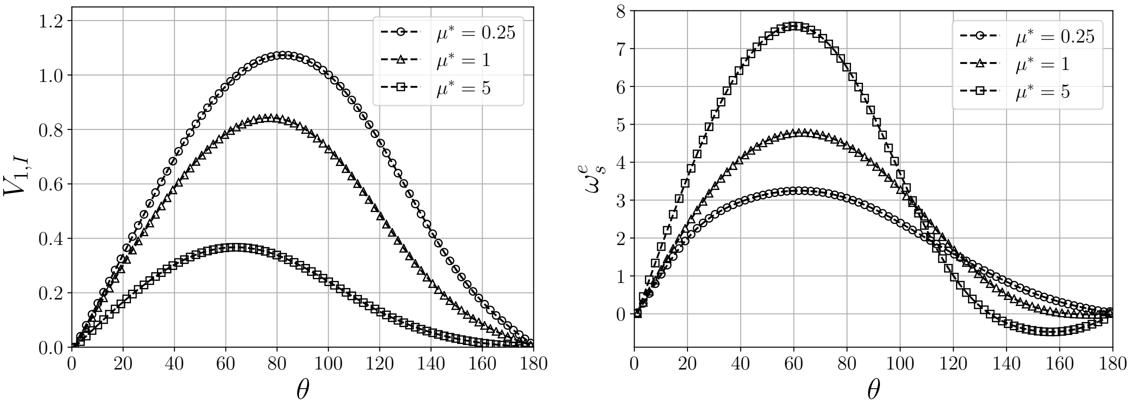

Figure 4.17: Effect of the viscosity ration on the interface velocity (left) and the interface vorticity (right).

### 4.2.2 External transfer

The aim of this section is to study the relation between the external Sherwood number of a conjugate problem $Sh^e$ and the one for an external problem $Sh^E$.

*External problem.* Regarding external problems, the transfer resistance is only located outside the drop, and the concentration is supposed constant and uniform at the interface. Many correlations have been developed for the external Sherwood number $Sh^E$ (see Sec. 1.2). Most of them are functions of the external Reynolds number $Re^e$, viscosity ratio $\mu^*$, and of the external Peclet number $Pe^e$.
Unless otherwise stated, all the $Sh^E$ values reported in this section are the ones that were calculated by DNS imposing a constant and uniform surface concentration. However, our results have shown excellent agreement with the correlation proposed by Feng and

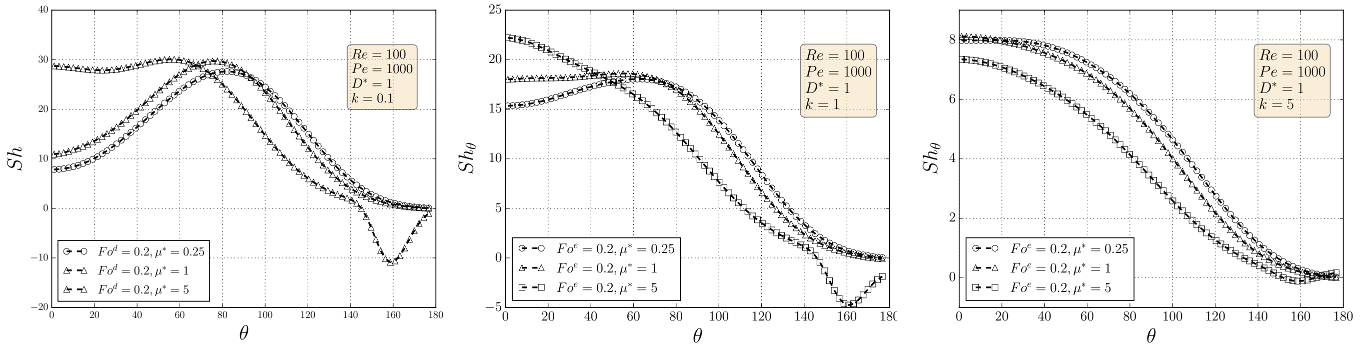

Figure 4.18: Combined effect of the viscosity ratio and the partition coefficient on the asymptotic local Sherwood number.

Michaelides [2001b], given in Tab. 1.3, and recalled below.

$$Sh^E(\mu^*, Pe^e, Re^e) = \begin{cases} \dfrac{2-\mu^*}{2} Sh^E(0, Pe^e, Re^e) + \dfrac{4\mu^*}{6+\mu^*} Sh^E(2, Pe^e, Re^e) & 0 \le \mu^* \le 2 \\ \dfrac{4}{\mu^*+2} Sh^E(2, Pe^e, Re^e) + \dfrac{\mu^*-2}{\mu^*+2} Sh^E(\infty, Pe^e, Re^e) & 2 \le \mu^* \le \infty \end{cases} \tag{4.2.1}$$

where:

$$\begin{cases} Sh^E(0, Pe^e, Re^e) = 0.651 Pe^{e1/2} \left(1.032 + \dfrac{0.61 Re^e}{Re^e + 21}\right) + \left(1.6 - \dfrac{0.61 Re^e}{Re^e + 21}\right) \\ Sh^E(\infty, Pe^e, Re^e) = 0.852 Pe^{e1/3} \left(1 + 0.233 Re^{e0.287}\right) + 1.3 - 0.182 Re^{e0.355} \\ Sh^E(2, Pe^e, Re^e) = 0.64 Pe^{e0.43} \left(1 + 0.233 Re^{e0.287}\right) + 1.41 - 0.15 Re^{e0.287} \end{cases} \tag{4.2.2}$$

*External resistance.* In a conjugate problem, increasing $D^*$ results in a shift of the transfer resistance to the outer phase, and the transfer is mainly external. Figure 4.20 gives the temporal evolution of the external Sherwood number $Sh^e$ for different values of $D^*$. Two external Peclet numbers, $Pe^e = 100$ and $Pe^e = 1000$, are considered. The $Sh^E$ value obtained from the simulation of the external problem is also reported (red line). In every case, the steady value of $Sh^e$ slightly deviates from $Sh^E$, even at elevated $D^*$. The difference is about 10% for $Pe^e = 1000$ and $D^* = 100$. In order to understand the origin of this gap between the steady value of $Sh^e$ and $Sh^E$, we plotted the steady-state concentration at the interface (Figure 4.21). A non uniform concentration distribution is evidenced at $D^* = 100$, for both the cases: $Pe^e = 100$ and $Pe^e = 1000$. This non uniform angular distribution explains why $Sh^e \neq Sh^E$. Indeed, as already mentioned, in an external problem a uniform concentration is considered at the interface, whereas a non uniform concentration is evidenced in the conjugated problem, even at high $D^*$.

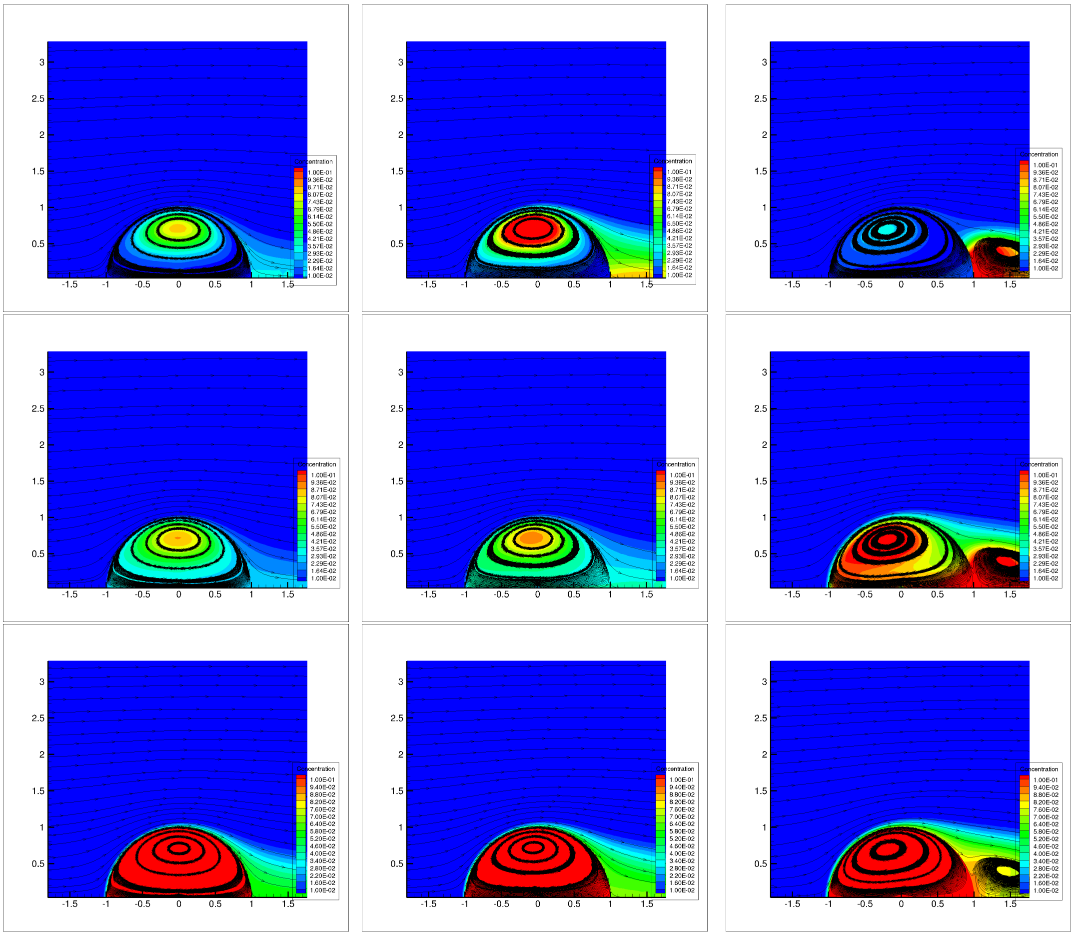

Figure 4.19: Combined effect of $k$ and $\mu^*$ on the spatial distribution of the solute and on streamlines ($Fo^i = 0.15$, $Re = 100$, $Pe^e = 1000$, $D^* = 1$). From top to bottom: $k = 0.1$, 1, and 5. From left to right: $\mu^* = 0.25$, 1, and 5.

In the previous analysis, the equilibrium coefficient $k$ has been fixed to 1. It has been observed in the local analysis (Sec. 4.2.1) that $k$ plays a fundamental role in defining the steady value of $Sh^e$. This is again illustrated in Figure 4.22 for $D^* = 100$. We can observe that as $k$ increases, the steady value of $Sh^e$ gets closer to the corresponding $Sh^E$. The mass transfer resistance is further shifted outwards by the equilibrium conditions. This result has also been verified for smaller $Pe^e$.

On the other hand, if we consider a configuration where $D^* = 1$ with similar hydrodynamic properties as before ($Re = 100$, $\mu^* = 1$), the steady value of $Sh^e$ converges rapidly and monotonically toward the corresponding value $Sh^E$, for both external Peclet numbers ($Pe^e = 100$ and $Pe^e = 1000$). The deviation between $Sh^e$ and $Sh^E$ is less than 1% for $k = 10$. The similarity with the external problem is moreover

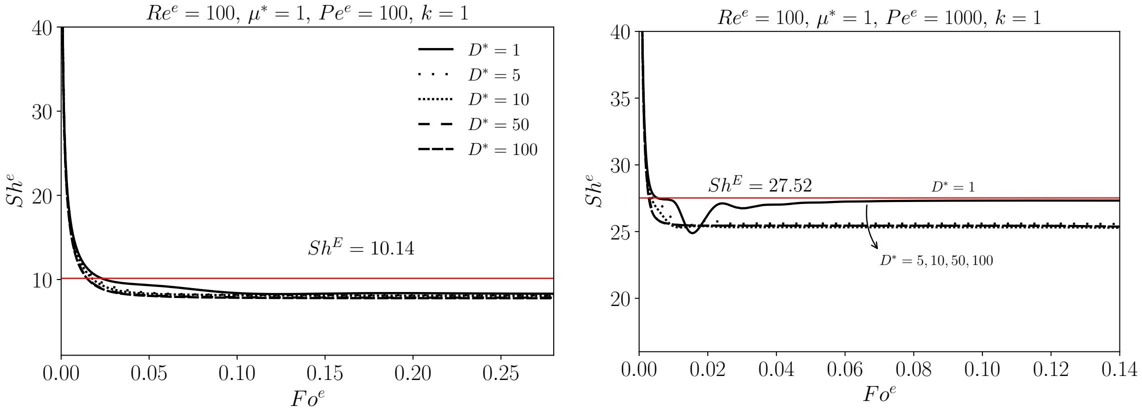

Figure 4.20: Temporal evolution of external Sherwood number $Sh^e$ with the external dimensionless time $Fo^e$: $Re^e = 100$, $\mu^* = 1$, $k = 1$ - $Pe^e = 100$ (left), $Pe^e = 1000$ (right).

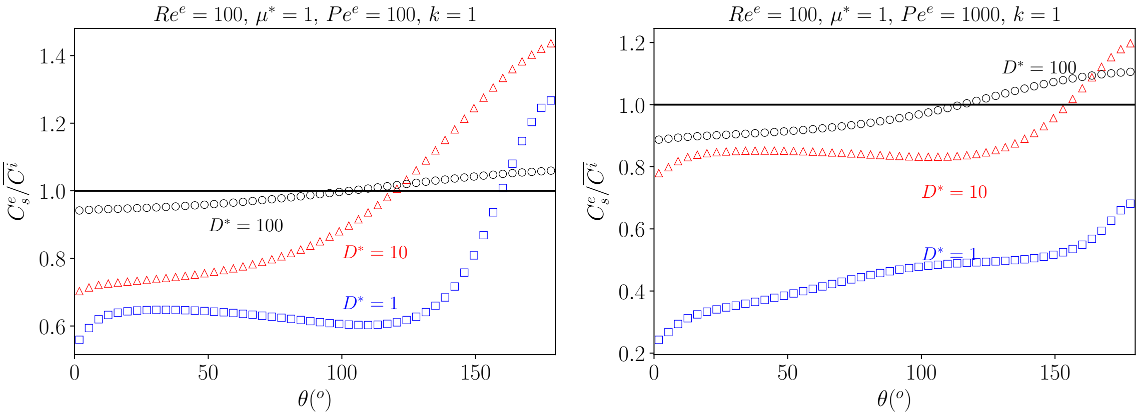

Figure 4.21: Steady profile of normalized concentration at the interface $C_s^e/\overline{C^i}$: $Re^e = 100$, $\mu^* = 1$, $k = 1$ - $Pe^e = 100$ (left), $Pe^e = 1000$ (right).

confirmed by the solute concentration at the interface. Indeed, Figure 4.24 illustrates that for the conjugate problem with $k \geq 10$, the quantity $C_s^e/\overline{C^i}$ is almost constant. Consequently, for high values of $k$, the mass transfer resistance is located outside the drop, and a good agreement is found between $Sh^e$ and $Sh^E$. In such configuration, where the solute exchange is mainly controlled by the thermodynamic equilibrium, the impact of $D^*$ is negligible, (see Figure 4.25).

*Main trends on external transfer.* Figure 4.26 gathers all the previously analyzed results on $Sh^e$ and $Sh^E$ for two configurations: $D^* = 100$, $k = 1$ on the left) and $D^* = 1$,

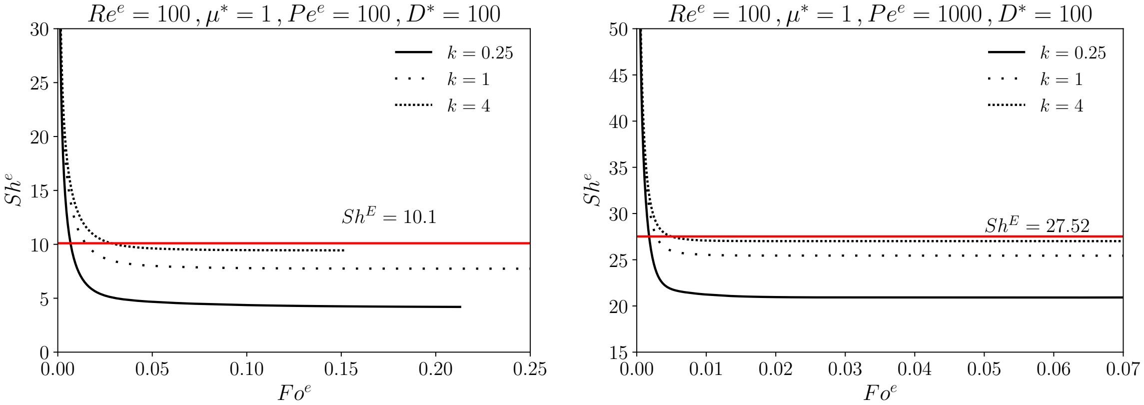

Figure 4.22: Temporal evolution of external Sherwood number $Sh^e$ with external dimensionless time $Fo^e$: $Re^e = 100$, $\mu^* = 1$, $D^* = 100$ - $Pe^e = 100$ (left), $Pe^e = 1000$ (right).

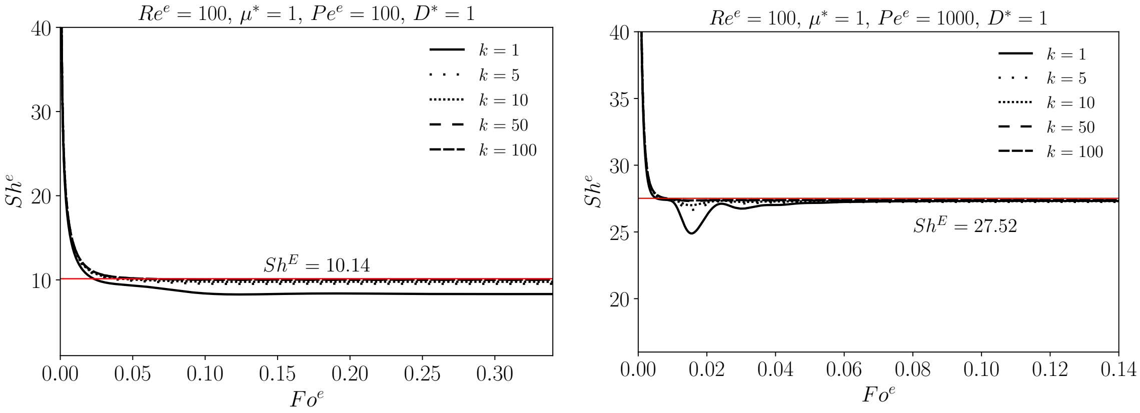

Figure 4.23: Temporal evolution of external Sherwood number $Sh^e$ with external dimensionless time $Fo^e$: $Re^e = 100$, $\mu^* = 1$, $D^* = 1$ - $Pe^e = 100$ (left), $Pe^e = 1000$ (right).

$k = 100$ (on the right). The data and correlations from Feng and Michaelides [2001b] are indicated for comparison. Additional values of $Sh^e$ (black dots) are also reported to assess the evolution of the external transfer coefficient with increasing $D^*$ while keeping $k$ constant, and vice versa. For $k \geq 10$, $Sh^e$ converges to the corresponding $Sh^E$ for every values of $Pe^e$. However, $D^*$ seems to play an effective role in high $Pe^e$ flows. Indeed, at high $D^*$ (here $D^* = 100$), $Sh^e$ converges toward $Sh^E$. For the same $D^*$ however, a deviation is clearly noticeable between $Sh^e$ and $Sh^E$ for smaller values of $Pe^e$, namely $Pe^e = 100$. While the corresponding value for the external problem

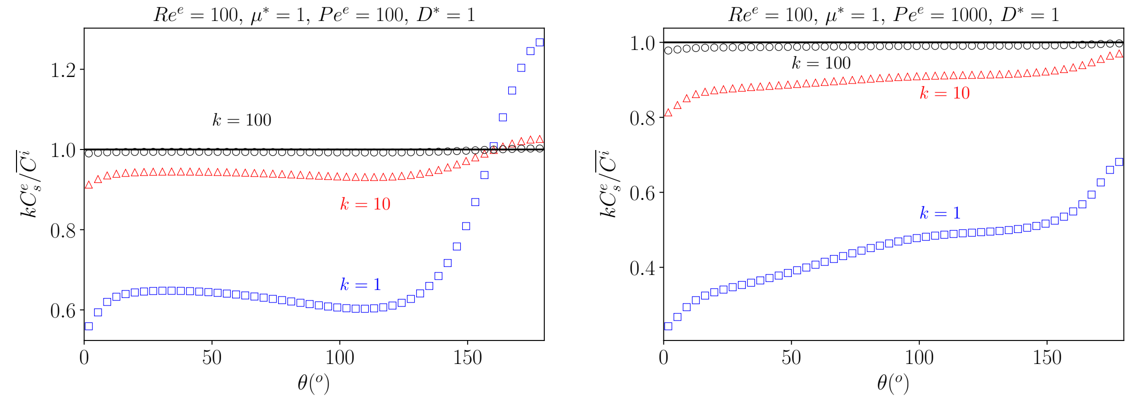

Figure 4.24: Steady profile of normalized concentration at the interface $kC_s^e/\overline{C^i}$: $Re^e = 100$, $\mu^* = 1$, $D^* = 1$ - $Pe^e = 100$ (left), $Pe^e = 1000$ (right).

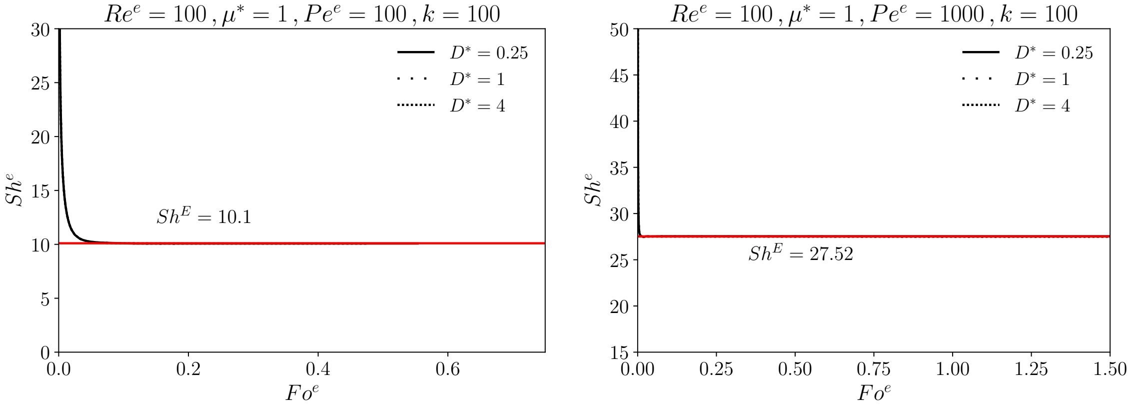

Figure 4.25: Temporal evolution of external Sherwood number $Sh^e$: $Re^e = 100$, $\mu^* = 1$, $k = 0.01$ - $Pe^e = 100$ (left), $Pe^e = 1000$ (right).

is $Sh^E = 4.27$, the $Sh^e$ converges slowly towards $Sh^e = 1.76$ (successive values are: $Sh^e(\overline{C^i} = 0.1) = 1.95$, $Sh^e(\overline{C^i} = 0.001) = 1.766$).

Thus, one must be very vigilant before using the external problem coefficient (that can be easily derived from *e.g.* Eq. 4.2.1) in the limiting conjugate problem at $k\sqrt{D^*}$, because the equivalence between $Sh^E$ and $Sh^e$ is not always true. This is particularly the case for low $Pe^e$ flows. Other hydrodynamic configurations were studied for different values of $\mu*$ in the range of $0.25 \leq \mu^* \leq 4$, and the conclusions were the same.

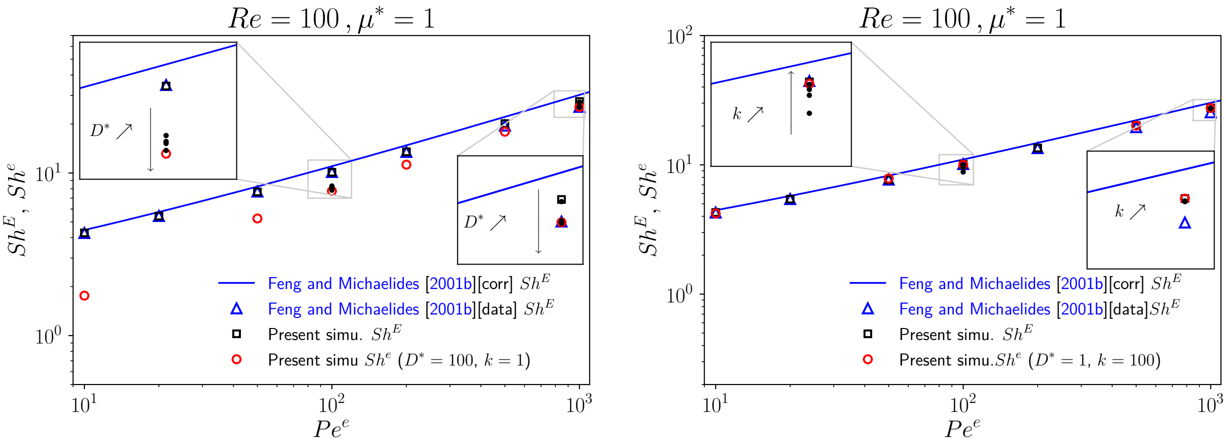

Figure 4.26: Evolution of external Sherwood number $Sh^E$ and $Sh^e$ of conjugate transfer: $Re^e = 100$, $\mu^* = 1$.

### 4.2.3 Internal transfer

*Internal problem.* Many numerical studies have been dedicated to internal problems in viscous drops or bubbles where the transfer in the outer phase is not limiting and the concentration on the interface is uniform (see Juncu [2010], Alexandrova et al. [2014a], Colombet et al. [2013], Oliver and De Witt [1995]). In all these studies, the solute transport equation is resolved inside a viscous sphere considering steady hydrodynamic configuration. The main purpose was to characterize the impact of hydrodynamic parameters (i.e. $Re$, $\mu^*$) and internal Peclet $Pe^i$ on the evolution of the Sherwood number $Sh^I$. In chapter 3, the simulation of internal problems has been validated in low Reynolds configurations, by comparison with available data from literature. Results have shown that the temporal evolution of the internal Sherwood number in this configuration converges to a steady value, that will be referred to as $Sh^I$. The comparison between existing $Sh^I$ correlations is not trivial, as the scaling parameters are generally not the same. For instance, the effective internal Peclet numbers, $Pe^i_{eff}$, introduced by Oliver and De Witt [1995] for droplets, and by Colombet et al. [2013] for bubbles are not the same. In this work, the expression proposed by Colombet et al. [2013] has been adapted, replacing $Pe^i$ by $Pe^i/(\mu^*+1)$ to fit the droplet case, as shown in Eq 4.2.3. This enables to compare the values of $Sh^I$ corresponding to different parameters.

$$Pe^i_{eff} = \frac{16 + 3.315 Re^{e\,1/2} + 3 Re^e}{16 + 3.315 Re^{e\,1/2} + Re^e} \cdot \frac{Pe^i}{\mu^* + 1} \tag{4.2.3}$$

The following correlation of the internal Sherwood number has been proposed by Colombet et al. [2013].

$$\frac{Sh^I - Sh^I(Pe^i \to 0)}{Sh^I(Pe^i \to \infty) - Sh^I(Pe^i \to 0)} = \frac{1}{1 + \exp\left(-1.89 \cdot (\log(Pe^i_{eff}) - 3.49)\right)} \tag{4.2.4}$$

For low internal Peclet number, the Sherwood number of the internal problem depends weakly on the Reynold number or the viscosity ratio. Figure 4.27 (left) shows that at $Pe^i = 10$, $Sh^I$ stays close to the value reported by Newman [1931] (i.e. $Sh^I(Pe^i \to 0) \approx Sh_{Newmann} = 6.58$) where internal transfer is controlled by pure diffusion, the variation is less then 10%. However, for high values of $Pe^i$, Colombet et al. [2013] reported that in the case of a bubble, $Sh^I$ slightly increases with $Re^e$ for $Re^e > 1$. The variation from the Sherwood number reported by Kronig and Brink [1951] (i.e. $Sh^I(Re^e \longrightarrow 0, Pe^i \longrightarrow \infty) = 17.9$) is about $2 - 3\%$ and can be described using the relation:

$$Sh^I(Pe^i \to \infty) = Sh^I(Re^e \longrightarrow 0, Pe^i \longrightarrow \infty)\,(1 + Re^e)^{0.0044} \tag{4.2.5}$$

In the range of $Re$ and $\mu^*$ investigated in our droplet's simulations, the high $Pe^i$ limit $Sh^I(Pe^i \to \infty)$ remains in between the two curves as illustrated in Figure 4.27 (right), and the deviation from $Sh^I_{Kronig} = 17.9$ is less than 10%.

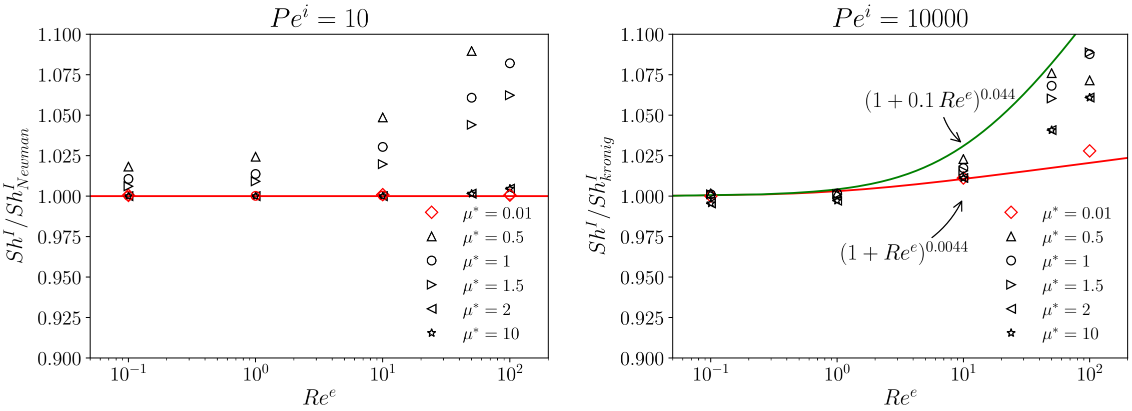

Figure 4.27: Evolution of internal normalized Sherwood number with external Reynolds number for different viscosity ratios - $Pe^i = 10$ (left), $Pe^i = 10000$ (right).

At last, reported results from literature along with our simulations agree very well with the correlation Eq 4.2.4 (see Figure 4.28).

*Internal resistance.* A problem is assumed to be controlled by internal transfer when $k\sqrt{D^*} \ll 1$. Here we investigate the relation between the Sherwood number of an internal problem $Sh^I$ and the actual internal Sherwood number $Sh^i$ predicted by the

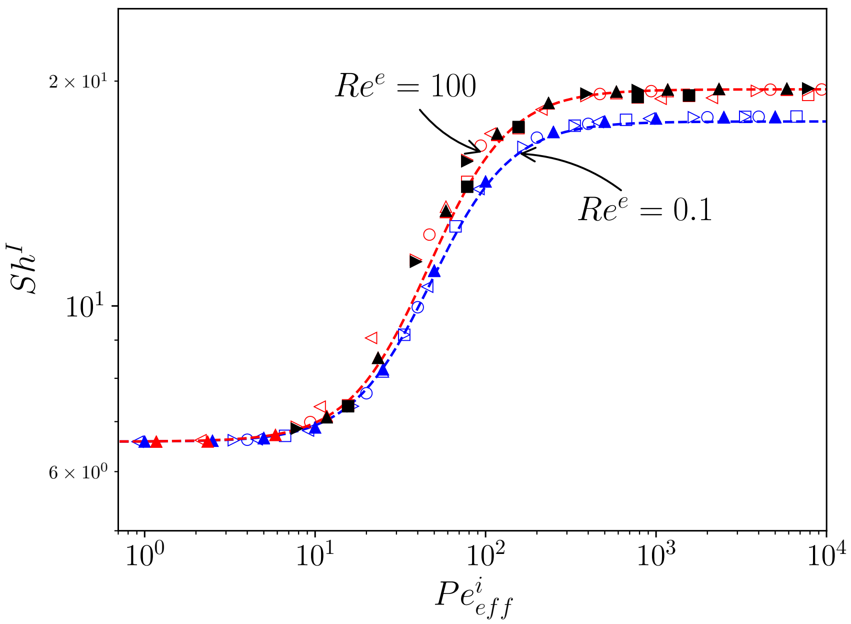

Figure 4.28: Evolution of steady internal Sherwood number with internal effective Peclet number $Pe^i_{eff}$. Alexandrova et al. [2014a]: $Re^e = 100$, $\mu^* = 0.5$(□) $\mu^* = 1$(△) $\mu^* = 1.5$(○) $\mu^* = 2$(▷) $\mu^* = 10$(◁); *Creeping flow*, $\mu^* = 0.5$(□) $\mu^* = 1$(△) $\mu^* = 1.5$(○) $\mu^* = 2$ (▷) $\mu^* = 10$(◁). Juncu [2010]: *Creeping flow*, $\mu^* = 1$(▲); $Re^e = 100$, $\mu^* = 1$(▲). This work: $Re^e = 100$, $\mu^* = 0.5$(■) $\mu^* = 1$(▲) $\mu^* = 2$(▶). dashed lines: Equation 4.2.4.

conjugate problem. Indeed, as previously observed, the basic assumption for internal problems (i.e. uniform $C_s$) is not always valid.

For a partition coefficient $k = 1$ and a given internal Peclet number $Pe^i$, when $D^*$ decreases (corresponding to decreasing $D^e$), the spatial distribution of the solute outside the drop is nearly uniform, and so is its interface concentration. In such case, the situation is comparable to an internal problem. Figure 4.29 displays the temporal evolution of $Sh^i$ in a steady hydrodynamic configuration ($Re^e = 100$, $\mu^* = 1$) for two configurations: $Pe^i = 100$ and $Pe^i = 1000$. The value of $Sh^I$ corresponding to internal problem is represented by a red line. For the higher internal Peclet number (on the right), the steady value of $Sh^i$ is observed to converge monotonically towards the value of $Sh^I$ as $D^*$ decreases. The deviation is less than $3 - 4\%$ for $D^* = 0.01$. However, on the left figure (for $Pe^i = 100$), the temporal evolution of $Sh^i$ for low $D^*$ (i.e. $D^* \leq 0.02$) does not converge to well defined value as it was the case for higher $Pe^i$, as moreover highlighted in Figure 4.30. In that case, the time-average of $Sh^i$, between the instant at which the last last oscillation is observed ($Fo^i \approx 0.2$ as shown in Figure 4.30), and the final value of $Fo^i$ (corresponding to $\overline{C^i} \approx 10^{-4}$) is considered. Note that when $Sh^i$

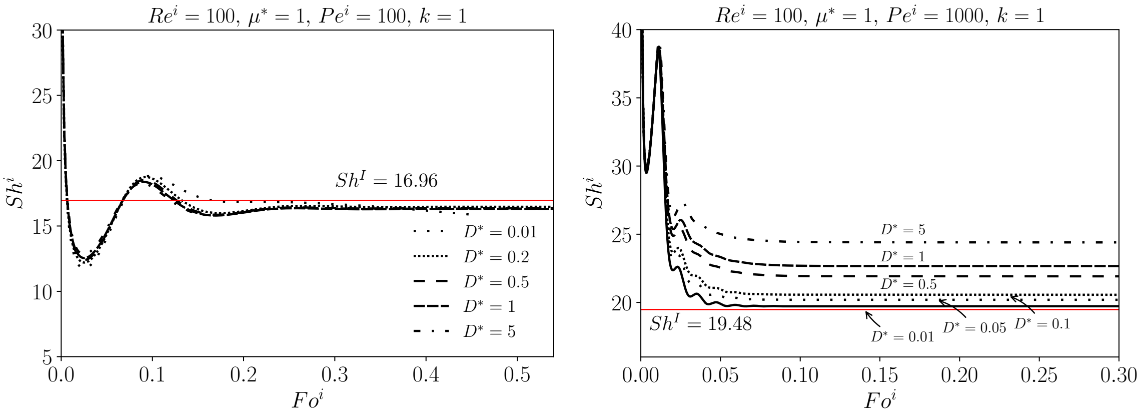

Figure 4.29: Temporal evolution of internal Sherwood number $Sh^i$ with internal dimensionless time $Fo^i$: $Re^e = 100$, $\mu^* = 1$, $k = 1$ - $Pe^i = 100$ (left), $Pe^i = 1000$ (right).

converges (*i.e.* in the case $D^* = 0.05$), no averaging is needed. Despite this evolution, the obtained average value is close to the corresponding $Sh^I$, and a deviation of less than 4% is observed. A similar behaviour is observed at low $Pe^i$ and $D^*$, and the same method is used to define the steady value of $Sh^i$.

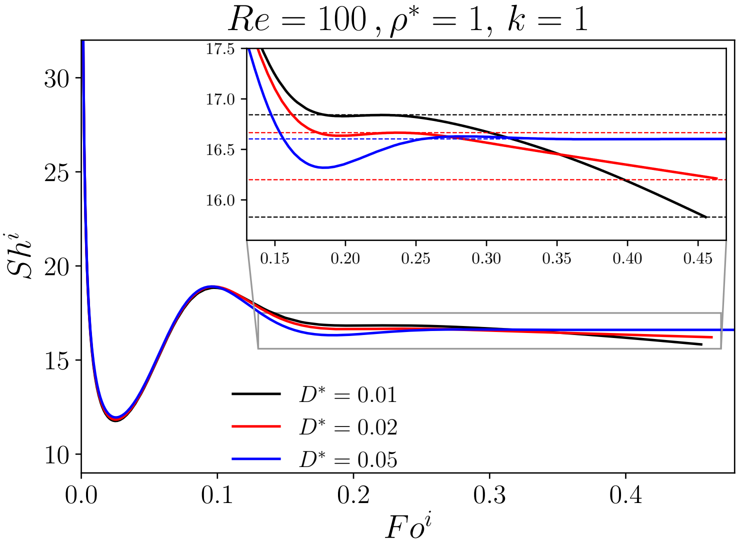

Figure 4.30: Temporal evolution of internal Sherwood number $Sh^i$ with internal dimensionless time $Fo^i$ for small $D^*$: $Re^e = 100$, $\mu^* = 1$, $k = 1$ - $Pe^i = 100$.

*Main trends on internal transfer.* In cases where $D^*$ is low (i.e. $D^* = 0.01$), some values of $Pe^i$ (less than 100) provide an unsteady temporal evolution of $Sh^i$, although it stays close to the corresponding $Sh^I$. These results were obtained for $k = 1$. However, the effect of $k$ should not be neglected in the condition $k\sqrt{D^*} << 1$ related to internal problems, especially for small values of diffusivity ratio $D^*$. Figure 4.31 displays, with the same hydrodynamic configuration as before ($Re^e = 100$, $\mu^* = 1$), the temporal evolution of $Sh^i$ for $D^* = 0.01$. For both internal Peclet $Pe^i = 100$ and $Pe^i = 1000$, as $k$ decreases, a steady value of $Sh^i$ is recovered and gets closer to the corresponding value of internal problem $Sh^I$. The same results have been obtained for smaller $Pe^i$.

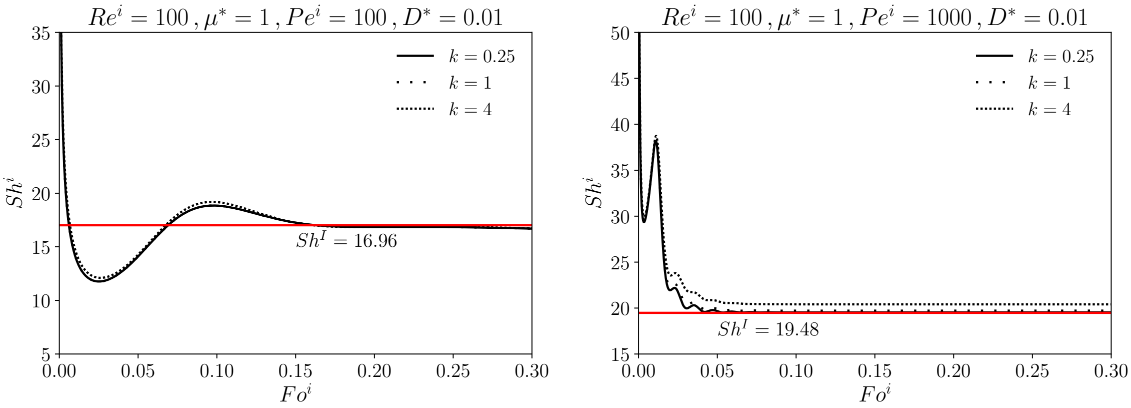

Figure 4.31: Temporal evolution of internal Sherwood number $Sh^i$ with internal $Fo^i$: $Re^e = 100$, $\mu^* = 1$, $k = 1$ - $Pe^i = 100$ (left), $Pe^i = 1000$ (right).

For a given diffusivity ratio (i.e. $D^* = 1$), $k$ has a major effect on shifting the transfer resistance from one phase to the other. A decrease of $k$ confines the solute inside the drop hence preventing transfer to the outer phase. Similarly to the analysis of the $D^*$ impact, in the hydrodynamic configuration where $Re^e = 100$, $\mu^* = 1$, Figure 4.32 highlights the temporal evolution of $Sh^i$ for two values of $Pe^i$. For high $Pe^i = 1000$ (on the right) the steady value of $Sh^i$ decreases monotonically to the corresponding value of an internal problem $Sh^I$ (red line). The same limit is achieved for the low Peclet case ($Pe^i = 100$, on the left) although in this case $Sh^i$ increases toward $Sh^I$. The partition coefficient thus appears to have a similar effect as $D^*$ on the evolution of $Sh^i$. However, for very small value, *e.g.* $k = 0.01$, the effect of the diffusivity ratio on the evolution of $Sh^i$ is negligible (see Figure 4.25), meaning that the transfer process is only controlled by the thermodynamic equilibrium.

The same analysis has been carried out for different hydrodynamic configurations ($Re^e$ and $\mu^*$), and the outcome is practically the same. The results are summarized in Figure 4.34, where the evolutions of $Sh^I$ along with $Sh^i$ are plotted against the internal Peclet number $Pe^i$, for $k = 1$ and $D^* = 0.01$ on the right, and $k = 0.01$ and $D^* = 1$ on the left. The correlation proposed by Colombet et al. [2013] and the data reported

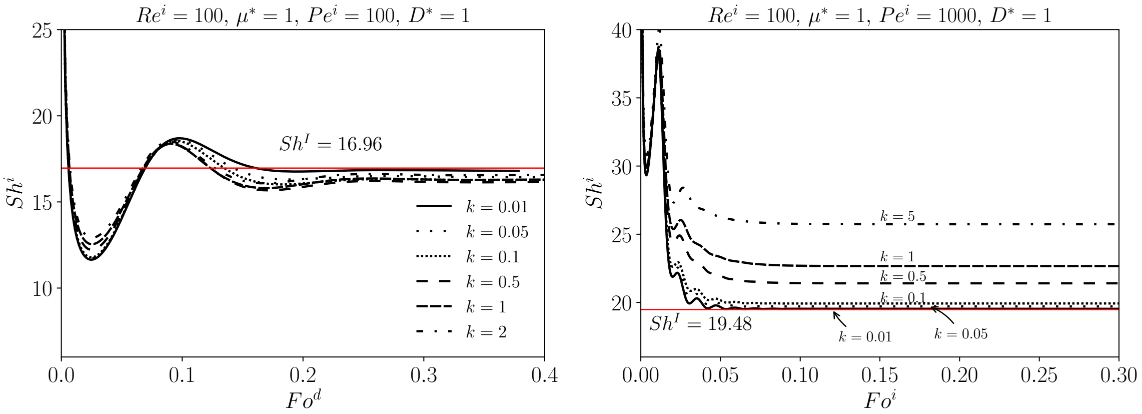

Figure 4.32: Temporal evolution of internal Sherwood number $Sh^i$ with internal $Fo^i$: $Re^e = 100$, $\mu^* = 1$, $k = 1$ - $Pe^i = 100$ (left), $Pe^i = 1000$ (right).

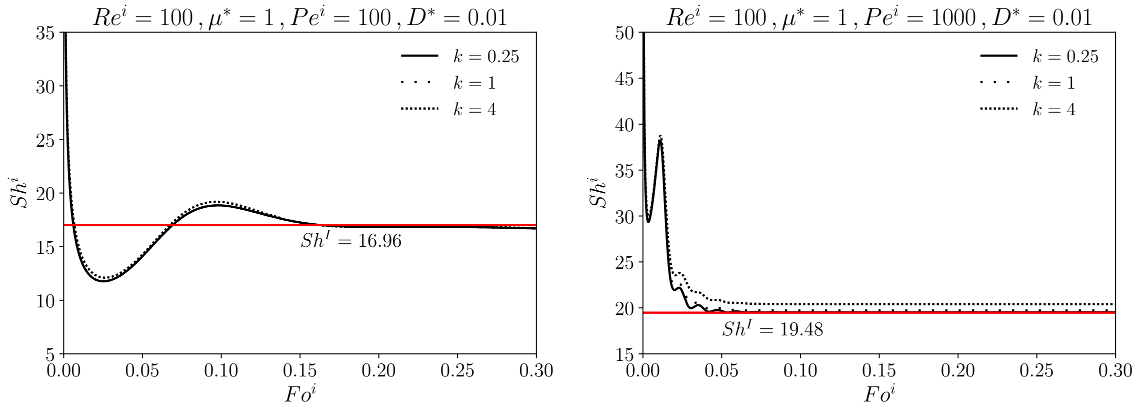

Figure 4.33: Temporal evolution of internal Sherwood number $Sh^i$ with internal $Fo^i$: $Re^e = 100$, $\mu^* = 1$, $D^* = 0.01$ - $Pe^i = 100$ (left), $Pe^i = 1000$ (right).

by Alexandrova et al. [2014b] and Juncu [2010] are also reported for comparison. The variation of $Sh^i$ with $D^*$ and $k$ studied for both $Pe^i = 100$ and $Pe^i = 1000$ have been added to the figures (black dots). Other configurations $\mu^* = 0.5$ and $\mu^* = 2$ are presented in Figure 4.35.

### 4.2.4 Conjugate transfer

In this last section, we consider the global (or apparent) mass transfer coefficient. The latter is again expressed in its dimensionless form $Sh$. In a first hand, a parametric study is carried out in order to assess the $Sh$ sensitivity to the flow and physico-chemical

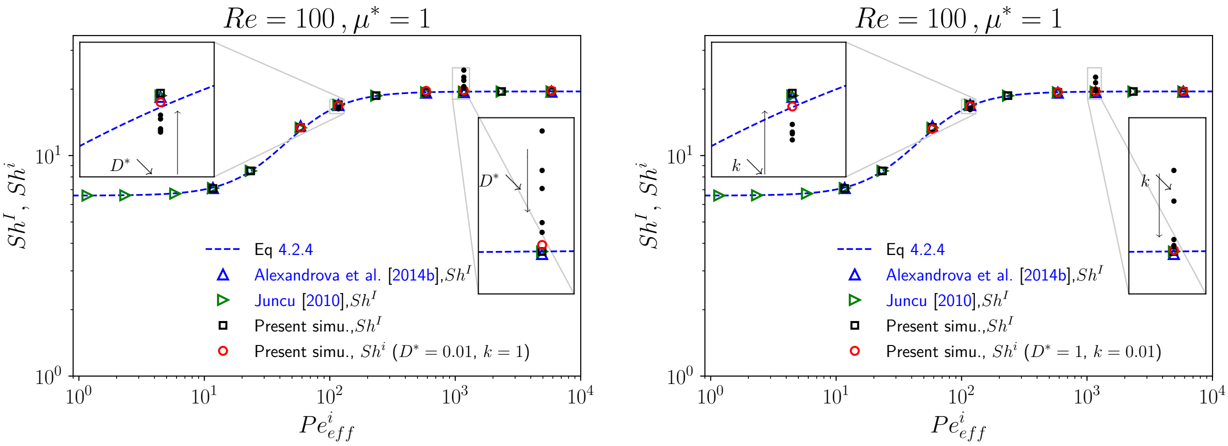

Figure 4.34: Evolution of internal Sherwood number $Sh^I$ and $Sh^i$: $Re^e = 100$, $\mu^* = 1$.

parameters. In a second time, as we did for the drag coefficient, we try to provide a general correlation for the global $Sh$. We remind that the superscript "e" is omitted when referring to external Reynolds number or Peclet number.

*Parametric study.* In the limit of small $Re$, the existence of a steady state for the Sherwood number is non-trivial. It has been discussed by Johns and Beckmann [1966], using the separation of variables. Although both the concentration gradient at the interface and the bulk concentration decay exponentially, the ratio of the latter quantities (which defines the Sherwood number) converges toward a non zero value. Oliver and Chung [1990] found the same asymptotic behaviour of the Sherwood number in their numerical investigation of conjugate heat transfer from a translating fluid sphere, for intermediate Reynolds flows up ($Re \leq 50$).

A parametric study has been conducted to investigate the effect of some key parameters on $Sh$ for higher Reynolds numbers. Figures 4.36 shows the time-evolution of global Sherwood number $Sh$ for $Re = 100$. The $Sh$ evolution with $Pe$, $\mu^*$, $D^*$, and $k$ shows similar trend as in creeping flow case (illustrated in Figure 3.17). Decreasing $Pe$ or increasing $\mu^*$, $D^*$ or $k$ slows down the solute transfer and the $Sh$ converges slowly to an asymptotic value. The transient regime is also impacted as both the oscillations magnitude and frequency are dampened. Physico-chemical parameters, namely $k$ and $D^*$, still have big impact on the oscillations magnitude and the steady value of $Sh$.
The same conclusion can be drawn regarding the $Re$ influence on the steady value of $Sh$ as shown in Figure 4.37. Different scenarios might occur regarding the effect of hydrodynamic parameters, especially as the latter are related by $Pe = Re \times Sc$. The $Re$ effect on the solute transfer depends strongly on the $Pe$ magnitude. Whereas for large

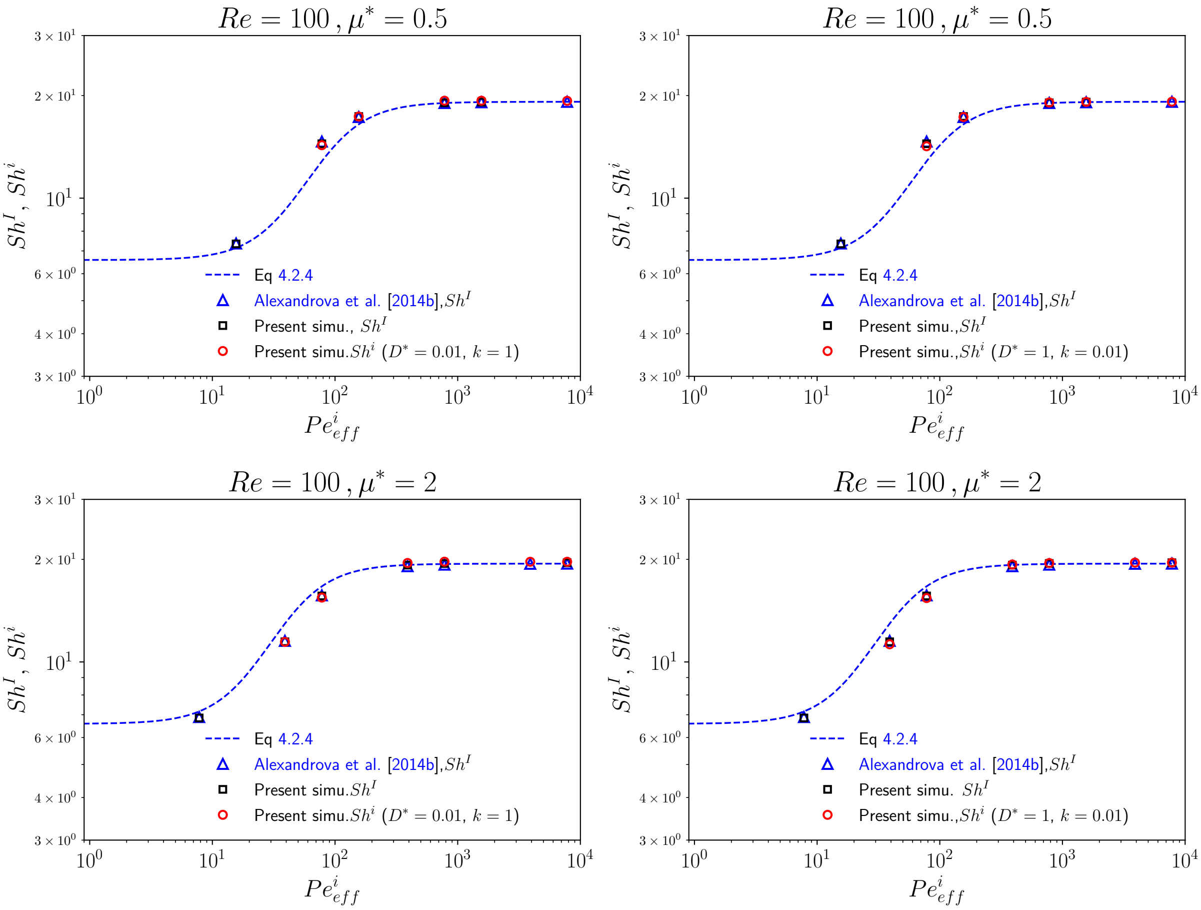

Figure 4.35: Evolution of internal Sherwood number $Sh^I$ and $Sh^i$: $Re^e = 100$, $\mu^* = 0.5$ (top row), $\mu^* = 2$ (bottom row).

$Pe$, an increasing $Re$ yields drastic change in the transient $Sh$ evolution, as depicted on the right part of Figure 4.37, for the diffusion governed low $Pe$ processes, the $Sh$ value is small and its temporal evolution is barely impacted by $Re$ (left figure).

The impact of the previous parameters on the mean solute concentration inside the droplet is furthermore depicted in Figure 4.38. In the considered range, the influence of the viscosity ratio is much less important than that of the other physico-chemical parameters (partition coefficient $k$ and diffusivity ratio $D^*$). For a small diffusivity ratio ($D^* = 1$), the mass transfer resistance is mainly located inside the droplet, therefore the solute mean concentration decays slowly from the droplet to the continuous phase (bottom right figure). It is also interesting to note that for early times, the effect of the recirculation is not yet visible (Clift et al. [1978]). The transfer is mainly diffusive and $\overline{C^i}$ decreases in the same way regardless of the $Pe$ value (top left figure). The convective

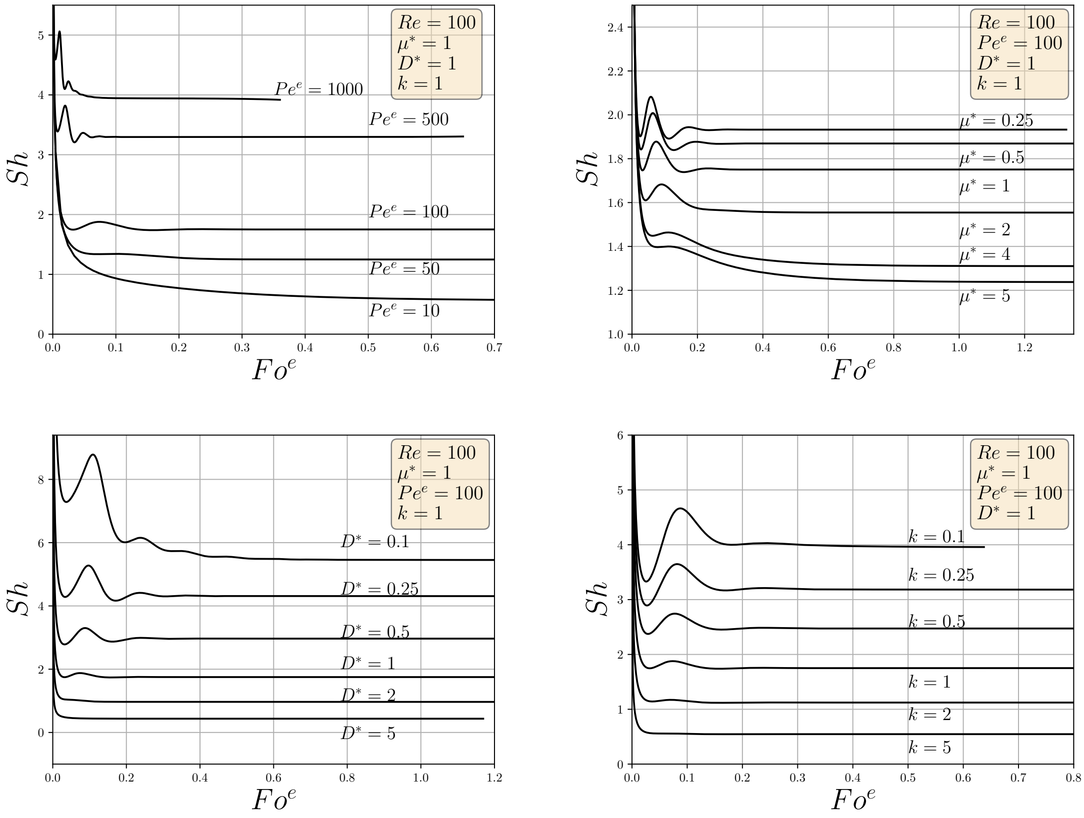

Figure 4.36: Temporal evolution of global Sherwood number - top left: $Pe$ impact, top right: $\mu^*$, bottom left: $k$ impact, bottom right: $D^*$ impact.

process triggers only after $Fo^e \approx 10^{-3}$, subsequently the solute transfer speeds up as $Pe$ increases. Based on this analysis, we can conclude that, an increasing viscosity ratio $\mu^*$ is responsible for a slow transfer and a decreasing asymptotic value of the global Sherwood number (Figures 4.38 and 4.36). For a diffusive regime ($Pe = 100$), the previous rule is respected for small values of the partition coefficient ($k \leq 1$). However as the Peclet number increases, an unexpected behaviour occurs (Figure 4.39). For $k = 0.1$, as the viscosity ratio increases from 0.25 to 1, a slight increase of the steady value of the Sherwood number is observed (from 18.04 to 18.63). These results have been proven independent of the used mesh. This behaviour is well illustrated in Figure 4.40. For $Pe < 50$, the steady value of the Sherwood number decreases monotonically with the viscosity ratio for the range of studied coefficient $k$. However, for Peclet number equals to 1000, two behaviours are observed. On the one hand, for $k \geq 1$ (*i.e.* when the solute transfer is not favoured by the thermodynamics), the steady value of the the global Sherwood number $Sh$ decreases monotonically with the viscosity ratio. On the other

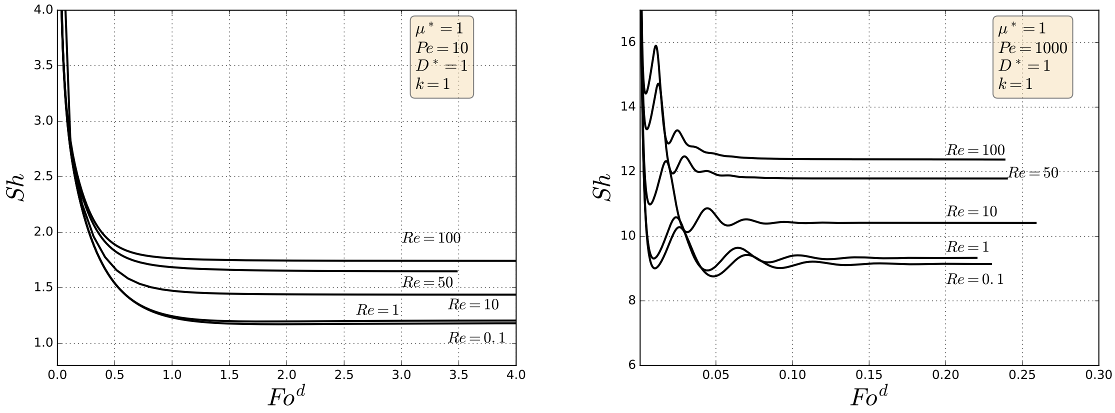

Figure 4.37: Temporal evolution of Sherwood number.

hand, for $k < 1$, the evolution of $Sh$ with $\mu^*$ is no longer monotonic, and an extremum occurs at $\mu^* < 2$ in the function $Sh(\mu^*)$ as is highlighted in Figure 4.40 . For small $Pe$ ($Pe < 10$), the slope of the decreasing function $Sh(\mu^*)$ decreases as the partition coefficient increases. The asymptotic Sherwood number becomes then less dependent on the viscosity ratio. On the other hand, the steady Sherwood number keeps practically decreasing with slightly the same rate for $Pe = 1000$ and $k > 1$. A similar behaviour is observed when the diffusivity ratio varies for a given partition coefficient ($k = 1$) in Figure 4.41.

*Toward a correlation.* Many attempts have been made to relate the global Sherwood number of a conjugate problem to the Sherwood numbers associated respectively to the internal $Sh^I$ and external $Sh^E$ problems. The additivity rule of the transfer resistances (Eq. (4.2.6)) has been tested in many works (Kleinman and Reed [1996], Oliver and Chung [1990], Nguyen et al. [1993]). However, due to the solute flux conservation, this rule is exact only provinding the internal and external Sherwood numbers $Sh^i$, $Sh^e$ are used (see Eq. 2.2.8).

$$\frac{1}{Sh} = \frac{1}{Sh^I} + \frac{kD^*}{Sh^E} \tag{4.2.6}$$

Though, as discussed in Sections 4.2.2 and 4.2.3, the equivalence between $Sh^i$ and $Sh^I$ on the one hand, and $Sh^e$ and $Sh^E$, on the other hand, is generally not verified. In this section, a special care is taken to shed some light on the accuracy of Eq. 4.2.6. Correlations 4.2.1 and 4.2.4 related to the external and internal problems respectively, will be used in the analysis. The global Sherwood number in Eq. 4.2.6 will be expressed in terms of $Pe^i$. For this reason, since $Sh^E$ correlation relies on $Pe^e$, $(D^* \cdot Pe^i)$ will be inserted in place of $Pe^e$.

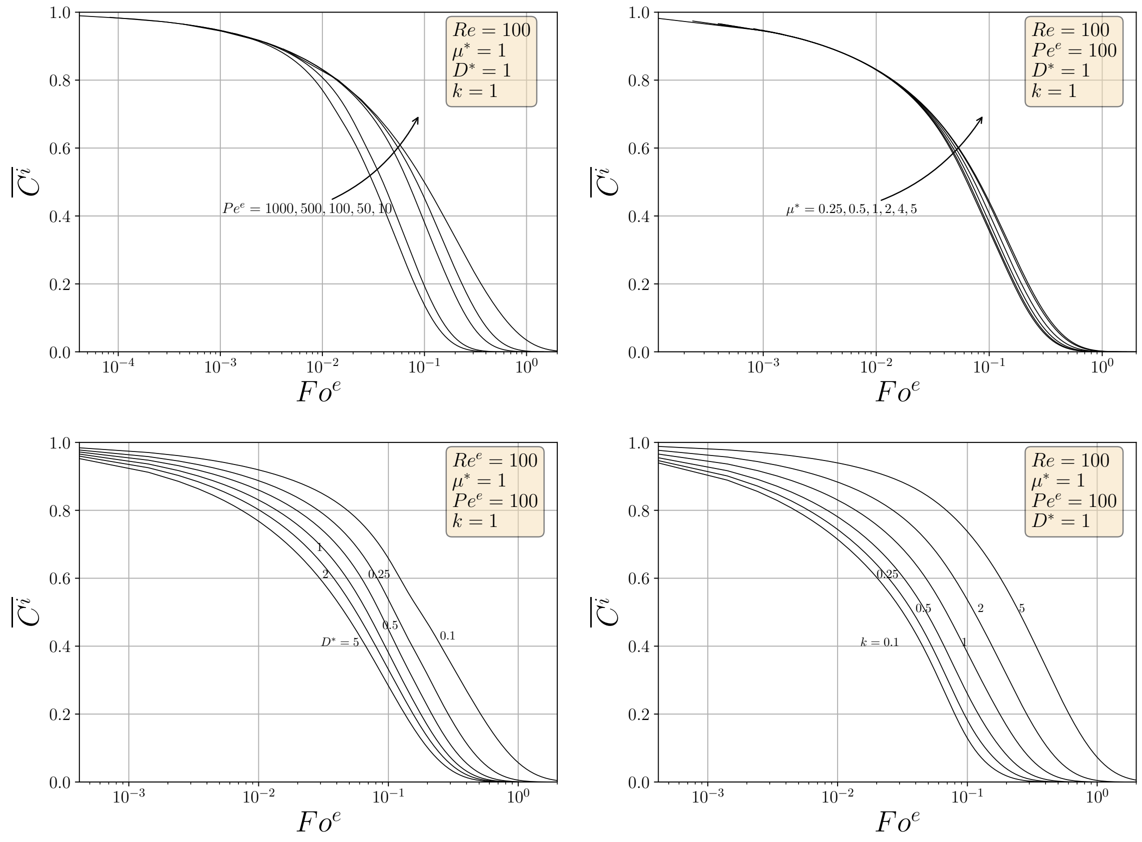

Figure 4.38: Temporal evolution of the mean concentration - top left: effect of $Pe$, top right: effect of $\mu^*$, bottom left: effect of $k$, bottom right: effect of $D^*$.

For $D^* = 1$, in configurations of low internal $Pe^i$ and $k$, the temporal evolution of the global Sherwood number $Sh$ does not converge to a well defined steady value. The identification of the steady value is then made according to the averaging previously explained in Section 4.2.3.

The evolution of the global Sherwood number with $Pe^i$ is illustrated in Figures 4.42, 4.43 and 4.44 at $Re = 100$, for three distinct hydrodynamic configurations: $\mu^* = 1$, $\mu^* = 2$ and $\mu^* = 0.5$ respectively. All figures compare the real value of the Sherwood number, $Sh_{sim}$, to the predictions of Eq. 4.2.6 noted $Sh_{corr}$. In left figures, the influence of $D\hat{a}st$ can be assessed for $k = 1$, while those of partition coefficient is illustrated at a constant diffusivity ratio $D^* = 1$ in the figures on the right.
It can be observed that, for large values of Peclet number and for $D^* = 1$, the agreement between $Sh_{sim}$ and $Sh_{corr}$ improves as $k$ increases. However for small $k$, only high $Pe^i$ yields good agreement between the simulation and the correlation. A deviation is noticeable as $Pe^i$ decreases. Moreover, for $k = 1$, $Sh_{sim}$ and $Sh_{corr}$ agree well only

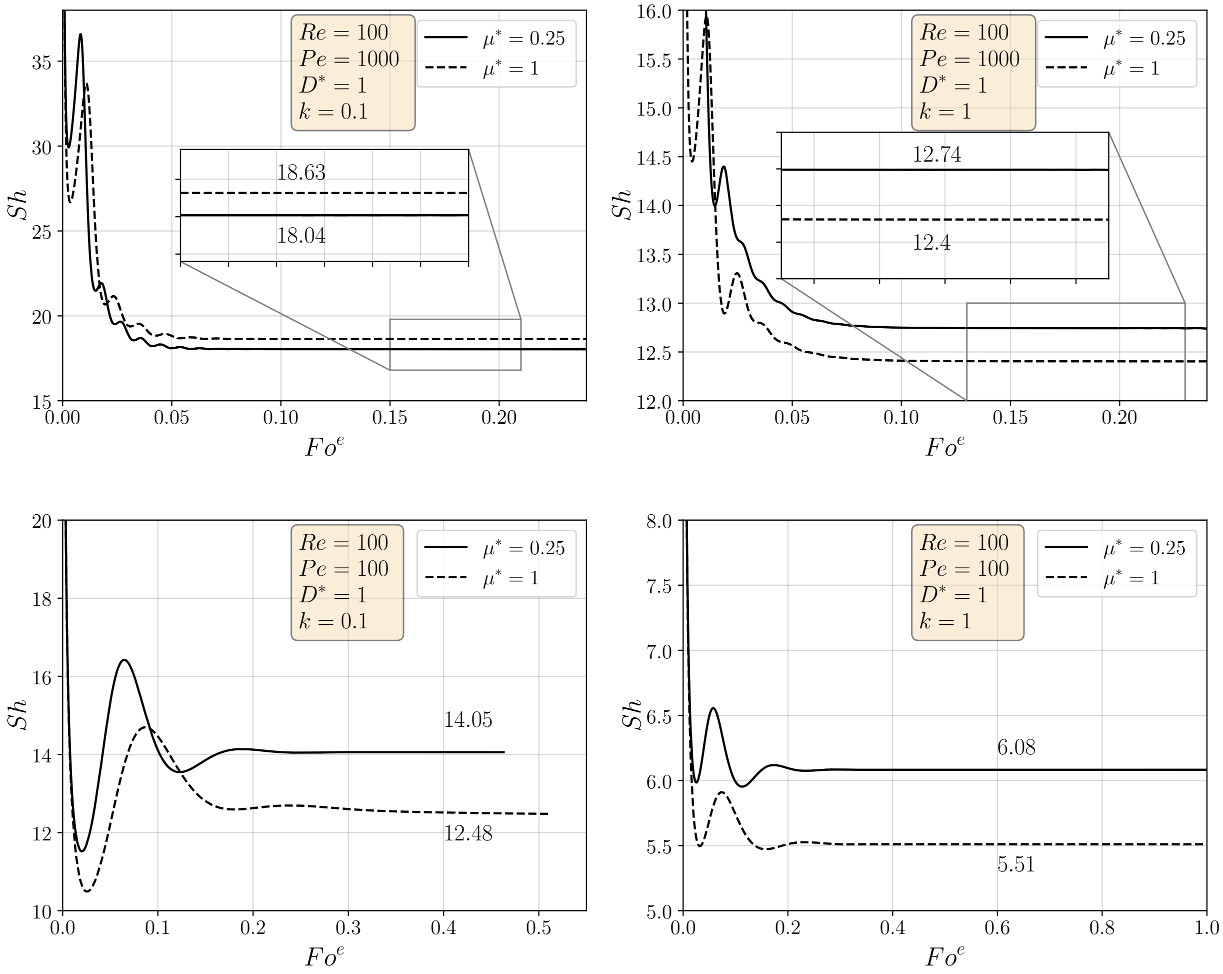

Figure 4.39: Temporal evolution of Sherwood number - Top: $Pe = 1000$, Bottom: $Pe = 100$.

for $Pe^i > 100$, regardless of the $D^*$ value. The same conclusions hold for the three configurations (i.e. $\mu^* = 0.5, 1, 2$).

A wide parametric study has been carried out for external Reynolds number up to 100: the viscosity ratio varies from 0.25 to 5, the diffusivity ratio $D^* =$ and the equilibrium coefficient $k$ were both varied from 0.25 to 5. Following the previous analysis, parity plots of the Sherwood number (see Figures 4.45 and 4.46) have been used to compare all the values obtained for a given $Re^e$. For every values of $Pe^i$, $Sh_{sim}$ and $Sh_{corr}$ have been represented with the same color, independently of the values of $\mu^*$ , $D^*$ and $k$. In agreement with the previous observations and discussion, the present simulations and the predictions based on additivity rule agree with an acceptable error

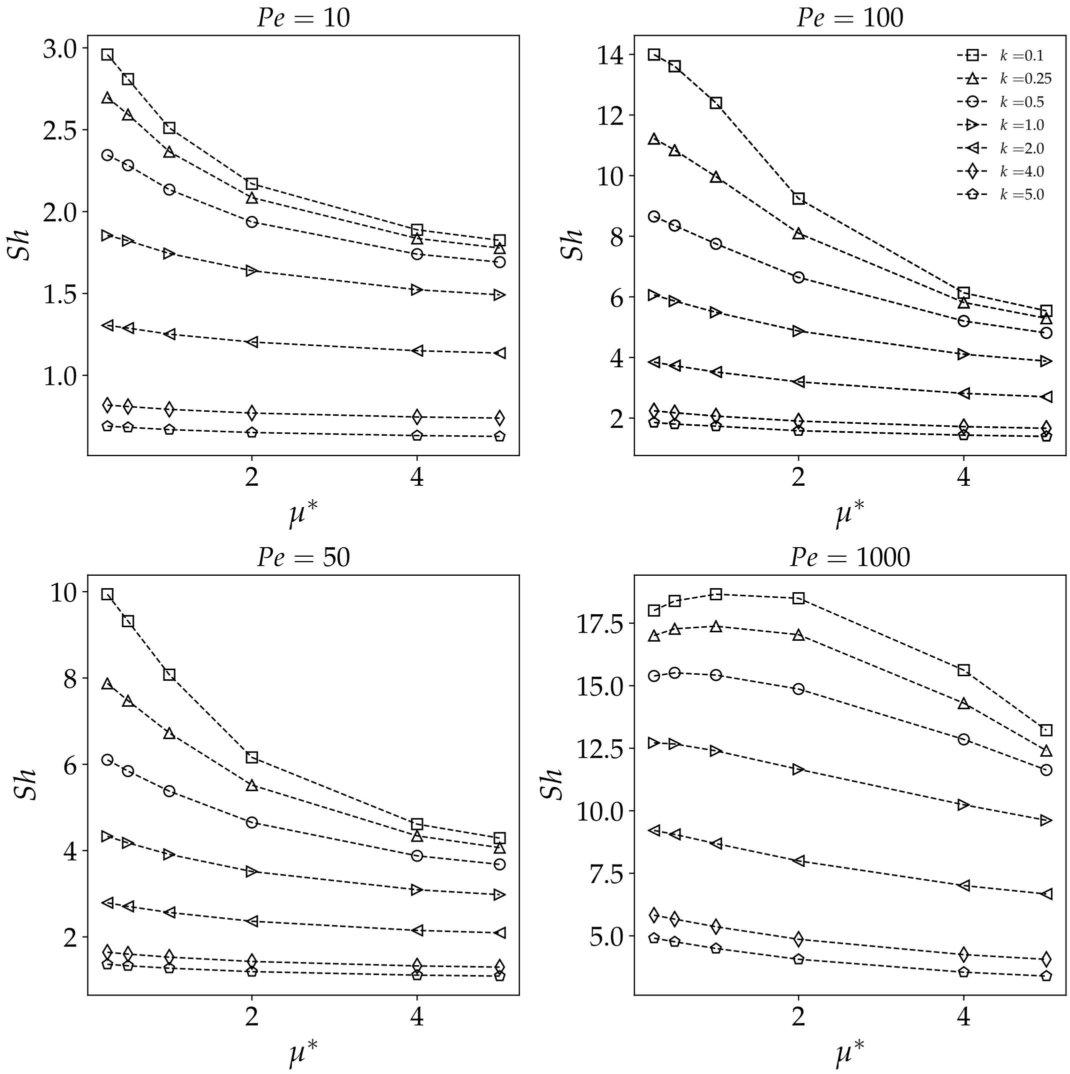

Figure 4.40: Asymptotic Sherwood number as function of the viscosity ratio for different partition coefficients ($Re = 100$, $D^* = 1$).

for $Pe^i \geq 500$. When the internal Peclet decreases, a clear deviation is observed between $Sh_{sim}$ and $Sh_{corr}$.

Additional figures of $Re = 0.1$, $Re = 1$ and $Re = 10$ are available in the Appendix along with Table of global Sherwood values.

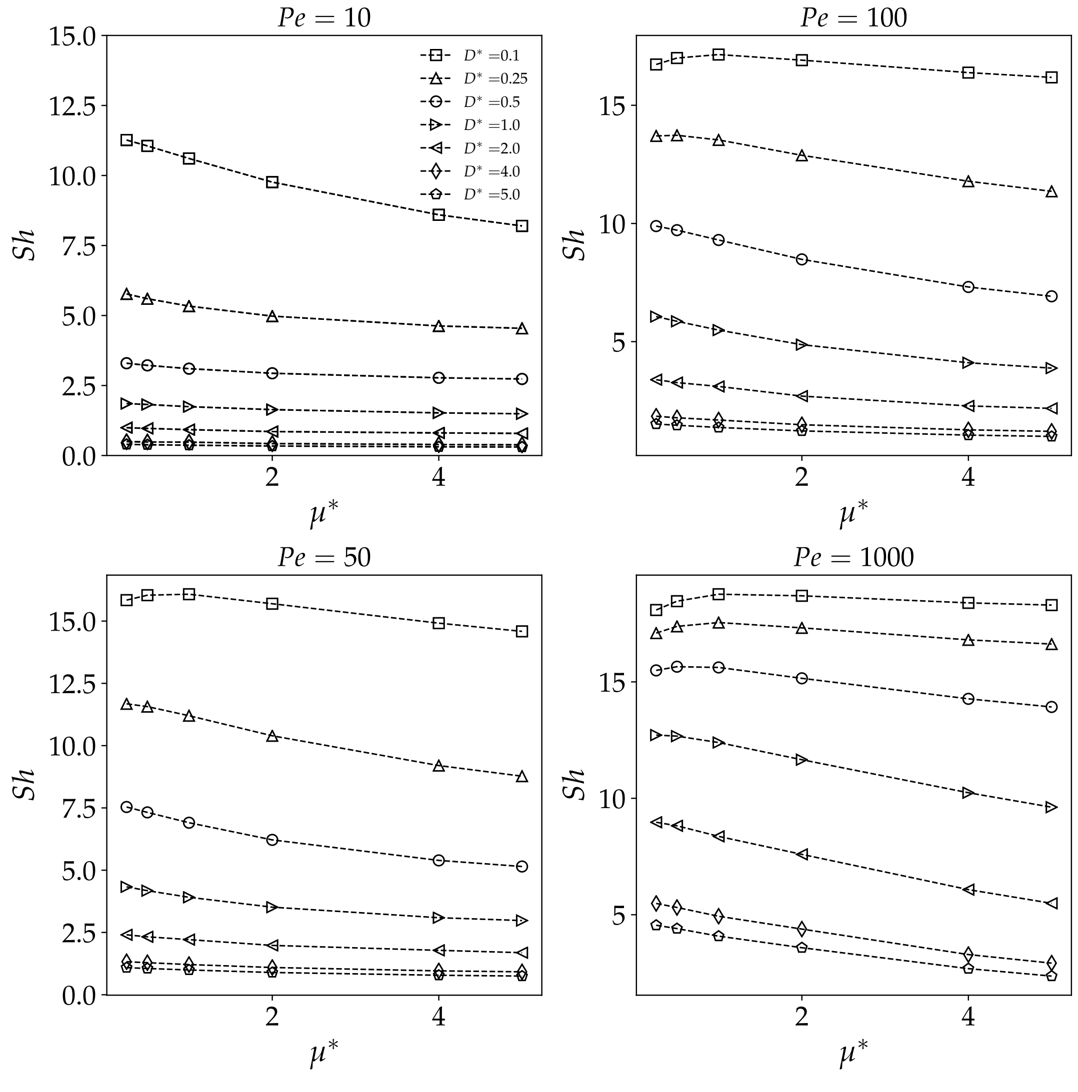

Figure 4.41: Asymptotic Sherwood number as function of the viscosity ratio for different diffusivity ratios ($Re = 100$, $k = 1$).

## 4.3 Conclusions

In this chapter, a complete hydrodynamic analysis of a droplet in a moderate Reynolds flow has been carried out. The effect of different external Reynolds and viscosity ratios have been studied where both internal and external flows are described. Using the limit of high viscosity ratio typical of a rigid particle case and low viscosity ratio corresponding to a bubble, a correlation of the drag have been proposed and validated in the range of the studied $Re^e$. Moreover, the condition under which an external circulation occurs in the wake of the drop has been defined. New correlation of the separation angle has

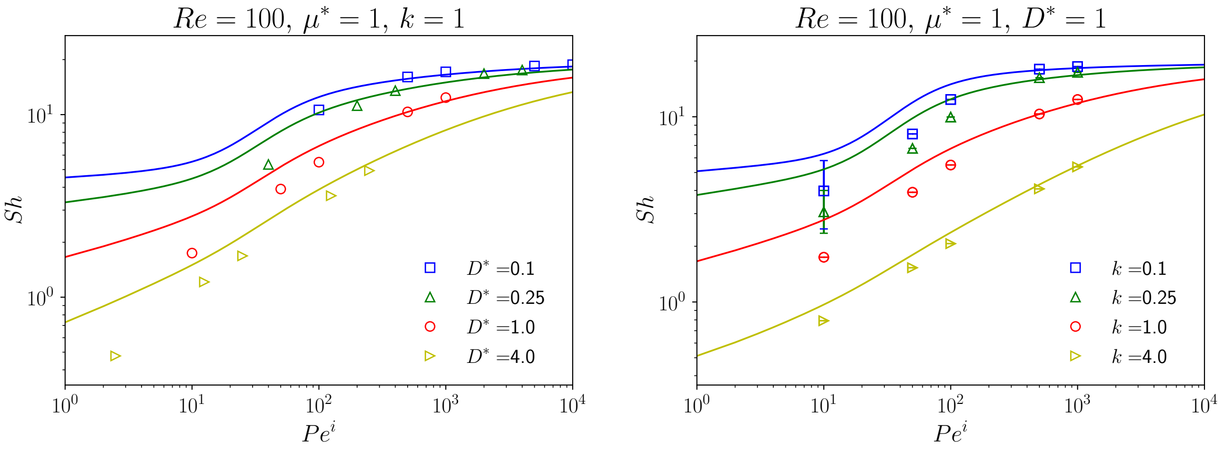

Figure 4.42: Evolution of global Sherwood number $Sh$ with internal Peclet $Pe^i$: continuous lines: Eq 4.2.6, symbols: Numerical simulations of conjugate transfer.

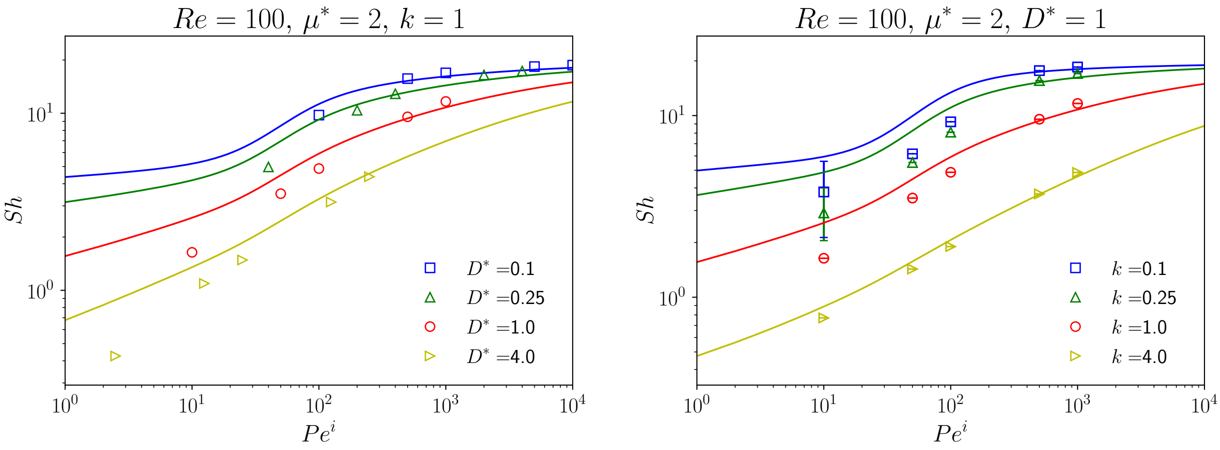

Figure 4.43: Evolution of global Sherwood number $Sh$ with internal Peclet $Pe^i$: continuous lines: Eq 4.2.6, symbols: Numerical simulations of conjugate transfer.

been given as a function of external Reynolds number and viscosity ratio. The relation between viscosity ratio and slip length at a fluid sphere interface was discussed. The link between the solid particle Basset-Boussinesq force and the Yang & Leal expression for bubble is made through the viscosity ratio.

For mass transfer, the impact of hydrodynamic and physical properties on local Sherwood and the global Sherwood numbers, and the spatial distribution of the solute concentration have been analyzed. The possible relation with the internal/external problems has been described. Regarding internal transfer, the diffusivity ratio and

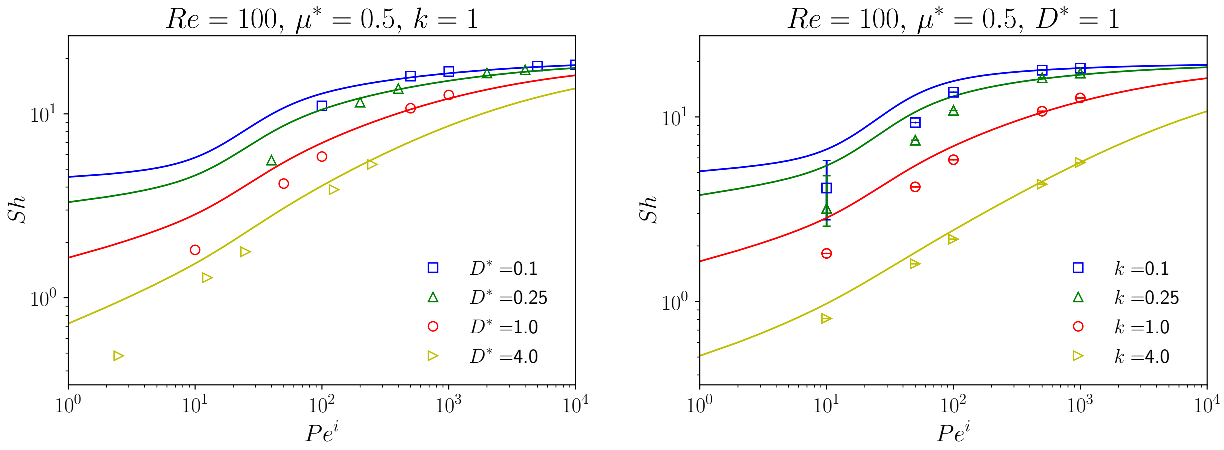

Figure 4.44: Evolution of global Sherwood number $Sh$ with internal Peclet $Pe^i$: continuous lines: Eq 4.2.6, symbols: Numerical simulations of conjugate transfer.

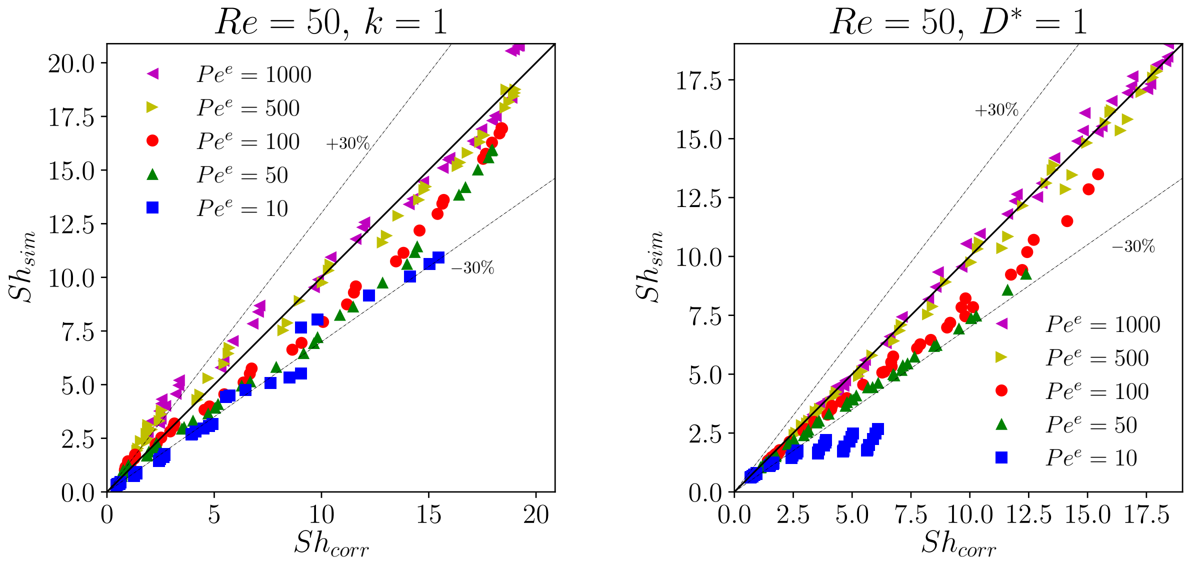

Figure 4.45: Parity plot of Sherwood number: present simulations vs Eq 4.2.6, $Re^e = 50$, $k = 1$ (left), $D^* = 1$ (right).

partition coefficient play equal role in shifting the mass transfer resistance inside the drop. The internal Sherwood number $Sh^i$ converges to the corresponding value $Sh^I$ of an internal problem. However, for external transfer, only $k$ plays a major role in moving the resistance in the outer phase. The impact of $D^*$ for high $k$ is blurred, in a high

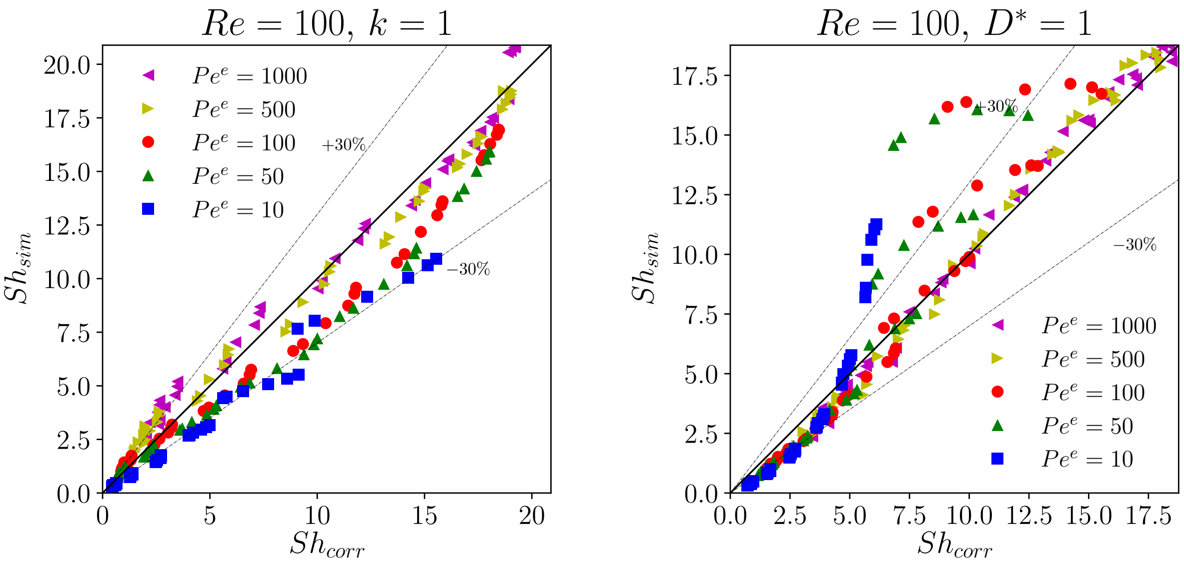

Figure 4.46: Parity plot of Sherwood number: psresent simulations vs Eq 4.2.6, $Re^e = 100$, $k = 1$ (left), $D^* = 1$ (right).

diffusivity ratio case, concentration at the interface is usually not uniform which results in a deviation between the external Sherwood number $Sh^e$ and corresponding $Sh^E$ for low $Pe^e$. In this case, an increase in $k$ allows to fill the gap between $Sh^e$ and $Sh^E$. The relevance of the additivity rule of transfer resistances for the prediction of Sherwood number was evidenced in high internal Peclet number and high partition coefficient.

# Chapter 5

# 3D simulations

## Contents

In industrially relevant situations, the flow is generally non uniform, and/or highly turbulent, meaning that elevated particles $Re$ can prevail. In order to address this kind of problems, the purpose of this chapter is to extend the developed numerical approach to three dimensional problems. For that purpose, a full resolution of the equations governing hydrodynamics and mass transfer for a spherical drop is performed in 3D grids . The background of the physical modelling, mathematical description and numerical solving have already been detailed in Chapter 3.

The LCE mesh is adopted, and a special care is paid to the implementation of the boundary conditions at the interface, to enable the flow to cross what was the symmetry axis of the mesh in 2D.

As in the 2D-axi case, a thorough validation of the 3D model was carried out based on recently published results at high $Re$ Edelmann et al. [2017]. In particular, the onset of internal circulations is investigated and a parametric study has been conducted to analyze 3D effects, and assess the impact of the internal circulation mode on both the Sherwood number and the concentration distribution.

In this chapter we start by giving an overview of the state of art concerning particles in high Reynolds number. We present afterwards the developped mesh and the resolution methodology. Finally, validation tests and results on the hydrodynamics and mass transfer are presented and discussed.

## 5.1 Particles in high $Re$ flow: overview

In the reviewed literature, most of the numerical and theoretical studies on drops are based on the axisymmetry condition. This latter assumption has been adopted as well in the previous chapters to address numerically the hydrodynamics and mass transfer of a droplet in an immiscible liquid phase.

Taneda [1956] was the first to highlight experimentally the flow structure around a sphere for $5 < Re < 300$, and along with earlier numerical simulations (Natarajan and Acrivos [1993],Tomboulides and Orszag [2000],Johnson and Patel [1999]) a consensus was reached to describe the flow structure around the sphere. A separation occurs from the rear of the sphere at $Re \approx 24$ and results in the generation of an axisymmetric external recirculation (vortex ring). The flow is axisymmetric for Reynolds numbers up to $Re \approx 212$. In the range $212 < Re < 272$, the flow becomes non-axisymmetric as the ring vortex shift toward one side of the axis, and a regular bifurcation takes place with one symmetry plane. For Reynolds numbers which are slightly higher, a Hopf bifurcation develop making the flow periodic. Finally, periodicity is lost for $Re > 300$.

In some configurations, drops remain nearly spherical at moderate Reynolds numbers providing that the surface tension is sufficiently high. Winnikow and Chao [1966] experiments show that drops of m-nitrotoluene in water ($\mu^* = 2.2$) with $d = 3.1mm$ remain spherical at $Re = 506$, while bubbles can be spherical for Reynolds numbers up to $Re = 250$. For systems exhibiting high viscosity ratio Albert et al. [2015] or because of surface contaminants, the external flow is similar to that around a solid sphere at the same $Re$. Correlations are proposed for the terminal velocity of a falling or rising droplet, based on experimental investigations (Greene et al. [1993]; Thorsen et al. [1968]; Winnikow and Chao [1966]). Most of these works consider droplets from organic liquids with viscosities close to the continuous phase $\mu^* \approx 1$.

Concerning the dynamical behaviour inside drops, unlike the case of droplets in a gas phase, few studies have been devoted to this problem, especially for high internal Reynolds number and comparable phase viscosities and densities. Engberg and Kenig [2015] used Level-Set 3D simulation to study the rising of a toluene droplet in water. Internal bifurcations were observed for a slightly deformed droplet. A recent study by Edelmann et al. [2017] highlighted that the axisymmetry assumption is valid only in a limited range of inner Reynolds numbers. Their results highlighted different internal flow modes. Beyond a certain value of inner Reynolds number, an internal bifurcation develops inside the droplet that breaks the Hill's vortices, and makes the problem three dimensional. These newly evidenced internal flow patterns can significantly affect the flow structure inside and around the drop, and therefore the heat and mass transfer processes.

As previously mentionned, most of the studies dedicated to conjugate heat/mass transfer addressed low to intermediate Reynolds, where the problem was considered axisymmetric (Kleinman and Reed [1996]; Oliver and Chung [1986]), and Juncu [2010] considered the internal problem in the case of low, intermediate and high Reynolds numbers. Recently, Edelmann et al. [2017] evidenced that the flow symmetry breaking at elevated inner Reynolds numbers is likely to strongly impact the steady value of the Sherwood number of an internal problem. In the Hill's vortex-like cases, the streamlines are two-dimensional and closed, with an ellipsoidal shape. This means that at high Peclet numbers the diffusion is the rate-limiting mechanism, leading to asymptotic Sherwood $Sh_\infty = 17.9$ for high Peclet number. The authors show that this value is no longer a limit and that $Sh_\infty$ can be as high 130 when complex three-dimensional streamlines take place inside the drop.

To our knowledge, no study has dealt with conjugate mass transfer in such configurations. In this chapter, the hydrodynamics and the conjugate mass transfer of a translating liquid droplet in an immiscible liquid phase is investigated. Considering moderate Reynolds where 3D effects are expected, a special care will be given to the conditions under which discrepancies may occur between axisymmetric and three dimensional configurations.

## 5.2 Numerical Method

### 5.2.1 3D mesh

The 3D mesh is generated by rotating the two-dimensional LCE mesh around the $\mathbf{e_x}$ axis with an angle $\varphi$ and a given discretization in the 3rd direction (Figure 5.1). Note that the $\mathbf{e_x}$-axis remains an axis of symmetry for the mesh but not necessarily for the flow, which represents one of the main challenge of the 3D model development. It is important to note that the cells number $nz$ in the 3rd direction (*i.e.* around the axis) must be a power of 2 ($nz = 2^n$) for reasons that will be explained in the next section.

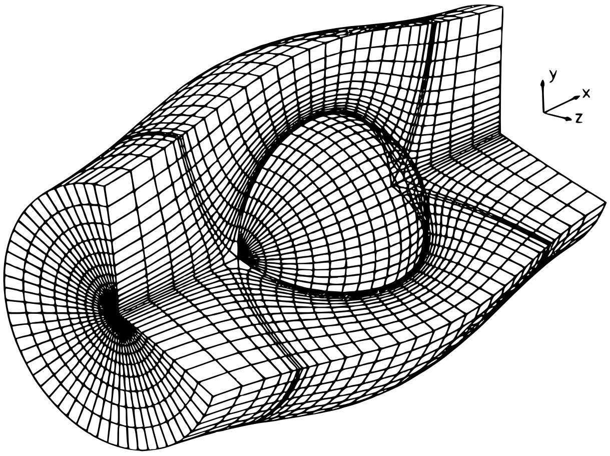

Figure 5.1: Representation of the LCE 3D mesh Legendre [1996].

## 5.2.2 Boundary conditions

### 5.2.2.1 Conditions on the $e_x$ axis

In the 3D configuration, mass and momentum flux crossing must be allowed through the cells connected to the axis. Therefore, a specific boundary condition is implemented to take into account possible mass flux across the axis. In the same way as what was done for 2D-axi case, specific conditions at the interface have been implemented, the velocity value at the axis being an extrapolation of the four neighbouring cells (see Legendre and Magnaudet [1998]).

On the left figure of Figure 5.2, a schematic representation depicts the mesh view in a plane (YZ) outside the drop. Velocity components $V_{i,0}$ at the axis for each slice $k$ are calculated by extrapolating the value of the four cells highlighted in blue. On the right figure, we show a schematic representation of the considered cells.

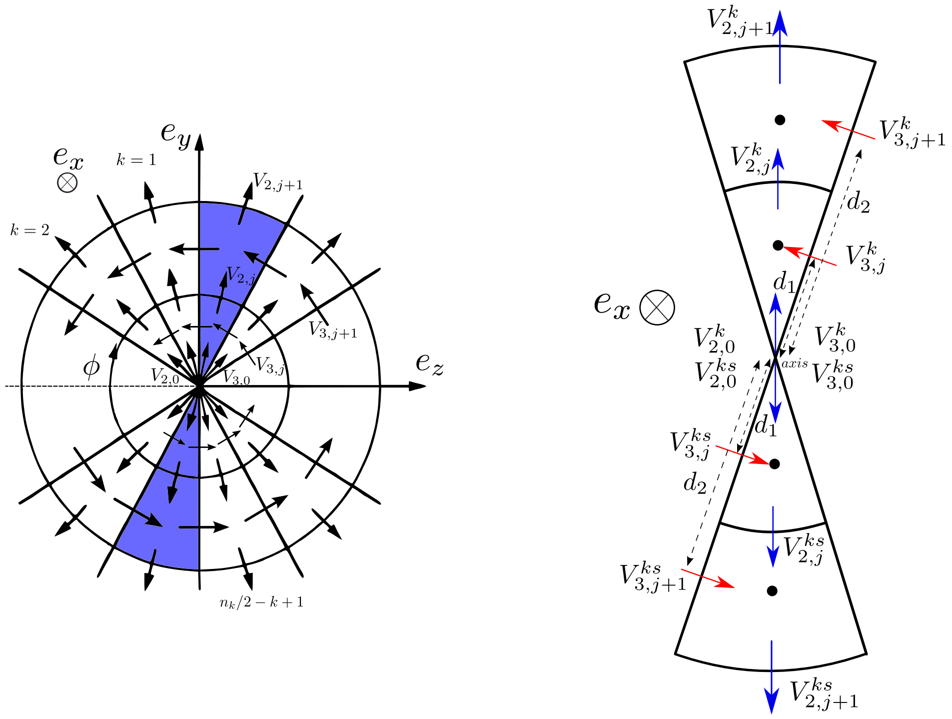

Figure 5.2: Schematic representation of the boundary conditions at the axis (left), zoom into the blue cells (right).

With the notations provided by Figure 5.2, an expansion to the second order is performed on the third velocity component. After simplification we obtain the following equations:

$$\begin{cases} d_2^2 V^k_{3,j} - d_1^2 V^k_{3,j+1} = (d_2^2 - d_1^2) V^k_{3,0} + d_1 d_2 (d_2 - d_1) \left( \dfrac{\partial V^k_3}{\partial \xi_2} \right)_k \\ d_2^2 V^{ks}_{3,j} - d_1^2 V^{ks}_{3,j+1} = (d_2^2 - d_1^2) V^{ks}_{3,0} + d_1 d_2 (d_2 - d_1) \left( \dfrac{\partial V^{ks}_3}{\partial \xi_2} \right)_{ks} \end{cases} \tag{5.2.1}$$

where $V^k_{3,0}$ (resp. $V^{ks}_{3,0}$) is the value of the third component of the velocity at the axis in the plan $k$ (resp. $ks$). Since $nz = 2^n$, each plan $k$ has a diagonally-opposite corespondent plan $ks$. From the schematic representation we write:

$$\begin{cases} V^k_{3,0} = -V^{ks}_{3,0} \\ \left( \dfrac{\partial V^k_3}{\partial \xi_2} \right)_k = \left( \dfrac{\partial V^{ks}_3}{\partial \xi_2} \right)_{ks} \end{cases} \tag{5.2.2}$$

After simplifications, the following expression is used as a boundary condition at the axis:

$$V^k_{3,0} = \frac{d_2^2}{2(d_2^2 - d_1^2)} \left( V^k_{3,j} - V^{ks}_{3,j} \right) - \frac{d_1^2}{2(d_2^2 - d_1^2)} \left( V^k_{3,j+1} - V^{ks}_{3,j+1} \right) \tag{5.2.3}$$

Thus we see that the velocity on the axis is related to the velocity on both sides of the axis of symmetry. The same method is used to evaluate $V_{1,0}^k$ and $V_{2,0}^k$

The boundary conditions at the center of the droplet are more difficult to define. In fact, curvature terms can be expressed analytically in a polar coordinates as follow:

$$\begin{aligned} H_1^2 &= \frac{1}{r} \\ H_3^2 &= \frac{1}{r} \\ H_3^1 &= \frac{1}{r\tan(\theta)} \end{aligned} \tag{5.2.4}$$

These expressions, appearing in the shear stress Eq 5.2.5, take infinite values in the droplet center and on the droplet axis $\theta = 0$ or $\theta = \pi$. On the other hand, these terms balance gradients in the expression of the shear stress, in fact, gradients along $r\partial\theta$ of $r\sin(\theta)\partial\varphi$ take high values at the center. In order to avoid numerical divergence, a reconstruction of the velocity at center is performed where infinite values are avoided by extrapolating neighbouring cells velocity to the center. Figure 5.3 (left) highlights a simplified representation of the mesh at the droplet center. Unlike the boundary condition implemented at the axis that uses four neighbouring cells, the velocity at the center is obtained from two neighbouring cells only (see right figure of Figure 5.3), as the use of four cells induces a divergent shear stress at the center.

$$\begin{cases} \tau_{11} = \dfrac{2}{Re}\left[\dfrac{\partial V_1}{r\partial\theta} + H_1^2 V_2 + H_1^3 V_3\right] \\ \tau_{22} = \dfrac{2}{Re}\left[\dfrac{\partial V_2}{\partial r} + H_2^1 V_1 + H_2^3 V_3\right] \\ \tau_{33} = \dfrac{2}{Re}\left[\dfrac{\partial V_3}{r\sin(\theta)\partial\varphi} + H_3^1 V_1 + H_3^2 V_2\right] \\ \tau_{12} = \dfrac{1}{Re}\left[\dfrac{\partial V_1}{\partial r} + \dfrac{\partial V_2}{r\partial\theta} - H_2^1 V_2 - H_1^2 V_1\right] \\ \tau_{13} = \dfrac{1}{Re}\left[\dfrac{\partial V_1}{r\sin(\theta)\partial\varphi} + \dfrac{\partial V_3}{r\partial\theta} - H_3^1 V_3 - H_1^3 V_1\right] \\ \tau_{23} = \dfrac{1}{Re}\left[\dfrac{\partial V_2}{r\sin(\theta)\partial\varphi} + \dfrac{\partial V_3}{\partial r} - H_3^2 V_3\right] \end{cases} \tag{5.2.5}$$

Using the notations shown in Figure 5.3, the first component of velocity is extrapolated (red cells) to the droplet center following the expression:

$$V_{1,0}^k = \frac{d_2}{d_2 - d_1} V_{1,j}^k - \frac{d_1}{d_2 - d_1} V_{1,j+1}^k \tag{5.2.6}$$

The same method is used to evaluate $V_{3,0}^k$. At $\theta = 0$, green cells are used to extrapolate $V_2$ to the axis. Using similar expansion as in Eq. 5.2.1, with the notations of Figure 5.3 (right). The expressions of $V_{2,0}$ and $V_{3,0}$ at the axis are:

$$V_{2,0}^{k}=\frac{d_2^2}{2(d_2^2-d_1^2)}\left(V_{2,i}^{k}+V_{2,i}^{ks}\right)-\frac{d_1^2}{2(d_2^2-d_1^2)}\left(V_{2,i+1}^{k}+V_{2,i+1}^{ks}\right) \tag{5.2.7}$$

$$V_{3,0}^{k}=\frac{d_2^2}{2(d_2^2-d_1^2)}\left(V_{3,i}^{k}-V_{3,i}^{ks}\right)-\frac{d_1^2}{2(d_2^2-d_1^2)}\left(V_{3,i+1}^{k}-V_{3,i+1}^{ks}\right) \tag{5.2.8}$$

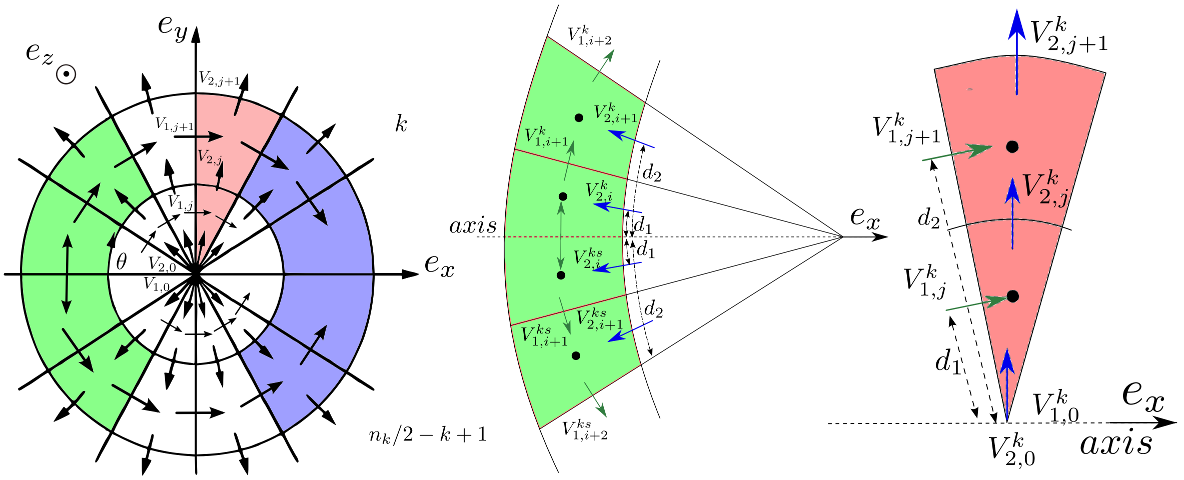

Figure 5.3: Schematic representation of the boundary conditions at the droplet center (left), zoom into the coloured regions (middle and right).

A periodicity condition is applied on the two faces which meet after a complete rotation of 2D-axi mesh around the axis.

#### 5.2.2.2 Conditions at the interface

To complete the implemented conditions at the interface in 2D-axi simulations Eq. 3.5.1 (see Chapter 3), two additional hydrodynamics conditions at the interface have to be considered, for the velocity and shear stress (Eq 5.2.9), to take into account the third dimension. The discretization was performed in the way as detailed in Chapter 3.

$$\begin{gathered}V_3^i=V_3^e\\ \tau_{23,I}^i=\tau_{23,I}^e\end{gathered} \tag{5.2.9}$$

These additional conditions are discretized through coupling the velocity and the shear stress, as detailed in Section 3.5.3 for $V_{1,I}^e$ and $\tau_{12,I}^e$. The coupled discretization of the shear stress $\tau_{23,I}^i$ and thirst velocity component at the interface is given by Equations 5.2.10 and 5.2.11:

$$\tau^{e}_{23,I} = \frac{\mu^i}{\mu^e}\frac{d3w^i\,V_{3,j-2} - d2w^i V_{3,j-1} + \dfrac{(d1w^i - H_3^2)(d2w^e\,V_{3,j} - d3w^e\,V_{3,j+1})}{d1w^e + H_3^2}}{1 + \dfrac{\mu^i}{\mu^e}\dfrac{d1w^i - H_3^2}{d1w^e + H_3^2}} \tag{5.2.10}$$

$$V^{e}_{3,I} = \frac{d2w^e\,V_{3,j} - d3w^e\,V_{3,j+1} - \tau^{e}_{23,I}}{d1w^e + H_3^2} \tag{5.2.11}$$

where the following dimensionless parameters have been introduced to simplify the above expressions:

$$\begin{cases} d1w^\delta = \dfrac{d_2^{\delta 2} - d_1^{\delta 2}}{d^\delta{}_1 d^\delta{}_2 (d^\delta{}_2 - d^\delta{}_1)} \\ d2w^\delta = \dfrac{d_2^{\delta 2}}{d^\delta{}_1 d^\delta{}_2 (d^\delta{}_2 - d^\delta{}_1)} \\ d3w^\delta = \dfrac{d^{\delta 2}_{\ 1}}{d^\delta{}_1 d^\delta{}_2 (d^\delta{}_2 - d^\delta{}_1)} \end{cases} \tag{5.2.12}$$

### 5.2.3 Numerical study

The numerical method used in this chapter has been introduced earlier. The algorithm of resolution is the same as the one previously detailed. In the 3D configuration of reference, the computational domain is discretized using a set of $nz = 64$ cells around the axis.

For each configuration, the corresponding 2D-axi simulations are performed. First, an axisymmetric simulation is conducted with the 2D-axi LCE mesh where a symmetry condition is set on the axis. Afterwards 3D simulations are performed using the same 2D-axi mesh rotated around the axis. As described in Chapter 3 for the 2D-axi simulations, the hydrodynamics problem is first solved for a given external Reynolds number $Re^e$, viscosity ratio $\mu^*$, and density ratio $\rho^*$ until a steady-state is reached. The transport equation of the solute is resolved subsequently in the frozen velocity field with an initial value of $C_0^i = 1$ inside the droplet and 0 everywhere outside.

## 5.3 3D Validations

*Hydrodynamics: drop in a uniform flow*

For intermediate $Re$ (i.e. $Re = 100$), both the drag coefficient and the streamlines derived from 3D simulations show good agreement with previous axisymmetric simulations. Recent data from Edelmann et al. [2017] have been used to compare the drag coefficient for higher Reynolds numbers. The results are summarized in Table 5.1. The calculated drag coefficients are in excellent agreement with the literature data in the range of Reynolds number considered.

| $Re$ | 100 | 150 | 200 | 250 | 300 |
|---|---|---|---|---|---|
| Present 3D simulations | 0.531 | 0.503 | 0.466 | 0.443 | 0.425 |
| Edelmann et al. [2017] | 0.538 | 0.492 | 0.466 | 0.442 | 0.421 |

Table 5.1: Drag coefficient ($\mu^* = 0.5$, $\rho^* = 1.5$).

The mesh convergence study (see Table 5.2) indicates that results are grid-independent in the investigated range of Reynolds number. The refining has been performed around the axis.

| $Re \setminus nz$ | 32 | 64 | 128 | 256 |
|---|---|---|---|---|
| 100 | 0.533 | 0.532 | 0.532 | 0.53 |
| 150 | 0.5191 | 0.5031 | 0.498 | 0.496 |
| 200 | 0.4848 | 0.4668 | 0.462 | 0.461 |

Table 5.2: Effect of the refinement in the azimuthal direction on the drag coefficient: $\rho^* = 1.5$, $\mu^* = 0.5$.

*Hydrodynamics: drop in a simple shear flow*

Other typical 3D hydrodynamic configurations have been visited where the droplet is placed in a simple shear flow (i.e. Figure 5.4). Many studies have been dedicated to particles and drops in such configurations (see Subramanian and Koch [2006], Mikulencak and Morris [2004], Li et al. [2015]). In the limit of Stokes flow (i.e. $\dot{\gamma}R^2/\nu^e \ll 1$), Kennedy et al. [1994] showed that the droplet shape and internal/external streamlines depends only on the viscosity ratio and the capillary number $Ca = \dot{\gamma}R_e\mu^e/\sigma$. For negligible $Ca$, the droplet sustains a spherical shape and no deformation is observed. Figure 5.5 illustrates internal and external streamlines for three different $\mu^*$. The streamlines behaviour shows a similar trend to the cases reported by Kennedy et al. [1994].

*Conjugate mass transfer*

For the mass transfer validation in 3D, the time evolution of the Sherwood number is compared with previous axisymmetric simulations for moderate Reynolds number. Figure 5.6 compares the temporal evolutions of the global Sherwood number obtained for 2D-axi and 3D simulations for $\mu^* = 0.5$ and $\rho^* = 1.5$. At $Re = 100$ (i.e. $Re^i = 300$), no significant change is observed in the global Sherwood number that converges to the same asymptotic value $Sh = 12.57$. This provides validation of the 3D configuration. Note

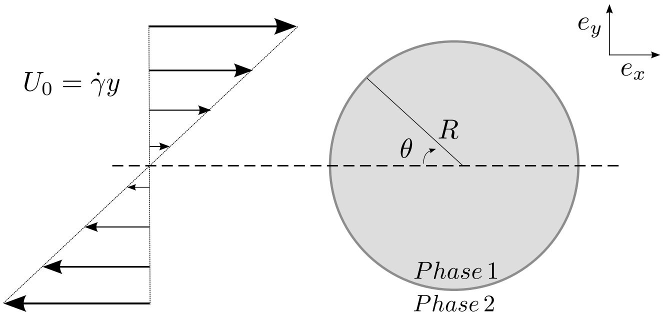

Figure 5.4: Schematic representation of a drop in simple linear shear flow, $\dot{\gamma}$ is the velocity gradient of the shear flow.

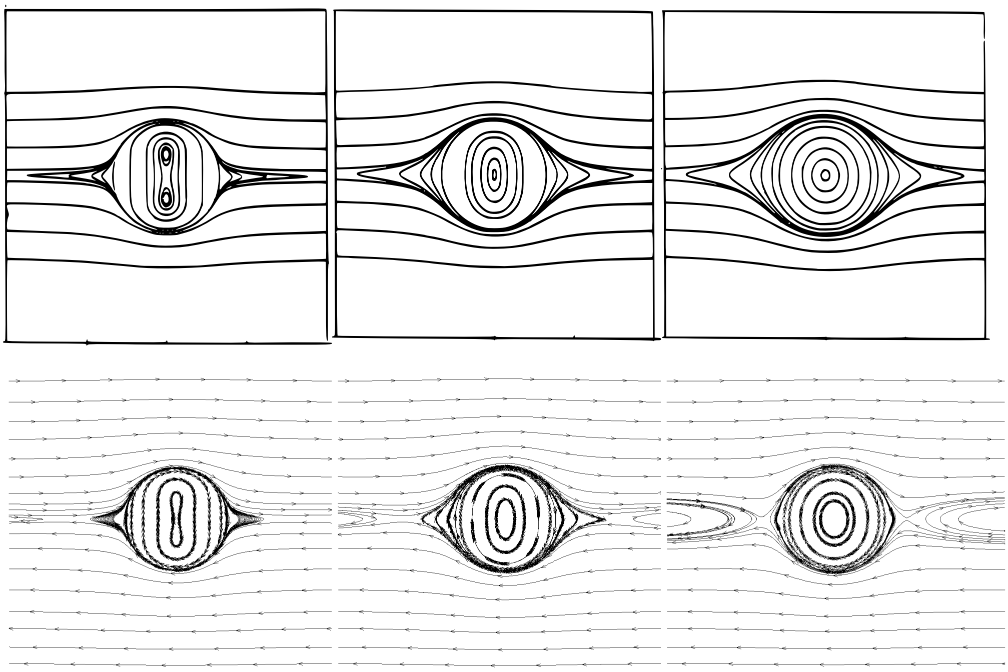

Figure 5.5: Streamlines in simple linear shear Stokes flow: top Kennedy et al. [1994] (from left to right ($\mu^* = 0$, $\mu^* = 1$, $\mu^* = 6.4$)), bottom: present result, ($Re = 0.01$, from left to right $\mu^* = 0.1$, $\mu^* = 1$, $\mu^* = 5$).

that in the other hand, as it will be discussed later , for higher Reynolds number, typically $Re = 150$ and $Re^i = 450$ with the considered fluids, the two numerical approaches lead to completely different evolutions of the Sherwood number (see Section 5.5).

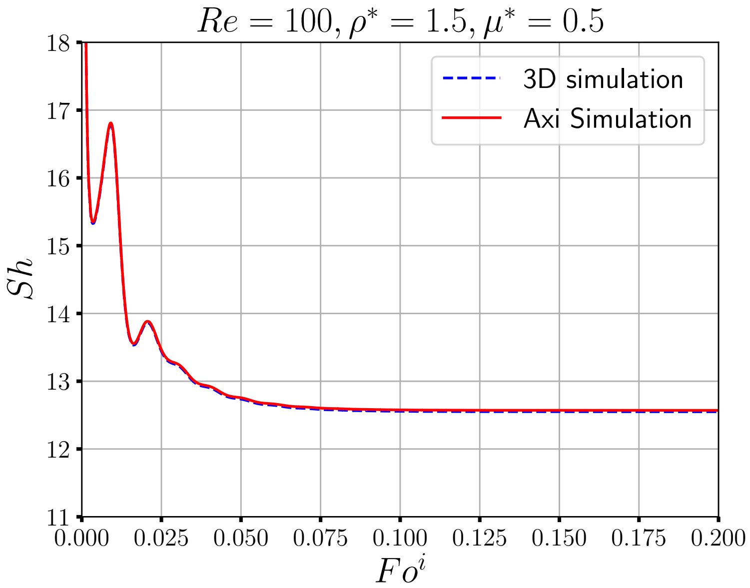

Figure 5.6: Comparison of the 2D (red) and 3D (red) time-evolutions of the global Sherwood number $Sh$. $Pe = 1000$, $D^* = 1$, $k = 1$, $Re = 100$.

## 5.4 Hydrodynamics

### 5.4.1 3D steady bifurcations of the flow

Our 3D simulations for high Reynolds show that a steady state is reached up to $Re = 300$, but that it is not necessary the case beyond that. Results reveal that the convergence or the steady state depends highly on $\rho^*$ and $\mu^*$, in other words, it depends on the inner Reynolds number $Re^i$. For $\mu^* = 0.5$ and $\rho^* = 1.5$, Figure 5.7 depicts the time evolution of the third component $V_3$ of the velocity. Note that the flow is initially parallel to the symmetry axis ($V_3 = 0$). For low to intermediate Reynolds numbers, $V_3$ stays close to 0 at machine precision and does not vary with time (see $Re = 100$). For higher Reynolds numbers ($Re \geq 150$), $V_3$ starts taking non null values and a sudden change in $dV_3/dt$ profile is observed. As $dV_3/dt$ converges toward small but not zero values ($\approx 10^{-5}$) and a steady state is reached. In order to check the robustness of the 3D destabilization and the transition from a 2D to a 3D character, the velocity condition has been imposed perpendicular to the axis of symmetry. In this case $V_{3,0} \neq 0$ and $\max\left(\frac{\partial V_3}{\partial t}\right)$ is decreasing over time until reaching a small value (see Figure 5.8). The internal/external streamline are compared to the reference cases where the imposed velocity is parallel to the axis (see Figure 5.14).

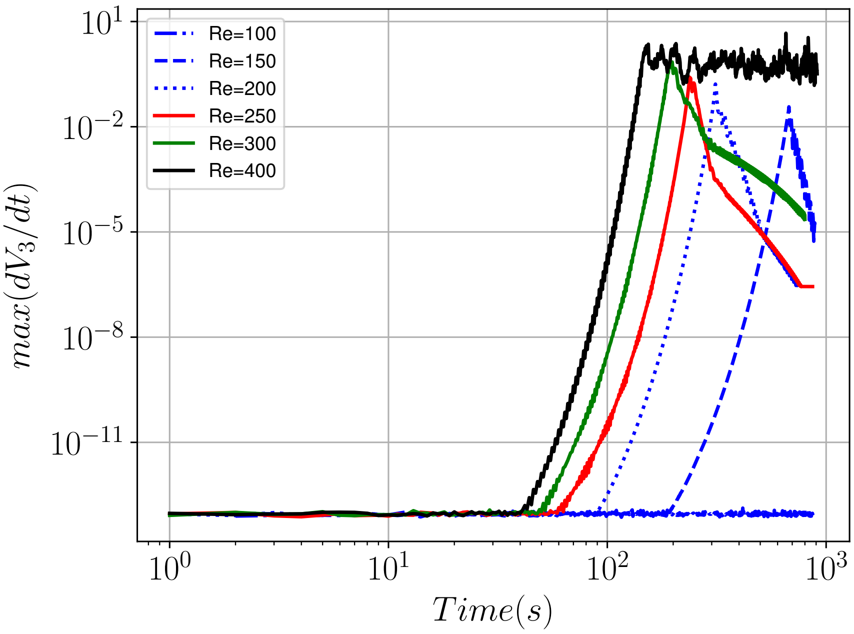

Figure 5.7: Temporal evolution of max $\left(\frac{\partial V_3}{\partial t}\right)$ in all computational domain: $\rho = 1.5$, $\mu^* = 0.5$.

#### 5.4.1.1 Drag coefficient

With regards to a relatively intermediate external Reynolds number (i.e. $Re = 100$), for $\rho^* = 1.5$, $\mu^* = 0.5$, $C_D$ converges monotonically to a steady value that corresponds to the steady state of an axisymmetric simulation. As the Reynolds number increases ($Re \geq 150$), the 3D simulation indicates that $C_D$ first decreases toward an asymptotic value, which corresponds to the axisymmetric problem value. When 3D effects develop a sudden increase occurs that changes the asymptotic value of the drag coefficient, this elevated $C_D$ value is an indicator of 3D effects. Figure 5.9 shows the temporal evolution of the drag coefficient. As clearly shown, the first effect of 3D bifurcation is a significant increase of the drag (around 100% for the cases shown in Figure 5.9).

Figure 5.11 (resp Figure 5.10), referred to as case 1 (resp. case 2), highlights the evolution of the steady value of the drag coefficient $C_D$ with the Reynolds number for $\mu^* = 0.5$, $\rho^* = 1.5$ (resp. $\mu^* = 1$, $\rho^* = 2.5$). With regards to case 1, for $Re < 150$ (i.e. $Re^i < 450$), 2D-axi and 3D simulations yield basically the same value for $C_D$. The velocity field has moreover been found identical between 2D-axi and 3D simulations. Deviations are observed as $Re \geq 150$ (i.e. $Re^i \geq 450$). For case 2, the threshold value of the Reynolds number responsible of the bifurcation is $Re = 275$ (i.e. $Re^i < 437.5$) as shown Figure 5.10. At elevated inner Reynolds numbers, the 3D simulations are in good agreement with the experimental results of Thorsen et al. [1968], and with recent 3D numerical studies by Edelmann et al. [2017]. On the other hand, the axisymmetric

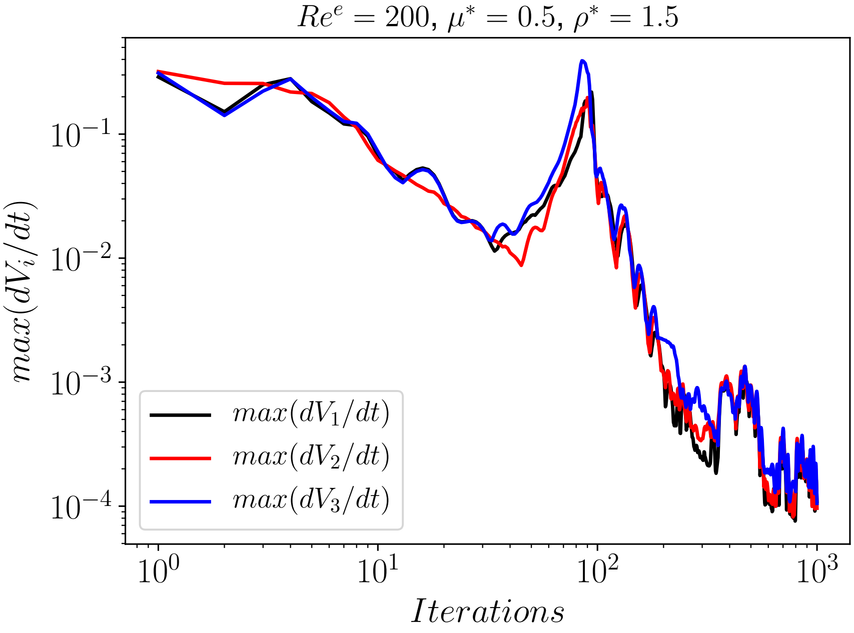

Figure 5.8: Time evolution of max $\left(\frac{\partial V_i}{\partial t}\right)$ in all the computational domain for all velocity components: $Re^e = 200$, $\rho = 1.5$, $\mu^* = 0.5$.

simulation is found to underestimate the drag coefficient $C_D$ value by almost 20% for $Re = 200$. These results are clearly questionning the reliability of the literature correlations based on the axisymmetry condition for high inner Reynolds flow.

### 5.4.1.2 Internal and external streamlines

Regarding most of the cases considered here (2D-axi or 3D), hydrodynamic simulation reaches a steady state regarding the previous criterion, which means, the temporal derivative of velocity components reaches small values (typically less than $10^{-6}$). The internal and external flow structures are then frozen and no longer vary with time. Figures 5.12, 5.13 and 5.14 illustrate in three different projections, the internal and the external streamlines corresponding to three external Reynolds configurations: $Re = 100$, $Re = 150$ and $Re = 200$ respectively. The density and viscosity ratios are fixed to $\rho^* = 1.5$, $\mu^* = 0.5$ in each case. For relatively intermediate Reynolds numbers ($Re = 100$, $Re^i = 300$), the streamlines structure is axisymmetric and a Hill's vortex develops inside the drop. However, for elevated Reynolds number, as illustrated in Figure 5.13 ($Re = 150$, $Re^i = 450$) and Figure 5.14 ($Re = 200$, $Re^i = 600$), the axisymmetry is broken and the toroidal circulation (Hill's vortex) gives way to a much more complex internal circulation. These internal bifurcations also impact the near-interface external flow. The $X = 0$-plane view suggests that four circulations are taking place inside the drop. The intensity of these circulations increases with the Reynolds number as evidenced in cases

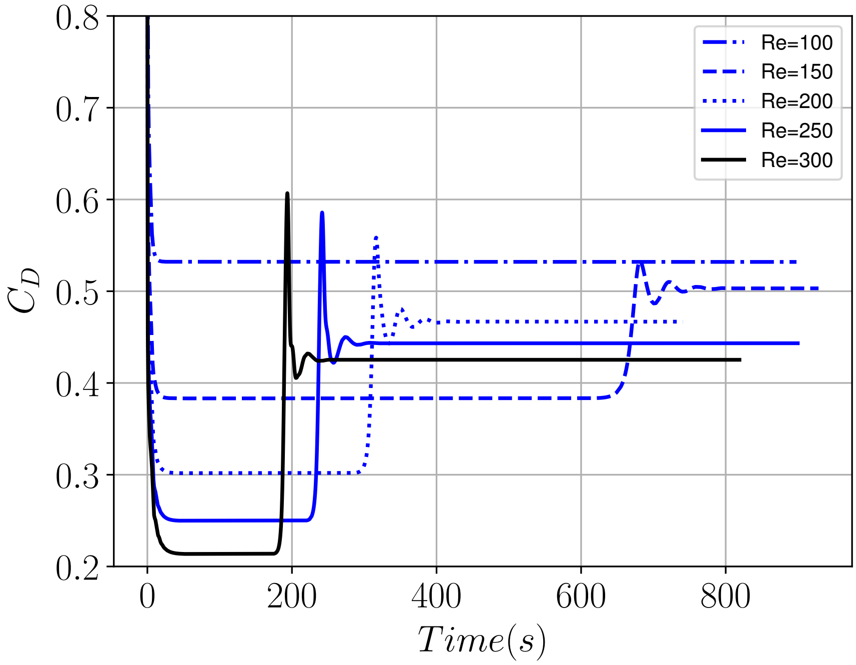

Figure 5.9: Time evolution of the drag coefficient: $\rho = 1.5$, $\mu^* = 0.5$.

$Re = 150$ and $Re = 200$. For $Re > 300$ and $Re^i = 900$, the flow shows an non-steady behaviour. Although this case will not be discussed in the manuscript, our findings are consistent with Edelmann et al. [2017] results. The slight rotation of the streamlines on plane $X = 0$ compared to the literature results is due to the Cartesian mesh used in Edelmann et al. [2017] as mentioned by the authors. Complementary mesh convergence study (see Figure 5.15) showed that the streamlines orientation at $X = 0$ does not rely on the mesh but are rather randomly fixed by the numerical model.

### 5.4.2 Influence of the Viscosity and density ratios

In this section, the connection between the internal Reynolds number $Re^i$ and the internal bifurcation is examined. For this purpose, the impacts of the density ratio and the viscosity ratio are investigated. Two different scenarios are considered for a given external Reynolds number. The density ratio is fixed to $\rho^* = 1.5$ in the first case, while $\mu^* = 0.5$ is imposed for the second case.
Given the relationship between $Re$ and $Re^i$ (i.e. $Re = (\rho^*/\mu^*)Re^i$), for the first case an increase of the viscosity ratio $\mu^*$ results in a direct decrease in the inner Reynolds number $Re^i$, while $Re^i$ increases as $\rho^*$ increases, in the second case. Figures 5.16 and 5.17 illustrate the two configurations for an external Reynolds number $Re = 200$.
Figure 5.16 depicts the $C_D$ evolution with $\mu^*$ while density ratio is fixed to $\rho^* = 1.5$. 2D-axi simulations and 3D simulations yield substantially the same value of $C_D$ for

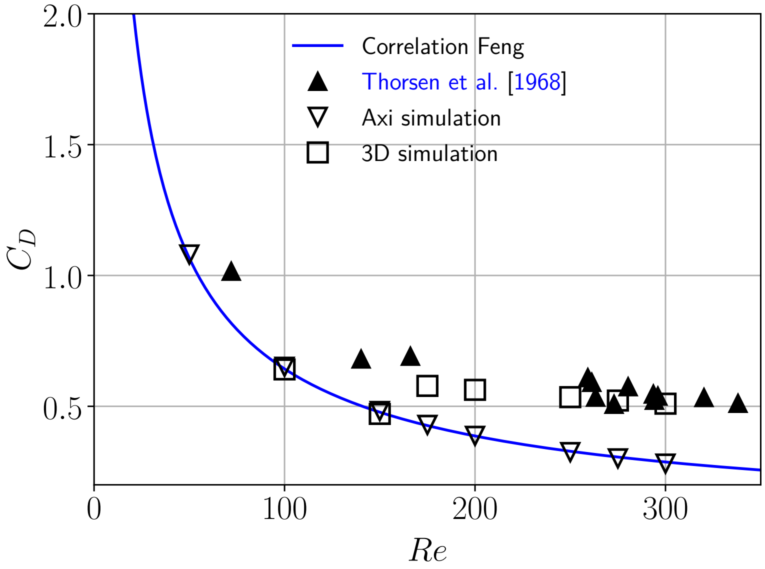

Figure 5.10: Evolution of the drag coefficient with $Re$ ($\rho^* = 2.5$, $\mu^* = 1$), experimental data: Methylene bromide drop in water Thorsen et al. [1968].

$1 \le \mu^* \le 2.5$ which corresponds to $Re^i \le 300$. However, as $0.25 < \mu^* \le 0.75$ (i.e. $400 \le Re^i < 1200$) discrepancies appear between 2D-axi and 3D simulations. It has been observed that for $\mu^* = 0.25$ (i.e. $Re^i = 1200$) no steady state is reached, and the drag coefficient keeps fluctuating. Correspondingly, Figure 5.18 displays internal and external streamlines in three planes of three different cases: $\mu^* = 0.5$ $\mu^* = 0.75$ and $\mu^* = 1$. Hill's recirculation takes place in the latter case (i.e. $Re^i = 300$) where the flow is axisymmetric while bifurcations initiate when $Re^i \ge 400$. Therefore, the observed deviation in the drag coefficient between 2D-axi and 3D simulation (see Figures 5.10 and 5.11) relies primarily on the presence of internal bifurcations.

Regarding Figure 5.17, the considered viscosity ratio is fixed to $\mu^* = 0.5$. In their axisymmetric numerical study, Feng and Michaelides [2001a] stated that the density ratio has nearly no influence on the drag which is not confirmed with the present results. As $\rho^* \ge 1$ (i.e. $Re^i \ge 400$) a deviation takes place between 2D-axi and 3D simulations. At $\rho^* = 3$ which correspond to $Re^i = 1200$, the simulation predicts unsteady behaviour of the drag coefficient and internal/external streamlines. Figure 5.19 shows streamlines for three cases, $\rho^* = 0.5$, $\rho^* = 1$ and $\rho^* = 1.5$. Again, a critical value of internal Reynolds number $Re^i \approx 400$ (i.e. $\rho^* = 1$) characterizes the transition between an axisymmetric streamline and internal bifurcations. Besides what has been stated in the previous sections, where viscosity and density ratios are kept constant (i.e. $\mu^* = 0.5$, $\rho^* = 1.5$) while varying $Re$, it becomes clear that internal Reynolds number is the main indicator of internal circulation mode. This results has been observed for the range of

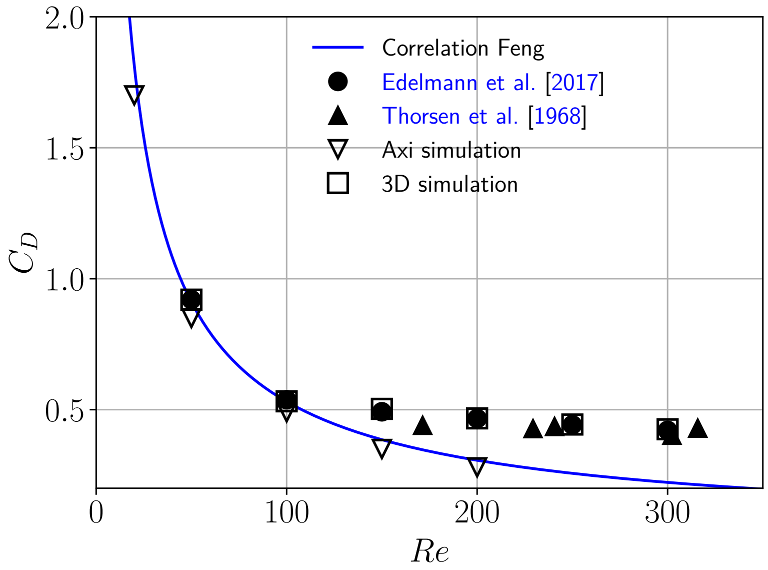

Figure 5.11: Evolution of the drag coefficient with $Re$ ($\rho^* = 1.5$, $\mu^* = 0.5$), experimental data: Ethyl bromide drop in water Thorsen et al. [1968].

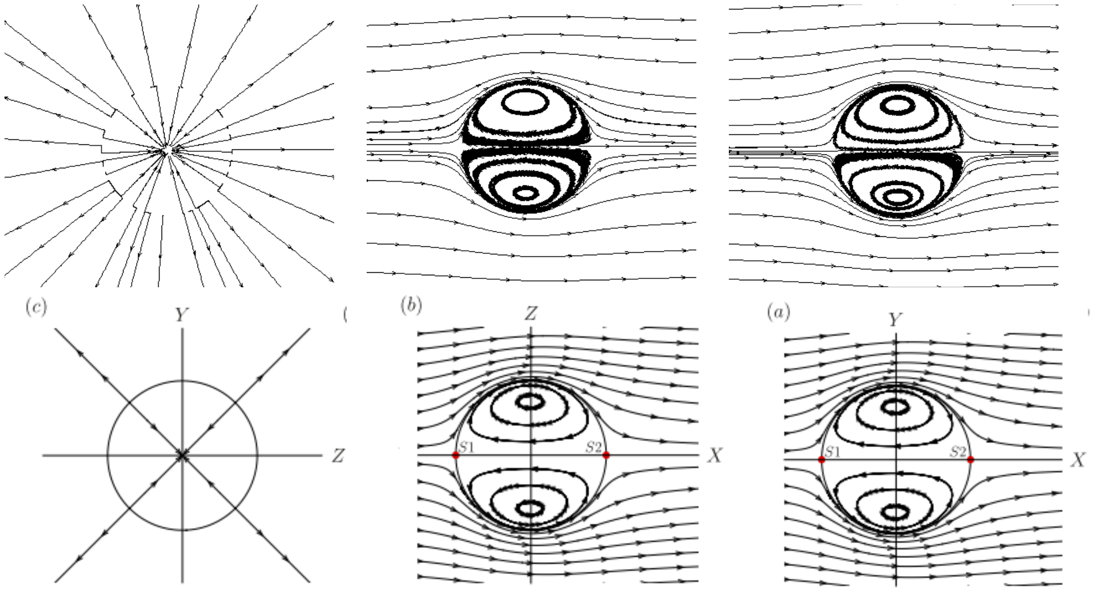

Figure 5.12: Streamlines: $Re = 100$, $\mu^* = 0.5$, $\rho^* = 1.5$ - top: Present work, bottom :Edelmann et al. [2017].

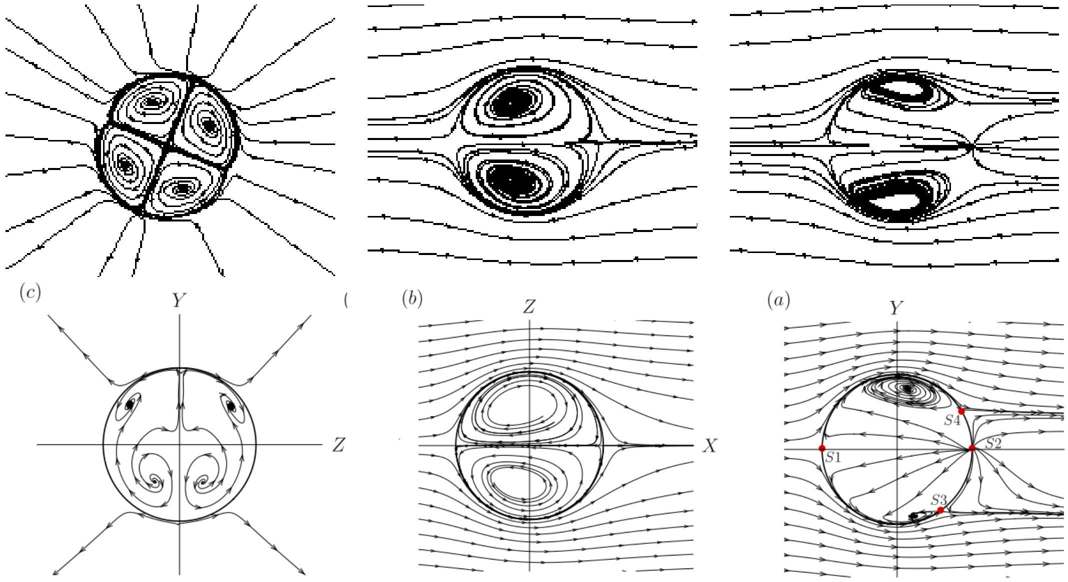

Figure 5.13: Streamlines: $Re = 150$, $\mu^* = 0.5$, $\rho^* = 1.5$ - top: Present work, bottom :Edelmann et al. [2017].

parameters $100 \leq Re \leq 250$, $0.25 \leq \mu^* \leq 2.5$ and $0.25 \leq \mu^* \leq 3$. Such results maybe not relevant if extrapolated to situations where the external flow has stronger influence on the internal recirculation, for example for smaller value of $\mu^*$.

In chapter 4, axisymmetric simulations are presented for $Re = 100$ with a range of viscosity ratios $0.25 \leq \mu^* \leq 5$, while the density ratio being set to unity since it has no significant effect in 2D-axi simulations. In 3D simulations, $\rho^*$ appears to have a significant effect on the droplet hydrodynamic. Indeed, for $\rho^* = 2$ and $\mu^* = 0.5$ (i.e. $R^i = 400$), internal bifurcations break out that impact significantly the flow inside and outside the droplet (see Table 5.3). In addition, for $\rho^* = 1.5$ and $\mu^* = 0.25$, a clear disparity is evidenced between 2D-axi and 3D simulations (see Table 5.4). Note that the development of this 3D flow inside the drop also induced a 3D force on the drop since the flow loose its axisymmetry. Therefore, results from Chapter 4 must be treated with caution especially for cases where $Re^i > 400$. We have checked the magnitude of the induced transverse force and compared it to the drag force. For all the cases considered the value of the transverse of lift force remains several order of magnitude smaller than the drag force so that it is not expected to influence the drop trajectory.

## 5.5 Mass transfer

In this section, the influence of the different modes of internal circulation on the mass transfer inside the drop (internal problem) and across the droplet interface (conjugate problem) will be discussed. Only hydrodynamic steady states are considered. For cases

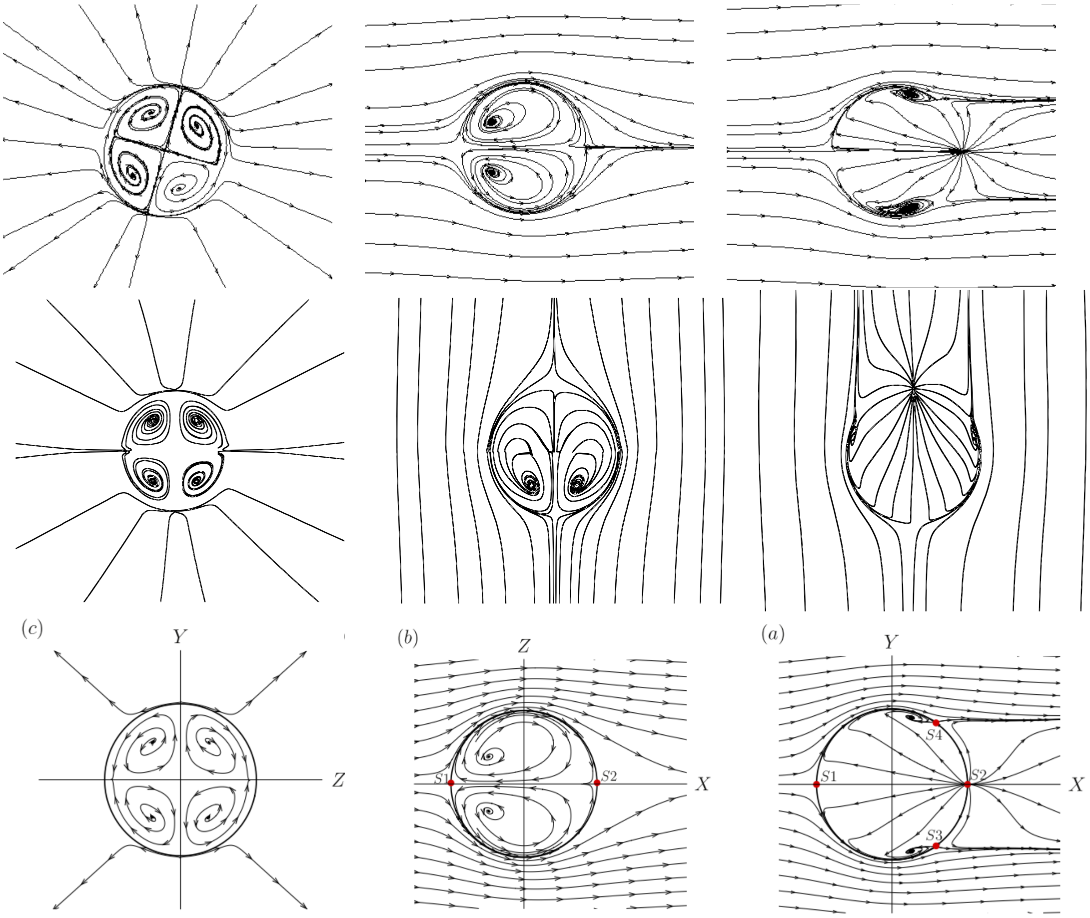

Figure 5.14: Streamlines: $Re = 200$, $\mu^* = 0.5$, $\rho^* = 1.5$ - top: present work (initialization of velocity parallel to the axis), middle: recent work (velocity perpendicular to the axis), bottom: Edelmann et al. [2017].

| $\rho^*$ | 0.25 | 0.5 | 0.75 | 1 | 1.5 | 2 | 2.5 | 3 |
|---|---|---|---|---|---|---|---|---|
| $Re^i$ | 50 | 100 | 150 | 200 | 300 | 400 | 500 | 600 |
| Present work (Axi) | 0.547 | 0.544 | 0.543 | 0.541 | 0.54 | 0.539 | 0.539 | 0.539 |
| Present work (3D) | 0.529 | 0.537 | 0.535 | 0.534 | 0.532 | 0.764 | 0.671 | 0.701 |

Table 5.3: Drag coefficient: comparison between 2D-axi and 3D ($Re = 100$, $\mu^* = 0.5$).

with a Hill's vortex-like internal flow a fluid particle inside a drop always stays on a two-dimensional (see Figure 5.12), nearly ellipsoidal path. However, when that cylindrical symmetry is broken, a fluid particle inside a drop has a much more complicated, three dimensional path (see Figure 5.14). Thus, at least for high Peclet numbers, it is expected

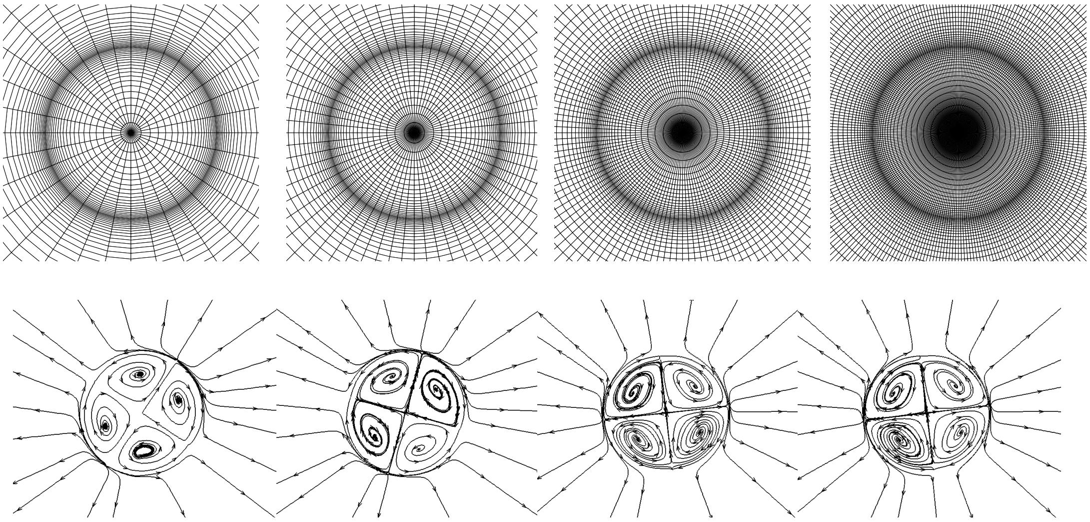

Figure 5.15: Mesh & Streamlines: effect on the development of the 3D internal flow ($Re = 200$, $\mu^* = 0.5$, $\rho^* = 1.5$): From left to right $nz = 32, 64, 128, 256$. We can observe that the symmetry plane is clearly not related to the mesh structure.

| $\mu^*$ | 0.25 | 0.375 | 0.5 | 0.75 | 1 | 1.5 | 2 |
|---|---|---|---|---|---|---|---|
| $Re^i$ | 600 | 400 | 300 | 200 | 150 | 100 | 75 |
| Present work (Axi) | 0.465 | 0.504 | 0.54 | 0.602 | 0.655 | 0.737 | 0.797 |
| Present work (3D) | 0.569 | 0.496 | 0.532 | 0.593 | 0.646 | 0.728 | - |

Table 5.4: Drag coefficient: comparison between 2D-axi and 3D ($Re = 100$, $\rho^* = 1.5$).

that the mode of internal circulation has a major influence on the internal transfer for internal problem and global transfer of a conjugate transfer. In the following, we concentrate at first step on the internal problem of mass transfer, conjugate mass transfer is discussed afterwards. Following the methodology explained above, for each configuration, both 2D-axi and 3D simulations are performed.

## 5.5.1 Internal Mass transfer

In this section we assume that the main transfer resistance is located inside the drop. Subsequently, concentration at the interface $C_s$ is set to a fixed value. Figure 5.20 depicts the time evolution predicted by 2D-axi and 3D simulations for the internal Sherwood number, at different internal Peclet numbers, and for a high Reynolds flow $Re = 200$, with $\mu^* = 0.5$ and $\rho^* = 1.5$. While in both cases the Sherwood numbers are nearly identical at small times, the longer term evolution eventually depends on the internal Peclet number. For 2D-axi simulations, the Sherwood number of all reported

$Pe^i$ converge toward a steady value. This latter saturates to a value close to 20 as $Pe^i$ increases. In such 2D-axi configuration, streamlines are close to a Hill's vortex structure which makes the transfer diffusive-limited at high $Pe^i$.
However, in a 3D simulation, as it has been reported in Figure 5.14, internal bifurcation is obtained for the studied configuration. Interestingly, the Sherwood number does not converge to a constant value when $Pe^i$ is increased. In fact, the symmetry breaking improves the mixing inside the droplet, so that for an increasing internal Peclet number $Pe^i$ the stabilized value of the internal Sherwood number increases accordingly. The steady internal Sherwood number predicted by the 2D-axi simulations significantly underpredicts the rate at which mass transfer occurs (40% for $Pe = 1000$). Table 5.5 points out the discrepancies between the steady Sherwood numbers predicted by the 2D-axi and 3D simulations, for different Peclet numbers.
Our 3D results are consistent with the value reported by Edelmann et al. [2017]. Figure 5.21 illustrates the evolution of $Sh^I$ in terms of the previously defined $Pe^i_{eff}$ (see Eq 4.2.3). The $Sh^I$ given by 3D simulations seems to overtake the limit at which $Sh^I$ stagnates in 2D-axi simulations. The deviation can reach 70% for $Pe^i = 2400$. The same comparison has been performed considering $Re = 100$ and no significant difference has been observed between the two approaches since the velocity field are almost identical between 2D-axi and 3D simulations.

| $Pe^e$ | 50 | 100 | 163 | 500 | 1000 | 2400 |
|---|---|---|---|---|---|---|
| present work (Axi) | 14.9 | 17.18 | 17.9 | 18.43 | 18.5 | 18.53 |
| Present work (3D) | 9.85 | 12.24 | 13.84 | 20.37 | 31.49 | 63.27 |
| Edelmann et al. [2017] | - | - | 13.99 | - | - | 63.97 |

Table 5.5: Asymptotic Sherwood number for internal problem $Sh^I$: $Re = 200$, $\mu^* = 0.5$, $\rho^* = 1.5$.

The spatial distribution of the solute concentration is also significantly affected by the droplet hydrodynamics. Figure 5.22 illustrates the instantaneous spatial concentration, where $\overline{C^i} = 0.5$, in the case of a high and a moderate inner Reynolds flow, at $Pe = 1000$. Unlike the cylindrical symmetry of the concentration field observed for $Re = 100$ ($Re^i = 300$), at high Reynolds $Re = 200$ ($Re^i = 600$), where internal/external bifurcations take place, spatial distribution of the solute concentration inside and outside the drop exhibit non symmetric structure which enhances internal mixing, and therefore increases the internal Sherwood number value. For low internal Peclet number (here $Pe^i = 50$), even in a high inner Reynolds configuration, the solute spatial distribution shows a quasi-spherical symmetry which means that the transfer is mainly diffusive (see Figure 5.23).

### 5.5.2 Conjugate Mass transfer

In the case of a conjugate problem, no a priori assumption is made on the transfer resistance. Solute transport equations are solved inside and outside the droplet. In this

section the diffusivity ratio $D^*$ and equilibrium coefficient $k$ are set to $D^* = 1$ and $k = 1$. Again, each configuration has been addressed using both 2D-axi and 3D approach. This latter is particularly interesting in high inner Reynolds number configurations where 3D structures develop inside the drop and break the velocity field symmetry inside and outside the drop. Figure 5.24 compares the time evolutions of the global Sherwood number given by 2D-axi and 3D simulations for ($\mu^* = 0.5$, $\rho^* = 1.5$) at high Reynolds number $Re = 200$ (i.e. $Re^i = 600$).
The 3D simulations exhibit the same trends as the 2D-axi approach: the time evolution of the Sherwood number reaches a steady value, the magnitude of which increases as expected with the internal Peclet number (see Table 5.6). It is interesting to note that at high internal Peclet number, $Pe^i \geq 1000$ (i.e. $Pe \geq 1000$), the deviation between steady global Sherwood number given by 3D simulation and the one predicted by 2D-axi simulation increases (see Figure 5.24). This is due essentially to the internal 3D structures that optimizes the mixing inside the drop and keep sharp concentration gradients at the interface. However, 2D-axi results seem to overestimate the steady Sherwood number for low Peclet numbers.

| $Pe^e$ | 50 | 100 | 163 | 500 | 1000 | 2400 |
|---|---|---|---|---|---|---|
| present work (Axi) | 4.42 | 6.17 | 7.57 | 10.87 | 12.66 | 14.48 |
| Present work (3D) | 4.01 | 5.26 | 6.44 | 10.4 | 14.48 | 23.94 |

Table 5.6: Asymptotic global Sherwood number (Conjugate problem): $Re = 200$, $\mu^* = 0.5$, $\rho^* = 1.5$, $D^* = 1$, $k = 1$.

The spatial distribution of the solute concentration is also affected by the flow structure. Figure 5.27 illustrates an instantaneous capture of the solute distribution after half the solute has passed across the interface ($\overline{C^i} = 0.5$) in a high internal Peclet configurations $Pe^i = 1000$. With regards to the case $Re = 100$, the concentration distribution is identical to the one reported by 2D-axi simulations. However, in the high inner Reynolds case (i.e. $Re = 200$ and $Re^i = 600$), the concentration distribution seems to agree with the streamlines structure (see Figure 5.14). On the plan $X = 0$, an additional convection is ensured by the four recirculations structure which drives the solute from the droplet vicinity to the interface.

## 5.6 Conclusions

In this chapter, 2D-axi and 3D direct numerical simulations of the Navier-Stokes and solute transport equations inside and outside a spherical droplet have been carried out and compared. Three dimensional simulations results highlighted the limits of the axisymmetry assumption at high Re numbers. This assumption is however widely used in literature. Our results evidenced the presence of internal bifurcations which depends primarily on the inner Reynolds number, which is consistent with the recent findings of Edelmann et al. [2017]. The error made on the drag coefficient calculation in literature

can reach up to 100% with high internal Reynolds correlation.
This strong modification of the internal flow was moreover shown to alter significantly the spacial distribution of the solute in the droplet, for both internal or conjugate problems. For the internal problem, the difference between the internal Sherwood number $Sh^I$ between 2D-axi and 3D can attain 70% in high internal Peclet cases. For the conjugate problem, at high $Pe^e$ configuration the difference increase to 40%. These results outline the relevance of developing accurate modelling for the transfer in cases where this 3D bifurcation appears. A parametric study as performed in the previous chapter should be conducted with 3D simulations.

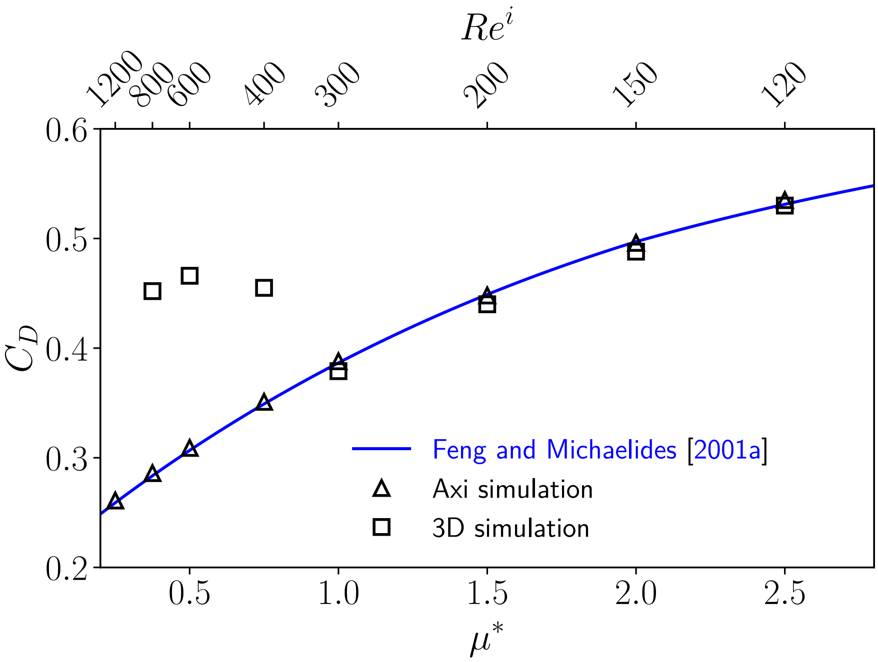

Figure 5.16: Drag coefficient evolution with viscosity ratio for $Re = 200$ and $\rho^* = 1.5$.

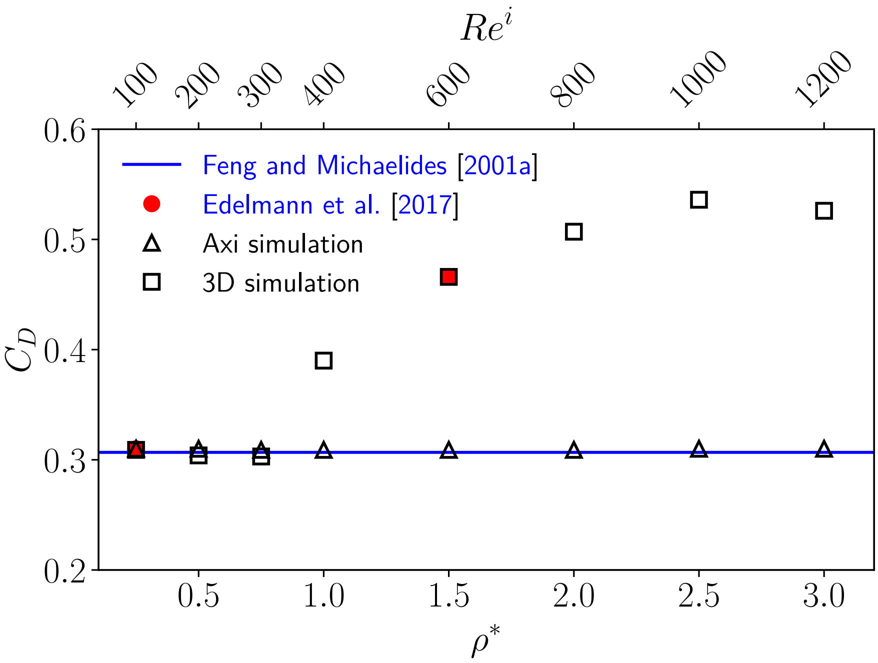

Figure 5.17: Drag coefficient evolution with density ratio for $Re = 200$ and $\mu^* = 0.5$.

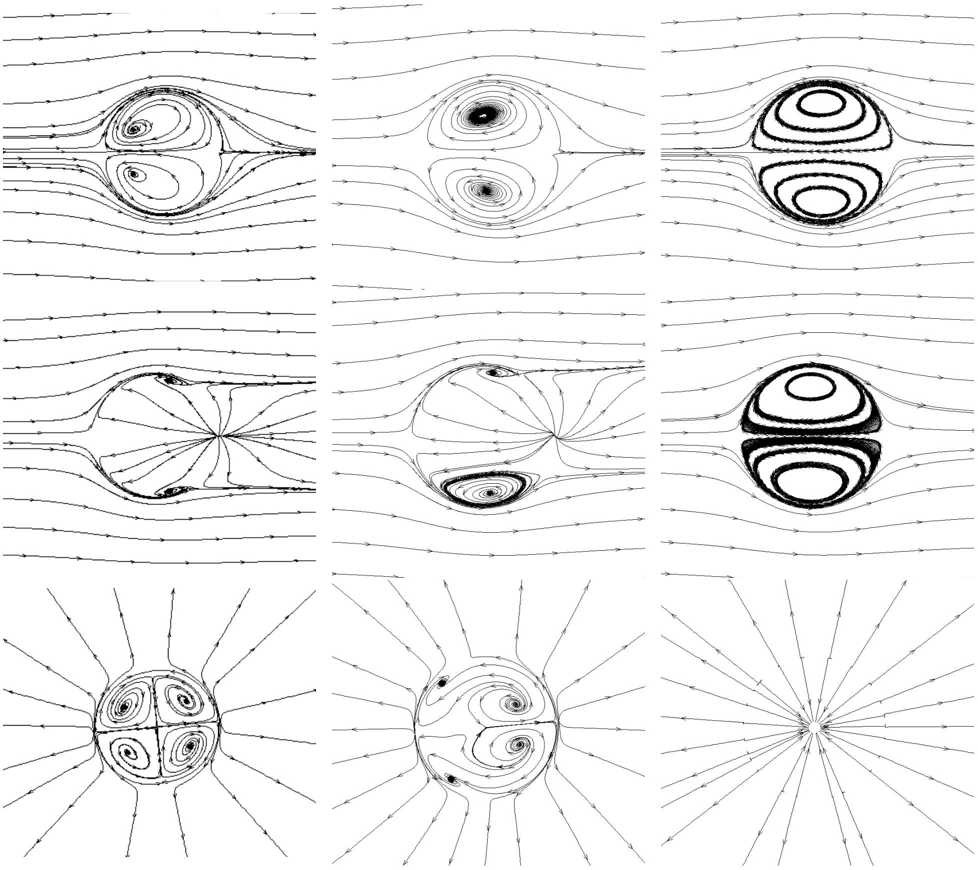

Figure 5.18: Streamlines ($Re = 200$, $\rho^* = 1.5$): from left to right $\mu^* = 0.5, 0.75, 1$. From top to bottom: XY, XZ, YZ.

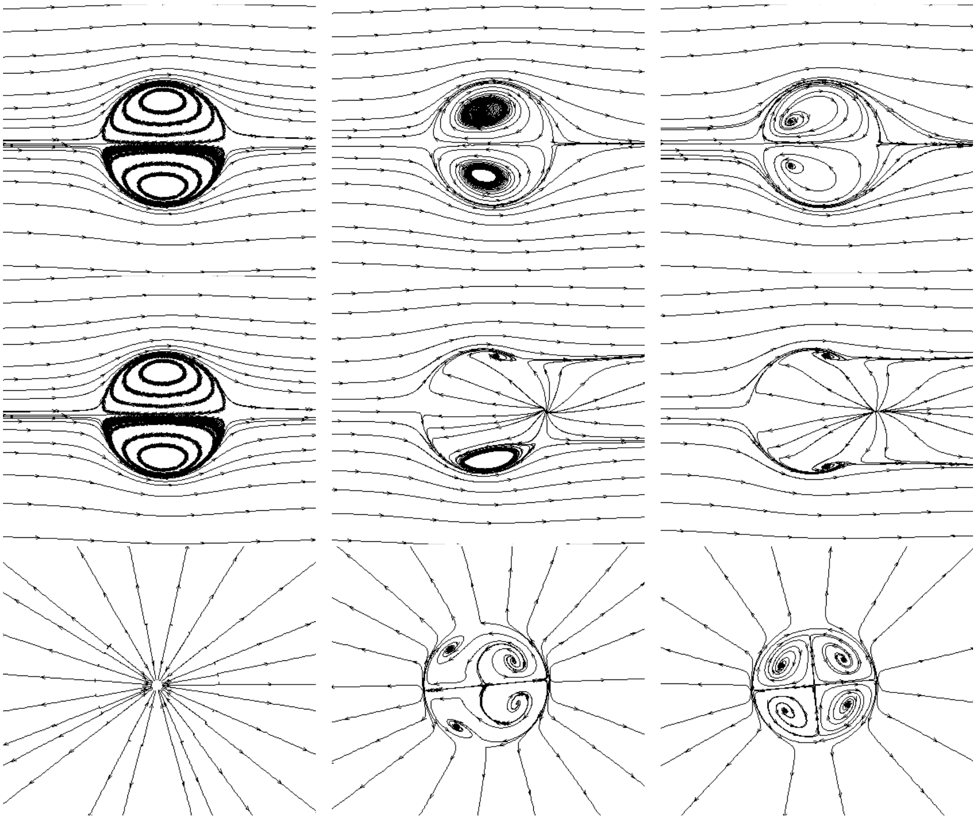

Figure 5.19: Streamlines ($Re = 200$, $\mu^* = 0.5$): from left to right $\rho^* = 0.5, 1, 1.5$. From top to bottom: $XY$, $XZ$, $YZ$.

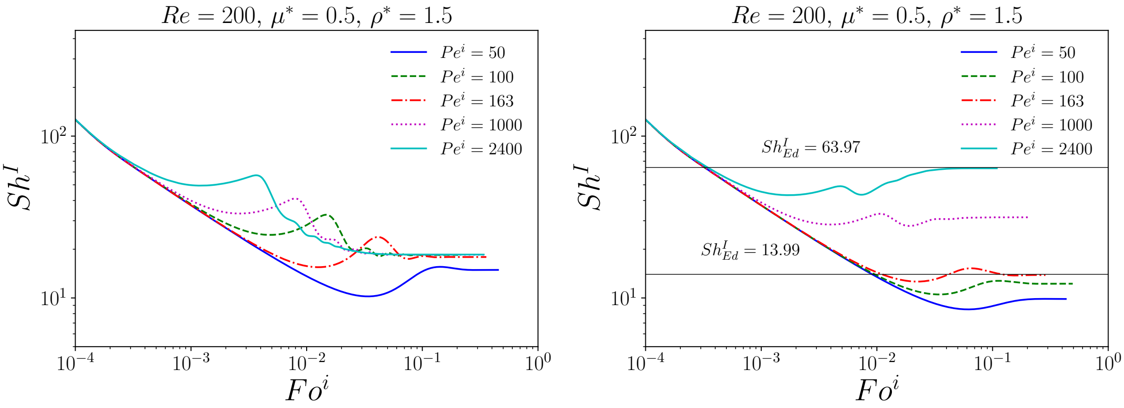

Figure 5.20: Temporal evolution of internal Sherwood number: ($Re = 200$, $\mu^* = 0.5$, $\rho^* = 1.5$), 2D-axi simulation (left), 3D simulation (right), $Sh^I_{Ed}$ is the Sherwood number reported by Edelmann et al. [2017].

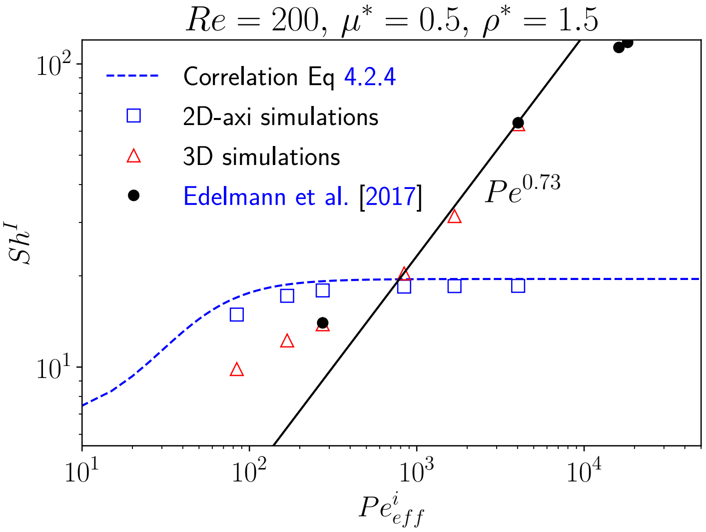

Figure 5.21: Evolution of steady $Sh^I$ with $Pe^i_{eff}$ ($Re = 200$, $\rho = 1.5$, $\mu^* = 0.5$): a comparison between 2D-axi and 3D simulations.

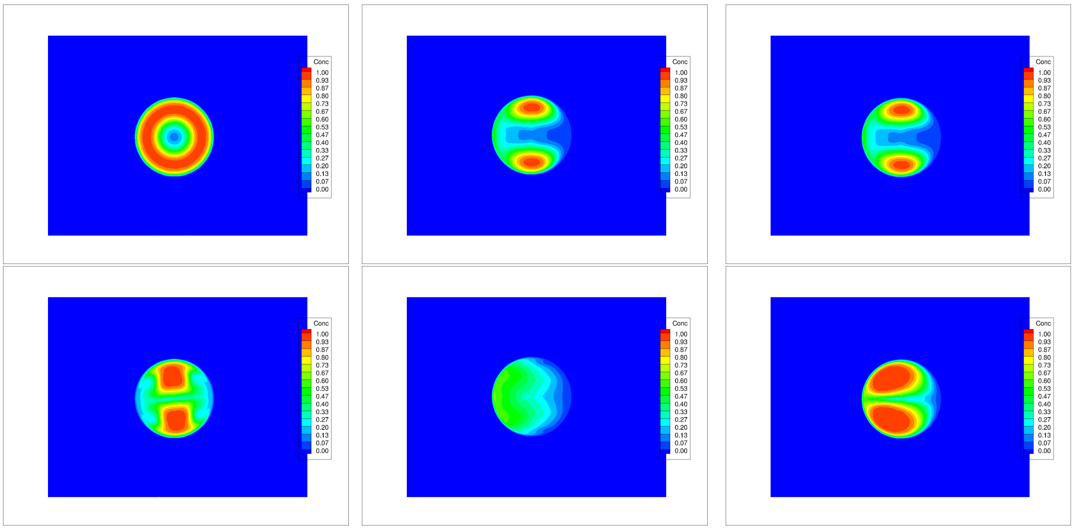

Figure 5.22: Concentration distribution (Internal problem): $\overline{C^i} = 0.5$, $\mu^* = 0.5$, $\rho^* = 1.5$, $Pe = 1000$, top: $Re = 100$, bottom: $Re = 200$, from left to right: $X = 0$, $Y = 0$, $Z = 0$.

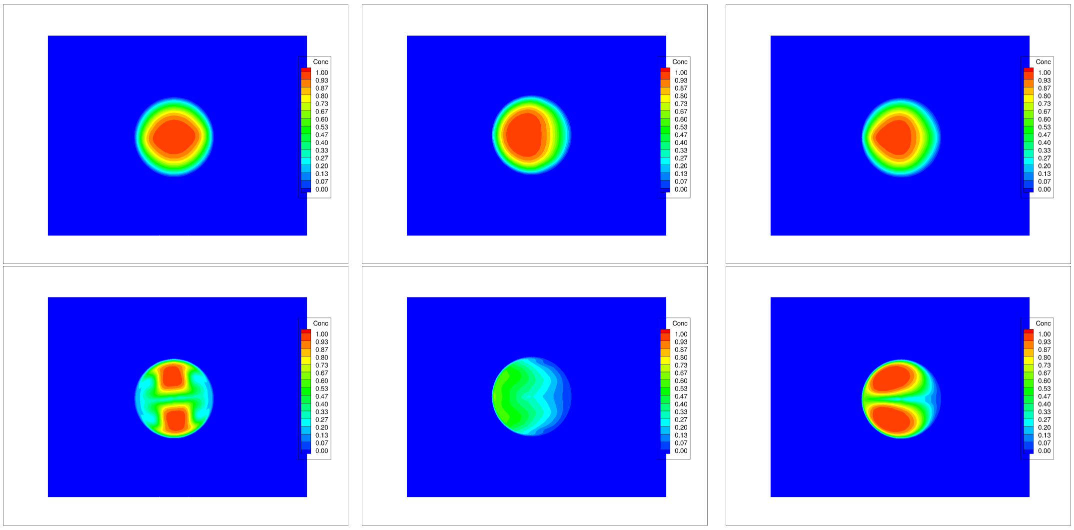

Figure 5.23: Concentration distribution evolution (Internal problem): $Re = 200$, $\mu^* = 0.5$, $\rho^* = 1.5$, $Pe = 50$, from left to right: $X = 0$, $Y = 0$, $Z = 0$.

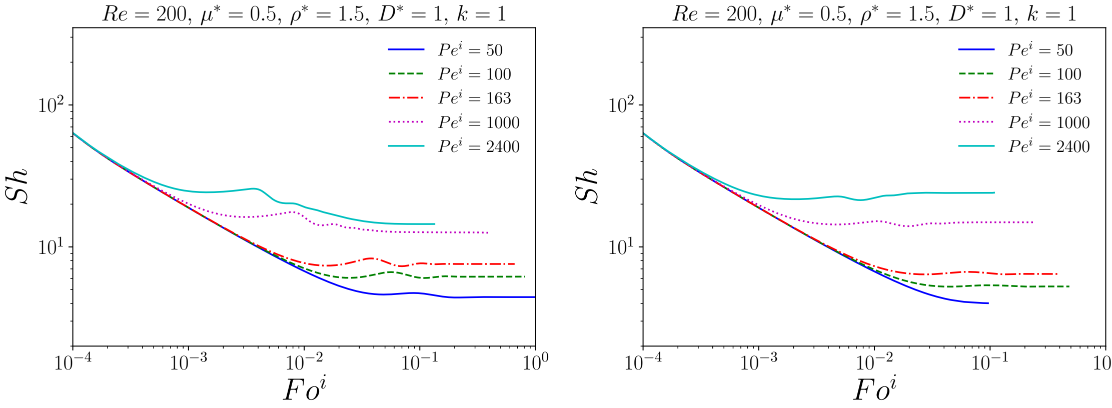

Figure 5.24: Time evolution of the global Sherwood number: ($Re = 200$, $\mu^* = 0.5$, $\rho^* = 1.5$), 2D simulation (left), 3D simulation (right).

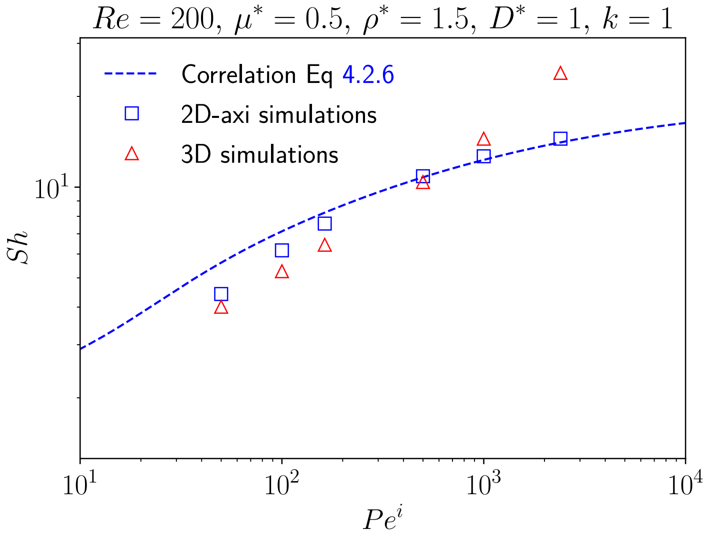

Figure 5.25: Evolution of steady global Sherwood number $Sh$ with $Pe^i$ ($Re = 200$, $\rho = 1.5$, $\mu^* = 0.5$, $D^* = 1$, $k = 1$): comparison between 2D-axi and 3D simulation.

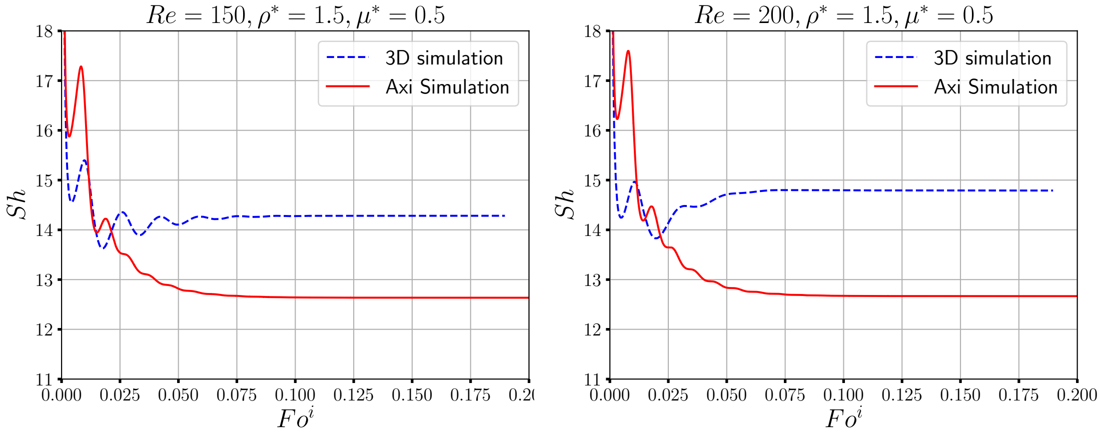

Figure 5.26: Global Sherwood temporal evolution [$Pe = 1000$, $D^* = 1$, $k = 1$]: $Re = 150$ (left), $Re = 200$ (right).

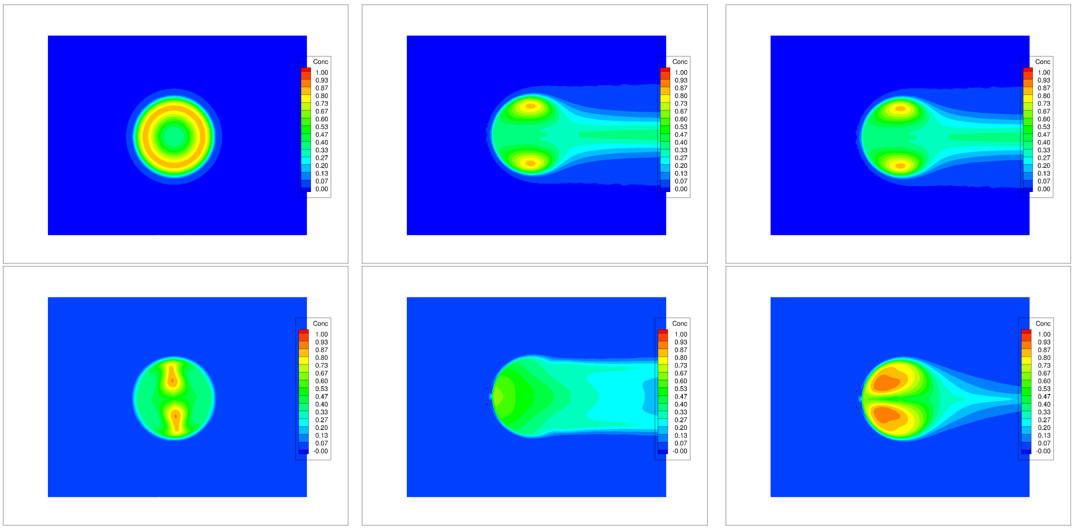

Figure 5.27: Instantaneous solute concentration distribution: $Re = 100$ (top) and $Re = 200$ (bottom), from left to right: $X = 0$, $Y = 0$, $Z = 0$. ($\overline{C_d} = 0.5$, $\rho^* = 1.5$, $\mu^* = 0.5$, $D^* = 1$, $k = 1$).

# Chapter 6

# Conclusion & Outlooks

## Contents

## 6.1 Conclusions

This work has been dedicated to study, by means of direct numerical simulations, the hydrodynamics of a spherical liquid droplet placed in a uniform flow of an outer immiscible liquid phase. Various configurations have been considered where physical properties of both phases and operating conditions changed. In such a hydrodynamic configuration, a solute transfer from the droplet to the continuous phase has been considered, investigating the impact of the relevant dimensionless parameters. The purpose of the study was to predict the evolution of the global Sherwood number, a dimensionless quantity that characterizes the solute transfer rate, as a function of all physical parameters. Such a correlation is of great interest for liquid-liquid extraction processes, such as those used for the treatment of nuclear fuel.

With regards to the industrial context, a succinct description of the PUREX process has been presented where the challenges of liquid-liquid extraction were raised. The intensive look into literature allowed to outline and describe the two aspects of the present study especially the coupling between hydrodynamics and mass transfer. Concerning the hydrodynamics, the droplet shape in an immiscible phase is fully directed by the Clift diagram, which, using three dimensionless numbers: Reynolds, Eötv̈os and Morton numbers, allows to predict the shape of a droplet under given hydrodynamic configuration. Under operating conditions of CEA, droplets with diameter lower than $2mm$ generally adopt a spherical shape in extraction apparatus. For the mass transfer aspect, an overview of literature reveals very limited contributions to the conjugate mass transfer at the scale of a droplet which motivate our study.

Considering physical assumptions, a mathematical model has been developed to describe both hydrodynamics and mass transfer for a single droplet in an unbounded fluid domain. The dimensionless partial differential equations of this model have been fully solved using JADIM code with a body fitted method. The features of the code had to be adapted to resolve Navier-Stokes equation and solute transport equations both outside and inside the drop. New hydrodynamic and the mass transfer coupling conditions at the interface have been implemented during this PhD. Validation tests showed excellent agreement with previous studies for both the hydrodynamic part (drag coefficient, streamlines and Hill's vortices, interface quantities) and for the transfer process (the time evolution of the Sherwood number, local concentration, solute spatial distribution).

For a regime corresponding to a moderate Reynolds number, we validated correlations related to particle/bubble to propose correlations for the drag coefficient and separation angle valid in the case of a droplet, and only based on physical arguments. The appearance of an external recirculation depends only on the values of the external Reynolds number and the viscosity ratio, while in 2D-axi simulations the density ratio seems to have no effect on the drag coefficient nor the droplet hydrodynamics.

A schematic map developed in this work highlights the conditions under which the external recirculation occurs. For conjugate mass transfer, a detailed analysis has been conducted to illustrate the relationship between internal and external problem, that are frequently addressed in literature, and the conjugate mass transfer. For $k\sqrt{D^*} << 1$, either fixing $k$ and decreasing $D^*$ or vice versa, a clear convergence of the internal Sherwood $Sh^i$ to the value typical of the internal problem, $Sh^I$, was evidenced for every $Pe^i$ situation ($k$ and $D^*$ play similar roles). However, for $k\sqrt{D^*} >> 1$, the partition coefficient blurs the effect of $D^*$. In fact, for high $D^*$, a deviation of around 50% was highlighted between $Sh^e$ and $Sh^E$ for low external Peclet number (thermodynamics indeed fully controls the physics of the transfer in this case, as an increase in $k$ allows to fill the gap between $Sh^e$ and $Sh^E$). On the other hand, for high $k$, $Sh^e$ converges rapidly to the corresponding $Sh^E$ value for almost all values of $Pe^e$ (the diffusivity ratio has no significant influence on the transfer in this case). The conclusions have been extended to other hydrodynamic configuration.

Using literature results of $Sh^I$ and $Sh^E$, along with the rule of additivity of the transfer resistances, the global Sherwood number obtained by DNS, $Sh_{sim}$, has been compared with the one predicted by the correlation, $Sh_{corr}$. This allowed to test the validity of the correlation. For a given $k = 1$ and internal Peclet numbers larger than 100, good agreement is observed between simulation results and correlation. With $D^* = 1$, high $k$ configurations give good results for all $Pe^i$ values, satisfactory results have been found for other values of $k$ as $Pe^i > 100$. In low internal Peclet cases however, a deviation is revealed between simulations and correlation.

The last part of the manuscript has been dedicated to 3D simulations to investigate the limits of axisymmetry assumption. From low to moderate internal Reynolds number flow, it has been proved that 3D simulations and 2D-axi approach yield basically the same hydrodynamics and solute transfer physics. Results have shown that internal Reynolds number defined unequivocally the circulation mode inside the drop for a moderate external Reynolds number. For values of internal Reynolds number larger than 400, the axysmmetric behaviour of the flow is lost while complex internal bifurcations develop inside the drop. These latters impact as well the outer flow close to the interface. The internal flow circulation modes alter significantly the evolution of the drag coefficient which seem to reach a plateau value beyond the critical value of Reynolds number. The adopted strategy of comparing 2D-axi and 3D simulations allowed to define the error made when forcing the axisymmetry condition. The impact of these circulations mode on mass transfer is also significant. For high internal Peclet number, the symmetry breaking enhances the internal mixing, therefore the obtained global Sherwood number is larger then the one of 2D-axi simulations. However, in low internal Peclet regime, the 2D-axi simulations seem to underestimates the global Sherwood number given by the 3D simulations. The results of this part, allow to reconsider the results of numerical studies enforcing the axismmetry condition in high internal Reynolds number flow.

## 6.2 Outlooks

Our study may covers a large portion of the Clift diagram where the drop attain a spherical shape. However, increasing in the Reynolds number or decreasing surface tension may lead to a deformed droplets (a slight deviation from the spherical shape may lead to spheroid with an ellipsoidal shape). Other than numerical studies with VOF method, no numerical study have tackled the topic of a slightly deformed droplet. Such a deformation would impact both the hydrodynamics and the mass transfer. During our study, an ellipsoidal mesh have been generated where the external mesh is based on the analytical solution of a potential flow around an ellipsoidal cylinder, and the internal mesh is an extension of potential lines at the interface in prolate spheroidal coordinates (see Figure 6.1). Some difficulties have been encountered to obtain an accurate internal flow since, due to the mesh structure, one of the boundary conditions is located within the computational domain. These preliminary developments will allow to extend the characterisation of the Sherwood number evolution to slightly deformed droplets, thus covering the wider spectrum of droplets shape encountered in an extraction column.

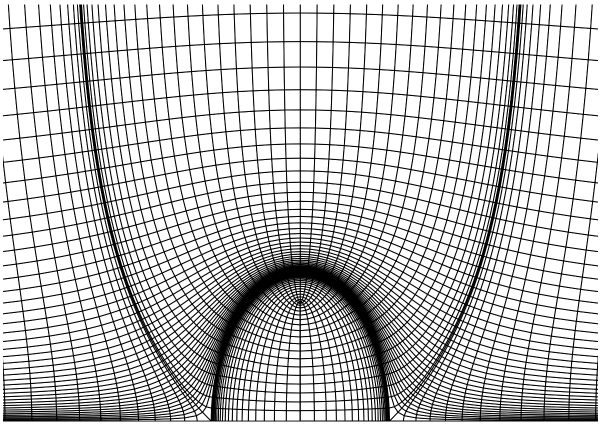

Figure 6.1: Ellipsoidal mesh which could be used by JADIM - aspect ratio $b/a = 0.6$.

The developed numerical tool opens up several research avenues that may be exploited to study various hydrodynamic and solute transfer configurations related to a drop.

Droplets in an extraction column undergo various obstacles and their movement is not usually uniform. Stirring and interaction with walls and other droplets may deviate their motion. Besides, the carrier phase may also experience a sheared flow which changes completely the hydrodynamic configuration. Validation tests of the hydrodynamics of a droplet placed in simple shear flow and an extensional flow have been performed. Only transfer validation have been carried out in an extensional flow case, but we couldn't conclude the study. Under such conditions, both the hydrodynamics and mass transfer change completely from a uniform flow case. The physics of transfer is intricate in a simple shear flow where, depending on the operating conditions, streamlines may be closed or open which lead to a drastic change in the Sherwood number.

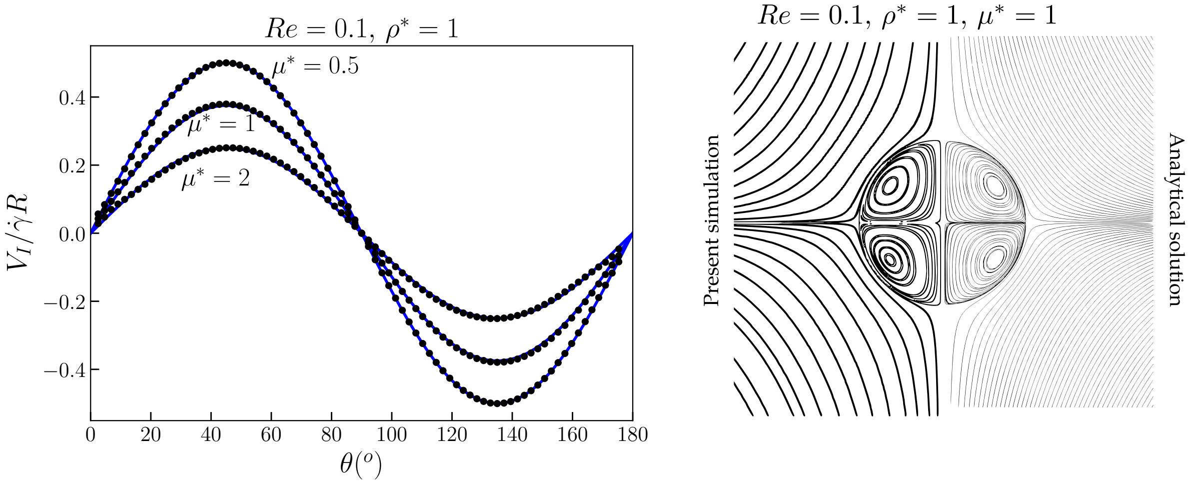

Figure 6.2: Droplet in a simple extensional Stokes flow - Left: Interface velocity for different $\mu^*$ (symbols: present simulation, blue line: analytical solution Gary Leal [1993]. Right: Comparison of streamlines between present simulation and analytical solution by Gary Leal [1993].

The single droplet case study is a fundamental start toward complex situations, since in an extraction column, droplet usually cannot be considered in an unbounded medium given the neighbouring droplets. The study of the interaction between two distant droplets in a uniform flow might be very interesting. No study to our knowledge have considered such configuration unlike the bubble case where the impact of the relative position between two bubbles on the drag and lift coefficient is studied. Such a study would permit to quantify the influence of neighbouring droplets on the solute transfer and especially derive the conditions under which a droplet may be assumed in a unbounded medium.

Throughout the whole study, physical properties were assumed to be constant which allowed us to resolve hydrodynamics and solute transport separately. This assumption is possibly not valid in some processes where hydrodynamics properties, such as the viscosity or density, may depend on the solute concentration (viscosity increases with solute concentration). Thus, separated resolutions are no longer valid: hydrodynamics

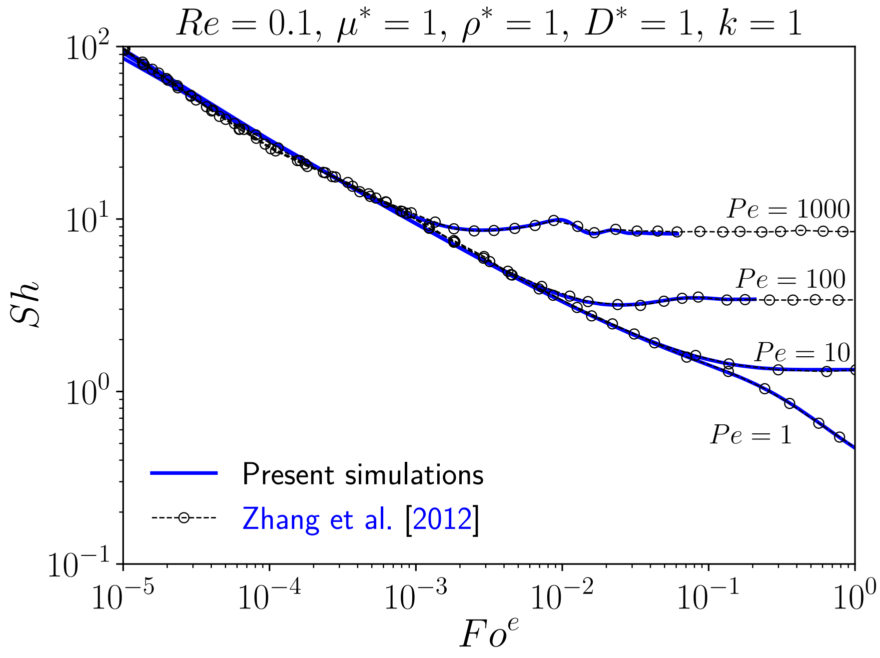

| $Pe$ | 1 | 50 | 100 | 500 | 1000 |
|---|---|---|---|---|---|
| Present simulations | 0.308 | 2.464 | 3.042 | 6.71 | 8.244 |
| Zhang et al. [2012] | 0.306 | 2.452 | 3.401 | 6.628 | 8.369 |

Figure 6.3: Conjugate mass transfer from a spherical droplet in a simple extensional Stokes flow - Left: Time evolution of the global Sherwood number $Sh$ for different $Pe$. Right: Comparison of the steady Sherwood for different $Pe$ with values by Zhang et al. [2012] ($Re = 0.1$, $\mu^* = 1$, $\rho^* = 1$, $k = 1$, $D^* = 1$).

and mass transfer must be resolved simultaneously which might arise some numerical problems of stability. It is not guaranteed that the Sherwood number converges to a well defined steady value in such cases. No study to our knowledge has focused on such a situation other than the Marangoni convection.

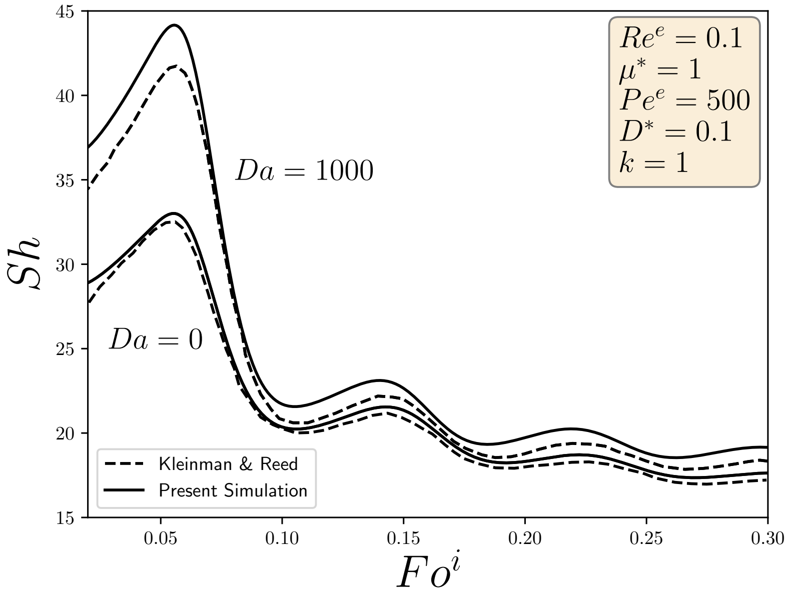

Figure 6.4: Time evolution of Sherwood number: a first order external reaction has been implemented.

At last, in liquid-liquid extraction processes, a chemical reaction may intervene either inside or in the outer phase. Under such circumstance, another dimensionless number (Damköhler) is usually considered in the studies. Literature results have shown that chemical reaction can enhance the transfer rate, therefore increasing considerably the global Sherwood number. Most of the studies consider very limited hydrodynamic configurations (small Reynolds number). An investigation of Damköhler number influence on the Sherwood number may be of high interest to CEA's application where chemical kinetics has sometimes to be considered.

# Appendix A

# Appendix

## A.1 Droplet

| | | $Pe^e$ | | | | |
|---|---|---|---|---|---|---|
| $D^*$ | $\mu^*$ | 10 | 50 | 100 | 500 | 1000 |
| 0.1 | 0.25 | 8.097 | 13.96 | 15.297 | 16.9 | 17.276 |
| 0.1 | 0.5 | 7.961 | 13.631 | 15.081 | 16.799 | 17.199 |
| 0.1 | 1 | 7.1269 | 13.0698 | 14.723 | 16.635 | 17.074 |
| 0.1 | 2 | 6.474 | 12.163 | 14.158 | 16.404 | 16.897 |
| 0.1 | 4 | 5.912 | 10.796 | 13.253 | 16.111 | 16.68 |
| 0.1 | 5 | 5.7833 | 10.259 | 12.85 | 16.003 | 16.6049 |
| 0.25 | 0.25 | 4.075 | 8.812 | 11.181 | 14.893 | 15.818 |
| 0.25 | 0.5 | 3.942 | 8.385 | 10.742 | 14.646 | 15.631 |
| 0.25 | 1 | 3.788 | 7.7 | 10.058 | 14.248 | 15.327 |
| 0.25 | 2 | 3.652 | 6.897 | 9.122 | 13.679 | 14.89 |
| 0.25 | 4 | 3.588 | 6.088 | 8.004 | 12.947 | 14.343 |
| 0.25 | 5 | 3.537 | 5.8569 | 7.625 | 12.67 | 14.148 |
| 0.5 | 0.25 | 2.352 | 5.239 | 7.183 | 12.005 | 13.5947 |
| 0.5 | 0.5 | 2.2769 | 4.954 | 6.777 | 11.606 | 13.264 |
| 0.5 | 1 | 2.1818 | 4.588 | 6.21 | 10.9848 | 12.736 |
| 0.5 | 2 | 2.085 | 4.219 | 5.559 | 10.144 | 12.001 |
| 0.5 | 4 | 2.007 | 3.953 | 4.958 | 9.149 | 11.115 |
| 0.5 | 5 | 1.987 | 3.892 | 4.7969 | 8.804 | 10.808 |
| 1 | 0.25 | 1.288 | 3.007 | 4.137 | 8.237 | 10.213 |
| 1 | 0.5 | 1.238 | 2.873 | 3.898 | 7.8 | 9.771 |
| 1 | 1 | 1.175 | 2.711 | 3.593 | 7.161 | 9.1 |
| 1 | 2 | 1.112 | 2.562 | 3.292 | 6.377 | 8.234 |
| 1 | 4 | 1.063 | 2.454 | 3.077 | 5.576 | 7.2917 |
| 1 | 5 | 1.051 | 2.429 | 3.032 | 5.335 | 6.991 |
| 2 | 0.25 | 0.641 | 1.7118 | 2.322 | 4.893 | 6.544 |
| 2 | 0.5 | 0.607 | 1.6392 | 2.205 | 4.571 | 6.146 |
| 2 | 1 | 0.573 | 1.546 | 2.062 | 4.129 | 5.577 |
| 2 | 2 | 0.54 | 1.449 | 1.923 | 3.364 | 4.899 |
| 2 | 4 | 0.52 | 1.383 | 1.815 | 3.200 | 4.242 |
| 2 | 5 | 0.505 | 1.362 | 1.792 | 3.089 | 4.055 |
| 3 | 0.25 | 0.4246 | 1.208 | 1.652 | 3.466 | 4.758 |
| 3 | 0.5 | 0.406 | 1.1517 | 1.572 | 3.2289 | 4.4375 |
| 3 | 1 | 0.383 | 1.0788 | 1.47 | 2.912 | 3.99 |
| 3 | 2 | 0.361 | 1.002 | 1.365 | 2.574 | 3.48 |
| 3 | 4 | 0.3389 | 0.94 | 1.277 | 2.301 | 3.0169 |
| 3 | 5 | 0.33747 | 0.924 | 1.255 | 2.237 | 2.894 |
| 4 | 0.25 | 0.3129 | 0.923 | 1.29 | 2.689 | 3.73 |
| 4 | 0.5 | 0.3 | 0.877 | 1.226 | 2.505 | 3.467 |
| 4 | 1 | 0.282 | 0.817 | 1.143 | 2.263 | 3.107 |
| 4 | 2 | 0.266 | 0.753 | 1.055 | 2.013 | 2.708 |
| 4 | 4 | 0.2536 | 0.7039 | 0.981 | 1.817 | 2.3609 |
| 4 | 5 | 0.25 | 0.689 | 0.962 | 1.772 | 2.273 |

Table A.1: Sherwood number ($Re = 0.1$,$k = 1$).

| | | $Pe^e$ | | | | |
|---|---|---|---|---|---|---|
| $k$ | $\mu^*$ | 10 | 50 | 100 | 500 | 1000 |
| 0.25 | 0.25 | 1.727 | 5.2487 | 7.561 | 13.999 | 15.488 |
| 0.25 | 0.5 | 1.641 | 4.964 | 7.038 | 13.534 | 15.203 |
| 0.25 | 1 | 1.535 | 4.626 | 6.362 | 12.727 | 14.702 |
| 0.25 | 2 | 1.432 | 4.322 | 5.679 | 11.482 | 13.877 |
| 0.25 | 4 | 1.352 | 4.114 | 5.1779 | 9.881 | 12.632 |
| 0.25 | 5 | 1.332 | 4.066 | 5.07 | 9.336 | 12.132 |
| 0.5 | 0.25 | 1.5478 | 4.144 | 5.839 | 11.73 | 13.302 |
| 0.5 | 0.5 | 1.477 | 3.94 | 5.467 | 10.863 | 12.904 |
| 0.5 | 1 | 1.39 | 3.696 | 4.991 | 10.066 | 12.251 |
| 0.5 | 2 | 1.3048 | 3.475 | 4.518 | 8.988 | 11.303 |
| 0.5 | 4 | 1.238 | 3.32 | 4.177 | 7.774 | 10.107 |
| 0.5 | 5 | 1.221 | 3.284 | 4.105 | 7.388 | 9.685 |
| 1 | 0.25 | 1.288 | 3.007 | 4.137 | 8.237 | 10.213 |
| 1 | 0.5 | 1.238 | 2.873 | 3.898 | 7.8 | 9.771 |
| 1 | 1 | 1.175 | 2.711 | 3.593 | 7.161 | 9.1 |
| 1 | 2 | 1.112 | 2.562 | 3.292 | 6.377 | 8.234 |
| 1 | 4 | 1.063 | 2.454 | 3.077 | 5.576 | 7.2917 |
| 1 | 5 | 1.051 | 2.429 | 3.032 | 5.335 | 6.991 |
| 2 | 0.25 | 0.962 | 1.979 | 2.664 | 5.313 | 6.877 |
| 2 | 0.5 | 0.932 | 1.898 | 2.524 | 5.006 | 6.506 |
| 2 | 1 | 0.893 | 1.799 | 2.345 | 4.58 | 5.976 |
| 2 | 2 | 0.855 | 1.706 | 2.169 | 4.087 | 5.345 |
| 2 | 4 | 0.8249 | 1.637 | 2.042 | 3.618 | 4.724 |
| 2 | 5 | 0.817 | 1.62 | 2.014 | 3.484 | 4.541 |
| 3 | 0.25 | 0.7649 | 1.4818 | 1.974 | 3.924 | 5.164 |
| 3 | 0.5 | 0.7438 | 1.423 | 1.875 | 3.692 | 4.864 |
| 3 | 1 | 0.717 | 1.352 | 1.749 | 3.375 | 4.4448 |
| 3 | 2 | 0.6908 | 1.284 | 1.624 | 3.018 | 3.96 |
| 3 | 4 | 0.6695 | 1.233 | 1.533 | 2.689 | 3.5039 |
| 3 | 5 | 0.664 | 1.22 | 1.512 | 2.5978 | 3.373 |
| 4 | 0.25 | 0.633 | 1.1859 | 1.57 | 3.112 | 4.1307 |
| 4 | 0.5 | 0.617 | 1.14 | 1.494 | 2.926 | 3.881 |
| 4 | 1 | 0.597 | 1.084 | 1.396 | 2.674 | 3.5377 |
| 4 | 2 | 0.577 | 1.03 | 1.3 | 2.395 | 3.147 |
| 4 | 4 | 0.5616 | 0.9897 | 1.228 | 2.142 | 2.7868 |
| 4 | 5 | 0.557 | 0.9798 | 1.211 | 2.073 | 2.685 |

Table A.2: Sherwood number ($Re = 0.1$, $D^* = 1$).

| | | $Pe^e$ | | | | |
|---|---|---|---|---|---|---|
| $k$ | $\mu^*$ | 10 | 50 | 100 | 500 | 1000 |
| 0.1 | 0.25 | 1.8944 | 6.7953 | 10.0007 | 16.3347 | 17.0232 |
| 0.1 | 0.5 | 1.7942 | 6.3812 | 9.273 | 15.8843 | 17.1158 |
| 0.1 | 1. | 1.6717 | 5.8801 | 8.2872 | 15.0631 | 16.625 |
| 0.1 | 2. | 1.5528 | 5.4221 | 7.2336 | 13.8869 | 17.8298 |
| 0.1 | 4. | 1.4607 | 5.1127 | 6.391 | 12.4431 | 15.1662 |
| 0.1 | 5. | 1.4382 | 5.0449 | 6.2013 | 11.8863 | 14.6537 |
| 0.25 | 0.25 | 1.7671 | 5.4514 | 7.8613 | 14.3873 | 15.5603 |
| 0.25 | 0.5 | 1.6801 | 5.1528 | 7.3281 | 13.6361 | 16.9656 |
| 0.25 | 1. | 1.5725 | 4.7922 | 6.6234 | 12.4217 | 14.8759 |
| 0.25 | 2. | 1.4669 | 4.4633 | 5.891 | 11.1004 | 15.6395 |
| 0.25 | 4. | 1.3844 | 4.2386 | 5.3276 | 10.1025 | 12.9208 |
| 0.25 | 5. | 1.3641 | 4.189 | 5.2034 | 9.7963 | 12.4064 |
| 0.5 | 0.25 | 1.586 | 4.2937 | 6.06 | 11.9159 | 13.4893 |
| 0.5 | 0.5 | 1.5153 | 4.0801 | 5.6806 | 10.9747 | 13.1962 |
| 0.5 | 1. | 1.427 | 3.8216 | 5.1843 | 9.5986 | 12.4742 |
| 0.5 | 2. | 1.3394 | 3.5845 | 4.6763 | 8.3926 | 11.6947 |
| 0.5 | 4. | 1.2702 | 3.4199 | 4.295 | 8.0669 | 10.3938 |
| 0.5 | 5. | 1.253 | 3.3827 | 4.2128 | 7.6808 | 9.9774 |
| 1. | 0.25 | 1.3185 | 3.1081 | 4.2851 | 8.8382 | 10.438 |
| 1. | 0.5 | 1.2682 | 2.9681 | 4.0409 | 7.9469 | 10.008 |
| 1. | 1. | 1.2047 | 2.7978 | 3.723 | 7.3816 | 9.3389 |
| 1. | 2. | 1.1409 | 2.6395 | 3.4002 | 5.9938 | 8.5148 |
| 1. | 4. | 1.0899 | 2.5266 | 3.1617 | 5.7846 | 7.5274 |
| 1. | 5. | 1.0772 | 2.5005 | 3.1106 | 5.538 | 7.2256 |
| 2. | 0.25 | 0.983 | 2.0408 | 2.7546 | 5.4759 | 7.0658 |
| 2. | 0.5 | 0.9527 | 1.957 | 2.6114 | 5.1655 | 6.6998 |
| 2. | 1. | 0.9143 | 1.854 | 2.4256 | 4.7374 | 6.1663 |
| 2. | 2. | 0.8754 | 1.7562 | 2.2375 | 4.2319 | 5.5287 |
| 2. | 4. | 0.8439 | 1.6841 | 2.0988 | 3.75 | 4.888 |
| 2. | 5. | 0.836 | 1.667 | 2.0683 | 3.6103 | 4.6995 |
| 4. | 0.25 | 0.6463 | 1.221 | 1.6214 | 3.2152 | 4.265 |
| 4. | 0.5 | 0.6305 | 1.1743 | 1.5435 | 3.0274 | 4.0155 |
| 4. | 1. | 0.6104 | 1.1164 | 1.4423 | 2.7705 | 3.6637 |
| 4. | 2. | 0.59 | 1.0601 | 1.3399 | 2.4819 | 3.262 |
| 4. | 4. | 0.5735 | 1.0172 | 1.2624 | 2.2186 | 2.8862 |
| 4. | 5. | 0.5694 | 1.0068 | 1.2447 | 2.1457 | 2.781 |
| 5. | 0.25 | 0.5509 | 1.0178 | 1.3461 | 2.6657 | 3.5565 |
| 5. | 0.5 | 0.5383 | 0.9796 | 1.2825 | 2.5089 | 3.3426 |
| 5. | 1. | 0.5222 | 0.932 | 1.2004 | 2.2956 | 3.045 |
| 5. | 2. | 0.506 | 0.8854 | 1.117 | 2.0581 | 2.7082 |
| 5. | 4. | 0.4929 | 0.8497 | 1.0533 | 1.844 | 2.3973 |
| 5. | 5. | 0.4897 | 0.8409 | 1.0386 | 1.7854 | 2.3112 |

Table A.3: Sherwood number ($Re = 1$,$D^* = 1$).

| | | $Pe^e$ | | | | |
|---|---|---|---|---|---|---|
| $D^*$ | $\mu^*$ | 10 | 50 | 100 | 500 | 1000 |
| 0.1 | 0.25 | 8.4527 | 14.0995 | 15.3483 | 16.8736 | 17.2744 |
| 0.1 | 0.5 | 8.0383 | 13.7978 | 15.1477 | 16.7752 | 17.1938 |
| 0.1 | 1. | 7.4478 | 13.2843 | 14.817 | 16.6202 | 17.0433 |
| 0.1 | 2. | 6.7412 | 12.4485 | 14.2998 | 16.4057 | 16.9144 |
| 0.1 | 4. | 6.095 | 11.1536 | 13.4788 | 16.1071 | 16.688 |
| 0.1 | 5. | 5.9393 | 10.6303 | 13.1093 | 16.0294 | 16.6256 |
| 0.25 | 0.25 | 4.2634 | 9.0747 | 11.3923 | 14.9593 | 15.8477 |
| 0.25 | 0.5 | 4.1234 | 8.6316 | 10.9766 | 14.7241 | 15.6701 |
| 0.25 | 1. | 3.9582 | 7.9778 | 10.3228 | 14.3332 | 15.3839 |
| 0.25 | 2. | 3.8124 | 7.1607 | 9.4124 | 13.8073 | 14.9676 |
| 0.25 | 4. | 3.7156 | 6.3095 | 8.2977 | 13.1188 | 14.4455 |
| 0.25 | 5. | 3.6946 | 6.0581 | 7.9151 | 12.8616 | 14.2571 |
| 0.5 | 0.25 | 2.4615 | 5.4288 | 7.4118 | 12.2183 | 13.7198 |
| 0.5 | 0.5 | 2.3864 | 5.1385 | 7.0101 | 11.7542 | 13.4126 |
| 0.5 | 1. | 2.2917 | 4.7571 | 6.4394 | 10.4046 | 12.9648 |
| 0.5 | 2. | 2.1954 | 4.3615 | 5.7681 | 10.2976 | 12.205 |
| 0.5 | 4. | 2.1163 | 4.06 | 5.1296 | 9.4073 | 11.3318 |
| 0.5 | 5. | 2.0962 | 3.9954 | 4.9539 | 9.0858 | 11.0263 |
| 1. | 0.25 | 1.3185 | 3.1081 | 4.2851 | 8.8382 | 10.4428 |
| 1. | 0.5 | 1.2682 | 2.9681 | 4.0409 | 7.8753 | 10.163 |
| 1. | 1. | 1.2047 | 2.7978 | 3.723 | 6.5919 | 9.334 |
| 1. | 2. | 1.1409 | 2.6395 | 3.4002 | 5.84 | 8.5797 |
| 1. | 4. | 1.0899 | 2.5266 | 3.1617 | 5.5943 | 7.5379 |
| 1. | 5. | 1.0772 | 2.5005 | 3.1106 | 5.587 | 7.2024 |
| 2. | 0.25 | 0.6647 | 1.7622 | 2.3981 | 5.3807 | 7.4026 |
| 2. | 0.5 | 0.6368 | 1.689 | 2.2778 | 4.6225 | 7.4548 |
| 2. | 1. | 0.6022 | 1.5952 | 2.1279 | 3.6921 | 5.776 |
| 2. | 2. | 0.5682 | 1.4974 | 1.982 | 3.1321 | 5.3549 |
| 2. | 4. | 0.5416 | 1.4151 | 1.8697 | 3.3015 | 4.4092 |
| 2. | 5. | 0.535 | 1.3939 | 1.842 | 3.2725 | 4.1323 |
| 4. | 0.25 | 0.3276 | 0.9529 | 1.3282 | 3.0015 | 4.3659 |
| 4. | 0.5 | 0.3137 | 0.9068 | 1.2638 | 2.5269 | 6.3436 |
| 4. | 1. | 0.2966 | 0.8467 | 1.1794 | 1.9809 | 7.9259 |
| 4. | 2. | 0.2799 | 0.7839 | 1.0897 | 1.7031 | 3.7096 |
| 4. | 4. | 0.2669 | 0.7321 | 1.0132 | 1.8496 | 2.4512 |
| 4. | 5. | 0.2637 | 0.719 | 0.9934 | 1.872 | 2.2699 |
| 5. | 0.25 | 0.2607 | 0.7715 | 1.0899 | 2.4658 | 3.4435 |
| 5. | 0.5 | 0.2497 | 0.7326 | 1.0351 | 2.0686 | 5.3546 |
| 5. | 1. | 0.2361 | 0.682 | 0.9628 | 1.621 | 6.7084 |
| 5. | 2. | 0.2229 | 0.6298 | 0.8855 | 1.4018 | 3.5351 |
| 5. | 4. | 0.2126 | 0.5872 | 0.8199 | 1.523 | 2.0225 |
| 5. | 5. | 0.21 | 0.5764 | 0.803 | 1.5547 | 1.8103 |

Table A.4: Sherwood number ($Re = 1$,$k = 1$).

| | | $Pe^e$ | | | | |
|---|---|---|---|---|---|---|
| $D^*$ | $\mu^*$ | 10 | 50 | 100 | 500 | 1000 |
| 0.1 | 0.25 | 9.7051 | 15.057 | 16.149 | 17.51 | 17.835 |
| 0.1 | 0.5 | 9.2876 | 14.754 | 15.9 | 17.317 | 17.655 |
| 0.1 | 1. | 8.6485 | 14.326 | 15.59 | 17.122 | 17.486 |
| 0.1 | 2. | 7.8008 | 13.678 | 15.173 | 16.906 | 17.31 |
| 0.1 | 4. | 6.8715 | 12.642 | 14.568 | 16.663 | 17.118 |
| 0.1 | 5. | 6.5994 | 12.189 | 14.304 | 16.579 | 17.054 |
| 0.25 | 0.25 | 4.8722 | 10.261 | 12.511 | 15.785 | 16.579 |
| 0.25 | 0.5 | 4.706 | 9.8405 | 12.119 | 15.504 | 16.334 |
| 0.25 | 1. | 4.4881 | 9.1998 | 11.534 | 15.141 | 16.041 |
| 0.25 | 2. | 4.2731 | 8.3316 | 10.706 | 14.663 | 15.672 |
| 0.25 | 4. | 4.1256 | 7.323 | 9.616 | 14.068 | 15.224 |
| 0.25 | 5. | 4.096 | 6.9948 | 9.2133 | 13.852 | 15.066 |
| 0.5 | 0.25 | 2.8234 | 6.2717 | 8.4648 | 13.194 | 14.615 |
| 0.5 | 0.5 | 2.7456 | 5.9597 | 8.0677 | 12.813 | 14.282 |
| 0.5 | 1. | 2.6458 | 5.5148 | 7.478 | 12.259 | 13.819 |
| 0.5 | 2. | 2.5438 | 4.9988 | 6.7266 | 11.505 | 13.191 |
| 0.5 | 4. | 2.4604 | 4.5335 | 5.9291 | 10.59 | 12.401 |
| 0.5 | 5. | 2.4391 | 4.415 | 5.6868 | 10.27 | 12.152 |
| 1. | 0.25 | 1.5573 | 3.5601 | 4.9651 | 9.4925 | 11.431 |
| 1. | 0.5 | 1.5057 | 3.3961 | 4.6991 | 9.0718 | 11.017 |
| 1. | 1. | 1.4375 | 3.178 | 4.3246 | 8.4464 | 10.406 |
| 1. | 2. | 1.3653 | 2.956 | 3.9013 | 7.6337 | 9.586 |
| 1. | 4. | 1.305 | 2.7919 | 3.5371 | 6.7391 | 8.6389 |
| 1. | 5. | 1.2897 | 2.7557 | 3.4481 | 6.4535 | 8.3268 |
| 2. | 0.25 | 0.81017 | 2.0013 | 2.7556 | 5.8429 | 7.618 |
| 2. | 0.5 | 0.77965 | 1.9202 | 2.6164 | 5.5123 | 7.2399 |
| 2. | 1. | 0.73988 | 1.813 | 2.4298 | 5.0295 | 6.677 |
| 2. | 2. | 0.69875 | 1.7003 | 2.2362 | 4.4408 | 5.9536 |
| 2. | 4. | 0.66523 | 1.6055 | 2.0858 | 3.861 | 5.1864 |
| 2. | 5. | 0.65682 | 1.581 | 2.0502 | 3.6958 | 4.952 |
| 4. | 0.25 | 0.39995 | 1.0994 | 1.5168 | 3.2546 | 4.4259 |
| 4. | 0.5 | 0.3844 | 1.0515 | 1.4462 | 3.0526 | 4.1831 |
| 4. | 1. | 0.3643 | 0.9862 | 1.3511 | 2.7655 | 3.8064 |
| 4. | 2. | 0.3437 | 0.91456 | 1.248 | 2.4356 | 3.3369 |
| 4. | 4. | 0.32706 | 0.85264 | 1.1587 | 2.1435 | 2.8767 |
| 4. | 5. | 0.32289 | 0.83656 | 1.1352 | 2.0691 | 2.7472 |
| 5. | 0.25 | 0.31807 | 0.89691 | 1.248 | 2.6659 | 3.6398 |
| 5. | 0.5 | 0.30572 | 0.85513 | 1.1896 | 2.4994 | 3.4446 |
| 5. | 1. | 0.28877 | 0.79892 | 1.11 | 2.2648 | 3.129 |
| 5. | 2. | 0.27346 | 0.73854 | 1.0221 | 1.9998 | 2.7378 |
| 5. | 4. | 0.2617 | 0.6883 | 0.94499 | 1.7712 | 2.3636 |
| 5. | 5. | 0.25698 | 0.67313 | 0.92468 | 1.7141 | 2.2612 |

Table A.5: Sherwood number ($Re = 10.$,$k = 1$).

| | | $Pe^e$ | | | | |
|---|---|---|---|---|---|---|
| $k$ | $\mu^*$ | 10 | 50 | 100 | 500 | 1000 |
| 0.1 | 0.25 | 2.6666 | 9.2666 | 13.4919 | 17.86 | 19.0343 |
| 0.1 | 0.5 | 2.4908 | 8.5877 | 12.8511 | 17.8935 | 18.4747 |
| 0.1 | 1. | 2.2434 | 7.4911 | 11.4999 | 17.599 | 18.2891 |
| 0.1 | 2. | 1.9941 | 6.1994 | 9.4229 | 16.9806 | 18.1484 |
| 0.1 | 4. | 1.8094 | 5.183 | 7.459 | 15.8241 | 17.3243 |
| 0.1 | 5. | 1.7669 | 4.95 | 6.9818 | 15.3467 | 17.1044 |
| 0.25 | 0.25 | 2.4766 | 7.3826 | 10.7048 | 16.2141 | 17.6522 |
| 0.25 | 0.5 | 2.3411 | 6.9427 | 10.185 | 16.1221 | 17.2346 |
| 0.25 | 1. | 2.1395 | 6.243 | 9.2268 | 15.6742 | 16.9519 |
| 0.25 | 2. | 1.9242 | 5.3794 | 7.8467 | 14.8205 | 16.605 |
| 0.25 | 4. | 1.7578 | 4.6352 | 6.4547 | 13.4604 | 15.5249 |
| 0.25 | 5. | 1.7188 | 4.4557 | 6.0934 | 12.8556 | 15.2932 |
| 0.5 | 0.25 | 2.1965 | 5.749 | 8.2188 | 13.8815 | 16.0918 |
| 0.5 | 0.5 | 2.106 | 5.4603 | 7.84 | 13.6685 | 15.34 |
| 0.5 | 1. | 1.9636 | 5.0073 | 7.1827 | 13.1134 | 14.8985 |
| 0.5 | 2. | 1.7994 | 4.4436 | 6.2685 | 12.1556 | 14.1782 |
| 0.5 | 4. | 1.6639 | 3.941 | 5.3276 | 10.847 | 13.1067 |
| 0.5 | 5. | 1.6311 | 3.8172 | 5.0681 | 10.3502 | 12.5268 |
| 1. | 0.25 | 1.768 | 4.0998 | 5.7519 | 10.5994 | 12.6423 |
| 1. | 0.5 | 1.7183 | 3.927 | 5.5084 | 10.3202 | 12.3527 |
| 1. | 1. | 1.6387 | 3.6587 | 5.1016 | 9.753 | 11.8026 |
| 1. | 2. | 1.5415 | 3.3247 | 4.5515 | 8.9149 | 10.9655 |
| 1. | 4. | 1.4551 | 3.0248 | 3.9849 | 7.8766 | 10.538 |
| 1. | 5. | 1.4332 | 2.9508 | 3.8258 | 7.5398 | 9.5573 |
| 2. | 0.25 | 1.2585 | 2.6518 | 3.6526 | 7.0942 | 9.3354 |
| 2. | 0.5 | 1.2335 | 2.557 | 3.5116 | 6.8503 | 8.7039 |
| 2. | 1. | 1.1944 | 2.4103 | 3.2821 | 6.4111 | 8.1764 |
| 2. | 2. | 1.1466 | 2.2286 | 2.9789 | 5.7987 | 7.4341 |
| 2. | 4. | 1.1031 | 2.0654 | 2.6713 | 5.1248 | 6.597 |
| 2. | 5. | 1.0918 | 2.0252 | 2.5851 | 4.9185 | 6.3137 |
| 4. | 0.25 | 0.7942 | 1.5674 | 2.1285 | 4.2424 | 5.6 |
| 4. | 0.5 | 0.7819 | 1.5183 | 2.0522 | 4.0756 | 5.3721 |
| 4. | 1. | 0.7629 | 1.4425 | 1.9307 | 3.7952 | 4.9946 |
| 4. | 2. | 0.7399 | 1.349 | 1.7736 | 3.4193 | 4.4859 |
| 4. | 4. | 0.719 | 1.2649 | 1.6177 | 3.0296 | 3.9483 |
| 4. | 5. | 0.7136 | 1.244 | 1.5745 | 2.9141 | 3.793 |
| 5. | 0.25 | 0.6701 | 1.3026 | 1.7627 | 3.5304 | 4.7288 |
| 5. | 0.5 | 0.6603 | 1.2631 | 1.7007 | 3.3881 | 4.5022 |
| 5. | 1. | 0.6452 | 1.2022 | 1.6025 | 3.1518 | 4.1791 |
| 5. | 2. | 0.6269 | 1.1273 | 1.4763 | 2.8386 | 3.7427 |
| 5. | 4. | 0.6104 | 1.0597 | 1.352 | 2.5167 | 3.2878 |
| 5. | 5. | 0.606 | 1.0428 | 1.3177 | 2.4228 | 3.1607 |

Table A.6: Sherwood number ($Re = 50.$,$D^* = 1$).

| | | | | $Pe^e$ | | |
|---|---|---|---|---|---|---|
| $D^*$ | $\mu^*$ | 10 | 50 | 100 | 500 | 1000 |
| 0.1 | 0.25 | 10.9343 | 15.9591 | 16.9325 | 18.7609 | 20.7987 |
| 0.1 | 0.5 | 10.6268 | 15.9206 | 16.9554 | 18.5944 | 20.89 |
| 0.1 | 1. | 10.0427 | 15.5969 | 16.7094 | 18.4445 | 20.7831 |
| 0.1 | 2. | 9.1514 | 15.0271 | 16.2796 | 18.1796 | 20.6153 |
| 0.1 | 4. | 8.0396 | 14.2084 | 15.7605 | 18.7558 | 18.3649 |
| 0.1 | 5. | 7.6668 | 13.8541 | 15.5233 | 17.9002 | 20.5523 |
| 0.25 | 0.25 | 5.5131 | 11.4464 | 13.6081 | 16.6298 | 17.5035 |
| 0.25 | 0.5 | 5.3365 | 11.1841 | 13.4333 | 16.6008 | 17.5351 |
| 0.25 | 1. | 5.0726 | 10.6287 | 12.9562 | 16.3048 | 17.304 |
| 0.25 | 2. | 4.7565 | 9.76 | 12.182 | 15.8047 | 16.908 |
| 0.25 | 4. | 4.4837 | 8.6437 | 11.1431 | 15.3546 | 16.2112 |
| 0.25 | 5. | 4.4204 | 8.2544 | 10.7452 | 15.1824 | 16.3522 |
| 0.5 | 0.25 | 3.1606 | 7.2161 | 9.5786 | 14.2294 | 15.5727 |
| 0.5 | 0.5 | 3.0791 | 6.9407 | 9.2911 | 14.0738 | 15.4867 |
| 0.5 | 1. | 2.9577 | 6.4722 | 8.7402 | 13.6112 | 15.099 |
| 0.5 | 2. | 2.8173 | 5.8295 | 7.9221 | 12.8699 | 14.4592 |
| 0.5 | 4. | 2.6983 | 5.1544 | 6.9462 | 11.9433 | 13.6571 |
| 0.5 | 5. | 2.669 | 4.9599 | 6.6278 | 11.6228 | 13.4031 |
| 1. | 0.25 | 1.768 | 4.0998 | 5.7519 | 10.5981 | 12.565 |
| 1. | 0.5 | 1.7183 | 3.927 | 5.5084 | 10.3202 | 12.3323 |
| 1. | 1. | 1.6387 | 3.6587 | 5.1016 | 9.7533 | 11.7867 |
| 1. | 2. | 1.5415 | 3.3247 | 4.5515 | 8.9031 | 10.9387 |
| 1. | 4. | 1.4551 | 3.0248 | 3.9849 | 7.8766 | 9.8956 |
| 1. | 5. | 1.4332 | 2.9508 | 3.8261 | 7.529 | 9.5372 |
| 2. | 0.25 | 0.9313 | 2.2767 | 3.1911 | 6.7186 | 8.6851 |
| 2. | 0.5 | 0.9004 | 2.1883 | 3.0462 | 6.449 | 8.3913 |
| 2. | 1. | 0.8519 | 2.0521 | 2.8191 | 5.9728 | 7.8387 |
| 2. | 2. | 0.7944 | 1.8856 | 2.5321 | 5.3002 | 7.0353 |
| 2. | 4. | 0.7448 | 1.7348 | 2.2652 | 4.5391 | 6.1049 |
| 2. | 5. | 0.7324 | 1.6957 | 2.1966 | 4.2975 | 5.7948 |
| 4. | 0.25 | 0.4705 | 1.2551 | 1.7393 | 3.8022 | 5.2037 |
| 4. | 0.5 | 0.4544 | 1.2074 | 1.6652 | 3.6182 | 4.9691 |
| 4. | 1. | 0.4296 | 1.1307 | 1.5495 | 3.3142 | 4.5674 |
| 4. | 2. | 0.4004 | 1.0339 | 1.4046 | 2.9042 | 4.0107 |
| 4. | 4. | 0.3753 | 0.9429 | 1.2678 | 2.4701 | 3.4062 |
| 4. | 5. | 0.3691 | 0.9187 | 1.231 | 2.3425 | 3.2035 |
| 5. | 0.25 | 0.3737 | 1.029 | 1.4299 | 3.121 | 4.3198 |
| 5. | 0.5 | 0.3609 | 0.9889 | 1.3701 | 2.9654 | 4.1145 |
| 5. | 1. | 0.3412 | 0.9244 | 1.2758 | 2.7121 | 3.7691 |
| 5. | 2. | 0.3181 | 0.843 | 1.1566 | 2.3746 | 3.2955 |
| 5. | 4. | 0.2983 | 0.7667 | 1.0425 | 2.0251 | 2.7858 |
| 5. | 5. | 0.2934 | 0.7465 | 1.0115 | 1.9243 | 2.6226 |

Table A.7: Sherwood number ($Re = 50.$,$k = 1$).

| | | $Pe^e$ | | | | |
|---|---|---|---|---|---|---|
| $D^*$ | $\mu^*$ | 10 | 50 | 100 | 500 | 1000 |
| 0.1 | 0.25 | 11.266 | 15.841 | 16.727 | 17.828 | 18.087 |
| 0.1 | 0.5 | 11.056 | 16.039 | 17.0 | 18.185 | 18.466 |
| 0.1 | 1 | 10.607 | 16.078 | 17.147 | 18.453 | 18.765 |
| 0.1 | 2 | 9.7629 | 15.696 | 16.91 | 18.352 | 18.697 |
| 0.1 | 4 | 8.5962 | 14.916 | 16.383 | 18.017 | 18.394 |
| 0.1 | 5 | 8.1982 | 14.587 | 16.181 | 17.908 | 18.298 |
| 0.25 | 0.25 | 5.7711 | 11.679 | 13.704 | 16.442 | 17.095 |
| 0.25 | 0.5 | 5.5985 | 11.566 | 13.731 | 16.678 | 17.384 |
| 0.25 | 1 | 5.3357 | 11.201 | 13.535 | 16.771 | 17.548 |
| 0.25 | 2 | 4.9775 | 10.395 | 12.884 | 16.456 | 17.32 |
| 0.25 | 4 | 4.6269 | 9.1996 | 11.787 | 15.833 | 16.805 |
| 0.25 | 5 | 4.5428 | 8.7735 | 11.36 | 15.603 | 16.624 |
| 0.5 | 0.25 | 3.2954 | 7.5365 | 9.8892 | 14.268 | 15.493 |
| 0.5 | 0.5 | 3.2197 | 7.3198 | 9.7166 | 14.331 | 15.652 |
| 0.5 | 1 | 3.1013 | 6.905 | 9.3007 | 14.181 | 15.62 |
| 0.5 | 2 | 2.9368 | 6.2162 | 8.4804 | 13.585 | 15.153 |
| 0.5 | 4 | 2.7754 | 5.3926 | 7.3127 | 12.498 | 14.272 |
| 0.5 | 5 | 2.7339 | 5.148 | 6.9186 | 12.043 | 13.923 |
| 1 | 0.25 | 1.8545 | 4.3319 | 6.0605 | 10.862 | 12.715 |
| 1 | 0.5 | 1.8221 | 4.1777 | 5.8604 | 10.737 | 12.67 |
| 1 | 1 | 1.744 | 3.9119 | 5.4889 | 10.351 | 12.395 |
| 1 | 2 | 1.6389 | 3.515 | 4.872 | 9.5466 | 11.657 |
| 1 | 4 | 1.5226 | 3.0919 | 4.1069 | 8.0948 | 10.239 |
| 1 | 5 | 1.4915 | 2.9785 | 3.8792 | 7.4905 | 9.6185 |
| 2 | 0.25 | 0.9931 | 2.4054 | 3.3894 | 7.0204 | 8.971 |
| 2 | 0.5 | 0.9689 | 2.3257 | 3.2677 | 6.823 | 8.8201 |
| 2 | 1 | 0.9237 | 2.2122 | 3.10428 | 6.444 | 8.3648 |
| 2 | 2 | 0.8556 | 1.9798 | 2.6952 | 5.7281 | 7.5921 |
| 2 | 4 | 0.8074 | 1.7825 | 2.2804 | 4.5486 | 6.0778 |
| 2 | 5 | 0.7896 | 1.6878 | 2.1759 | 4.1064 | 5.4892 |
| 4 | 0.25 | 0.4966 | 1.3263 | 1.844 | 4.0339 | 5.484 |
| 4 | 0.5 | 0.4837 | 1.2861 | 1.779 | 3.8748 | 5.3112 |
| 4 | 1 | 0.47675 | 1.2119 | 1.6839 | 3.5955 | 4.9335 |
| 4 | 2 | 0.4256 | 1.0933 | 1.484 | 3.1515 | 4.3836 |
| 4 | 4 | 0.3927 | 0.958 | 1.2681 | 2.4321 | 3.289 |
| 4 | 5 | 0.3825 | 0.9197 | 1.2039 | 2.1805 | 2.9206 |
| 5 | 0.25 | 0.39832 | 1.0877 | 1.5149 | 3.3195 | 4.5479 |
| 5 | 0.5 | 0.3852 | 1.0544 | 1.4624 | 3.1847 | 4.404 |
| 5 | 1 | 0.3678 | 0.9943 | 1.3695 | 2.9452 | 4.0797 |
| 5 | 2 | 0.3394 | 0.8931 | 1.2229 | 2.5805 | 3.5831 |
| 5 | 4 | 0.3123 | 0.7823 | 1.0454 | 1.9852 | 2.6842 |
| 5 | 5 | 0.3053 | 0.7488 | 0.9897 | 1.7789 | 2.3644 |

Table A.8: Sherwood number ($Re = 100$,$k = 1$).

| | | $Pe^e$ | | | | |
|---|---|---|---|---|---|---|
| $k$ | $\mu^*$ | 10 | 50 | 100 | 500 | 1000 |
| 0.1 | 0.25 | 2.959 | 9.9417 | 13.995 | 17.599 | 18.006 |
| 0.1 | 0.5 | 2.809 | 9.3184 | 13.609 | 17.912 | 18.387 |
| 0.1 | 1 | 2.5109 | 8.0764 | 12.398 | 18.071 | 18.657 |
| 0.1 | 2 | 2.1696 | 6.1596 | 9.242 | 17.677 | 18.496 |
| 0.1 | 4 | 1.8886 | 4.6128 | 6.133 | 11.249 | 15.622 |
| 0.1 | 5 | 1.8244 | 4.2896 | 5.5385 | 9.2848 | 13.219 |
| 0.25 | 0.25 | 2.697 | 7.8764 | 11.224 | 16.129 | 17.006 |
| 0.25 | 0.5 | 2.5931 | 7.474 | 10.843 | 16.295 | 17.275 |
| 0.5 | 1 | 2.3659 | 6.7248 | 9.9664 | 16.245 | 17.378 |
| 0.25 | 1 | 2.1341 | 5.3771 | 7.7492 | 13.734 | 15.425 |
| 0.25 | 2 | 2.0853 | 5.5179 | 8.0982 | 15.577 | 17.039 |
| 0.25 | 4 | 1.836 | 4.3418 | 5.8153 | 10.87 | 14.302 |
| 0.25 | 5 | 1.7774 | 4.0684 | 5.293 | 9.2158 | 12.405 |
| 0.5 | 0.25 | 2.3449 | 6.1041 | 8.6512 | 13.983 | 15.388 |
| 0.5 | 0.5 | 2.2824 | 5.8425 | 8.352 | 13.991 | 15.514 |
| 0.25 | 1 | 2.1341 | 5.3771 | 7.7492 | 13.734 | 15.425 |
| 0.5 | 2 | 1.9366 | 4.6514 | 6.6413 | 12.904 | 14.867 |
| 0.5 | 4 | 1.74 | 3.8787 | 5.2024 | 10.143 | 12.853 |
| 0.5 | 5 | 1.6912 | 3.6802 | 4.81 | 8.9233 | 11.63 |
| 1 | 0.25 | 1.8545 | 4.3319 | 6.0605 | 10.862 | 12.715 |
| 1 | 0.5 | 1.8221 | 4.1777 | 5.8604 | 10.737 | 12.67 |
| 1 | 1 | 1.744 | 3.9119 | 5.4889 | 10.351 | 12.395 |
| 1 | 2 | 1.6389 | 3.515 | 4.872 | 9.5466 | 11.657 |
| 1 | 4 | 1.5226 | 3.0919 | 4.1069 | 8.0948 | 10.239 |
| 1 | 5 | 1.4915 | 2.9785 | 3.8792 | 7.4905 | 9.6185 |
| 2 | 0.25 | 1.3048 | 2.7898 | 3.8469 | 7.373 | 9.2132 |
| 2 | 0.5 | 1.2884 | 2.7066 | 3.7289 | 7.2044 | 9.0555 |
| 2 | 1 | 1.2512 | 2.5661 | 3.5201 | 6.8615 | 8.6874 |
| 2 | 2 | 1.2032 | 2.3624 | 3.1953 | 6.2555 | 7.9951 |
| 2 | 4 | 1.1502 | 2.1504 | 2.8150 | 5.4420 | 7.0103 |
| 2 | 5 | 1.1357 | 2.0938 | 2.7014 | 5.1663 | 6.672 |
| 4 | 0.25 | 0.81797 | 1.6435 | 2.2397 | 4.4499 | 5.8248 |
| 4 | 0.5 | 0.8094 | 1.6012 | 2.1756 | 4.3213 | 5.6684 |
| 4 | 1 | 0.79185 | 1.5305 | 2.0654 | 4.0817 | 5.3627 |
| 4 | 2 | 0.76944 | 1.4299 | 1.9011 | 3.7041 | 4.8624 |
| 4 | 4 | 0.7455 | 1.3269 | 1.7175 | 3.2540 | 4.2483 |
| 4 | 5 | 0.739 | 1.2995 | 1.6637 | 3.116 | 4.0596 |
| 5 | 0.25 | 0.68924 | 1.3647 | 1.8543 | 3.71 | 4.9066 |
| 5 | 0.5 | 0.68235 | 1.3308 | 1.8021 | 3.5975 | 4.7636 |
| 5 | 1 | 0.6684 | 1.2745 | 1.7332 | 3.3936 | 4.4935 |
| 5 | 2 | 0.6507 | 1.1946 | 1.5819 | 3.0769 | 4.0622 |
| 5 | 4 | 0.6319 | 1.1131 | 1.4370 | 2.7084 | 3.5462 |
| 5 | 5 | 0.62684 | 1.0914 | 1.3948 | 2.5975 | 3.3904 |

Table A.9: Sherwood number ($Re = 100, D^* = 1$).

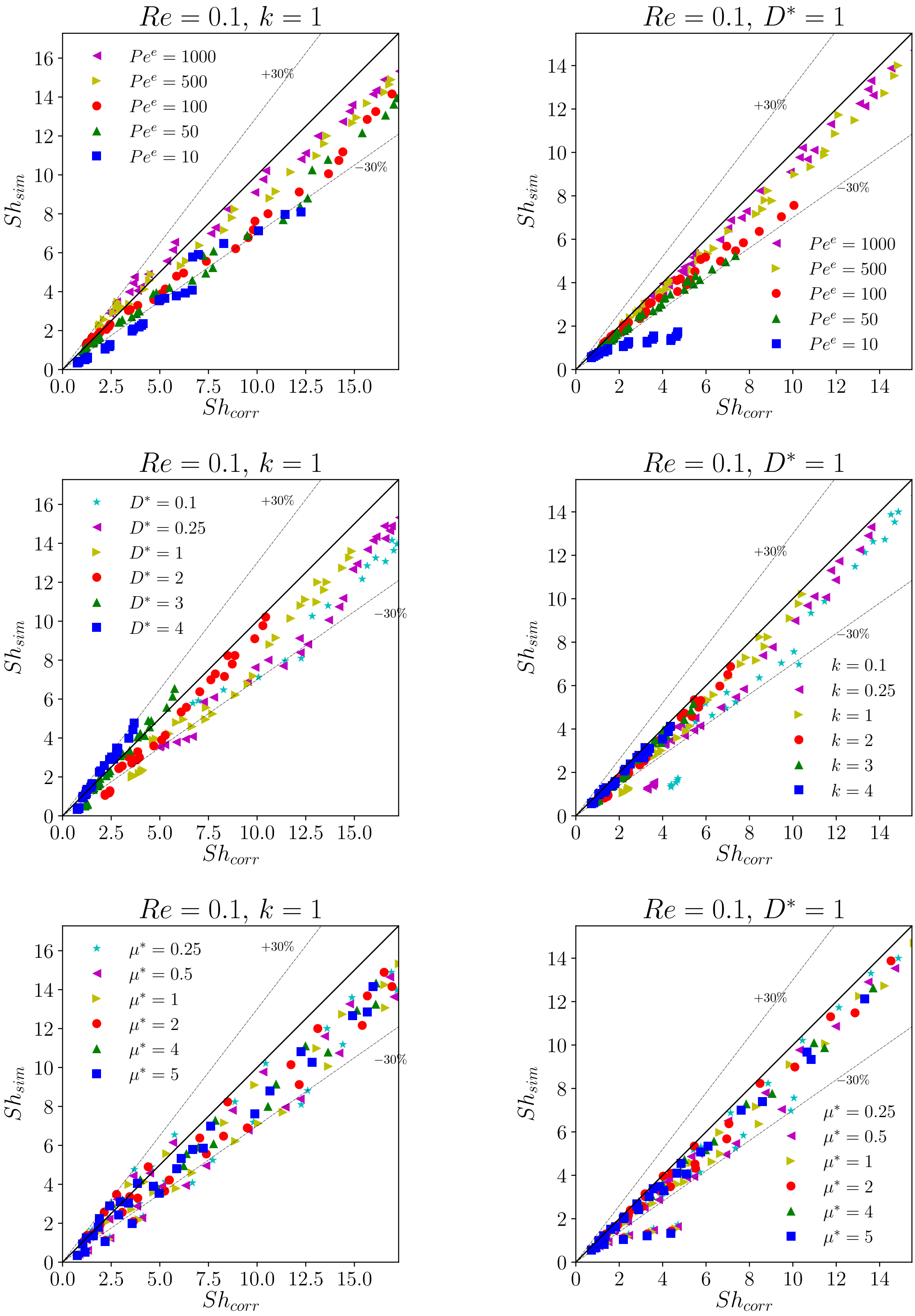

Figure A.1: Parity plot of Sherwood number: present simulations vs Eq 4.2.6, $Re = 0.1$, $k = 1$ (left), $D^* = 1$ (right).

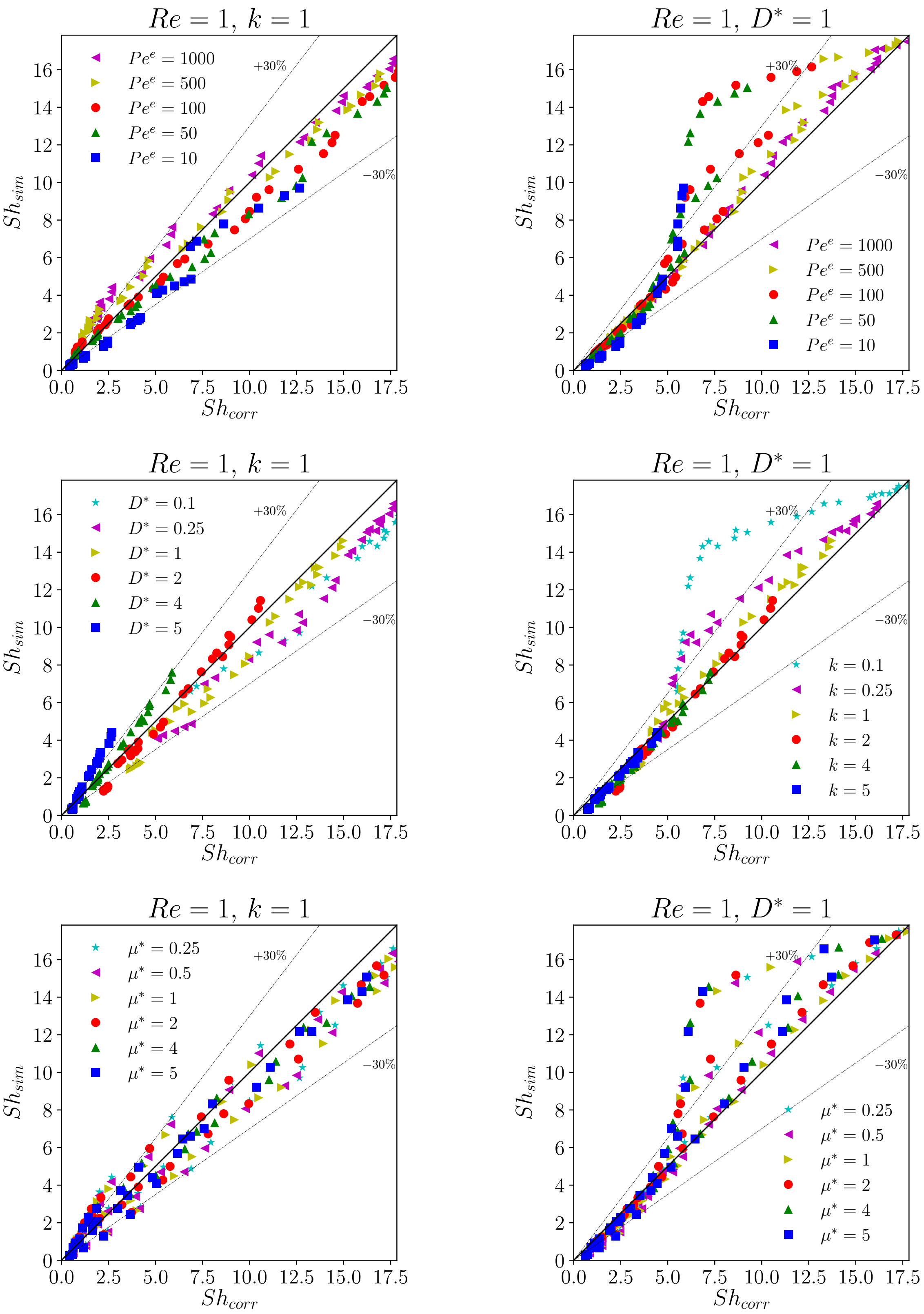

Figure A.2: Parity plot of Sherwood number: present simulations vs Eq 4.2.6, $Re = 1$, $k = 1$ (left), $D^* = 1$ (right).

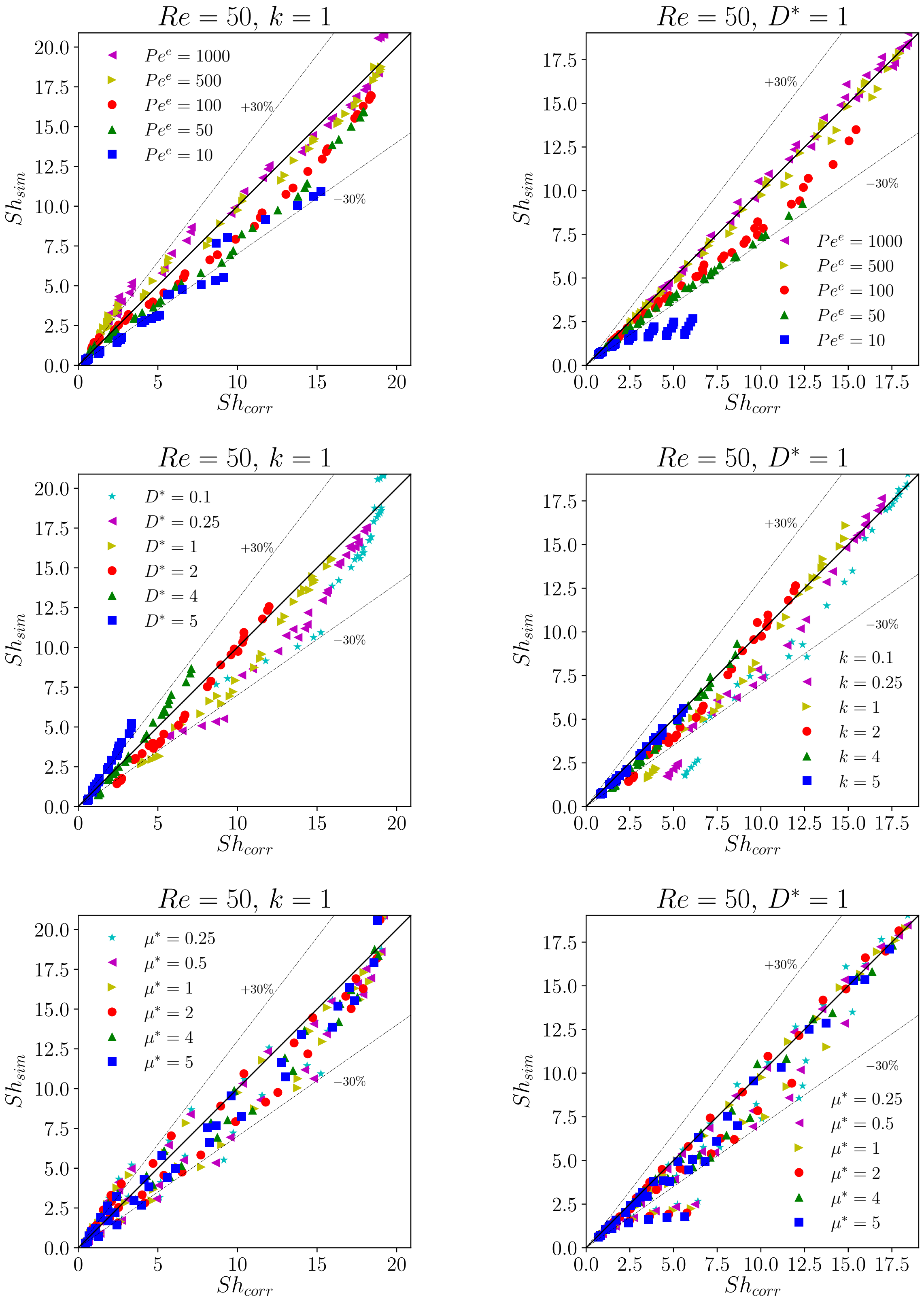

Figure A.3: Parity plot of Sherwood number: present simulations vs Eq 4.2.6, $Re = 50$, $k = 1$ (left), $D^* = 1$ (right).

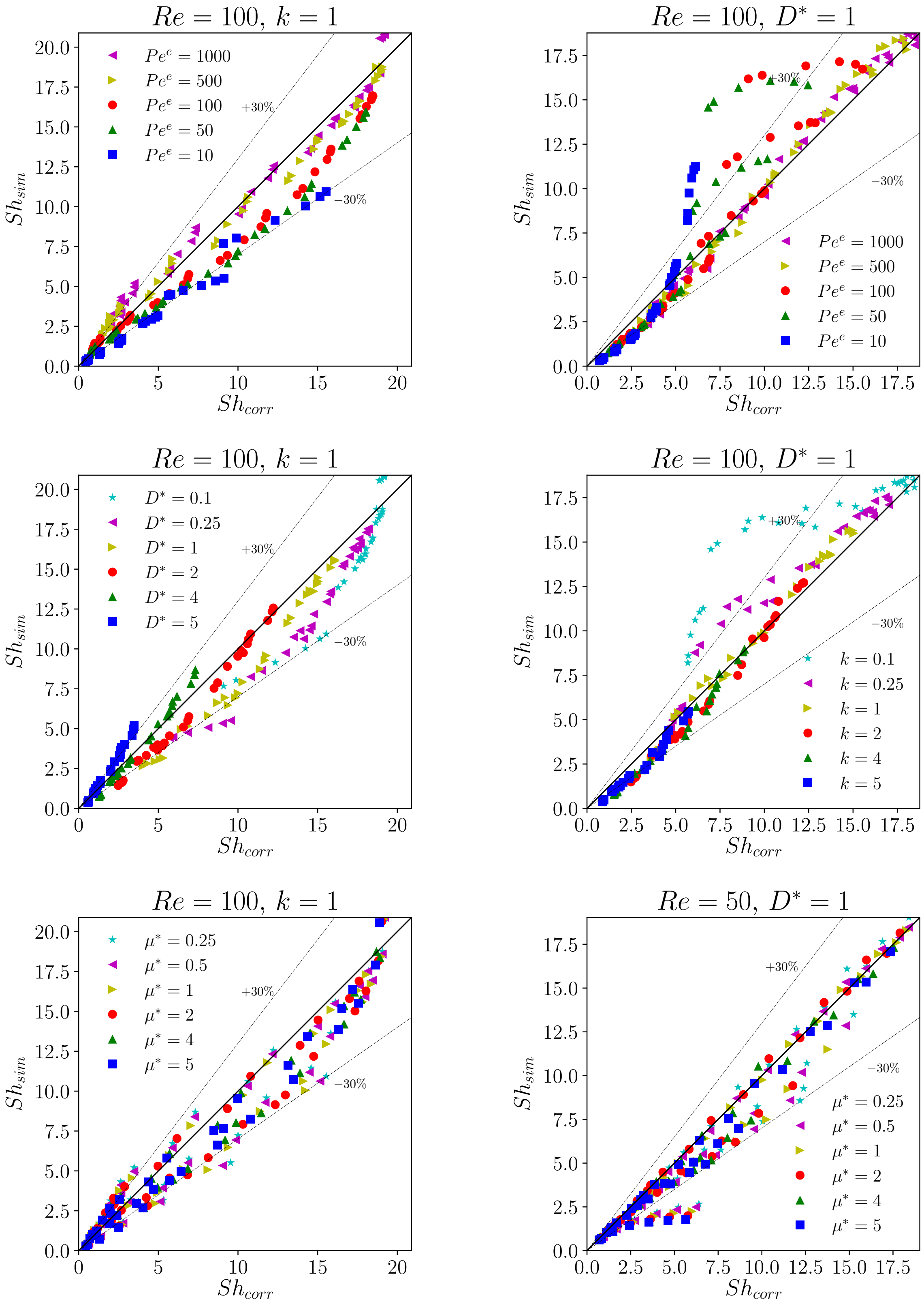

Figure A.4: Parity plot of Sherwood number: present simulations vs Eq 4.2.6, $Re = 100$, $k = 1$ (left), $D^* = 1$ (right).

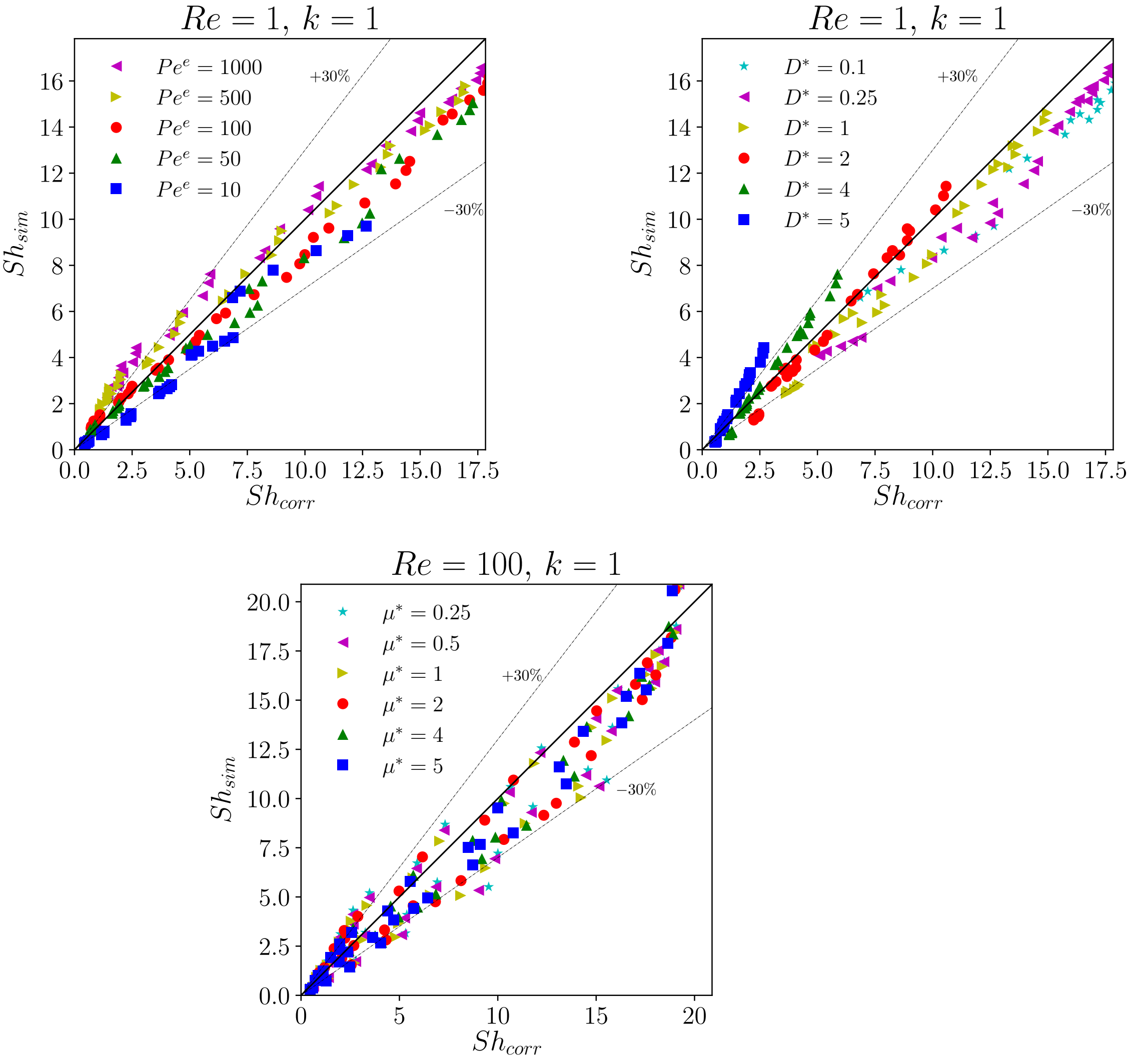

Figure A.5: Parity plot of Sherwood number: present simulations vs Eq 4.2.6, $Re = 10$, $k = 1$.

## A.2 Bubble

| | | $Pe^e$ | | | | |
|---|---|---|---|---|---|---|
| $Re$ | $D^*$ | 10 | 50 | 100 | 500 | 1000 |
| 0.1 | 0.1 | 8.887 | 14.371 | 15.526 | 16.95 | 17.291 |
| 0.1 | 0.25 | 4.427 | 9.5276 | 11.796 | 15.172 | 16.005 |
| 0.1 | 0.5 | 2.5451 | 5.7538 | 7.8367 | 15.5414 | 14.011 |
| 0.1 | 1 | 1.3743 | 3.2736 | 4.5619 | 8.8918 | 10.8428 |
| 0.1 | 2 | 0.6932 | 1.8464 | 2.54 | 5.4118 | 7.16 |
| 0.1 | 4 | 0.3433 | 1.0047 | 1.402 | 3.0008 | 4.158 |
| 0.1 | 5 | 0.2732 | 0.8154 | 1.152 | 2.458 | 3.4296 |
| 1 | 0.1 | 9.0264 | 14.483 | 15.624 | 17.034 | 17.367 |
| 1 | 0.25 | 4.4999 | 9.6583 | 11.922 | 15.2725 | 16.096 |
| 1 | 0.5 | 2.5921 | 5.8474 | 7.9526 | 12.659 | 14.118 |
| 1 | 1 | 1.4086 | 3.3258 | 4.6376 | 9.008 | 10.96 |
| 1 | 2 | 0.7235 | 1.8755 | 2.581 | 5.4977 | 7.261 |
| 1 | 4 | 0.3522 | 1.0234 | 1.4246 | 3.0522 | 4.225 |
| 1 | 5 | 0.2803 | 0.832 | 1.1711 | 2.5001 | 3.487 |
| 10 | 0.1 | 10.155 | 15.332 | 16.374 | 17.664 | 17.965 |
| 10 | 0.25 | 5.0872 | 10.697 | 12.903 | 16.055 | 16.812 |
| 10 | 0.5 | 2.9259 | 6.6356 | 8.8958 | 13.591 | 14.978 |
| 10 | 1 | 1.6221 | 3.7681 | 5.2801 | 9.9472 | 11.92 |
| 10 | 2 | 0.849 | 2.1058 | 2.9308 | 6.2143 | 8.107 |
| 10 | 4 | 0.4177 | 1.1586 | 1.6058 | 3.4912 | 4.8035 |
| 10 | 5 | 0.3328 | 0.947 | 1.3208 | 2.8636 | 3.9788 |
| 50 | 0.1 | 11.133 | 15.473 | 16.32 | 17.407 | 17.663 |
| 50 | 0.25 | 5.7209 | 11.504 | 13.412 | 16.054 | 16.6955 |
| 50 | 0.5 | 3.2523 | 7.4839 | 9.7462 | 13.955 | 15.144 |
| 50 | 1 | 1.8192 | 4.2985 | 6.0041 | 10.663 | 12.46 |
| 50 | 2 | 0.9702 | 2.3765 | 3.3567 | 6.946 | 8.8512 |
| 50 | 4 | 0.4823 | 1.3054 | 1.8222 | 3.9986 | 5.424 |
| 50 | 5 | 0.3847 | 1.0712 | 1.4955 | 3.2922 | 4.5264 |
| 100 | 0.1 | 11.427 | 15.512 | 16.297 | 17.31 | 17.555 |
| 100 | 0.25 | 5.9465 | 11.767 | 13.577 | 16.042 | 16.642 |
| 100 | 0.5 | 3.3704 | 7.7901 | 10.046 | 14.07 | 15.184 |
| 100 | 1 | 1.8881 | 4.5051 | 6.2788 | 10.919 | 12.645 |
| 100 | 2 | 1.0133 | 2.4868 | 3.5273 | 7.227 | 9.128 |
| 100 | 4 | 0.5055 | 1.3643 | 1.912 | 4.2 | 5.669 |
| 100 | 5 | 0.4032 | 1.1205 | 1.5681 | 3.4639 | 4.7438 |

Table A.10: Sherwood number ($k = 1$, $\mu^* = 0.02$).

| | | $Pe^e$ | | | | |
|---|---|---|---|---|---|---|
| $Re$ | $k$ | 10 | 50 | 100 | 500 | 1000 |
| 0.1 | 0.1 | 2.0239 | 7.3015 | 10.802 | 16.458 | 17.129 |
| 0.1 | 0.25 | 1.8754 | 5.8126 | 8.461 | 14.539 | 15.777 |
| 0.1 | 0.5 | 1.6691 | 4.5498 | 6.4896 | 12.051 | 13.799 |
| 0.1 | 1 | 1.3744 | 3.2736 | 4.5619 | 8.894 | 10.842 |
| 0.1 | 2 | 1.0154 | 2.1387 | 2.9165 | 5.8075 | 7.454 |
| 0.1 | 4 | 0.6631 | 1.2748 | 1.7099 | 3.4226 | 4.538 |
| 0.1 | 5 | 0.5643 | 1.0617 | 1.4182 | 2.8396 | 3.7918 |
| 1 | 0.1 | 2.0828 | 7.4354 | 10.991 | 16.561 | 17.2136 |
| 1 | 0.25 | 1.929 | 5.9151 | 8.6108 | 14.66 | 15.877 |
| 1 | 0.5 | 1.7155 | 4.6265 | 6.6018 | 12.179 | 13.913 |
| 1 | 1 | 1.4086 | 3.3258 | 4.6376 | 9.007 | 10.96 |
| 1 | 2 | 1.0359 | 2.1708 | 2.9627 | 5.8897 | 7.553 |
| 1 | 4 | 0.6728 | 1.293 | 1.7359 | 3.475 | 4.606 |
| 1 | 5 | 0.5721 | 1.0767 | 1.4396 | 2.883 | 3.849 |
| 10 | 0.1 | 2.4106 | 8.5538 | 12.514 | 17.305 | 17.85 |
| 10 | 0.25 | 2.2416 | 6.7802 | 9.8557 | 15.576 | 16.645 |
| 10 | 0.5 | 1.9964 | 5.2761 | 7.5471 | 13.19 | 14.814 |
| 10 | 1 | 1.6221 | 3.7681 | 5.2801 | 9.947 | 11.92 |
| 10 | 2 | 1.1687 | 2.4433 | 3.3566 | 6.5952 | 8.38 |
| 10 | 4 | 0.7445 | 1.4475 | 1.9585 | 3.9218 | 5.18 |
| 10 | 5 | 0.6299 | 1.2037 | 1.6225 | 3.2596 | 4.341 |
| 50 | 0.1 | 2.8572 | 9.9682 | 13.836 | 17.172 | 17.574 |
| 50 | 0.25 | 2.6167 | 7.8653 | 11.124 | 15.751 | 16.58 |
| 50 | 0.5 | 2.2877 | 6.0753 | 8.5768 | 13.69 | 15.035 |
| 50 | 1 | 1.8192 | 4.2985 | 6.041 | 10.663 | 12.462 |
| 50 | 2 | 1.2854 | 2.7618 | 3.8067 | 7.2676 | 9.065 |
| 50 | 4 | 0.8075 | 1.6245 | 2.2139 | 4.3977 | 5.751 |
| 50 | 5 | 0.681 | 1.3484 | 1.8324 | 3.6686 | 4.85 |
| 100 | 0.1 | 3.0861 | 10.568 | 14.238 | 17.127 | 17.483 |
| 100 | 0.25 | 2.7855 | 8.3111 | 11.564 | 15.804 | 16.555 |
| 100 | 0.5 | 2.402 | 6.3945 | 8.9559 | 13.855 | 15.1 |
| 100 | 1 | 1.8881 | 4.5051 | 6.2788 | 10.919 | 14.645 |
| 100 | 2 | 1.3237 | 2.8834 | 3.9798 | 7.5239 | 9.31 |
| 100 | 4 | 0.8283 | 1.6911 | 2.3125 | 4.5852 | 5.97 |
| 100 | 5 | 0.69760 | 1.4027 | 1.9135 | 3.8309 | 5.049 |

Table A.11: Sherwood number ($D^* = 1$, $\mu^* = 0.02$).

# A.3 Solid particle

| | | $Pe^e$ | | | | |
|---|---|---|---|---|---|---|
| $Re$ | $D^*$ | 10 | 50 | 100 | 500 | 1000 |
| 0.1 | 0.1 | 5.5345 | 6.0007 | 6.1075 | 6.2798 | 6.3328 |
| 0.1 | 0.25 | 3.5947 | 5.1227 | 5.424 | 5.8749 | 6.007 |
| 0.1 | 0.5 | 1.9897 | 3.8443 | 4.3803 | 5.2294 | 5.483 |
| 0.1 | 1 | 1.0153 | 2.3705 | 2.9579 | 4.1448 | 4.56 |
| 0.1 | 2 | 0.5095 | 1.2788 | 1.6952 | 2.7818 | 3.265 |
| 0.1 | 4 | 0.247 | 0.6514 | 0.8877 | 1.6065 | 1.989 |
| 0.1 | 5 | 0.1969 | 0.522 | 0.7143 | 1.3175 | 1.6508 |
| 1 | 0.1 | 5.5517 | 6.054 | 6.3672 | 10.435 | 14.18 |
| 1 | 0.25 | 3.5947 | 5.1227 | 5.434 | 6.6895 | 8.55 |
| 1 | 0.5 | 1.9897 | 3.8443 | 4.3803 | 5.328 | 6.0639 |
| 1 | 1 | 1.0153 | 2.3705 | 2.9579 | 4.1384 | 4.587 |
| 1 | 2 | 0.5095 | 1.2788 | 1.6952 | 2.805 | 3.2658 |
| 1 | 4 | 0.247 | 0.6514 | 0.8877 | 1.6389 | 2.018 |
| 1 | 5 | 0.1969 | 0.522 | 0.7143 | 1.3474 | 1.682 |
| 10 | 0.1 | 5.5517 | 6.054 | 6.3672 | 12.212 | 14.914 |
| 10 | 0.25 | 3.6591 | 5.13 | 5.4347 | 7.572 | 10.042 |
| 10 | 0.5 | 2.0396 | 3.8743 | 4.3911 | 5.6277 | 6.802 |
| 10 | 1 | 1.0403 | 2.4099 | 2.9917 | 4.306 | 4.855 |
| 10 | 2 | 0.5161 | 1.3066 | 1.7281 | 2.973 | 3.435 |
| 10 | 4 | 0.2546 | 0.6662 | 0.9082 | 1.782 | 1.172 |
| 10 | 5 | 0.2029 | 0.5334 | 0.7311 | 1.477 | 1.824 |
| 50 | 0.1 | 5.7684 | 6.5025 | 7.6913 | 14.422 | 16.402 |
| 50 | 0.25 | 4.2544 | 5.371 | 5.7488 | 9.086 | 12.02 |
| 50 | 0.5 | 2.5311 | 4.1735 | 4.6163 | 6.12 | 7.886 |
| 50 | 1 | 1.3315 | 2.6764 | 3.1937 | 4.287 | 5.075 |
| 50 | 2 | 0.6819 | 1.5061 | 1.9015 | 2.8344 | 3.298 |
| 50 | 4 | 0.3354 | 0.8004 | 1.046 | 1.707 | 2.05 |
| 50 | 5 | 0.2681 | 0.6488 | 0.8542 | 1.426 | 1.72 |
| 100 | 0.1 | 5.7972 | 6.7682 | 8.3787 | 15.396 | 17.035 |
| 100 | 0.25 | 4.2881 | 5.4012 | 5.8711 | 9.972 | 13.00 |
| 100 | 0.5 | 2.5349 | 4.0942 | 4.5412 | 6.496 | 8.61 |
| 100 | 1 | 1.3303 | 2.515 | 2.9578 | 4.2645 | 5.33 |
| 100 | 2 | 0.6827 | 1.3845 | 1.6811 | 2.626 | 3.243 |
| 100 | 4 | 0.3364 | 0.7342 | 0.9093 | 1.485 | 1.885 |
| 100 | 5 | 0.2691 | 0.5959 | 0.7415 | 1.224 | 1.559 |

Table A.12: Sherwood number ($k = 1$, $\mu^* = 100$).

|  |  | $Pe^e$ |  |  |  |  |
|---|---|---|---|---|---|---|
| *Re* | *k* | 10 | 50 | 100 | 500 | 1000 |
| 0.1 | 0.1 | 1.343 | 4.7597 | 5.7004 | 6.2236 | 6.309 |
| 0.1 | 0.25 | 1.2755 | 3.9682 | 4.8808 | 5.784 | 5.9625 |
| 0.1 | 0.5 | 1.1744 | 3.2081 | 3.9931 | 5.1365 | 5.4345 |
| 0.1 | 1 | 1.0153 | 2.3705 | 2.9579 | 4.144 | 4.56 |
| 0.1 | 2 | 0.7955 | 1.5781 | 1.9576 | 2.934 | 3.3755 |
| 0.1 | 4 | 0.5464 | 0.9517 | 1.1691 | 1.8195 | 2.167 |
| 0.1 | 5 | 0.4713 | 0.7947 | 0.9731 | 1.5243 | 1.8262 |
| 1 | 0.1 | 1.3751 | 4.823 | 5.7241 | 6.295 | 6.6 |
| 1 | 0.25 | 1.3071 | 4.0281 | 4.913 | 5.8235 | 6.175 |
| 1 | 0.5 | 1.2044 | 3.2599 | 4.0287 | 5.1506 | 5.552 |
| 1 | 1 | 1.0403 | 2.4099 | 2.9917 | 4.1449 | 4.586 |
| 1 | 2 | 0.8124 | 1.6041 | 1.9844 | 2.9334 | 3.3604 |
| 1 | 4 | 0.5566 | 0.967 | 1.1868 | 1.8284 | 2.158 |
| 1 | 5 | 0.4794 | 0.8073 | 0.9882 | 1.535 | 1.826 |
| 10 | 0.1 | 1.551 | 4.9167 | 6.165 | 6.42 | 7.008 |
| 10 | 0.25 | 1.4941 | 4.2215 | 5.6692 | 5.957 | 6.544 |
| 10 | 0.5 | 1.3986 | 3.4897 | 5.0134 | 5.298 | 5.87 |
| 10 | 1 | 1.2163 | 2.6223 | 4.0832 | 4.306 | 4.85 |
| 10 | 2 | 0.9359 | 1.7614 | 2.9801 | 3.099 | 3.57 |
| 10 | 4 | 0.6239 | 1.0648 | 1.9298 | 1.966 | 2.322 |
| 10 | 5 | 0.5334 | 0.889 | 1.6393 | 1.659 | 1.9724 |
| 50 | 0.1 | 1.5893 | 3.9953 | 5.1849 | 6.6001 | 7.857 |
| 50 | 0.25 | 1.5533 | 3.7169 | 4.6279 | 6.03 | 7.117 |
| 50 | 0.5 | 1.4872 | 3.3223 | 4.022 | 5.271 | 6.231 |
| 50 | 1 | 1.3315 | 2.6764 | 3.1937 | 4.288 | 5.066 |
| 50 | 2 | 1.0372 | 1.8819 | 2.2507 | 3.146 | 3.736 |
| 50 | 4 | 0.6862 | 1.1652 | 1.4054 | 2.0594 | 2.472 |
| 50 | 5 | 0.5845 | 0.9772 | 1.1815 | 1.7562 | 2.116 |
| 100 | 0.1 | 1.531 | 3.1288 | 3.8466 | 6.473 | 8.45 |
| 100 | 0.25 | 1.5042 | 3.043 | 3.6694 | 5.8289 | 7.55 |
| 100 | 0.5 | 1.4556 | 2.884 | 3.4308 | 5.154 | 6.75 |
| 100 | 1 | 1.3303 | 2.515 | 2.9578 | 4.266 | 5.315 |
| 100 | 2 | 1.0582 | 1.8786 | 2.2196 | 3.1974 | 3.953 |
| 100 | 4 | 0.7047 | 1.1967 | 1.4357 | 2.135 | 2.633 |
| 100 | 5 | 0.6004 | 1.0086 | 1.2157 | 1.83 | 2.258 |

Table A.13: Sherwood number ($D^* = 1$, $\mu^* = 100$).

## A.4 Elliptical droplet

In this section, a special care has been taken to generate the orthogonal curvilinear mesh inside a Prolate/Oblate Sphere. We will focus on the prolate ellipse in the simulation step unless otherwise stated. We will also see some problems and challenges encountered in JADIM to treat this case unlike the sphere case.

### A.4.1 Mesh

#### A.4.1.1 Oblate sphere: $a > b$

The external mesh of the ellipse used in the simulation is based on the streamlines lines past an elliptic cylinder. Milne-Thomson [1968] [Chapter VI] has given the theoretical background of the streamlines derivation. Thanks to the Joukowski transformation (circle ↔ ellipse) and the circle theorem. LM Milne-Thomson derived the expression of the streamlines and the velocity potential.
In the complex plan, the elliptic coordinates writes:

$$\begin{cases} z = x + iy = c\cosh(\zeta) \\ \zeta = \alpha + i\theta \end{cases} \tag{A.4.1}$$

These definitions correspond to ellipses and hyperbolas (see Figure A.6)

$$\begin{cases} x = c\cosh(\alpha)\cos(\theta) \\ y = c\sinh(\alpha)\sin(\theta) \end{cases} \tag{A.4.2}$$

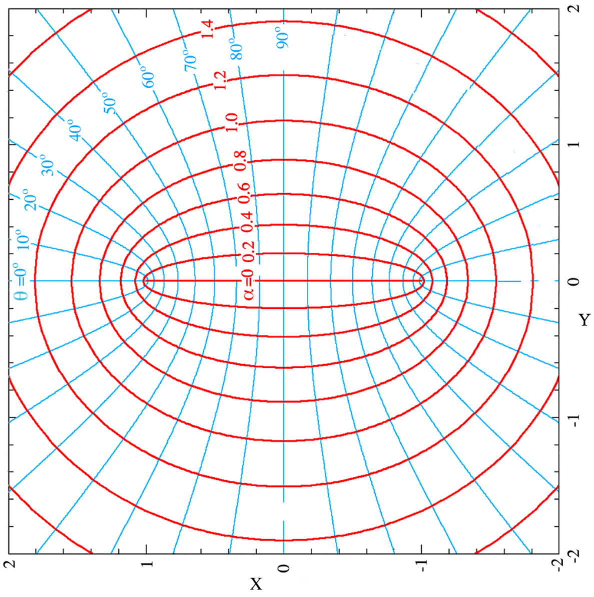

Figure A.6: Elliptic coordinates.

The Joukowski transformation is one of the simplest and most important transformations of two-dimensional. By means of this transformation we can map the Z-plane on the z-plane, we have and vice versa Figure A.7.

$$z = Z + \frac{c^2}{4Z} \tag{A.4.3}$$

The inverse transformation yields tow solutions. The one that maps the area outside the ellipse of semi-axes a, b writes :

$$Z = \frac{1}{2}\left[z + \sqrt{z^2 - c^2}\right] \qquad c^2 = a^2 - b^2 \tag{A.4.4}$$

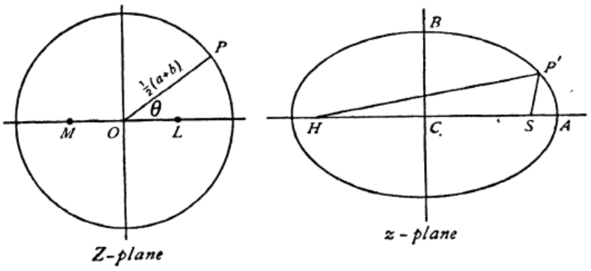

Figure A.7: The Joukowski transformation.

The incompressibility condition assures the existence of the stream function $\eta$ defined in two-dimensional motion as ($u = \frac{\partial \eta}{\partial y}$ and $v = -\frac{\partial \eta}{\partial x}$). For an irrotational flow (i.e. $\nabla \wedge \mathbf{u} = \mathbf{0}$), the velocity field derives from a potential function $\xi$ (i.e. $\mathbf{u} = -\nabla \cdot \xi$). In the complex plan, we define the complex potential as :

$$w = \underbrace{\xi}_{\text{Velocity potential}} + \underbrace{i\eta}_{\text{Stream function}} \tag{A.4.5}$$

If we take in the Z-plane a stream U ($U = 1$) which makes an angle $\theta_0$ with the real axis Figure A.8, the complex potential writes:

$$\begin{aligned} w &= U\left(Z\exp(-i\theta_0) + \frac{(a+b)^2\exp(i\theta_0)}{4Z}\right) \\ &= U(a+b)\cosh(\zeta - (\alpha_0 + i\theta_0)) \end{aligned} \tag{A.4.6}$$

Hence

$$\begin{cases} \xi = (a+b)\cosh(\alpha-\alpha_0)\cos(\theta-\theta_0) \\ \eta = (a+b)\sinh(\alpha-\alpha_0)\sin(\theta-\theta_0) \end{cases} \tag{A.4.7}$$

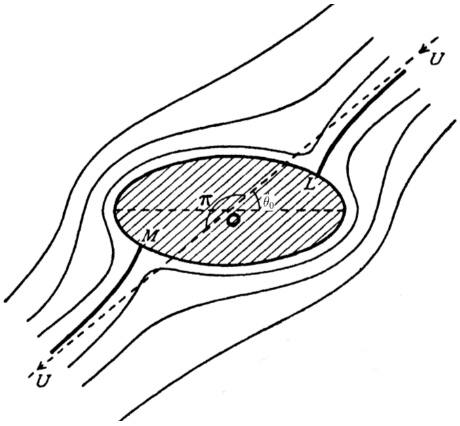

Figure A.8: Flow past elliptic cylinder.

Where $\alpha_0$ is defined on the ellipse ($a = \cosh(\alpha_0)$ and $b = \sinh(\alpha_0)$). $\theta_0 = 0$ in our study:

$$\alpha_0 = \frac{1}{2}\log\left(\frac{a+b}{a-b}\right) \tag{A.4.8}$$

Once $\xi$ and $\eta$ are defined in the plan $(\xi, \eta)$. In order to move to the Cartesian coordinates (Figure A.9) , one must solve the system A.4.7 where the unknowns are ($\alpha$ and $\theta$). After a quick calculation, the main equation to solve is given by A.4.9:

$$f(\alpha) = \cosh^4(\alpha-\alpha_0) - \left(1 + \frac{\xi^2+\eta^2}{(a+b)^2}\right)\cosh^2(\alpha-\alpha_0) + \frac{\xi^2}{(a+b)^2} = 0 \tag{A.4.9}$$

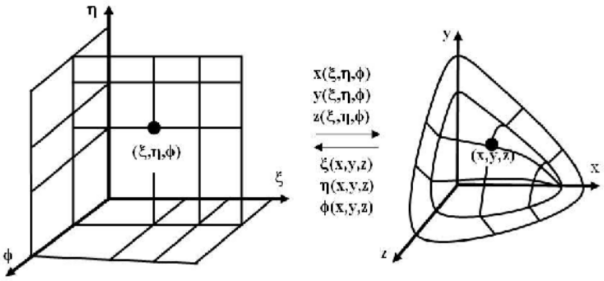

Figure A.9: Transformation: Cartesian mesh ↔ Curvilinear mesh.

A Newton algorithm has been used to solve the above equation in the old mesher version. In some initializations, the algorithm fails to converge. In the new version, the equation A.4.9 has been solved analytically. Therefore the derivation of $\alpha$ and $\theta$ is given by:

$$\cosh(\alpha-\alpha_0)=\sqrt{\frac{\left(1+\frac{\xi^2+\eta^2}{(a+b)^2}\right)+\sqrt{\left(1+\frac{\xi^2+\eta^2}{(a+b)^2}\right)^2-4\frac{\xi^2}{(a+b)^2}}}{2}} \tag{A.4.10}$$

$$\begin{cases}\alpha=\cosh^{-1}\left(\sqrt{\frac{\left(1+\frac{\xi^2+\eta^2}{(a+b)^2}\right)+\sqrt{\left(1+\frac{\xi^2+\eta^2}{(a+b)^2}\right)^2-4\frac{\xi^2}{(a+b)^2}}}{2}}\right)+\alpha_0\\ \theta=\cos^{-1}\left(\frac{\xi}{(a+b)\cosh(\alpha-\alpha_0)}\right)\end{cases} \tag{A.4.11}$$

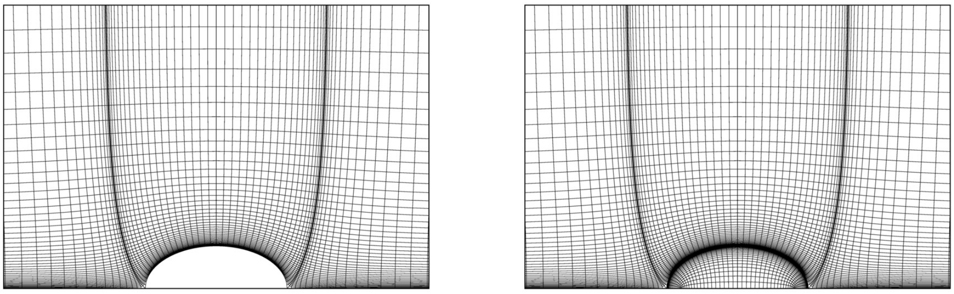

Figure A.10: Oblate sphere: Internal/external curvlinear mesh.

Hence, the external mesh is given by:

$$\begin{cases}x_{ext}=c\cosh(\alpha)\cos(\theta)\\ y_{ext}=c\sinh(\alpha)\sin(\theta)\end{cases} \tag{A.4.12}$$

In order to mesh inside the ellipse, the Cartesian coordinates used are given by:

$$\begin{cases}x_{int}=c\sinh(\alpha_{int})\cos(\theta_{int})\\ y_{int}=c\cosh(\alpha_{int})\sin(\theta_{int})\end{cases} \tag{A.4.13}$$

$\alpha_{int}$ is discretized in a way to refine next the interface. a Dichotomy algorithm has been used to discretize $\theta_{int}$ and assure the orthogonality and the continuity of the external mesh at the interface. The final mesh is given in Figure A.10.

### A.4.1.2 Prolate sphere: $a < b$

In the case of (a<b). All the calculations made previously are still valid. The only change is to rotate the previous geometry by $\pi/2$ $[\theta \leftrightarrow \frac{\pi}{2} - \theta]$ and exchange the role of x and y. The external mesh is then given by :

$$\begin{cases} x_{ext} = c\sinh(\alpha)\sin(\frac{\pi}{2} - \theta) = c\sinh(\alpha)\cos(\theta) \\ y_{ext} = c\cosh(\alpha)\cos(\frac{\pi}{2} - \theta) = c\cosh(\alpha)\sin(\theta) \end{cases} \tag{A.4.14}$$

The internal mesh writes

$$\begin{cases} x_{int} = c\cosh(\alpha)\cos(\theta) \\ y_{int} = c\sinh(\alpha)\sin(\theta) \end{cases} \tag{A.4.15}$$

The final mesh is given in Figure A.11.

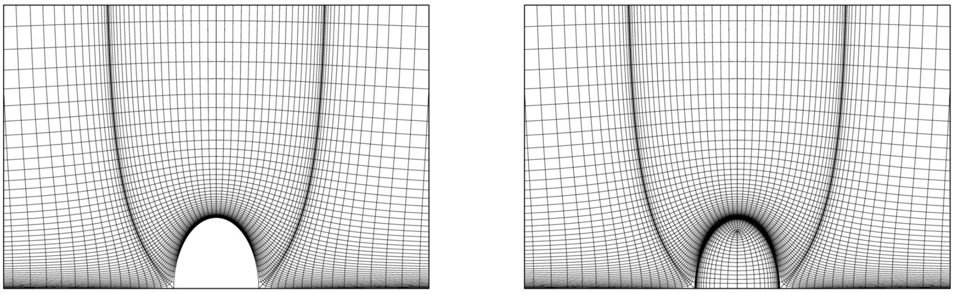

Figure A.11: Prolate sphere :Internal/external curvilinear mesh.

## A.4.2 Prolate sphere: JADIM Case

### A.4.2.1 Coordinate variation terms $H_j^i$

After many attempts to run the prolate sphere case with JADIM. The calculation of coordinate variation terms $H_j^i$ arises a problem inside a particular cell, this cell is presented in Figure A.12.JADIM fails to compute coordinate variation term $H_2^1$ at the distorted cell, $H_2^1 = 0$ in this cell by default. Therefore we propose to calculate analytically these terms and investigate their behaviour at this specific cell.

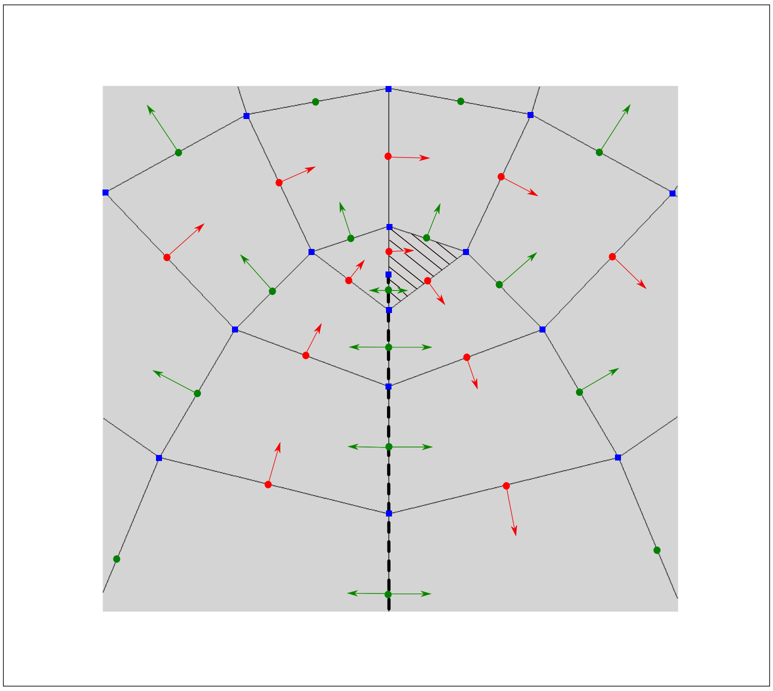

Figure A.12: A zoom into the center region of the droplet mesh.

The scale factors inside the ellipse may be calculated explicitly :

$$\begin{cases} h_\alpha = c\sqrt{\sinh^2(\alpha)+\sin^2(\theta)} \\ h_\theta = c\sqrt{\sinh^2(\alpha)+\sin^2(\theta)} \\ h_\phi = c\sinh(\alpha)\sin(\theta) \end{cases} \tag{A.4.16}$$

Hence, the coordinate variation terms $H^i_j$ are given by

$$H^i_j = \frac{1}{h_i h_j}\frac{\partial h_i}{\partial \xi_j} \qquad \xi_j \text{ are the curvlinear coordinates } (\alpha,\theta,\phi) \tag{A.4.17}$$

$$\begin{cases} H^2_2 = H^1_2 = \dfrac{\cosh(\alpha)\sinh(\alpha)}{c\left(\sinh^2(\alpha)+\sin^2(\theta)\right)^{3/2}} \\ H^1_1 = H^2_1 = \dfrac{\cos(\theta)\sin(\theta)}{c\left(\sinh^2(\alpha)+\sin^2(\theta)\right)^{3/2}} \end{cases} \tag{A.4.18}$$

In order to determine the value of $H^1_2$ when $(\alpha,\theta) \longrightarrow (0,0)$, we perform a Taylor expansion at this point

$$H_2^1 = \frac{\left(1+\frac{\alpha^2}{2}+O(\alpha^4)\right)\left(\alpha+\frac{\alpha^3}{6}+O(\alpha^4)\right)}{\left(\theta^2+\alpha^2+O(\alpha^4)+O(\theta^4)\right)^{(3/2)}}$$

If the choose the path $(\alpha,\alpha)$

$$\underbrace{H_2^1}_{(\alpha,\alpha)\longrightarrow(0,0)} \approx \frac{1}{2\sqrt{2\alpha}}$$

We can also note that $\|H_2^1\| > \frac{1}{c\sinh^2(\alpha)}$ which means that $H_2^1$ diverges when $\alpha$ goes to 0. According to Dominique, even if sometimes these terms diverge, they're compensated with other diverging terms in order to assure the fluxes balance at the scale of a cell. This is one hurdle of the actual case !

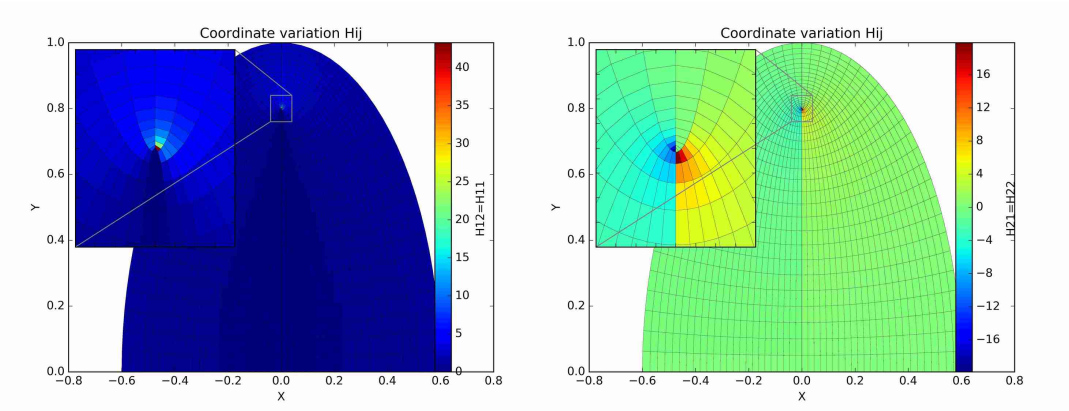

Figure A.13: Coordinate variation terms: $b = 1$ and $a = 0.6$.

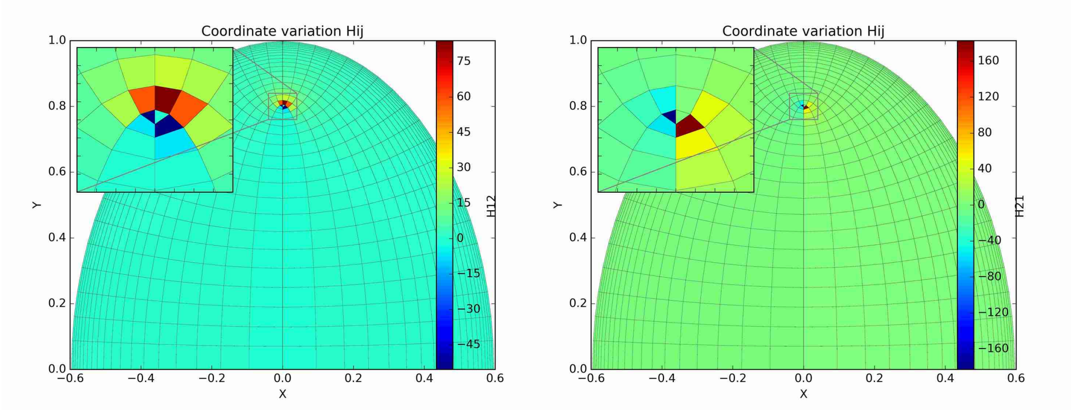

Figure A.14: Coordinate variation terms calculated in JADIM.

### A.4.2.2 Boundary conditions

Another difficulty of the prolate sphere case is the boundary conditions that are unusual. In fact, one boundary is placed inside the ellipse, a priori, values in this region are unknown. All we know is that all flow quantities must be continuous at this boundary. A close look to this boundary is presented in the Figure A.15.

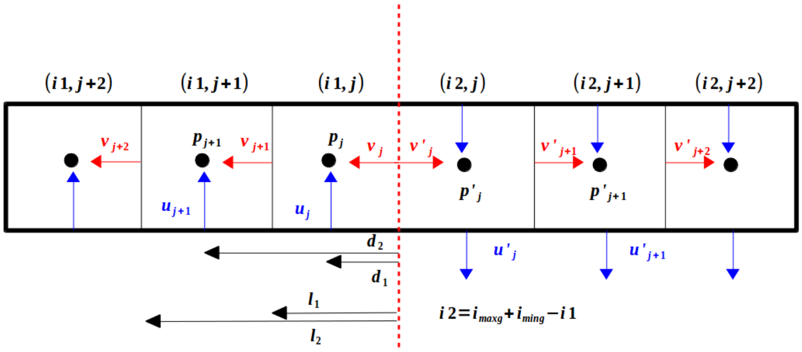

Figure A.15: Internal boundaries inside the ellipse.

The continuity of the velocity at this boundary might be written as :

$$\begin{cases} u_I = u_j - d_1 \left(\dfrac{\partial u}{\partial y}\right)_I + O(d_1^2) \\ \left(\dfrac{\partial u}{\partial y}\right)_I = \dfrac{u_j - u_j^{'}}{d_1 + d_1^{'}} \\ v_I = v_{j+1} - l_1 \left(\dfrac{\partial v}{\partial y}\right)_I + O({l_1}^2) \\ \left(\dfrac{\partial v}{\partial y}\right)_I = \dfrac{v_{j+1} - v_{j+1}^{'}}{l_1 + l_1^{'}} \end{cases} \tag{A.4.19}$$

$$\begin{cases} u_I = -u_I^{'} \\ v_I = -v_I^{'} \end{cases} \tag{A.4.20}$$

When we run the calculation with these implemented conditions, the results are depicted in the Figure A.16.

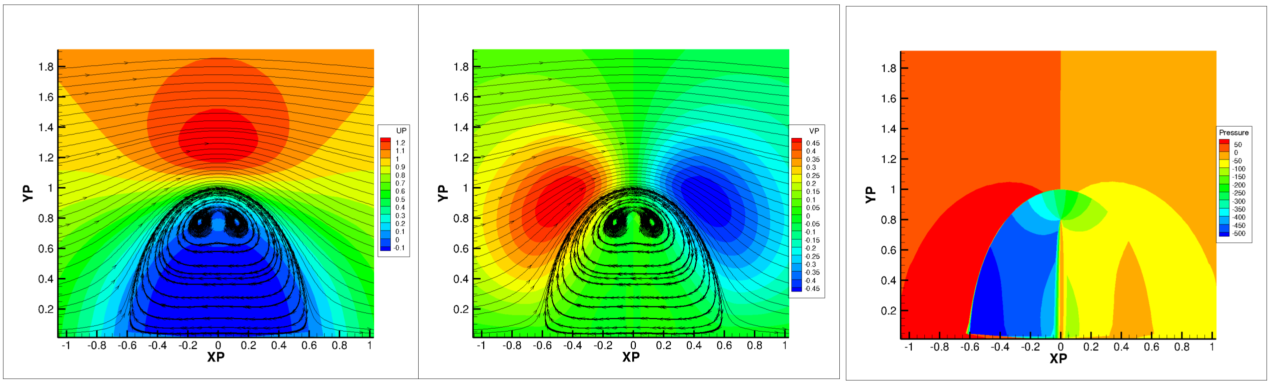

Figure A.16: Coordinate variation terms: $b = 1$ and $a = 0.6$.

A fish-eyes-non-physical behaviour can be seen around the cell mentioned before where $H_2^1 = 0$ !. We can also see the impact of the condition $\frac{\partial \Phi}{\partial n} = 0$ on the pressure distribution. One suggestion is to edit the pressure matrix in order to take fully into account the flow across the internal boundary.

The pressure in JADIM is solved by solving equation below.

$$\nabla \cdot \left(\frac{1}{\rho} \nabla \phi^{n+1}\right) = \frac{\nabla \cdot \widetilde{u}}{\Delta t}$$

By integrating the above equation over a cell, we obtain :

$$\iint\limits_S -\frac{1}{\rho}\nabla\phi^{n+1}dS = \left(\iint\limits_S \widetilde{u}\cdot ndS\right)\frac{1}{\Delta t}$$

$$a_p\phi_{i,j} + a_n\phi_{i,j+1} + a_s\phi_{i,j-1} + a_e\phi_{i+1,j} + a_w\phi_{i-1,j} = smf_{i,j}$$

Thus,The obtained matrix $[n_in_j \wedge n_in_j]$, called the pressure matrix is given by :

$$\begin{pmatrix}
a_p & a_n & \ddots & \ddots & a_e & \cdots & \cdots & \cdots & \cdots & \cdots & \cdots & \cdots & \cdots \\
a_s & a_p & a_n & \ddots & \ddots & a_e & \cdots & \cdots & \cdots & \cdots & \cdots & \cdots & \cdots \\
\ddots & a_s & a_p & a_n & \ddots & \ddots & a_e & \cdots & \cdots & \cdots & \cdots & \cdots & \cdots \\
\ddots & \ddots & a_s & a_p & a_n & \ddots & \ddots & a_e & \cdots & \cdots & \cdots & \cdots & \cdots \\
a_w & \ddots & \ddots & a_s & a_p & a_n & \ddots & \ddots & a_e & \cdots & \cdots & \cdots & \cdots \\
\cdots & a_w & \ddots & \ddots & a_s & a_p & a_s & \ddots & \ddots & a_e & \cdots & \cdots & \cdots \\
\cdots & \cdots & a_w & \ddots & \ddots & a_s & a_p & a_n & \ddots & \ddots & a_e & \cdots & \cdots \\
\cdots & \cdots & \cdots & a_w & \ddots & \ddots & a_s & a_p & a_n & \ddots & \ddots & a_e & \cdots \\
\cdots & \cdots & \cdots & \cdots & a_w & \ddots & \ddots & a_s & a_p & a_n & \ddots & \ddots & a_e \\
\cdots & \cdots & \cdots & \cdots & \cdots & a_w & \ddots & \ddots & a_s & a_p & a_n & \ddots & \ddots \\
\cdots & \cdots & \cdots & \cdots & \cdots & \cdots & a_w & \ddots & \ddots & a_s & a_p & a_n & \ddots \\
\cdots & \cdots & \cdots & \cdots & \cdots & \cdots & \cdots & a_w & \ddots & \ddots & a_s & a_p & a_n \\
\cdots & \cdots & \cdots & \cdots & \cdots & \cdots & \cdots & \cdots & a_w & \ddots & \ddots & a_s & a_p
\end{pmatrix}$$

Now lets consider the case of the prolate sphere, the mesh in the numerical domain is presented in the Figure A.17. The lower segment corresponds to the internal boundary in the Cartesian domain. So instead of using the condition $\frac{\partial\Phi}{\partial n} = 0$, we are going to link each cell with its immediate neighbour in the Cartesian mesh as presented in the Figure. The path used to loop over the cells is given by the blue arrow.

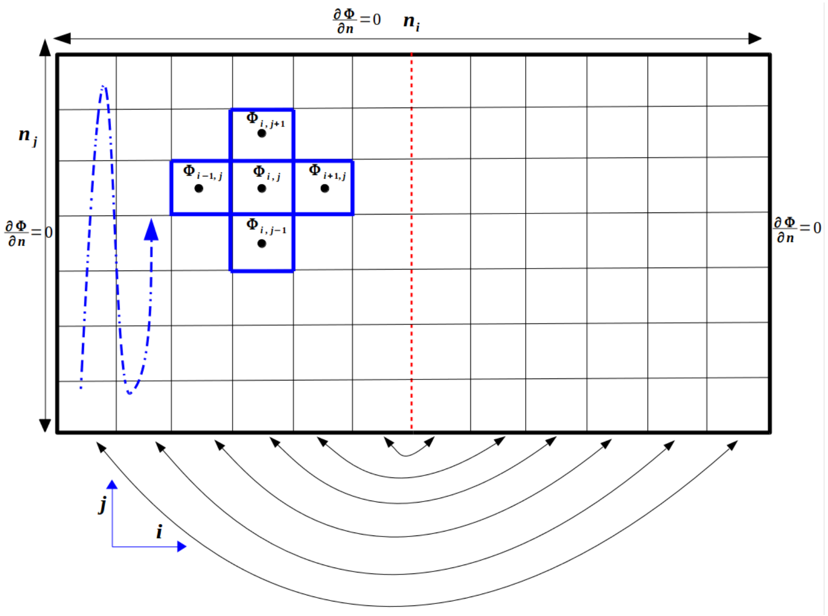

Figure A.17: The interior of the ellipse scheme in the numerical domain.

Therefore, the modified pressure matrix is given below. the red terms have been added to take into account of the neighbouring cells placed on the internal boundary. The blue terms as special, because they correspond to a cell that is placed at the south and the east (or the south and the west) of its neighbour at the same time, these terms correspond to the cells at the tip of the internal boundary. Ideas are needed concerning the treatment of these terms !

$$\begin{pmatrix}
a_p & a_n & \ddots & \ddots & a_e & \cdots & \cdots & \cdots & \cdots & \cdots & \cdots & \cdots & \cdots & \cdots & a_s & \cdots \\
a_s & a_p & a_n & \ddots & \ddots & a_e & \cdots & \cdots & \cdots & \cdots & \cdots & \cdots & \cdots & \cdots & \cdots & \cdots \\
\ddots & a_s & a_p & a_n & \ddots & \ddots & a_e & \cdots & \cdots & \cdots & \cdots & \cdots & a_s & \cdots & \cdots & \cdots \\
\ddots & \ddots & a_s & a_p & a_n & \ddots & \ddots & a_e & \cdots & \cdots & \cdots & \cdots & \cdots & \cdots & \cdots & \cdots \\
a_w & \ddots & \ddots & a_s & a_p & a_n & \ddots & \ddots & a_e & \cdots & a_s & \cdots & \cdots & \cdots & \cdots & \cdots \\
\cdots & a_w & \ddots & \ddots & a_s & a_p & a_s & \ddots & \ddots & a_{se} & \cdots & \cdots & \cdots & \cdots & \cdots & \cdots \\
\cdots & \cdots & a_w & \ddots & \ddots & a_s & a_p & a_n & \ddots & \ddots & a_e & \cdots & \cdots & \cdots & \cdots & \cdots \\
\cdots & \cdots & \cdots & a_w & \ddots & \ddots & a_s & a_p & a_n & \ddots & \ddots & a_e & \cdots & \cdots & \cdots & \cdots \\
\cdots & \cdots & \cdots & \cdots & a_w & \ddots & \ddots & a_s & a_p & a_n & \ddots & \ddots & a_e & \cdots & \cdots & \cdots \\
\cdots & \cdots & \cdots & \cdots & \cdots & a_{sw} & \ddots & \ddots & a_s & a_p & a_n & \ddots & \ddots & a_e & \cdots & \cdots \\
\cdots & \cdots & \cdots & \cdots & a_s & \cdots & a_w & \ddots & \ddots & a_s & a_p & a_n & \ddots & \ddots & a_e & \cdots \\
\cdots & \cdots & \cdots & \cdots & \cdots & \cdots & \cdots & a_w & \ddots & \ddots & a_s & a_p & a_n & \ddots & \ddots & a_e \\
\cdots & \cdots & a_s & \cdots & \cdots & \cdots & \cdots & \cdots & a_w & \ddots & \ddots & a_s & a_p & a_n & \ddots & \ddots \\
\cdots & \cdots & \cdots & \cdots & \cdots & \cdots & \cdots & \cdots & \cdots & a_w & \ddots & \ddots & a_s & a_p & a_n & \ddots \\
a_s & \cdots & \cdots & \cdots & \cdots & \cdots & \cdots & \cdots & \cdots & \cdots & a_w & \ddots & \ddots & a_s & a_p & a_n \\
\cdots & \cdots & \cdots & \cdots & \cdots & \cdots & \cdots & \cdots & \cdots & \cdots &  & a_w & \ddots & \ddots & a_s & a_p
\end{pmatrix}$$

## A.5 Particle in simple shear flow

In this section we will investigate three major cases of a particle in a simple shear flow ($u = \dot{\gamma} \cdot y$). All cases are inevitably 3D. The first one concerns a fixed particle where no-slip condition is given at its surface. Subsequently, a rotating particle with a fixed rotation rate is studied, hence a fixed velocity has to be implemented on the particle surface. Finally a free particle (torque-free) has been reviewed, the boundary conditions at the particle surface in this case have to vary in time in order to balance the torque applied by the flow.

Before we start, lets give the coordinate system used in JADIM (Figure A.18). These coordinates will help us to write the boundary conditions on the particle's surface.

The results will be compared with the analytical results given by R Mikulencak, these results are available for small Reynolds number ($Re = \frac{\dot{\gamma} D^2}{\nu} < 1$) only. That's why simulations have been run with small Reynolds number :

$$\begin{cases} u_x = \dot{\gamma}(\frac{1}{2}y(1-r^{-5}) + \frac{1}{2}y(1-r^{-3}) - \frac{5}{2}x^2y(r^{-5}-r^{-7})) - \frac{\Omega y}{r^3} \\ u_y = \dot{\gamma}(\frac{1}{2}x(1-r^{-3}) - \frac{1}{2}x(1-r^{-3}) - \frac{5}{2}y^2x(r^{-5}-r^{-7})) - \frac{\Omega x}{r^3} \\ u_z = -\frac{5}{2}\dot{\gamma}xyz(r^{-5}-r^{-7}) \end{cases}$$

The above equation is dimensionless, the coordinates have been scaled by the particle diameter ($R = 1$), and velocities with $R\dot{\gamma}$

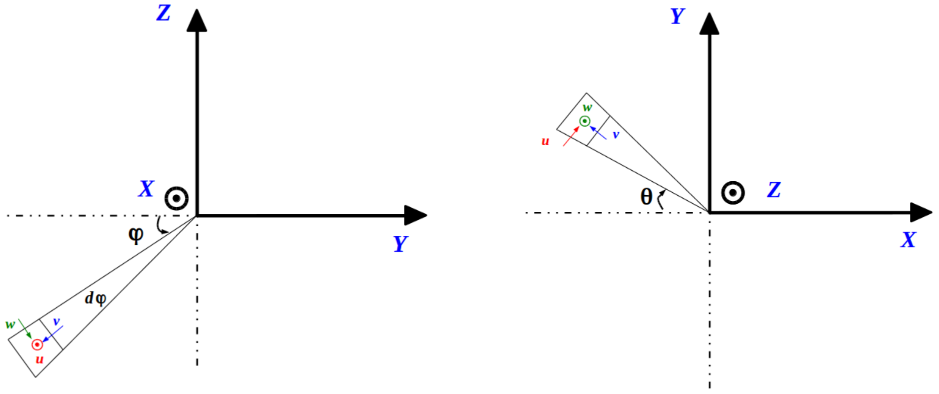

Figure A.18: Spherical coordinates used in JADIM code.

### A.5.1 Fixed particle

As presented in the previous reporting, the results show great agreement with analytical solutions. Figures A.19 and A.20 present the main comparisons with the analytical solutions

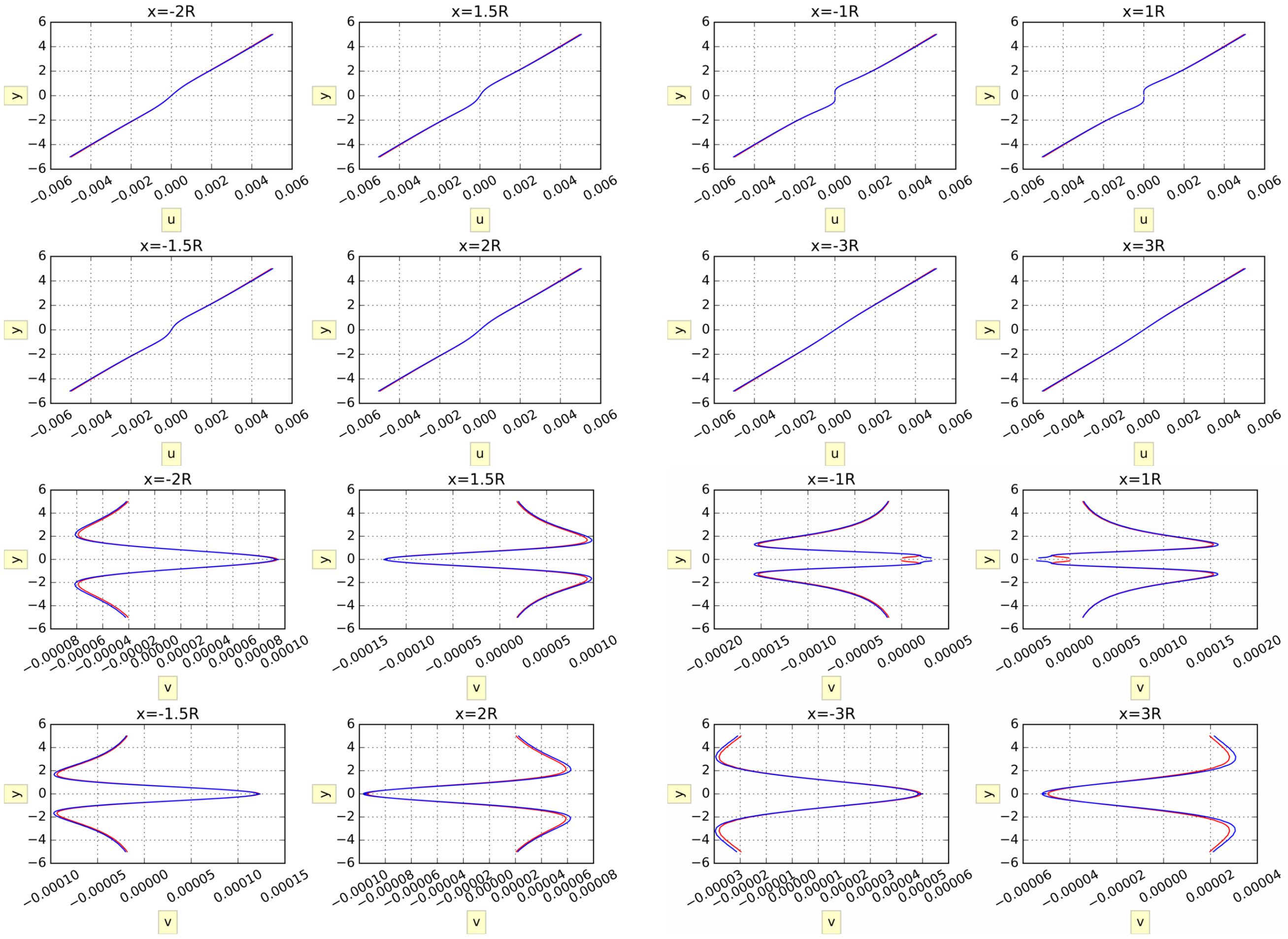

Figure A.19: Velocity profiles (Re=0.1) :Blue: JADIM computation, Red: Analytical solution.

### A.5.2 Rotating particle (Fixed rotation)

For a rotating particle with a given rotation rate $\Omega$, the velocity on its surface is given by $\mathbf{u} = \mathbf{\Omega} \wedge \mathbf{r}$. The previous results of a rotating particle in a simple shear flow diverges from the analytical solutions. I realize while playing with a small sphere that the boundary conditions at the particle's surface were just wrong ($w = 0$ in the previous

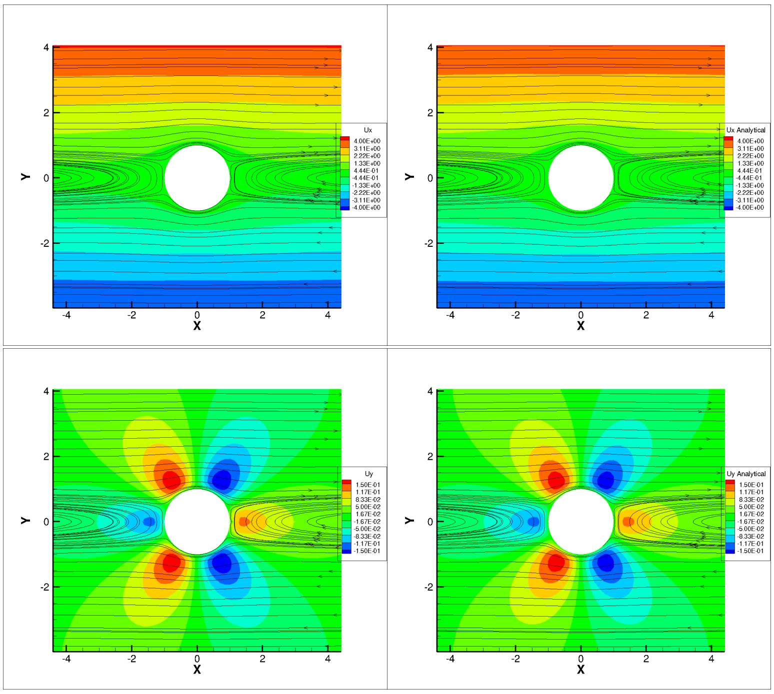

Figure A.20: Velocity field distribution ($Re = 0.01$): Left column: computation , Right column: Analytical results.

case) ! The new conditions are given as follows. $(u, v, w)$ are depicted in the Figure A.18.

$$\begin{cases} al1 = u = -\Omega\cos(\varphi) \\ al2 = v = 0 \\ al3 = w = \Omega\cos(\theta)\sin(\varphi) \end{cases} \tag{A.5.1}$$

Results show great agreement with the analytical solutions as shown in Figures A.21 and A.22

### A.5.3 Torque-free particle

In a simple shear flow, the particle is subject to a torque applied by the flow on the surface of the particle. A free particle will be draged by the torque, it hence starts rotation along the axis $\Delta$ as presented in Figure A.23.

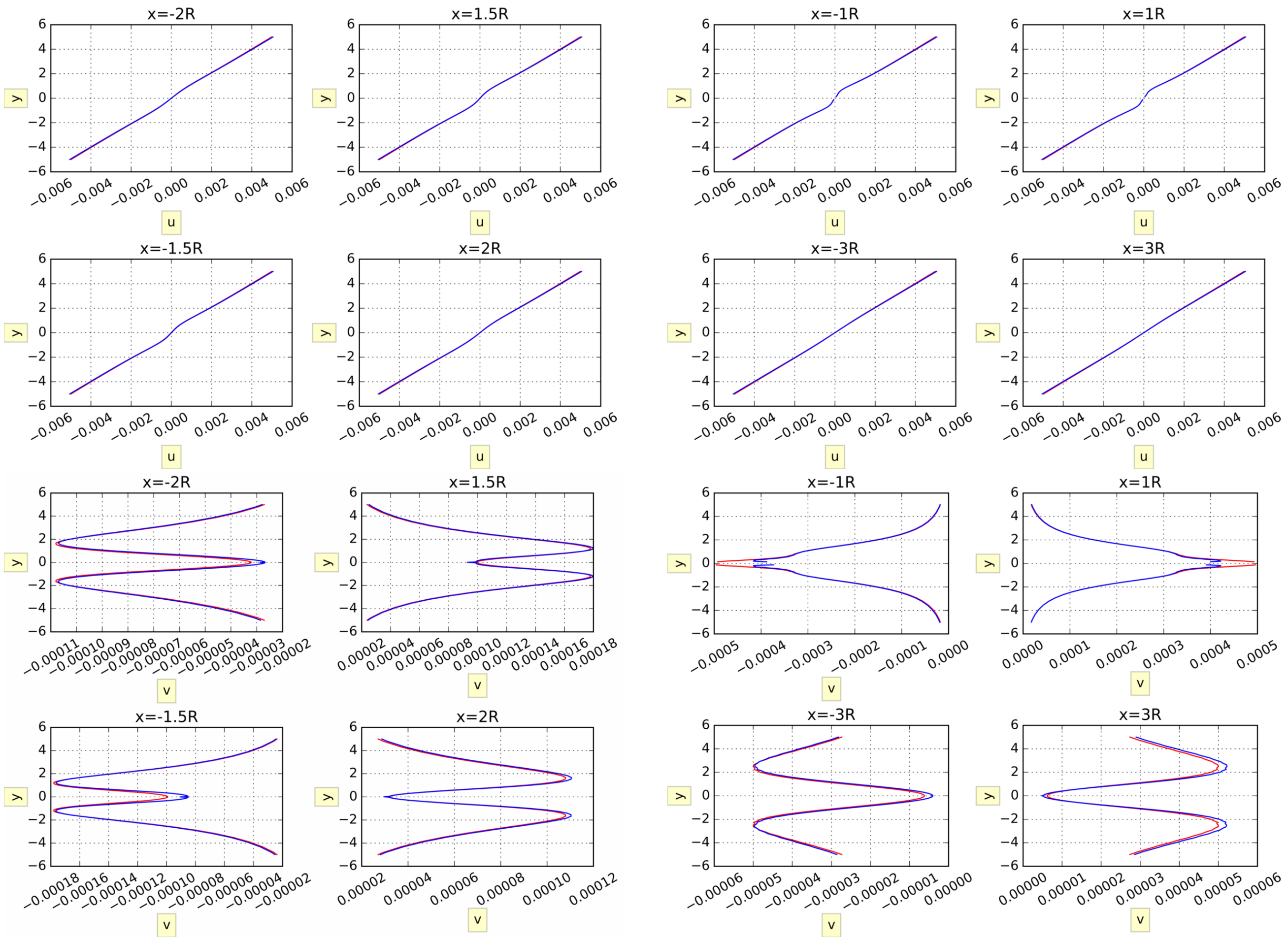

Figure A.21: Blue: JADIM computation, Red: Analytical solution.

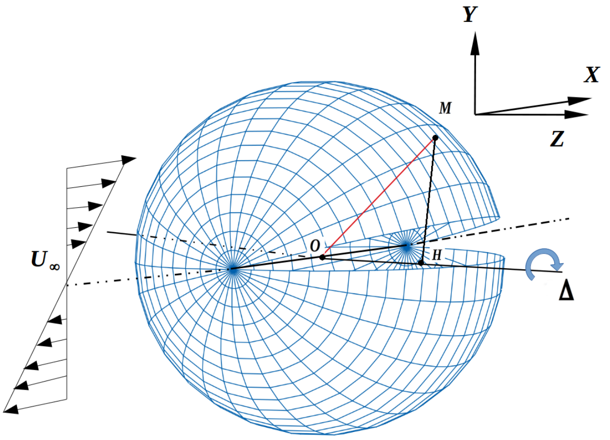

Figure A.23: Scheme of the rotating particle.

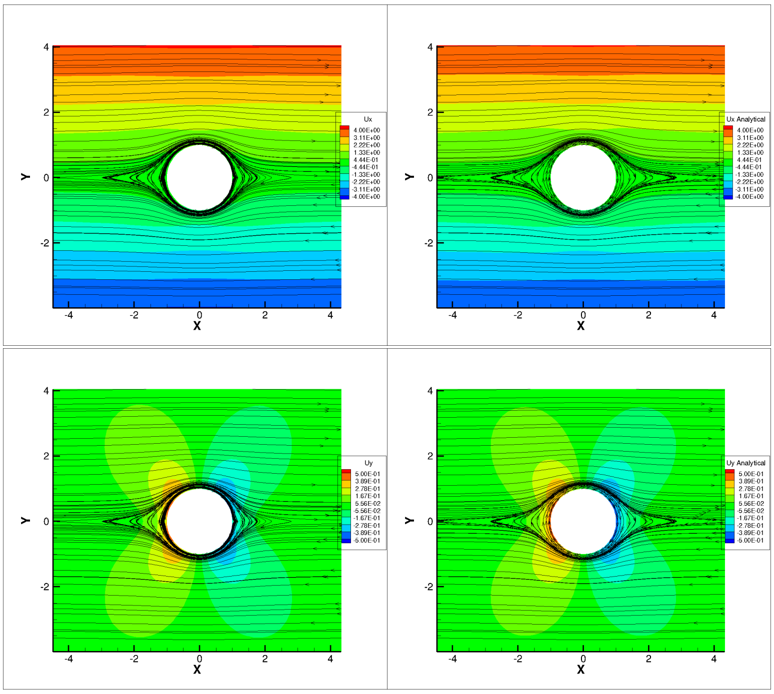

Figure A.22: Velocity field distribution ($Re = 0.01$): Left column: computation , Right column: Analytical results.

The transient evolution of the rotation rate is ruled by the second law of rotational motion (Eq A.5.2).

$$\frac{d\mathbf{L_o}}{dt} = \int_{Sphere} \mathbf{r} \wedge (\mathbf{T} \cdot \mathbf{n}) dA_s \tag{A.5.2}$$

We project the previous equation on the axis of rotation ($\Delta$), we note $J_\triangle$ as the moment of inertia along $\Delta$, Therefore :

$$\begin{cases} \mathbf{L_o} \cdot \mathbf{e_\Delta} = J_\triangle \overrightarrow{\boldsymbol{\Omega}} \cdot \mathbf{e_\Delta} = J_\triangle \dot{\theta} \\ \mathbf{T} \cdot \mathbf{n} = \underbrace{-p\mathbf{n}}_{pressure} + \underbrace{\boldsymbol{\tau} \cdot \mathbf{n}}_{viscous forces} \\ \mathbf{r} = \overrightarrow{OM} \end{cases} \tag{A.5.3}$$

We develop the previous equation in the following lines:

$$
\begin{aligned}
J_{\Delta}\ddot{\theta} &= \int_{Sphere} (\mathbf{r} \wedge \mathbf{T} \cdot \mathbf{n}) \cdot \mathbf{e}_{\boldsymbol{\Delta}} dA_s \\
&= \int_{Sphere} (\mathbf{T} \cdot \mathbf{n}) \cdot (\mathbf{e}_{\boldsymbol{\Delta}} \wedge (\overrightarrow{OH} + \overrightarrow{HM})) dA_s \\
As \quad & \overrightarrow{OH} // \mathbf{e}_{\boldsymbol{\Delta}} \quad \text{and} \quad |\overrightarrow{HM}| = h \\
J_{\Delta}\ddot{\theta} &= \int_{Sphere} (\mathbf{T} \cdot \mathbf{n}) \cdot (h\mathbf{e}_{\varphi}) dA_s \\
&= \int_{Sphere} h(\tau \cdot \mathbf{n}) \cdot \mathbf{e}_{\varphi} dA_s
\end{aligned}
$$

An explicit temporal scheme allows us to derive the previous equation as :

$$
\dot{\theta}^{n+1} = \dot{\theta}^{n} + \frac{1}{J_{\Delta}} \left[ \int_{Sphere} h\tau^{n}_{1,2} dA_s \right] \cdot dt \tag{A.5.4}
$$

Using the spherical coordinate, the torque along $\Delta$ can be calculated as :

$$
\int_{Sphere} (\mathbf{r} \wedge \mathbf{T} \cdot \mathbf{n}) \cdot \mathbf{e}_{\boldsymbol{\Delta}} dA_s = \int_{Sphere} (\cos(\varphi)\tau_{r,\theta} + \cos(\theta)\sin(\varphi)\tau_{r,\varphi}) dA_s \tag{A.5.5}
$$

The impact of $J_{\Delta}$ and the initialization of the rotation rate ($\Omega_0$) has been investigated through a parametric study. Before any calculation, we can say that for big $J_{\Delta}$, the particle has more inertia, thus it will respond slowly to the torque before it settle to a constant rotation rate. Therefore, $J_{\Delta}$ allows to control the transient time. $\Omega_0$ plays a different role. For $\Omega_0 = 0$ the torque is positive, it contribute to the rotation of the particle. At some values of $\Omega_0$, the torque becomes negative, and it will resist the particle rotation. In our study we will study three cases ($\Omega_0 = 10\dot{\Omega}$, $\Omega_0 = \dot{\Omega}$ and $\Omega_0 = \dot{\Omega}/2$). Figures A.24 and A.25 support our predictions. We can note that for all cases $\Omega/\dot{\gamma}$ converges toward a well defined value. In our simulations this values is $\Omega/\dot{\gamma} = 0.483$. It corresponds approximately to the analytical value (ie $\Omega/\dot{\gamma} = 0.5$). Figure A.26 displays a comparison with the analytical solutions.

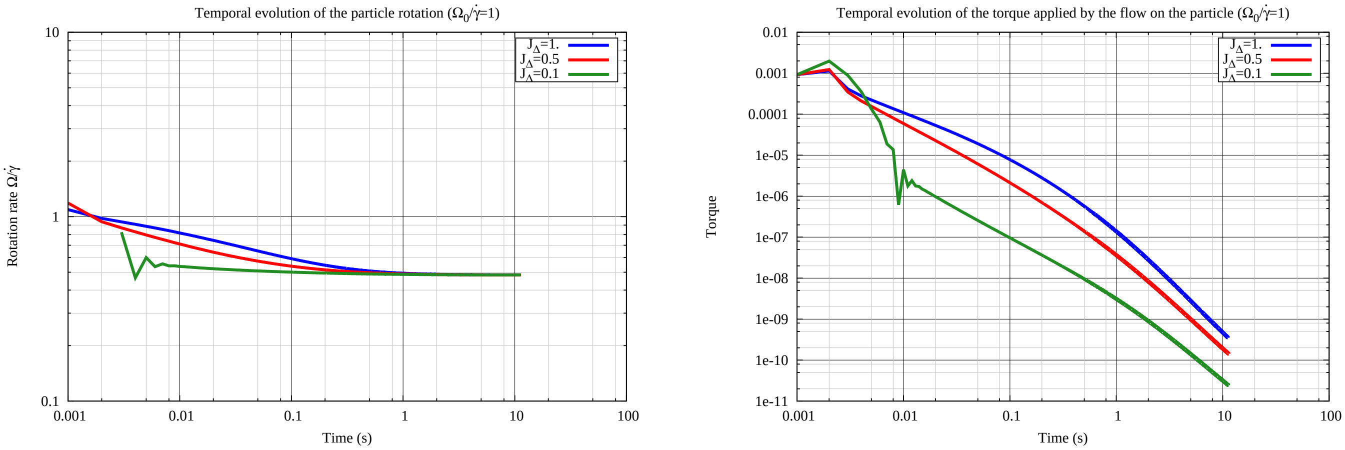
Temporal evolution of the particle rotation ($\Omega_0/\dot{\gamma}$=1)

Temporal evolution of the torque applied by the flow on the particle ($\Omega_0/\dot{\gamma}$=1)

Figure A.24: Temporal evolution of the particle's rotation rate and torque for different $J_\Delta$.

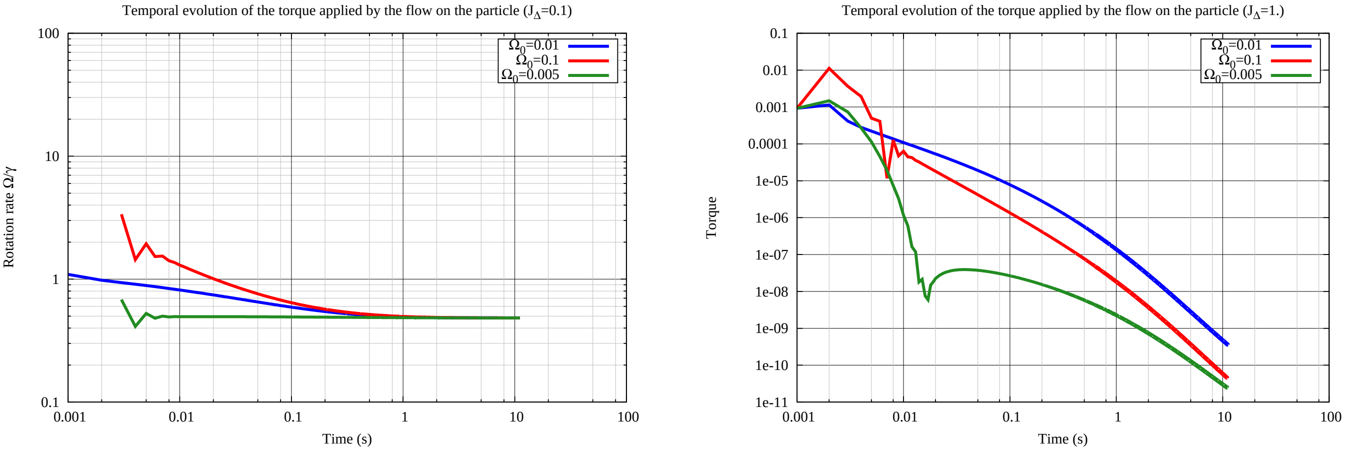
Temporal evolution of the torque applied by the flow on the particle ($J_\Delta$=0.1)

Temporal evolution of the torque applied by the flow on the particle ($J_\Delta$=1.)

Figure A.25: Temporal evolution of the particle's rotation rate and torque for different $\Omega_0$.

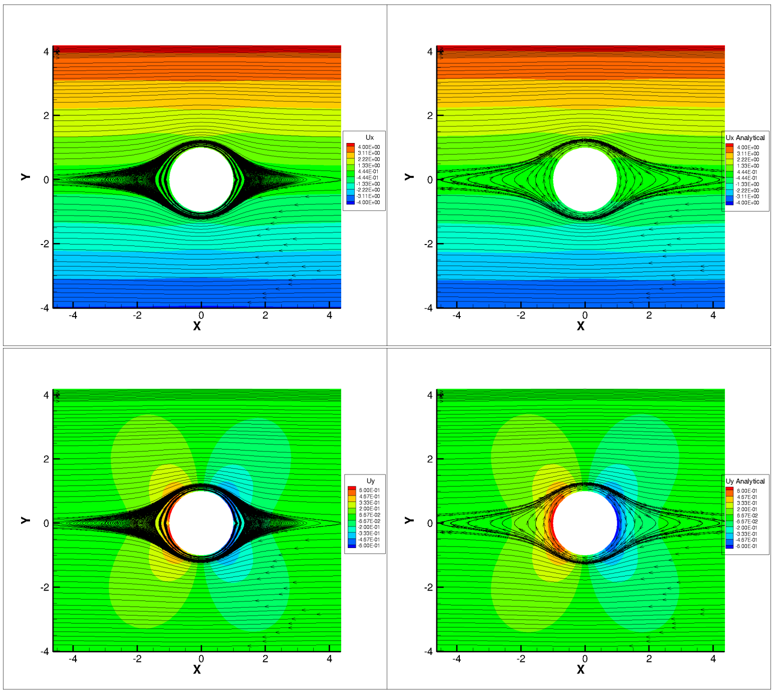

Figure A.26: Velocity field distribution ($Re = 0.1$): Left column: computation , Right column: Analytical results.

# References

Abramzon, B. and Elata, C. (1984). Unsteady heat transfer from a single sphere in stokes flow. *International journal of heat and mass transfer*, 27(5):687–695. 34

Abramzon, B. and Fishbein, G. (1977). Some problems of convective diffusion to a spherical particle with $pe \leq 1000$. *Journal of engineering physics*, 32(6):682–686. 34

Acrivos, A. and Taylor, T. D. (1962). Heat and mass transfer from single spheres in stokes flow. *The Physics of Fluids*, 5(4):387–394. 35

Albert, C., Kromer, J., Robertson, A., and Bothe, D. (2015). Dynamic behaviour of buoyant high viscosity droplets rising in a quiescent liquid. *Journal of Fluid Mechanics*, 778:485–533. 122

Alexandrova, S., Karsheva, M., Saboni, A., and Gourdon, C. (2014a). Effect of the viscosity ratio on the mass transfer into a spherical drop in liquid-liquid dispersions. *Journal of Chemical Technology and Metallurgy*, 49(5):429–434. 10, 35, 104, 106

Alexandrova, S., Karsheva, M., Saboni, A., and Gourdon, C. (2014b). Effect of the viscosity ratio on the mass transfer into a spherical drop in liquid-liquid dispersions. *Journal of Chemical Technology and Metallurgy*, 49(5):429–434. 109, 110, 111

Basset, A. B. (1887). On the motion of a sphere in a viscous liquid. *Proceedings of the Royal Society of London Series I*, 43:174–175. 85

Batchelor, G. K. (2000). *An introduction to fluid dynamics*. Cambridge university press. 44

Beitel, A. and Heideger, W. J. (1971). Surfactant effects on mass transfer from drops subject to interfacial instability. *Chemical Engineering Science*, 26(5):711–717. 35

Blanco, A. and Magnaudet, J. (1995). The structure of the axisymmetric high-reynolds number flow around an ellipsoidal bubble of fixed shape. *Physics of fluids*, 7(6):1265–1274. 81

Boussinesq, J. (1885). Sur la resistance quoppose un liquide indefini en repos, sans pesanteur, au movement varie d'une shere solide. *CR Acad. Sci. Paris*, 100:985–937. 85

Brauer, H. (1978). Unsteady state mass transfer through the interface of spherical particles—i: physical and mathematical description of the mass-transfer problem. *International Journal of Heat and Mass Transfer*, 21(4):445–453. 34, 95

Calmet, I. (1995). *Analyse par simulation des grandes échelles des mouvements turbulents et du transfert de masse sous une interface plane*. PhD thesis, Toulouse, INPT. 52, 57

Calmet, I. and Magnaudet, J. (1997). Large-eddy simulation of high-schmidt number mass transfer in a turbulent channel flow. *Physics of Fluids*, 9(2):438–455. 52, 54

Clift, R., Grace, J., and Weber, M. (1978). Bubbles, drops, and particles. 7, 8, 29, 31, 32, 34, 35, 70, 71, 78, 81, 111

Clift, R., Grace, J. R., and Weber, M. E. (2005). *Bubbles, drops, and particles*. Courier Corporation. 29

Colombet, D., Legendre, D., Cockx, A., and Guiraud, P. (2013). Mass or heat transfer inside a spherical gas bubble at low to moderate reynolds number. *International Journal of Heat and Mass Transfer*, 67:1096–1105. 36, 104, 105, 108

Cooper, F. (1977). Heat transfer from a sphere to an infinite medium. *International Journal of Heat and Mass Transfer*, 20(9):991–993. 36

Danckwerts, P. (1951). Significance of liquid-film coefficients in gas absorption. *Industrial & Engineering Chemistry*, 43(6):1460–1467. 38

Edelmann, C. A., Le Clercq, P. C., and Noll, B. (2017). Numerical investigation of different modes of internal circulation in spherical drops: Fluid dynamics and mass/heat transfer. *International Journal of Multiphase Flow*, 95:54–70. 12, 13, 122, 123, 128, 129, 132, 134, 136, 137, 138, 140, 141, 143, 145, 146

Engberg, R. F. and Kenig, E. Y. (2015). An investigation of the influence of initial deformation on fluid dynamics of toluene droplets in water. *International Journal of Multiphase Flow*, 76:144–157. 123

Feng, Z.-G. and Michaelides, E. E. (2001a). Drag coefficients of viscous spheres at intermediate and high reynolds numbers. *Journal of Fluids Engineering*, 123(4):841–849. 7, 8, 15, 33, 64, 65, 66, 67, 73, 79, 135, 143

Feng, Z.-G. and Michaelides, E. E. (2001b). Heat and mass transfer coefficients of viscous spheres. *International journal of heat and mass transfer*, 44(23):4445–4454. 35, 98, 102, 104

Gary Leal, L. (1993). *Laminar Flow and Convective Transport Processes*. Taylor & Francis. 13, 44, 45, 155

Gatignol, R. (1983). The faxén formulas for a rigid particle in an unsteady non-uniform stokes-flow. *Journal de Mécanique théorique et appliquée*, 2(2):143–160. 83

Gatignol, R. (2007). On the history term of boussinesq–basset when the viscous fluid slips on the particle. *Comptes Rendus Mécanique*, 335(9-10):606–616. 86

Grace, J., Wairegi, T., and Nguyen, T. (1976). Shapes and velocities of single drops and bubbles moving freely through immiscible liquids. *Trans. Inst. Chem. Eng*, 54(3):167–173. 30

Greene, G., Irvine Jr, T., Gyves, T., and Smith, T. (1993). Drag relationships for liquid droplets settling in a continuous liquid. *AIChE journal*, 39(1):37–41. 123

Hadamard, J. (1911). Mouvement permanent lent d'une sphere liquid et visqueuse dans un liquide visqueux. *CR Hebd. Seances Acad. Sci. Paris*, 152:1735–1738. 78, 87

Harper, J. (1972). The motion of bubbles and drops through liquids. *Adv. Appl. Mech*, 12(59):129. 32

Higbie, R. (1935). The rate of absorption of a pure gas into a still liquid during short periods of exposure. *Trans. AIChE*, 31:365–389. 38

Johns, L. and Beckmann, R. (1966). Mechanism of dispersed-phase mass transfer in viscous, single-drop extraction systems. *AIChE Journal*, 12(1):10–16. 110

Johnson, A. and Braida, L. (1957). The velocity of fall of circulating and oscillating liquid drops through quiescent liquid phases. *Can. J. Chem. Eng*, 35:165–172. 29

Johnson, T. and Patel, V. (1999). Flow past a sphere up to a reynolds number of 300. *Journal of Fluid Mechanics*, 378:19–70. 122

Juncu, G. (2001a). The influence of the henry number on the conjugate mass transfer from a sphere. *Heat and mass transfer*, 37(4-5):519–530. 36

Juncu, G. (2001b). Unsteady heat and/or mass transfer from a fluid sphere in creeping flow. *International journal of heat and mass transfer*, 44(12):2239–2246. 36

Juncu, G. (2010). A numerical study of the unsteady heat/mass transfer inside a circulating sphere. *International Journal of Heat and Mass Transfer*, 53(15-16):3006–3012. 8, 10, 36, 71, 72, 74, 104, 106, 109, 110, 123

Kennedy, M., Pozrikidis, C., and Skalak, R. (1994). Motion and deformation of liquid drops, and the rheology of dilute emulsions in simple shear flow. *Computers & fluids*, 23(2):251–278. 12, 129, 130

Kleinman, L. S. and Reed, X. (1996). Unsteady conjugate mass transfer between a single droplet and an ambient flow with external chemical reaction. *Industrial & engineering chemistry research*, 35(9):2875–2888. 8, 36, 73, 74, 113, 123

Kronig, R. and Brink, J. (1951). On the theory of extraction from falling droplets. *Applied Scientific Research*, 2(1):142. 35, 71, 73, 105

Kumar, A. and Hartland, S. (1999). Correlations for prediction of mass transfer coefficients in single drop systems and liquid–liquid extraction columns. *Chemical Engineering Research and Design*, 77(5):372–384. 35

Lautrup, B. (2011). *Physics of continuous matter: exotic and everyday phenomena in the macroscopic world*. CRC press. 45

Legendre, D. (1996). *Quelques aspects des forces hydrodynamiques et des transferts de chaleur sur une bulle sphérique*. PhD thesis, Toulouse, INPT. 7, 11, 52, 53, 56, 57, 86, 124

Legendre, D. and Magnaudet, J. (1997). A note on the lift force on a spherical bubble or drop in a low-reynolds-number shear flow. *Physics of Fluids*, 9(11):3572–3574. 52

Legendre, D. and Magnaudet, J. (1998). The lift force on a spherical bubble in a viscous linear shear flow. *Journal of Fluid Mechanics*, 368:81–126. 124

Levich, V. G., Technica, S., et al. (1962). *Physicochemical hydrodynamics*, volume 69. Prentice-hall Englewood Cliffs, NJ. 35

Lewis, J. and Pratt, H. (1953). Oscillating droplets. *Nature*, 171(4365):1155. 35

Lewis, W. and Whitman, W. (1924). Principles of gas absorption. *Industrial & Engineering Chemistry*, 16(12):1215–1220. 36

Li, R., Zhang, J., Yong, Y., Wang, Y., and Yang, C. (2015). Numerical simulation of steady flow past a liquid sphere immersed in simple shear flow at low and moderate re. *Chinese Journal of Chemical Engineering*, 23(1):15–21. 129

Lovalenti, P. M. and Brady, J. F. (1993). The force on a sphere in a uniform flow with small-amplitude oscillations at finite reynolds number. *Journal of Fluid Mechanics*, 256:607–614. 93

Magnaudet, J., Rivero, M., and Fabre, J. (1995). Accelerated flows past a rigid sphere or a spherical bubble. part 1. steady straining flow. *Journal of fluid mechanics*, 284:97–135. 52, 54, 57

Maxey, M. R. and Riley, J. J. (1983). Equation of motion for a small rigid sphere in a nonuniform flow. *The Physics of Fluids*, 26(4):883–889. 83

Mei, R. and Adrian, R. J. (1992). Flow past a sphere with an oscillation in the free-stream velocity and unsteady drag at finite reynolds number. *Journal of Fluid Mechanics*, 237:323–341. 93

Mei, R. and Klausner, J. F. (1992). Unsteady force on a spherical bubble at finite reynolds number with small fluctuations in the free-stream velocity. *Physics of Fluids A: Fluid Dynamics*, 4(1):63–70. 8, 33, 78, 79, 80

Michaelides, E. (2006). *Particles, bubbles & drops: their motion, heat and mass transfer*. World Scientific Publishing Company Incorporated. 29

Michaelides, E. and Feng, Z.-G. (1995). The equation of motion of a small viscous sphere in an unsteady flow with interface slip. *International Journal of Multiphase Flow*, 21(2):315–321. 85, 86

Mikulencak, D. R. and Morris, J. F. (2004). Stationary shear flow around fixed and free bodies at finite reynolds number. *Journal of Fluid Mechanics*, 520:215–242. 129

Milne-Thomson, L. M. (1968). *Theoretical hydrodynamics*. Courier Corporation. 181

Natarajan, R. and Acrivos, A. (1993). The instability of the steady flow past spheres and disks. *Journal of Fluid Mechanics*, 254:323–344. 122

Newman, A. B. (1931). The drying of porous solids: diffusion and surface emission equations. *AIChE Trans.*, 27:203–220. 35, 68, 105

Nguyen, H. D., Paik, S., and Chung, J. N. (1993). Unsteady conjugate heat transfer associated with a translating spherical droplet: a direct numerical simulation. *Numerical Heat Transfer, Part A: Applications*, 24(2):161–180. 113

Oliver, D. and Chung, J. (1987). Flow about a fluid sphere at low to moderate reynolds numbers. *Journal of Fluid Mechanics*, 177:1–18. 15, 64, 65, 66, 68, 73

Oliver, D. and Chung, J. (1990). Unsteady conjugate heat transfer from a translating fluid sphere at moderate reynolds numbers. *International Journal of Heat and Mass Transfer*, 33(3):401–408. 110, 113

Oliver, D. and De Witt, K. (1995). Heat transfer in bubbles and droplets at moderate reynolds numbers: interior problem. Technical report, American Inst. of Chemical Engineers, New York, NY (United States). 104

Oliver, D. L. and Chung, J. N. (1986). Conjugate unsteady heat transfer from a spherical droplet at low reynolds numbers. *International journal of heat and mass transfer*, 29(6):879–887. 8, 36, 72, 74, 123

Paschedag, A., Piarah, W., and Kraume, M. (2005). Sensitivity study for the mass transfer at a single droplet. *International journal of heat and mass transfer*, 48(16):3402–3410. 29, 36

Premlata, A.-R. and Wei, H.-H. (2019). The basset problem with dynamic slip: Slip-induced memory effect and slip-stick transition. *Journal of Fluid Mechanics*, Submitted. 86

Rivero, M. (1991). *Etude par simulation numérique des forces exercées sur une inclusion sphérique par un écoulement accéléré*. PhD thesis, Toulouse, INPT. 52, 53

Ruckenstein, E. (1967). Mass transfer between a single drop and a continuous phase. *International Journal of Heat and Mass Transfer*, 10(12):1785–1792. 36

Rybczynski, W. (1911). On the translatory motion of a fluid sphere in a viscous medium. *Bull. Acad. Sci., Cracow, Series A*, 40. 33, 78, 87

Ryvkind, V. and Ryskin, G. (1976). Flow structure in motion of a spherical drop in a fluid medium at intermediate reynolds number. *Fluid Dyn*, 11(5). 33, 78

Saboni, A. and Alexandrova, S. (2002). Numerical study of the drag on a fluid sphere. *AIChE journal*, 48(12):2992–2994. 33

Saboni, A., Alexandrova, S., Karsheva, M., and Gourdon, C. (2011). Mass transfer from a contaminated fluid sphere. *AIChE Journal*, 57(7):1684–1692. 35

Sadhal, S. and Johnson, R. E. (1983). Stokes flow past bubbles and drops partially coated with thin films. part 1. stagnant cap of surfactant film–exact solution. *Journal of Fluid Mechanics*, 126:237–250. 32

Schiller, L. (1933). Über die grundlegenden berechnungen bei der schwerkraftaufbereitung. *Z. Vereines Deutscher Inge.*, 77:318–321. 8, 33, 78, 79, 80

Schulze, K. (2007). Stoffaustausch und fluiddynamik am bewegten einzeltropfen unter dem einfluss von marangonikonvektion. 7, 28

Slater, M. (1994). Rate coefficients in liquid–liquid extraction systems. *Liquid-liquid extraction equipment*, 1:45–94. 27

Stokes, G. (1851). On the effect of internal friction of fluids on the motion of pendulums. trans. cambr. phil. 33, 78

Subramanian, G. and Koch, D. (2006). Centrifugal forces alter streamline topology and greatly enhance the rate of heat and mass transfer from neutrally buoyant particles to a shear flow. *Physical review letters*, 96(13):134503. 129

Taneda, S. (1956). Experimental investigation of the wake behind a sphere at low reynolds numbers. *Journal of the Physical Society of Japan*, 11(10):1104–1108. 122

Thorsen, G., Stordalen, R., and Terjesen, S. (1968). On the terminal velocity of circulating and oscillating liquid drops. *Chemical Engineering Science*, 23(5):413–426. 12, 123, 132, 135, 136

Tomboulides, A. G. and Orszag, S. A. (2000). Numerical investigation of transitional and weak turbulent flow past a sphere. *Journal of Fluid Mechanics*, 416:45–73. 122

Wegener, M., Paul, N., and Kraume, M. (2014). Fluid dynamics and mass transfer at single droplets in liquid/liquid systems. *International Journal of Heat and Mass Transfer*, 71:475–495. 34

Winnikow, S. and Chao, B. (1966). Droplet motion in purified systems. *the Physics of Fluids*, 9(1):50–61. 122, 123

Yang, S.-M. and Leal, L. (1991). A note on memory-integral contributions to the force on an accelerating spherical drop at low reynolds number. *Physics of Fluids A: Fluid Dynamics*, 3(7):1822–1824. 85

Zhang, J., Yang, C., and Mao, Z.-S. (2012). Mass and heat transfer from or to a single sphere in simple extensional creeping flow. *AIChE Journal*, 58(10):3214–3223. 13, 156